

**The Next Generation of Interferometry:
Multi-Frequency Optical Modelling, Control Concepts
and Implementation**

Vom Fachbereich Physik
der Universität Hannover
zur Erlangung des Grades

Doktor der Naturwissenschaften
– Dr. rer. nat. –

genehmigte Dissertation von

Dipl.-Phys. Andreas Freise

geboren am 24. Mai 1971 in Hildesheim

2003

Referent: Prof. K. Danzmann
Korreferent: Prof. W. Ertmer
Tag der Promotion: 04. Februar 2003
Druckdatum: 22. Februar 2003

Zusammenfassung

Albert Einstein hat in seiner allgemeinen Relativitätstheorie die Existenz von Gravitationswellen vorhergesagt. Die direkte Meßung dieser Wellen ist eine der großen Herausforderungen der Experimentalphysik. Mit Hilfe eines Netzwerkes von Gravitationswellendetektoren wird es möglich sein, das Universum unabhängig von elektro-magnetischer Strahlung zu beobachten. Die Gravitationswellenastronomie wird der Kosmologie und der Gravitationsphysik neue, bisher unerreichbare experimentelle Daten zur Verfügung stellen.

Zur Zeit werden weltweit fünf große interferometrische Gravitationswellendetektoren gebaut. Sie basieren auf klassischen Instrumenten wie z.B. dem Michelson-Interferometer. Für die Suche nach Gravitationswellen ist allerdings eine extrem hohe, bisher unerreichte Meßempfindlichkeit notwendig. Diese soll durch den Einsatz von weiterentwickelten, optimierten Teilsystemen des Interferometers und durch die Entwicklung neuer Interferometertopologien erreicht werden.

Diese Arbeit dokumentiert einen wichtigen Teil des Aufbaus des britisch-deutschen Detektors GEO 600, der sich zur Zeit in der Testphase befindet und erste Meßdaten aufnimmt. Im ersten Abschnitt werden das Modenfilter-System und die Laserfrequenzstabilisierung beschrieben, welche im Rahmen dieser Arbeit aufgebaut wurden. Um die benötigte extrem hohe Empfindlichkeit zu erreichen, muß der verwendete Laserstrahl bezüglich räumlicher und zeitlicher Fluktuationen gefiltert und stabilisiert werden. Dies wird erreicht durch zwei sequentielle Ringresonatoren, sogenannte Modenfilter, mit aufgehängten Spiegeln und einer Umlauflänge von jeweils 8 m. Diese Resonatoren ersetzen außerdem den üblichen festen Referenzresonator für die Frequenzstabilisierung des Lasers. Mit Hilfe von Pound-Drever-Hall-Regelungen wurde eine (in-loop) Frequenzstabilität von $100\mu\text{Hz}/\sqrt{\text{Hz}}$ bei 100 Hz erreicht. Die Modenfilter und die Frequenzstabilisierung arbeiten äußerst zuverlässig; es konnte ein kontinuierlicher Betrieb von über 120 Stunden demonstriert werden. Die Kontrollsysteme sind automatisiert, so daß im Normalbetrieb kein manueller Eingriff erforderlich ist.

Im zweiten Teil der Arbeit werden fortschrittliche Interferometermethoden besprochen. GEO 600 wird als erster Detektor das sogenannte Dual-Recycling verwenden, welches die Empfindlichkeit des Detektors erhöht und eine Abstimmung auf eine gewünschte Signalfrequenz der Gravitationswelle erlaubt. Dies wird durch einen zusätzlichen Spiegel im Interferometerausgang erreicht. Ein solches Interferometer hat drei longitudinale Freiheitsgrade, die mit Hilfe von Modulation-Demodulations-Methoden stabilisiert werden sollen. Für das Design und Verständnis eines Michelson-Interferometers mit Dual-Recycling ist es zwingend erforderlich, das optische System mit Hilfe einer Modellierung in einem multidimensionalen Parameterraum zu analysieren. Zu diesem Zweck wurde eine numerische Interferometersimulation entwickelt, die es erlaubt, beliebige Laserinterferometer zu simulieren. Das optische System wird hierbei durch ein lineares Gleichungssystem beschrieben, welches numerisch gelöst wird. Die Simulation unterstützt unter anderem Modulation-Demodulations-Techniken und höhere transversale Moden.

Des weiteren wurden im Rahmen dieser Arbeit weiterführende Topologien untersucht, wovon hier das Xylophon-Interferometer vorgestellt wird. Dieses Interferometer stellt eine direkte Erweiterung zum Dual-Recycling dar, die es ermöglicht, die Form der Empfindlichkeitskurve zu optimieren und somit die Empfindlichkeit in einem gewählten Frequenzbereich zu maximieren.

Stichworte: Gravitationswellendetektor, Frequenzstabilisierung, Dual Recycling

Summary

Albert Einstein predicted the existence of gravitational waves in his theory of general relativity. The direct measurement of gravitational waves is one of the most challenging projects in experimental physics. A network of detectors would be able to muster the sky independently of electro-magnetic waves. Gravitational-wave astronomy will provide fascinating new data for cosmology and gravitational physics.

To date, five large-scale interferometric gravitational-wave detectors are being build worldwide. These detectors make use of classic optical instruments such as the Michelson interferometer. The detection of gravitational waves, however, requires an extremely good sensitivity. We aim to achieve the required sensitivity by optimising the subsystems of the interferometer and by using new interferometer topologies.

This work describes important contributions to the British-German detector GEO 600, which is currently commissioned and records first data. First, the mode cleaners and the laser frequency stabilisation are discussed. These systems have been constructed and commissioned within this work. In order to guarantee a good sensitivity, the laser beam has to be filtered in space and time before it enters the Michelson interferometer. Two ring cavities with suspended mirrors and an optical path length of 8 m each have been installed as so-called mode cleaners. In addition, these cavities replace the commonly used rigid reference cavity of the laser frequency stabilisation. By using Pound-Drever-Hall control loops, an (in-loop) frequency stability of $100\mu\text{Hz}/\sqrt{\text{Hz}}$ at 100 Hz was achieved. The mode cleaners and the frequency stabilisation system work reliably; a continuous operation of more than 120 hours could be demonstrated. The control systems have been automated so that no human interaction is required during normal operation.

In the second part of this work, advanced interferometer concepts are discussed. GEO 600 will be the first large-scale detector to use Dual Recycling. By installing an additional mirror in the interferometer output, the shot-noise-limited sensitivity of the detector is enhanced. Furthermore, the detector can then be tuned to a chosen signal frequency (of the gravitational wave). The Dual-Recycled Michelson interferometer has three longitudinal degrees of freedom that are to be controlled using modulation-demodulation techniques. It is essential for the design and understanding of such an interferometer to analyse the optical system using a multi-parameter model. Consequently, a numerical simulation has been developed: A user-defined interferometer topology is described by a linear system of equation that is then solved numerically. The simulation computes a variety of output signals such as error signals and transfer functions; transverse modes of the light or modulation-demodulation schemes can be included in the analysis.

During this work, further advanced interferometer concepts were investigated, and the Xylophone interferometer is introduced here. This interferometer represents a direct extension to a Dual-Recycled Michelson interferometer; it allows to optimise the shape of the shot-noise spectral density and thus maximise the sensitivity in a given frequency band.

Keywords: Gravitational wave detector, frequency stabilisation, Dual Recycling

Contents

Zusammenfassung	i
Summary	iii
Contents	v
List of figures	ix
List of tables	xiii
Glossary	xv
1 The interferometric gravitational-wave detector GEO 600	1
1.1 Introduction	1
1.1.1 Sensitivity of GEO 600	2
1.1.2 Optical setup	5
1.2 Laser system	6
1.2.1 Master laser	7
1.2.2 Slave laser	8
1.2.3 Laser bench	10
1.3 Mode cleaners	12
1.3.1 Mode-cleaner design	14
1.3.2 Optical layout	15
1.3.3 Mounting units	17
1.3.4 Mode matching to the first mode cleaner	19
1.3.5 Optical properties of the mode cleaners	21
1.3.6 Mechanical setup of the suspension system	22
1.4 Michelson interferometer	24
1.4.1 Optical layout	26
1.4.2 Interferometer design	31
1.4.3 Optical properties	33
1.5 Output mode cleaner	34
2 The laser frequency stabilisation for GEO 600	37
2.1 Introduction	37
2.2 Frequency-noise specification	39

2.3	Concept of the length and frequency control	40
2.4	Pound-Drever-Hall control loops	41
2.4.1	Quadrant cameras	43
2.4.2	Piezo-electric transducer	45
2.4.3	Pockels cells	45
2.4.4	Coil-magnet actuator	46
2.5	Laser and first mode cleaner	48
2.5.1	Servo design	50
2.5.2	Error-point spectrum	51
2.5.3	Calibration of frequency-noise measurements	55
2.5.4	‘Current lock’: Feeding back to the pump diode current	57
2.6	Second mode cleaner	57
2.6.1	Servo design	58
2.6.2	Error-point spectrum	59
2.7	Power-Recycling cavity	61
2.7.1	The ‘1200 m experiment’	62
2.7.2	Error-point spectrum	65
2.7.3	Power-Recycled Michelson interferometer	65
2.7.4	Higher-order mode effects	68
2.7.5	DC loop	72
2.8	Remote control and automatic operation	72
2.8.1	Lock acquisition	73
2.8.2	Mode-cleaner control	75
2.8.3	Power-Recycling cavity control	76
2.9	Automatic alignment system	76
3	Advanced interferometer techniques	79
3.1	Introduction	79
3.1.1	Interferometer control	80
3.1.2	Michelson interferometer	81
3.1.3	Shot-noise-limited sensitivity	82
3.1.4	Quantum-noise correlations	84
3.2	Dual Recycling	85
3.2.1	Power Recycling	85
3.2.2	Signal Recycling	87
3.2.3	Dual Recycling for GEO 600	89
3.2.4	Interferometer control	91
3.3	Simulating GEO 600 with Dual Recycling	95
3.3.1	Detuning the Signal-Recycling mirror	97
3.3.2	Error signal for controlling the Michelson interferometer	97
3.3.3	Arm-length difference	99
3.3.4	Error signal for controlling the Signal-Recycling cavity	104
3.3.5	Coupling of noise into the output signal	109
3.4	The Xylophone interferometer	117
3.4.1	Multiple colours	118

3.4.2	Sensitivity	121
3.4.3	Additional control requirements	122
A	The optical layout of GEO 600	125
A.1	OPTOCAD drawing of GEO 600	125
A.2	FINESSE input file with GEO 600 parameters	127
B	Control loops	131
B.1	Open-loop gain	132
B.2	Closing the loop	133
B.3	Stable loops	134
B.3.1	Performance limits	136
B.4	Closed-loop transfer function	137
B.5	Split-feedback paths	141
B.5.1	Measuring the performance of the loop	143
C	Hermite-Gauss modes	145
C.1	Gaussian beams	145
C.2	Paraxial wave equation	146
C.3	Guoy phase shift	148
D	Mode cleaning	151
E	Numerical analysis of optical systems	155
E.1	Introduction	155
E.1.1	Time domain and frequency domain analysis	155
E.2	FINESSE, a numeric interferometer simulation	157
E.2.1	Analysis of optical systems with geometric optics	158
E.2.2	Static response and frequency response	158
E.2.3	Description of light fields	159
E.2.4	Lengths and tunings	159
E.2.5	Phase change on reflection and transmission	160
E.2.6	Modulation of light fields	161
E.2.7	Coupling of light field amplitudes	163
E.2.8	Light sources	168
E.2.9	Detectors and demodulation	173
E.3	Transverse electromagnetic modes	177
E.3.1	Electrical field with Hermite-Gauss modes	177
E.3.2	Coupling of Hermite-Gauss modes	180
E.3.3	Misalignment angles at a beam splitter	182
F	A factor of two	187
G	Electronics	189
G.1	Split photo diode	189
G.2	Electro-optic modulator	190

G.3	Electronic filters	190
G.3.1	First mode cleaner (MC1)	190
G.3.2	Second mode cleaner (MC2)	191
G.3.3	LISO file for the MC1 and MC2 servo electronics	199
H	LabView virtual instruments	207
H.1	Automation statistics	207
H.2	Mode-cleaner control	210
H.3	Power-Recycling cavity control	211
	Bibliography	215
	Acknowledgements	221
	Curriculum vitae	223
	Publications	225

List of figures

1.1	Designed sensitivity of GEO 600	4
1.2	Schematic optical setup of GEO 600	6
1.3	Master-laser system	7
1.4	Slave-laser system	9
1.5	Laser bench with input optics	11
1.6	Optical layout of the mode cleaners (TCMa, TCMb)	15
1.7	Output optics on breadboard east of mode-cleaner system	16
1.8	Mounting unit 3	18
1.9	Amplitude transmittance of higher-order modes through a mode cleaner	21
1.10	Double-pendulum mirror suspension	24
1.11	Schematic layout of the Michelson interferometer	25
1.12	Power-Recycling mirror (TCIb)	27
1.13	Central section of the Michelson interferometer with the beam splitter (TCC)	28
1.14	Output optics on breadboard west of mode-cleaner system	29
1.15	Output telescope and output mode cleaner (TCOa, TCOb)	30
1.16	Output mode cleaner	35
2.1	Frequency-noise requirements	38
2.2	Frequency-control concept	40
2.3	Optical layout with frequency-control loops	42
2.4	Layout of a Pound-Drever-Hall control loop	43
2.5	Electronic circuit of the mode-cleaner photo diodes	44
2.6	Mirror and reaction mass suspended as double pendulums	47
2.7	Control loop for MC1	49
2.8	Closed-loop transfer functions of the MC1 loop	50
2.9	Error-point spectrum of the MC1 control loop	52
2.10	Out-of-loop measurement of the MC1 frequency noise	54
2.11	Spectrum of the feedback signal to the master-laser PZT	55
2.12	Example Pound-Drever-Hall error signal	56
2.13	MC2 control loop	58
2.14	Closed-loop transfer function of the MC2 loop	59
2.15	Frequency-noise measurement of the MC2 loop	60
2.16	Control system for the Power-Recycling cavity	61
2.17	Closed-loop transfer function of the PRC loop	62
2.18	The frequency-stabilisation system of the 1200 m long cavity.	63
2.19	Measurement and simulation of a PRC fringe	64

2.20	Feedback signals during lock acquisition of the PRC control loop	65
2.21	Frequency-noise measurement of the control loop of the 1200 m cavity . .	66
2.22	Control loop for the operating point of the Michelson interferometer . . .	67
2.23	Measurement and simulation of Michelson-interferometer error signals . .	70
2.24	Frequency-noise coupling into the Michelson interferometer error signal . .	71
2.25	Visibility and error signal of a Pound-Drever-Hall loop	74
3.1	Michelson interferometer at the dark fringe	82
3.2	Michelson interferometer with Power Recycling	86
3.3	Michelson interferometer with Signal Recycling	87
3.4	Example sensitivity plots for different Dual-Recycling modes	90
3.5	Michelson interferometer with Schnupp modulation	92
3.6	Control scheme of the Dual-Recycled Michelson interferometer	94
3.7	Resonance condition in the Dual-Recycled Michelson interferometer . . .	95
3.8	Sensitivity maximum as a function of the detuning	98
3.9	Example error-signal slope	99
3.10	Optimisation of the MI error-signal slope	100
3.11	Error-signal slopes (MI loop) for three fixed cavity length differences . . .	101
3.12	The optimum Schnupp modulation frequency for a cavity length difference of 9 cm	101
3.13	Error signals for controlling the Michelson interferometer	102
3.14	MI loop error-signal slope for different MSR positions	103
3.15	MI loop error signals for different MSR displacements	104
3.16	Error signal for controlling the Signal-Recycling cavity	106
3.17	SR loop error signal, detuned to 200 Hz	106
3.18	SR loop error signals for deviations from the dark fringe (tuned recycling)	107
3.19	SR loop error signals for deviations from the dark fringe (detuned recycling)	108
3.20	Thermal-noise-limited sensitivity	110
3.21	Detector output signal for thermal noise	111
3.22	Computed transfer function: amplitude fluctuations to interferometer output	113
3.23	Computed relative power-noise requirement	113
3.24	Computed transfer function: frequency noise to interferometer output . .	115
3.25	Computed frequency-noise requirement	115
3.26	Computed transfer function, oscillator phase noise to interferometer output	116
3.27	Computed requirement for the oscillator phase noise	116
3.28	Phase noise of a HP 33120A signal generator	117
3.29	Optical layout of a Xylophone interferometer	118
3.30	Dark fringe condition as a function of light frequency	120
3.31	Shot-noise-limited sensitivity of a Xylophone interferometer compared to an equivalent Dual-Recycled interferometer	122
3.32	Example of a ‘matched’ shot-noise-limited sensitivity	123
A.1	OPTOCAD drawing of the optical layout of GEO 600	126

B.1 Example open-loop gain of an unconditionally stable loop.	135
B.2 Example open-loop gain of a conditionally stable loop	136
B.3 Measurement of closed-loop transfer functions	139
B.4 Measurement of the open-loop gain	140
E.1 Coupling of light fields at a simplified mirror.	163
E.2 Signal applied to a mirror: modulation of the mirror position	170
E.3 Mirroring a propagation vector at a beam splitter surface	184
E.4 Misalignment angles as functions of the angle of incidence	185
G.1 Schematic diagram of a split photo diode (Centrovision QD50-3T)	189
G.2 Transfer functions of the MC1 filter electronics	193
G.3 Schematic drawing of the filter electronics for MC1 and MC2 (part 1 of 5).	194
G.4 Schematic drawing of the filter electronics for MC1 and MC2 (part 2 of 5).	195
G.5 Schematic drawing of the filter electronics for MC1 and MC2 (part 3 of 5).	196
G.6 Schematic drawing of the filter electronics for MC1 and MC2 (part 4 of 5).	197
G.7 Schematic drawing of the filter electronics for MC1 and MC2 (part 5 of 5).	198
H.1 Virtual instrument ‘automation_stats’	208
H.2 Virtual instrument ‘automation_MC1+2’	210
H.3 Virtual instrument ‘automation_PRC’	211

List of tables

1.1	Specifications of the GEO 600 master laser	8
1.2	Specifications of the GEO 600 slave laser	10
1.3	Design parameters of the mode cleaners	13
1.4	Parameters of the mode-cleaner mirrors	14
1.5	Throughput, visibility and finesse of the mode cleaners	22
1.6	The lowest resonance frequencies of a double-pendulum suspension.	23
1.7	Typical beam radii of the eigen-mode in the Power-Recycling cavity	32
1.8	Design parameters of the Power-Recycling cavity	33
1.9	Design parameters of the output mode cleaner	34
2.1	Duty cycle of the optical systems of GEO 600 during the S1 test run	68
G.1	Specifications of the Centrovision QD50-3T photo diode	189
G.2	Specifications of the New Focus 4004 electro-optic modulator	190
H.1	List of LabView monitor channels	212
H.2	List of LabView control channels	213
H.3	List of LabView control channels (switches)	213

Glossary

ϵ_0	electric permeability of vacuum
\hbar	$h/2\pi$ Planck's constant
\mathcal{F}	finesse
α	angle (often angle of incidence)
$\beta\dots$	angle of misalignment
$\delta\dots$	angle of misalignment
φ	phase of a light field
ϕ	detuning of a mirror (Section E.2.4)
η	quantum efficiency of a photo diode
θ	demodulation phase (at an electronic mixer)
Ψ	Guoy phase
λ	wavelength (of the laser light)
ω	angular frequency
ω_g	angular frequency of a gravitational wave
ω_m	angular frequency of a modulation
ω_s	angular frequency of a test signal
c	speed of light
C	constant factor
E	electric field
f	(Fourier) frequency or focal length
Δf	bandwidth of a cavity as full width at half maximum (FWHM)
F	force
G, H	transfer function (sometimes just the magnitude or gain)
h	amplitude of a gravitational wave in strain
i	$\sqrt{-1}$
k	wave number ω/c

l, L	length
ΔL	arm-length difference of the Michelson interferometer
ΔL_{cav}	length difference between Power-Recycling cavity and Signal-Recycling cavity
m	modulation index
M	mass or matrix
n	index of refraction
N, n	integer
P	light power
q	Gaussian beam parameter
Q	quality factor
r	amplitude reflectance
R	power reflectance
R_C	radius of curvature
t	amplitude transmittance
T	power transmittance
T_{\dots}	transfer function
$u_{nm}(x, y, z)$	Hermite-Gauss mode
V_{π}	half wave voltage (Equation 2.4)
w	beam radius
w_0	beam waist radius
\tilde{x}	(linear single-sided) spectral density of x
z_R	Rayleigh range
z_0	beam waist position
FT $\{x\}$	Fourier transform of x
$J_k(m)$	Bessel function
Re $\{z\}$	real part of the complex number z
Im $\{z\}$	imaginary part of the complex number z

Acq	acquisition/acquire
AD	analogue-digital
arb. units	arbitrary units
AR	anti-reflection
BDI...	beam director input

BDO...	beam director output
BS	beam splitter
bst	beam steerer
CAD	computer-aided design
CMOS	complementary metal oxide semiconductor
cav	cavity
csb	control sideband
DC	very low or zero frequency
DR	Dual Recycling
EOM	electro-optic modulator
EP	error point
FFT	fast Fourier transform
FI...	Faraday isolator
ft	neutral density filter
FWHM	bandwidth of a cavity: full width at half maximum
FSR	free spectral range of a cavity
GEO 600	British-German gravitational-wave detector
GPS	global positioning system
Int	integrator
L	lens
LB	laser bench
LLB...	lens laser bench (Figure 1.5)
LP	low pass
MC	mode cleaner
MCe	mirror central east (Figure 1.11)
MCn	mirror central north (Figure 1.11)
MFe	mirror far east (Figure 1.11)
MFn	mirror far north (Figure 1.11)
MCP	master control computer
ML	master laser (Figure 1.2)
MMC1...	mirror mode cleaner 1 (Figure 1.6)
MMC2...	mirror mode cleaner 2 (Figure 1.6)
MI	Michelson interferometer
mod	modulation
MPR	Power-Recycling mirror
MSR	Signal-Recycling mirror

MU...	mounting unit
Nd:YAG	Neodymium doped Yttrium Aluminium Garnet
N,E,S,W	north, east, south, west
NPRO	non-planar ring oscillator
PBS	polarising beam splitter
OMC	output mode cleaner
PC...	Pockels cell
PD...	photo diode
PDH	Pound-Drever-Hall [Drever83]
pol	polarisation
PR	Power Recycling
PRC	Power-Recycling cavity
PZT	piezo-electric transducer
RF	radio frequency
RHS	'right hand side' of a linear set of equations
rms	root mean square
tr	round trip
qca	quadrant camera
quad	quadrature
shot	shot noise
SL	slave laser
SNR	signal-to-noise ratio
SR	Signal Recycling
SRC	Signal-Recycling cavity
ssb	signal sideband
TCL...	tank central input
TCO...	tank central output
TCM...	tank central mode cleaner
TEM	transverse electro-magnetic mode
TGG	Terbium Gallium Garnet
VI	LabView virtual instrument
Vis	visibility

Chapter 1

The interferometric gravitational-wave detector GEO 600

1.1 Introduction

The existence of gravitational waves was predicted by Albert Einstein, following his theory of general relativity. Gravitational waves are disturbances of space time, created by the acceleration of large masses and travelling through space at the speed of light. A passing gravitational wave changes the local metric of space time and can, in principle, be measured as an acceleration of a test mass. Einstein also believed that these waves would never be measured because of their extremely small amplitude. A first indirect proof of the existence of gravitational waves has been obtained by Hulse and Taylor [Hulse, Taylor]. They showed that the loss of kinetic energy of a binary system including a radio pulsar could be well explained by assuming that the system emits gravitational waves.

Thanks to modern advanced instruments and a more profound understanding of cosmic events we expect to perform a direct detection of gravitational waves in the near future. Furthermore, a network of gravitational-wave detectors can be used to search the sky for gravitational waves and thus create a new field of astronomy. Gravitational-wave astronomy can detect objects that do not emit sufficient amounts of electro-magnetic waves, and it can also see through ‘dark clouds’. A complementary image of the sky and of our universe may be seen with future gravitational-wave detectors.

GEO 600 is a large interferometric gravitational-wave detector. It forms part of a world-wide network of gravitational-wave detectors that strive to perform the first direct detection of gravitational waves. The first gravitational-wave detectors were so-called resonant-mass antennas. Several of these detectors are currently in operation. During the last decade, a number of large-scale interferometric gravitational-wave detectors have been built [GEO, LIGO, TAMA, VIRGO]. These detectors are now being commissioned and optimised to reach the designed sensitivity.

The GEO 600 project is a German-British collaboration; the construction of the detector at the site near Hannover (Germany) started in 1995, and the first optical systems of the

detector were installed during 2000. Since then, various subsystems have been tested, and by the end of 2001 the 600 m long Michelson interferometer started operation using test optics. Tests with continuous data taking are used for commissioning the instrument. In 2003, the test optics will be exchanged for final, top-quality, optics to complete the construction of the optical systems (see [Willke01] for a recent review article).

1.1.1 Sensitivity of GEO 600

All interferometric detectors to date are based on the Michelson interferometer. In its basic form, this interferometer type has been used for over a hundred years to measure differences in optical path length. When a gravitational wave passes the Michelson interferometer, it will change the phase of the light in the arms of the interferometer. In the following, we will assume for simplicity that the gravitational wave will be travelling perpendicular to the plane of the interferometer and the orientation of its polarisation is such that the maximum deviation of space time happens to be parallel to the interferometer arms. The strength of a gravitational wave is commonly described by the so-called *strain* h , which is defined as:

$$h = \frac{2\delta L}{L} \quad (1.1)$$

with L being some distance aligned along one polarisation axis of the gravitational wave and δL then being the length change induced by the passing gravitational wave. Assuming a sinusoidal gravitational wave with the amplitude:

$$h(t) = h_0 \cos(\omega_g t) \quad (1.2)$$

the change in the phase of a light field (after a round trip through one interferometer arm) is [Mizuno95]:

$$\delta\varphi(t) \simeq h_0 \frac{\omega_0 \sin(\omega_g l/c)}{\omega_g} \cos(\omega_g(t - l/c)) \quad (1.3)$$

with l being half the total optical path in one arm of the interferometer and ω_0 the frequency of the laser light.

The laser light is modulated in phase by the gravitational wave; the strength of the modulation is given by the factor $\omega_0 \sin(\omega_g l/c)/\omega_g$. Two simple conclusions can be derived from this statement:

- **Detector arm length:** The factor $\sin(\omega_g l/c)$ can be maximised by choosing the best arm length l with respect to the gravitational wave frequency. The frequency region, however, in which most of the gravitational wave signals are expected, lies below 1 kHz. The respective optimised lengths would be larger than 75 km, which is unrealistic for earth-based detectors.

For detectors with arms much shorter than the optimised length, the modulation strength increases almost proportional to the length. Therefore, gravitational-wave

detectors are built with large arm lengths. In addition, advanced optical techniques can be used to enlarge the round-trip time for the laser light in the interferometer arms by other means. A greater round-trip time can be interpreted as if the arm had a length greater than the geometrical length; thus the phase modulation by the gravitational wave is increased.

- **Optical signal:** Assuming an arm length of $l = 1$ km and a gravitational-wave frequency of $\omega_g = 2\pi \cdot 100$ Hz, the modulation strength would be approximately $h_0 \times 10^{10}$ radian. The strain amplitudes for gravitational waves are expected to be less than or $\lesssim 10^{-21}$, which results in an extremely small optical signal: a change of the phase of the light field by $\lesssim 10^{-11}$ radian.

In order to detect such tiny phase changes, the sensitivity of the gravitational-wave detectors must be markedly better than that for other tasks in interferometry. The sensitivity of a detector is defined as the ratio between signal and noise in the main output signal; it specifies the signal amplitude that can be detected with a signal-to-noise ratio (SNR) of unity. To increase the sensitivity, one has to either increase the signal (by means of the instrument gain) or reduce the noise.

In general, many noise contributions of different origin are present in the interferometer signal. The noise sources are traditionally divided into *technical* and *fundamental* noise. Technical noise is supposed to be due to an imperfect implementation or installation of the physical instrument, whereas fundamental noise represents unavoidable fluctuations of a physical quantity of the instrument. The term ‘fundamental’ noise in this context is misleading because this noise can often be removed or decreased by carefully designing the instrument; it does not represent a fundamental limit for the detection of gravitational waves in general, but a sensitivity limit of a certain kind of interferometer.

Figure 1.1 shows the designed sensitivity of the GEO 600 detector (for two possible configurations). The sensitivity is computed from the following fundamental noise contributions:

- Seismic noise: The motion of the ground changes the position of the optical components and thereby introduces a phase modulation that cannot be distinguished from a gravitational wave signal.
- Thermal and thermo-refractive noise: The random fluctuations of the atoms at non-zero temperatures cause distortions of mirror surfaces. The same random fluctuations cause fluctuations in the index of refraction of the beam splitter. Both effects also create phase fluctuations similar to a gravitational wave signal.
- Shot noise: The quantum fluctuations of light limit the accuracy of interferometric detection. In the case of GEO 600, the shot noise creates a false signal in the main photo detector.

The gravitational-wave detector must be built in a way that the coupling of the various noise sources into the main signal is minimised, whereas the coupling of the gravitational signal into the output signal is maximised. This task requires sophisticated techniques in many regimes. For example, the optical instruments are located in an ultra-high

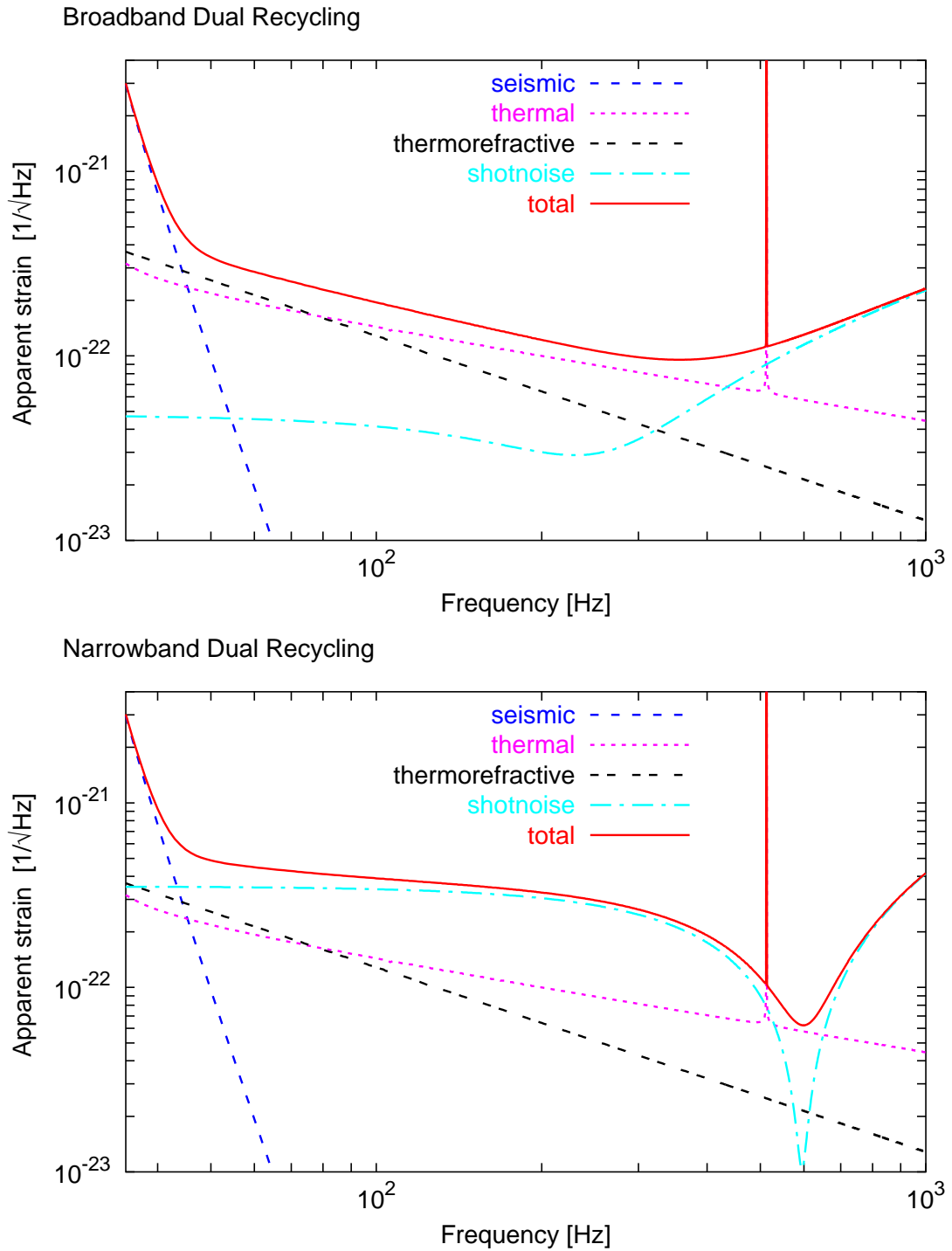


Figure 1.1: Designed sensitivity of the GEO 600 detector. Each plot shows the limits imposed on the detector sensitivity by fundamental noise sources and the corresponding total sensitivity. The two graphs refer to two typical setups of the Dual-Recycling scheme: The top graph shows a broadband setting (slightly detuned) and the lower graph gives an example for a narrowband mode, detuned to ≈ 500 Hz.

vacuum system to avoid fluctuations due to acoustics or a changing index of refraction (originating from the fluctuating number of atoms hit by the laser beam). All mirrors and beam splitters of the main instruments are suspended as pendulums with a very high quality factor to isolate the mirrors from the seismic motion of the ground. Furthermore, Dual Recycling is used to reduce the effects of the shot noise (see Chapter 3).

The noise contributions shown in Figure 1.1 are plotted as ‘false’ signals created by the respective noise. This shows the sensitivity limit as given by each noise signal. Such a graph is useful for weighing the different noise contributions. In addition, different noise-reducing techniques can be easily evaluated with respect to the total noise budget. The top graph in Figure 1.1, for example, shows the detector sensitivity with respect to a broadband Dual-Recycling mode, whereas the bottom graph shows the sensitivity for the same detector with narrow, detuned Dual Recycling (see Section 3.2).

1.1.2 Optical setup

Interferometric gravitational-wave detectors are highly sophisticated laser interferometers. They can be understood as a set of various optical cavities and interferometers that performs a very sensitive measurement of a differential change in the optical phase of the interfering light beams. The schematic layout of the optical instruments of GEO 600 is shown in Figure 1.2. In Appendix A you can find a CAD drawing of the complete optical layout. The following sections describe the optical subsystems; here, emphasis is placed on the input mode-cleaner section important for the laser frequency stabilisation described in Chapter 2. Starting with the laser source, the description follows the laser beam through the entire optical system. Several subsections from the CAD layout are used to show the exact beam path and the positions of the optical components. Simplified schematic drawings are added to give a better overview of single subsystems.

The laser system of GEO 600 is an injection-locked master and slave system that provides a 14 W beam with high stability in frequency and power. The beam is filtered by two mode-cleaner cavities. These triangular cavities have an optical path length of 8 m and are used to filter out geometry fluctuations. In addition, they filter out phase and amplitude fluctuations at high Fourier frequencies, and they serve as reference cavities for the pre-stabilisation of the laser frequency. The filtered beam enters the main interferometer, i. e., a Dual-Recycled Michelson interferometer with a geometric arm length of 600 m. The arms of the Michelson interferometer are folded once so that the optical path length of each arm is approximately 2400 m. The Michelson interferometer is the main optical system sensitive to gravitational waves. The signal (generated by noise or gravitational waves) will be detected in one output port of the Michelson interferometer. In order to minimise the light power of higher-order modes on the photo diode, the output beam is filtered through an output mode cleaner. The optical subsystems are located inside an ultra-high vacuum system, except for the laser system, some input and output optics and the photo diodes. The mirrors and beam splitters inside the vacuum system are suspended as pendulums for seismic isolation. The beam splitter of the Michelson interferometer as well as the mirrors in the interferometer arms are suspended as triple pendulums; other optical components inside the vacuum system are suspended as double or single pendulums.

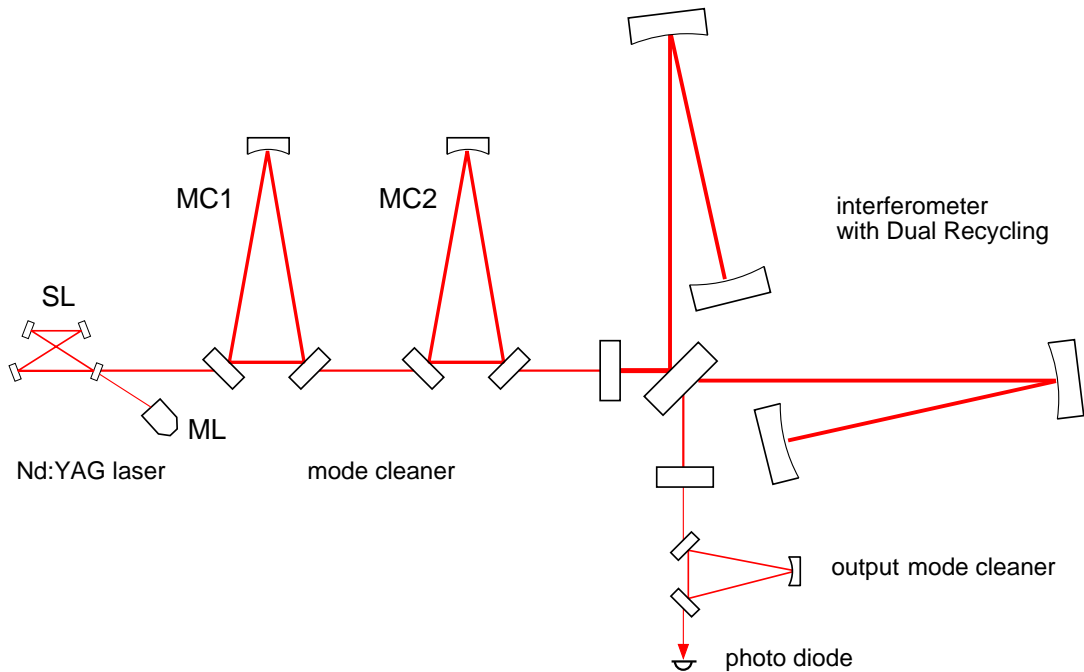


Figure 1.2: The optical layout of GEO 600: The laser consists of a monolithic master laser (ML) plus an injection-locked slave laser in a bow-tie setup (SL); the two mode cleaners (MC1, MC2) are suspended 8 m ring cavities, and the main interferometer is a Dual-Recycled Michelson interferometer with folded arms. The optical path length of each arm is 2400 m. The output mode cleaner is a small triangular ring cavity with an optical path length of 0.1 m. This schematic shows a simplified layout; the full optical layout can be found in Appendix A.

1.2 Laser system

The GEO 600 laser system uses two laser oscillators. The so-called *master laser* provides a laser beam with an output power of 0.8 W, which is very stable in amplitude and frequency. The second laser, the so-called *slave laser*, provides a high-power (14 W) output beam. The master and slave lasers are optically connected by the so-called *injection-locking* technique. The idea behind this injection locking is to couple a high-power oscillator to a stable single frequency oscillator [Man]. The high-power oscillator runs in a stable, single-frequency mode by following the master oscillator. The single-frequency laser beam from the master is injected as a seed beam into the slave-laser cavity. If the power of the master beam inside the slave cavity is large enough and the frequency of the master laser beam is within the gain profile of the slave laser, then this seed beam can initiate the high-power laser radiation at the master laser frequency. Thus, the slave laser inherits the good frequency stability of the master (Figure 1.4 shows the setup of the injection-locked laser system).

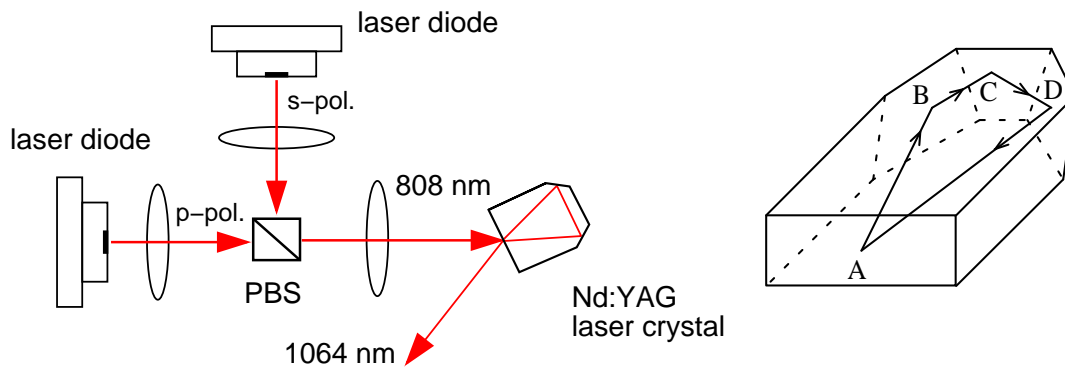


Figure 1.3: The laser crystal of the master laser ($3 \times 8 \times 12 \text{ mm}^3$) is pumped with two laser diodes at 808 nm. The beams of the laser diodes are superimposed at a polarising beam splitter. Three lenses are used for mode matching. The crystal itself forms the monolithic laser cavity. The cavity geometry is called **non-planar ring oscillator (NPRO)**.

1.2.1 Master laser

Both lasers of the master-slave system are diode-pumped Nd:YAG lasers. The master laser is a commercial device (‘Mephisto 800’ from Innolight). Figure 1.3 shows the design of the laser crystal and the optical layout with the pump diodes. The front surface of the Nd:YAG crystal cavity is coated to be anti-reflective for the pump light and highly reflective ($R = 97\%$) for 1064 nm light. Thus, the front surface functions as the coupling mirror. The laser cavity is formed by the front surface (A) and three total internal reflections (at points B, C and D in Figure 1.3). The cavity is designed as an NPRO (non-planar ring oscillator). The non-planar design of the cavity exploits the Faraday effect of the crystal together with different reflectances for s- and p-polarised light to obtain different gains for the two directions of propagation. The two pump diodes together provide 2 W of light power. The beams are overlapped and injected into the crystal on the optical axis. The laser cavity develops a stable geometry after the pump light has formed a thermal lens within the crystal. The small dimensions of the cavity (with a free spectral range of 6 GHz) and the pump geometry result in a stable beam with single mode and single frequency. The current design has been developed by the Laser Zentrum Hannover (LZH) following earlier work by Kane [Kane85].

The master laser can deliver 0.8 W of continuous output power at 1064 nm. The specifications of the GEO 600 master laser are listed in Table 1.1. The master-laser cavity is the frequency reference inside the laser system. Therefore, all feedback to the laser frequency will be applied to the master laser. Two actuators for changing the master laser frequency are built into the laser:

- A piezo-electric transducer (PZT) positioned on top of the laser crystal. Stretching or shrinking the PZT induces mechanical strain to the laser crystal. Stress-induced birefringence changes the optical path length and thus the resonance frequency of

output power	0.8 W
pump power	2 W
M^2	<1.1
FSR	6 GHz
beam waist size	340 μm (vertical) 290 μm (horizontal)
beam waist position	-547 mm (vertical) -355 mm (horizontal)
free running drift	1 MHz/min
thermal tuning coefficient	3 GHz/K
thermal actuation	1 K/V
thermal control bandwidth	<0.1 Hz
PZT actuation	2.28 MHz/V
PZT range	680 MHz

Table 1.1: Specifications of the GEO 600 master laser [Nagano01]. The value for the PZT actuation has been measured by analysing a frequency sweep with a small rigid cavity. The reference plane for the beam waist position is the front surface of the laser crystal.

the cavity. The PZT can be used for control loop purposes at up to relatively high frequencies as its first mechanical resonance is at ≈ 150 kHz.

- A Peltier element to control the crystal temperature. The index of refraction of the crystal and thus the optical path length can be varied by changing the operating point of the temperature control. The thermal control is limited to very low frequencies (< 0.1 Hz).

We have accurately measured the PZT actuation factor by applying a ramp signal to the PZT and by generating a Pound-Drever-Hall [Drever83] error signal with a small rigid cavity. From the known modulation frequency of the Pound-Drever-Hall modulation, we could determine the PZT actuation factor. This parameter is later on used as a reference for various other frequency actuation factors. Recently, the master laser was exchanged because of broken pump diodes. The new laser certainly has a slightly different PZT actuation factor. All measurements discussed here refer to the previous master laser with the given factor.

The range of the PZT is computed from the actuation factor and the maximum voltage (300 V) of the high-voltage amplifier used to drive the PZT.

1.2.2 Slave laser

Interferometric gravitational-wave detectors need high light power to improve the shot-noise-limited sensitivity. A laser with the desired stability in amplitude and frequency that can deliver more than 10 W output power was not available when the large-scale interferometers were planned. The master-slave system used in GEO 600 has been devel-

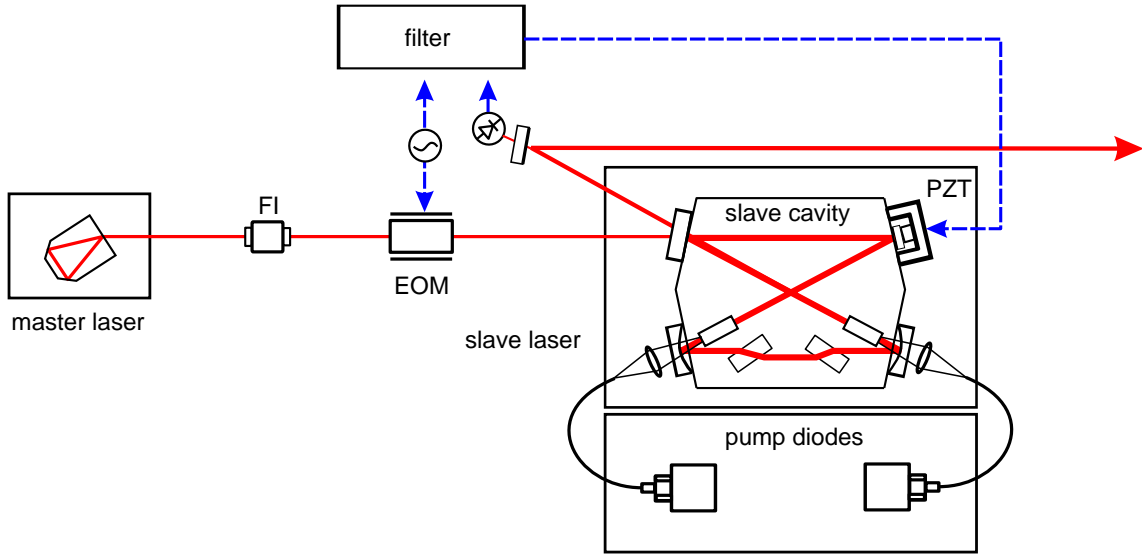


Figure 1.4: The laser system consisting of a monolithic master laser plus an injection-locked slave laser. The slave laser cavity is made of rigidly mounted single mirrors in a bow-tie setup. A Pound-Drever-Hall loop is used to maintain the injection locking. Two single-end-pumped Nd:YAG rods provide the light amplification, and two Brewster plates are used to select the p-polarisation.

oped at the Laser Zentrum Hannover. The design is similar to that of the laser system used in the TAMA project [TAMA].

Figure 1.4 shows the optical layout of the slave laser plus the injection locking. The optical path of the slave-laser cavity is 48 cm long and has a bow-tie geometry. Two Nd:YAG crystals are pumped with 808 nm light injected on the optical axis through two end mirrors of the cavity. The pump diodes are fiber-coupled and provide 17 W pump power each. The input-output coupling mirror has a power reflectance of 90%. Two Brewster plates inside the cavity ensure the p-polarisation of the laser mode. If the beam from the master laser is blocked, the modes in the slave laser cavity have no preferred direction. The frequency range of the amplification profile is much larger than the free spectral range of the cavity so that the laser can run on several longitudinal modes.

When the beam from the master laser is injected into the slave-laser cavity, the mode of the slave-laser cavity can couple to the master laser mode. This effect, called *injection locking*, requires, in principle, no active control. The frequency f_{ML} of the master laser must be close to a resonance f_{SL} of the slave-laser cavity. If the frequency difference $f_{\text{ML}} - f_{\text{SL}}$ is smaller than the *injection-locking bandwidth* Δf_{inject} , the slave laser automatically follows the master-laser frequency. The injection-locking bandwidth can be computed as [Siegman]:

$$\Delta f_{\text{inject}} = \Delta f_{\text{SL}} \sqrt{\frac{P_{\text{ML}}}{P_{\text{SL}}}} \approx \frac{T_{\text{in}} \cdot \text{FSR}_{\text{SL}}}{2\pi} \cdot \sqrt{\frac{P_{\text{ML}}}{P_{\text{SL}}}} \approx 2.5 \text{ MHz} \quad (1.4)$$

output power	14.4 W
pump power	34 W
M^2	<1.1
cavity length	0.45 m
FSR	660 MHz
beam waist size	285 μm (vertical) 295 μm (horizontal)
beam waist position	32 mm (vertical) 12 mm (horizontal)
injection lock bandwidth	2.5 MHz
phase lock bandwidth	10 kHz
PZT actuation	5.9 MHz/V

Table 1.2: Specifications of GEO 600 slave laser [Nagano01]. The reference plane for the beam waist position is the output coupler of the slave-laser cavity.

with Δf_{SL} the bandwidth of the slave-laser cavity, FSR_{SL} its free spectral range and T_{in} the power transmittance of the input mirror. P_{ML} and P_{SL} are the power levels of the master and slave laser, respectively. The injection-locking bandwidth gives the -3 dB point of the passive optical effect. Fluctuations of the master-laser frequency slower than 2.5 MHz will be followed by the slave-laser frequency.

In addition, an active control loop is used to enhance the dynamic range. Drifts at very low frequencies and acoustic disturbances can change the length of the slave-laser cavity so that the passive injection lock fails. The active control is done with a Pound-Drever-Hall control loop that stabilises the length of the slave-laser cavity to the master-laser frequency. One cavity mirror is mounted on a PZT used as the actuator of that loop. The bandwidth of the active control loop is approximately 10 kHz. This bandwidth may be much smaller than the injection-locking bandwidth, because it is designed to compensate noise at low frequencies (< 10 kHz).

The injection-locked slave laser is rigidly coupled to the frequency of the master laser. Thus, a single-frequency beam of a power of ≈ 14 W is emitted. The fluctuations in power were measured to be about $\delta P/P < 10^{-5}/\sqrt{\text{Hz}}$. For the specified detector sensitivity, a value of $\delta P/P < 10^{-8}/\sqrt{\text{Hz}}$ is required. An active stabilisation of the laser power is used to reduce the laser power noise [Seifert].

1.2.3 Laser bench

The laser system resides outside the vacuum system on an optical table, the *laser bench*. The schematic layout of the laser bench is shown in Figure 1.5. The light from the master laser is injected into the slave-laser cavity so that the high-power beam of the slave laser is generated at exactly the same frequency (and phase) as the master-laser beam. The 14 W beam from the slave laser is in p-polarisation, and the residual s-polarisation is taken out of the beam by a polarising beam splitter. The beam is passed through the first mounting

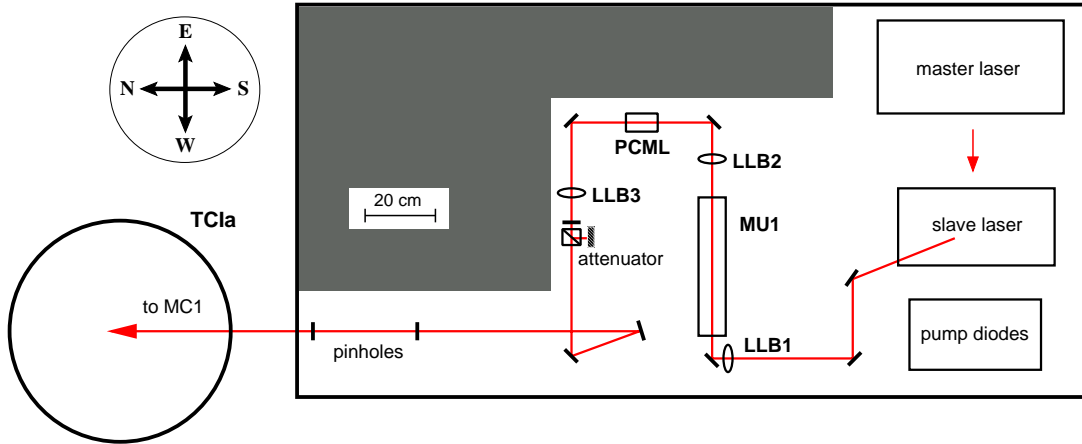


Figure 1.5: The optical table, called laser bench, with the laser system and the input optics. Not included in this sketch are the auxiliary reference cavity plus input optics (grey area) and several photo diodes for monitoring light power. The optics between the master and slave laser have also been omitted.

unit (MU1) which holds two Faraday isolators and an electro-optic modulator (FILBa, FILBb and PCLB, not shown in Figure 1.5). The specifications of the mounting units are given in Section 1.3.3. The electro-optic modulator is used to generate the phase-modulation sidebands for the Pound-Drever-Hall control loop of the first mode cleaner (MC1).

Before entering the mode cleaner, the light is attenuated to the proper power with a half-wave plate and a polarising beam splitter; currently, 2 W are injected into the vacuum system. This is convenient during the commissioning phase of the detector. In the final setup, approximately 10 W will be injected.

Three lenses (LLB1, LLB2, LLB3) are used for mode-matching the beam to the first mode cleaner (see Section 1.3.4), and two steering mirrors are used as input optics to the vacuum system. The beam enters the vacuum through a *view port* in the vacuum tank TCIa. Directly in front of the view port, position and angle of the beam are marked with two pinholes.

The electro-optic modulator PCML shown in Figure 1.5 is the fast phase corrector in the frequency control loop that stabilises the laser frequency to the first mode cleaner. During the work described here, the electro-optic modulator was located between the master laser and the slave laser. Recently, it was moved to the position shown. The reason for the move was to avoid that fast and strong signals in the control loop for MC1 affect the injection lock. We have confirmed the robustness of this setup and found no difference in the performance of the frequency stabilisation.

For clarity, some components have been omitted from Figure 1.5. These are:

- a) The optics between the master laser and the slave laser. The slightly elliptically polarised beam from the master is converted to s-polarisation with a quarter-wave

plate, a half-wave plate and a polariser. A Faraday isolator prevents light reflected back from the mode cleaners or the slave laser from disturbing the master laser. A resonant New Focus electro-optic modulator (4003) is used to generate the 12 MHz modulation sidebands for the Pound-Drever-Hall control of the slave laser.

- b) The components for stabilising the laser to a rigid reference cavity (located in the grey area). The reference cavity is not used at the moment but is kept for optional use and detector characterisation experiments.
- d) Several photo diodes that were used to monitor the laser power at various points and the photo diode for the injection lock.

1.3 Mode cleaners

After leaving the high-power slave laser, the laser light passes two mode cleaners before entering the main interferometer. The mode cleaners are similarly constructed ring cavities. Each cavity consists of three mirrors in a triangular setup, see the figure in Table 1.3. The cavities have several functions. Their primary task is to filter out the *transverse modes* of the laser beam, i. e., the geometrical shape and position of the beam [Rüdiger81]. Next, they filter laser power and laser frequency noise at Fourier frequencies above the cavity pole frequency. In addition, the mode cleaners are used as reference cavities for pre-stabilising the laser frequency. Chapter 2 describes in detail the experimental setup and the performance of the frequency stabilisation.

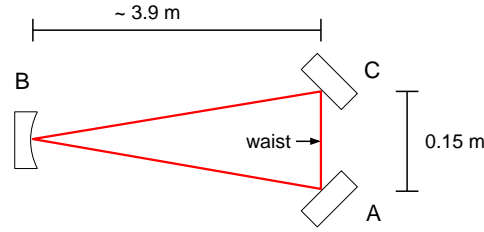
The geometry of a simple laser beam can be described by Hermite-Gauss modes. The mathematical expression describes the beam with separate functions for the longitudinal and the transverse degrees of freedom. For a linearly polarised beam (in one Hermite-Gauss mode) we can write:

$$\vec{E} = a \exp(i(\omega t - kz)) u_{nm}(x, y, z) \vec{e}_{\text{pol}} \quad (1.5)$$

The first part $a \exp(i(\omega t - kz))$ represents the (complex) amplitude of the field on the optical axis (for $t = 0$ and $z = 0$) and the phase propagation of a plane wave. The second term $u_{nm}(x, y, z)$ describes the spatial distribution of the field perpendicular to the beam axis. In Cartesian coordinates the functions for the spatial distribution are called *Hermite-Gauss modes*¹ (Appendix C gives a description of the Hermite-Gauss modes and explains how they are derived from the wave equation). Hermite-Gauss modes are usually distinguished by their order or mode number, which is given by the indices n and m in equation 1.5. Because of their transverse nature, they are labelled TEM_{*nm*} (**t**ransverse **e**lectro-**m**agnetic) modes.

The TEM_{*nm*} modes represent eigen-functions of a spherical cavity. They form a complete and orthogonal set of functions and are well suited for numerous applications because

¹ When cylinder coordinates are used, the functions are called *Laguerre-Gauss*. Throughout this work only the Hermite-Gauss version is used.



	MC1	MC2
round-trip length	8.002 m	8.068 m
FSR	37.465 MHz	37.160 MHz
FWHM	21.55 kHz	18.90 kHz
finesse	1740	1970
beam waist w_0 (tangential)	1.0564 mm	1.0553 mm
beam waist w_0 (sagittal)	1.0574 mm	1.0563 mm
Rayleigh range z_R (tangential)	3.295 m	3.289 m
Rayleigh range z_R (sagittal)	3.301 m	3.295 m
Guoy phase (tangential)	101.05°	101.62°
Guoy phase (sagittal)	100.95°	101.52°
mode separation	10.51 MHz	10.55 MHz

Table 1.3: The designed optical parameters of the GEO 600 mode cleaners. The length of MC2 has been measured. All other values are calculated from the specifications. Measurements of the finesse of MC1 show greater values (up to 2700).

many lasers and other optical systems use spherical cavities. Especially in GEO 600 all optical cavities use spherical mirrors.

Any par-axial beam can be described as a superposition of Hermite-Gauss modes. In practice, however, this mathematical concept is used regularly only for beams that can be described by a superposition of only a few lower-order modes. In fact, mostly when referring to a laser beam one assumes a circular beam shape with a Gaussian intensity distribution perpendicular to the beam axis. A beam like this can always be represented by a lowest-order Hermite-Gauss mode (TEM_{00}). The beam diameter of the TEM_{nm} modes increases with increasing mode index. Therefore, the lowest-order mode experiences the lowest diffraction loss inside a common spherical cavity. Many optical systems that include lasers and cavities are designed in such a manner that in the perfect operating condition the laser light will always be in a TEM_{00} mode. Deviations in the geometry, like misalignment or imperfections of optical components, will cause disturbances so that, in general, a superposition of many TEM_{nm} modes must be used to describe the beam. For small deviations a good approximation can be done by using only modes with $n + m \leq 2$. The theoretical analysis of light fields in a mode-cleaner cavity and the mode-cleaning effect are given in Appendix D.

Mirror	Curvature front/back	Transmittance [ppm]	Scatter Loss [ppm]	Bulk absorption [ppm/cm]	Wedge [arcmin]
MMC1a	flat/flat	1778	23	5	-
MMC1b	concave/flat	35	35	5	30
MMC1c	flat/flat	1606	33	5	-
MMC2a	flat/flat	1532	37	5	-
MMC2b	concave/convex	1360	28	5	30
MMC2c	flat/flat	114	32	5	-

Table 1.4: Mechanical and optical parameters of the mode-cleaner mirrors: The substrates are made of Suprasil 1; the numbers for transmittance and scatter are specified by the manufacturer. The absorption of 5 ppm/cm is an estimate derived from the specifications for fused silica. All other parameters are specifications.

1.3.1 Mode-cleaner design

The mode-cleaning effect does not simply depend on the cavity length but on the ratio between cavity length and radius of curvature of the cavity mirrors. In principle, both a long and a short mode cleaner can achieve the same amount of mode filtering. On the other hand, the mode-cleaner cavity can be used for filtering the amplitude and frequency of the laser light. A light beam that is passed through a cavity is filtered in amplitude and frequency for Fourier frequencies above the cavity pole (half the cavity linewidth). A cavity with the same finesse and equal mode cleaning gets a smaller linewidth the longer the cavity is. In addition, the residual length noise of the cavity improves with longer cavities. The absolute motion of the mirrors (induced, for example, by seismic noise) does not depend on the length of the cavity so that the relative stability $\delta L/L$ is improved for larger L .

The GEO 600 mode cleaners are triangular cavities with a round-trip length of ≈ 8 m. The size was limited due to restrictions in space and funding. Table 1.3 shows the mode cleaner specification and a simplified optical layout of a mode-cleaner cavity. Two similar mode cleaners (labelled MC1 and MC2) are used in succession to increase the filter effect. The mirrors of each mode cleaner are labelled a , b and c . The full acronyms for the mirrors are MMC1a (mode cleaner 1, mirror a), MMC1b (mode cleaner 1, mirror b), MMC2a (mode cleaner 2, mirror a) and so on. All mode-cleaner mirrors are cylindrical pieces of fused silica. They are 50 mm thick with a diameter of 100 mm and a weight of 864 g. The mirrors are suspended as double pendulums (see Section 1.3.6). The mechanical and optical parameters of the cavity mirrors are shown in Table 1.4. In addition to the cavity mirrors, there are several *beam directors* and *pick-off mirrors*. Beam directors are steering mirrors for the main beam. They have the same design as the cavity mirrors and are also suspended as double pendulums. The coating is highly reflective for an angle of incidence of 45° . The pick-off mirrors (not in the main beam) are small mirrors mounted with simple posts on the bottom plate of the vacuum tanks. The pick-off mirrors inside the mode-cleaner section have a diameter of 40 mm.

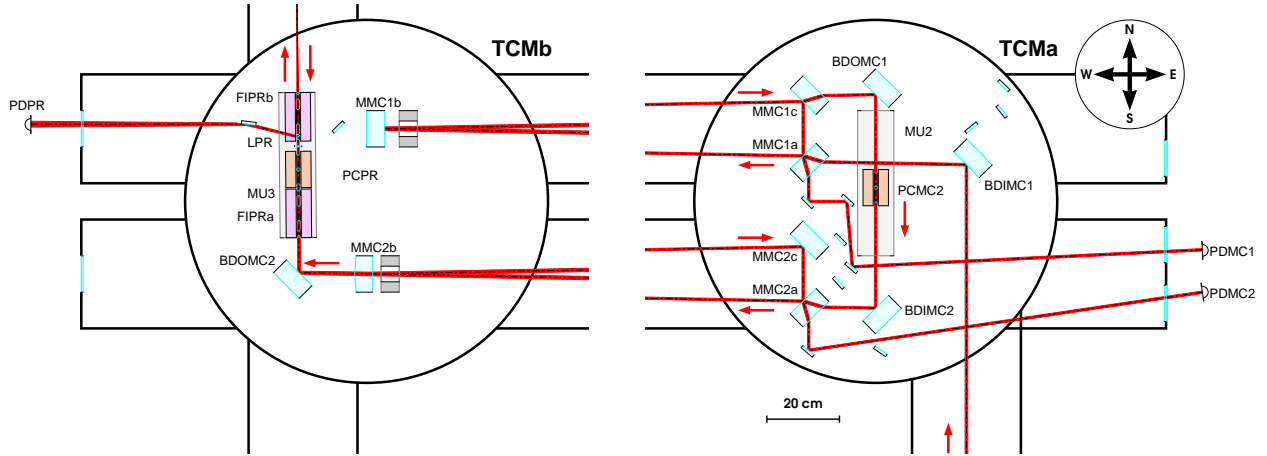


Figure 1.6: The optical layout of the two mode cleaners. The directions are labelled north, south, east and west. The red arrows indicate the direction of the laser beam. Two vacuum tanks (TCMa and TCMb), connected by two vacuum tubes, hold the mode-cleaner optics. The laser beam enters tank TCMa from the south. It enters MC1 at MMC1a, leaves MC1 at MMC1c, is injected to MC2 through MMC2a and leaves MC2 at MMC2b (in TCMb). It is then sent north towards the main interferometer.

1.3.2 Optical layout

Figure 1.6 shows two sections of the CAD drawing depicted in Appendix A. The drawing provides the exact locations of the beams and all optical components in the vacuum system. Only the photo diodes are place holders for a set of output optics and photo diodes positioned on breadboards outside the vacuum (see Figures 1.7 and 1.14).

The beam coming from the laser bench enters the vacuum through an empty tank (TCIa, see Figure 1.5). Further north, it enters the first mode cleaner tank (TCMa). The beam director BDIMC1 injects the beam into MC1 through MMC1a. The beam reflected at MMC1a is detected with the quadrant camera (PDMC1) outside the vacuum. The camera provides the visibility signal for MC1 and the error point signal for the MC1 control loop (which stabilises the laser frequency against MC1).

The output mirror of MC1 is MMC1c. Another beam director (BDOMC1) is used to send the output beam through the second mounting unit (MU2). This mounting unit holds only the electro-optic modulator (PCMC2). The Faraday isolators (FIs) have not been installed. It is expected that the two Faraday isolators of MU1 (on the laser bench) will provide sufficient suppression of the light going back to the laser. The advantage of leaving out the FIs at this stage is that the length (optical path) of the structure decreases to approximately 100 mm so that the misalignment tolerance of the mounting unit is relaxed.

The electro-optic modulator on MU2 is used to generate two pairs of phase-modulation sidebands: one for the control of MC2 and one passed through MC2 and used in the control loop of the Power-Recycling cavity. Behind MU2 the beam is re-directed by

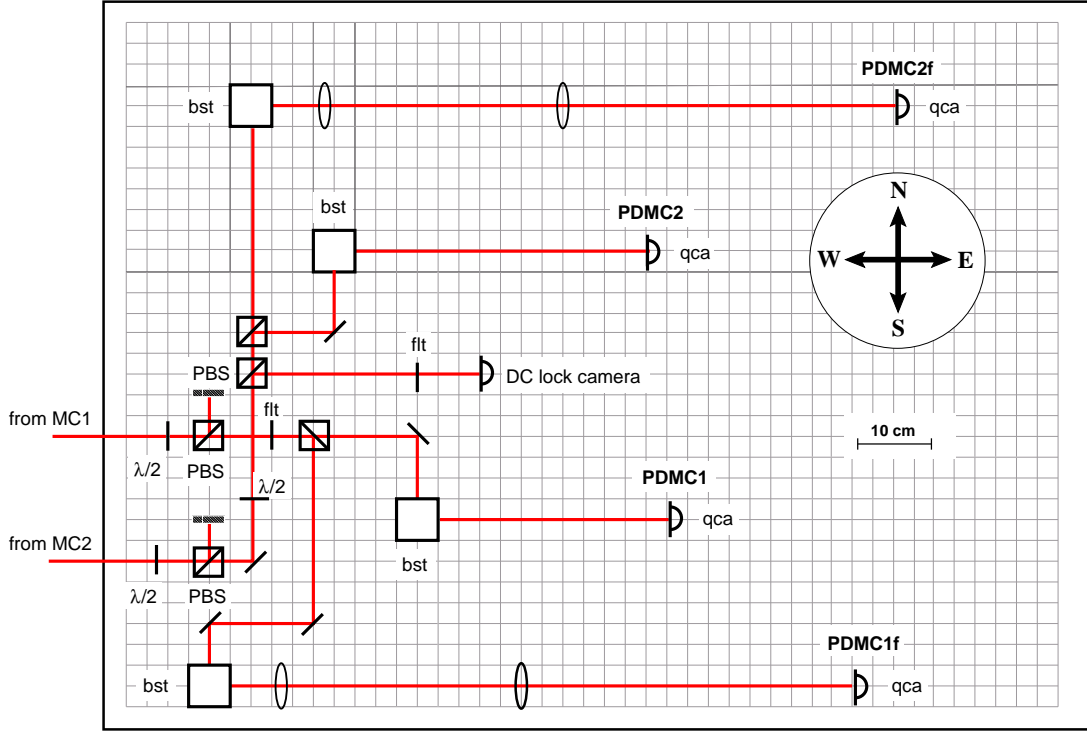


Figure 1.7: Mode-cleaner output optics on the breadboard east of TCMa. The beams reflected from MMC1a and MMC2a are directed onto the breadboard through a viewport and two periscopes. (bst = beam steerer, qca = quadrant camera, flt = neutral density filter, PBS = polarising beam splitter)

BDIMC2 and injected into MC2 through MMC2a. The Rayleigh range of the beam at this point is larger ($z_R = 3.3$ m) than the distance between the two mode cleaners (≈ 2 m). Therefore, a good mode matching is achieved without a lens or telescope. Again, the reflected beam is detected by a quadrant camera (PDMC2), which in turn is the sensor of the length- and frequency-control loop for MC2.

The second mode-cleaner cavity is very similar to the first one, with two exceptions: it has a slightly different length and a different output mirror. The output mirror is MMC2b located in the second mode-cleaner tank (TCMb). Both b mirrors have a concave front face with a radius of curvature of $R_C = 6720$ mm (specification). The output coupler of the second mode cleaner MMC2b also serves as a lens for mode matching the beam into the Power-Recycling cavity. Therefore, the back surface is convex with a radius of curvature of $R_C = 350$ mm. The subsequent beam director (BDOMC2) sends the beam through MU3. This mounting unit holds an electro-optic modulator (PCPR), two Faraday isolators (FIPRa and FIPRb) and another lens (LPR). The lens on the mounting unit, the lens provided by MMC2b and the lens formed by the Power-Recycling mirror (MPR, see Figure 1.11) are used as a mode-matching telescope for matching the beam to the eigen-mode of the Power-Recycling cavity. The electro-optic modulator is used

to generate the control sidebands for controlling the Michelson interferometer and the Signal-Recycling cavity. It is also used as a fast phase corrector in the control loop of the Power-Recycling cavity (see Section 2.7). The beam leaving the mounting unit travels north through the so-called telescope tube towards TC1b where it enters the main interferometer.

The output optics for detecting the mode-cleaner signals are shown in Figure 1.7. Most mode-cleaner signals are derived from the two beams that are reflected from the input mirrors. These beams are directed out of the vacuum to the output optics mounted on a breadboard. Both beams are attenuated to power levels that are adequate for the photo diodes used (with a half-wave plate, a polarising beam splitter and a beam dump). Some additional neutral-density filters (flt) are provided where more attenuation in one of the split paths is necessary. Two quadrant cameras (qca) are required for each mode-cleaner system. A beam steerer (bst) in front of each quadrant camera centers the beam onto the quadrant diode. The different quadrant cameras are needed for the automatic alignment system [Grote02]: The so called *near-field camera* detects the deviation of the incoming beam from the eigen-mode of the mode cleaner as close as possible to the beam waist (PDMC1, PDMC2). A telescope in front of the second camera (PDMC1f, PDMC2f) transforms the beam into the far field. The near-field camera and the ‘DC lock camera’ are used for the length- and frequency-control systems (see Chapter 2).

1.3.3 Mounting units

The *mounting units* are mechanical structures designed for holding two Faraday isolators, an electro-optic modulator (containing two independent crystals) and, optionally, a lens. The structure can be suspended as the lower mass of a double pendulum inside a vacuum tank or mounted directly on an optical table. Each mounting unit is 400 mm long, approximately 150 mm high and 70 mm wide.

The Faraday isolators (FIs) are vacuum-compatible components made by Gsaenger. They weigh 1.5 kg each and contain permanent magnets, a Terbium Gallium Garnet (TGG) crystal and two polarisers. The TGG crystal is 40 mm long and 8 mm in diameter. The index of refraction of TGG is $n = 1.94$. The polarisers can be adjusted by rotating them around the optical axis. The isolators are adjusted for maximum extinction for the reverse pass. The transmittance of two sequential Faradays in MU3 was measured to be 90%, whereas the power suppression of the reverse pass is ≈ 60 dB [Klövekorn].

The GEO 600 setup contains three mounting units:

MU1: The first mounting unit is located on the laser bench. Two FIs are in place. The electro-optic modulator is a PM25 from Gsaenger used in a resonant circuit to generate 25 MHz modulation sidebands for the control loop for MC1. The aperture of the mounting unit as defined by the FI is 8 mm.

MU2: The second mounting unit is suspended as a double pendulum in the first mode cleaner tank TC1a. On the optical path, it is located between MC1 and MC2. The FIs

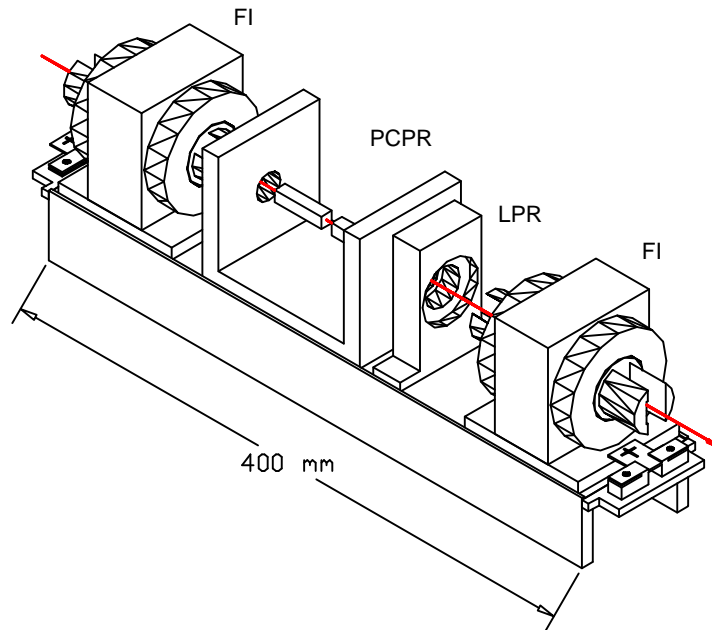


Figure 1.8: Schematic view of mounting unit 3 (MU3). Faraday isolators (FIs) are located at both ends; the two crystals of the electro-optic modulator (PCPR) and the mount for the mode-matching lens LPR are shown. The crystals of the electro-optic modulator are cut at Brewster angle (not shown here).

have been omitted to make the system less sensitive to misalignments. The electro-optic modulator (PCMC2) uses two LiNbO_3 crystals from Leysop. The crystals are 35 mm long and 8 mm wide and high.

The two modulator crystals can be used independently; the first crystal generates the 13 MHz modulation sidebands for the Pound-Drever-Hall control loop for MC2, and the second one is used for the 37 MHz modulation for the Power-Recycling cavity control.

MU3: Figure 1.8 shows a schematic drawing of MU3. The Faraday isolators (FIPRa, FIPRb) are positioned at the ends. Both the crystals of the electro-optic modulator (PCPR) and the mount for a mode-matching lens (LPR) are indicated. This mounting unit is suspended as a double pendulum in TCMB. It is located behind the second mode cleaner. The light reflected back from the Power-Recycling mirror is directed out of the vacuum towards a photo diode by the second polariser (away from the Power-Recycling mirror) and a beam director. The electro-optic modulator is equivalent to the modulator on MU2. Again, two pairs of phase-modulation sidebands are generated. One at ≈ 15 MHz for controlling the Michelson interferometer and one at ≈ 9 MHz for controlling the Signal-Recycling cavity. In addition, one modulator crystal is used as a fast actuator in the control loop of the Power-Recycling cavity. MU3 also holds an additional lens (LPR) used for mode-matching the beam from the second mode cleaner into the Power-Recycling cavity.

Alignment of the mounting units

The mounting units have to be aligned carefully to avoid clipping or distorting the passing beam. The beam radius at the mounting units is approximately 1 mm. The aperture is 8 mm. The length is 400 mm (with isolators) or 100 mm (without isolators). For a length of 400 mm, the maximum tolerable misalignment between the beam and the optical axis of the mounting unit is $\approx 1^\circ$.

The input and output polarisers (of the FIs) at both ends of the mounting units reflect some light downwards. These auxiliary light beams are used for aligning the mounting units in the vacuum system; if the auxiliary beam from the polarisers is centered on a little cross engraved below the polariser, the alignment is perfect.

Most of the alignment of the mounting units in the vacuum tanks has to be done during the suspension process (so called pre-alignment). At that time, the vacuum system is open and it is not possible to control the mode cleaners. Consequently, it is impossible to properly pass the laser beam through the cavities and use it to align the optics. Portable lasers are used to ‘mark’ the optical axis, and the optical components are pre-aligned according to these marks. As soon as the mounting unit is in place and the system evacuated, the final alignment can be done with coil-magnet actuators at the intermediate mass.

This alignment faces a number of difficulties. The actuators had been designed for aligning much lighter mirrors so that the ranges for tilt and rotation of the mounting unit are very small (less than 1 mrad). No control for lateral displacement is provided. Furthermore, there is only one steering mirror in front of each mounting unit. The axis of the outgoing beam is defined by the cavity mirrors so that the mounting unit should be aligned accordingly. However, in practice the mounting unit cannot be suspended exactly onto that axis. To compensate for the misalignment of the mounting unit, the eigen-mode of the mode-cleaner cavity is adjusted accordingly. Thus, the positions of the eigen-mode on the mirror surfaces deviate from the center of the surface by as little as 1 to 2 mm.

The alignment of MU3 is critical because this unit is located behind the mode cleaners, and any distortion of the beam can couple into the main output signal. Furthermore, the two isolators and the lens are installed on MU3 so that the alignment tolerance is small. The range of the local control of MU3 had to be increased to rotate the mounting unit around a vertical axis with at range of ≈ 5 mrad. The alignment in tilt (rotation around the horizontal axis perpendicular to the optical axis) has to be done by carefully adjusting the wire lengths of the suspension.

1.3.4 Mode matching to the first mode cleaner

Figure 1.5 shows the three lenses installed to mode-match the beam from the slave laser to the first mode cleaner. The first lens (LLB1, $f = 800$ mm) is needed to match the beam size to the small (8 mm) aperture of the MU1. Behind the mounting unit two lenses (LLB2, $f = 340$ mm and LLB3, $f = 458$ mm) are used as a mode-matching telescope for

matching size and divergence of the beam to MC1. With this setup, the theoretical coupling efficiency is 99.5% [Nagano02]. The design has to take into account all thermal lenses in the modulators and Faraday isolators located in the high-power beam. During the installation, the mode-matching telescope was adjusted by moving lens LLB2 and simultaneously measuring the visibility of MC1. The maximum measured visibility to date has been 96%. Based on the measured throughput of more than 80% a visibility greater than 99% can be expected for impedance matching. Therefore, the mode-matching efficiency can be estimated to be 96%, probably limited by the imperfect output mode of the slave laser.

The thermal lenses in the modulators and Faraday isolators can be observed when the injection lock of the slave laser is switched on after a long pause. When the slave laser is not locked to the master, the mode will change its direction randomly and thus emit on average only 50% of the light power into the forward direction. As soon as the slave laser is locked to the master, the full power is directed forward. Measuring the visibility of MC1 then shows that it slowly increases with time while the thermal lenses in the optical components in the high-power beam change in response to the sudden change in light power.

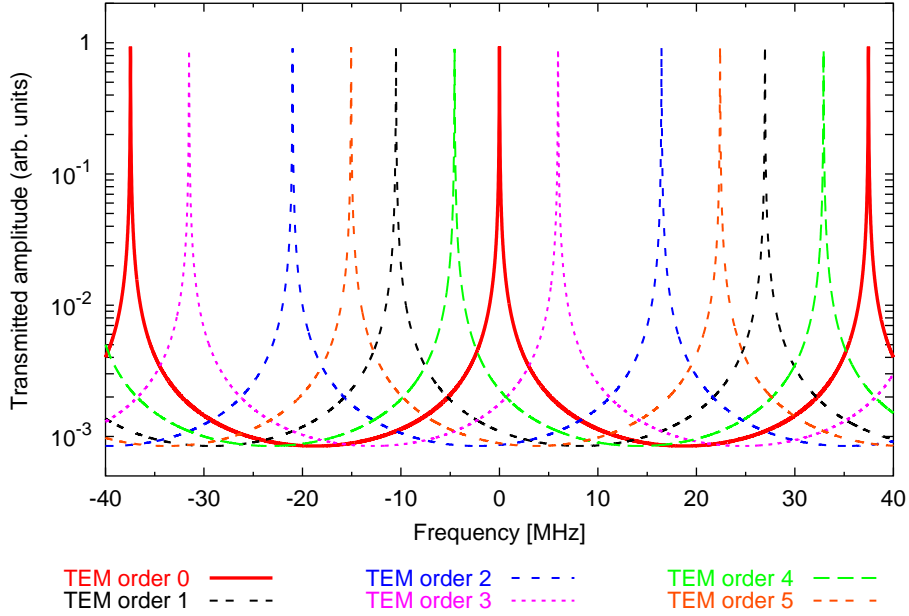


Figure 1.9: The graph shows the computed relative amplitude transmittance for a single GEO 600 mode cleaner (MC1). The table lists the resulting amplitude suppression factors.

1.3.5 Optical properties of the mode cleaners

The mode separation of the MC1 cavity is ≈ 10.51 MHz (see Appendix D). Figure 1.9 shows the amplitude transmittance of the first GEO 600 mode cleaner for the first six orders of Hermite-Gauss modes as a function of laser frequency with zero being the resonance frequency (the cavity is assumed to be on resonance for the TEM₀₀ mode). The additional table shows the resulting suppression factors for the non-zero modes. The amplitude suppression of these higher-order modes is at least five orders of magnitude. These factors are calculated with the specified transmittances of the cavity mirrors, and the specified values meet the requirements. Measurements indicate that the finesse of MC1 is greater than expected. This would increase the suppression factors.

The mode-cleaner section was designed to transmit approximately 50% of the injected light. First measurements yielded a significantly lower throughput. Investigations showed that the mirrors of MC1 had been polluted. In fact, a thin white layer was visible on all surfaces of the mirrors. Consequently, the mirrors were taken out and cleaned with

a CO₂ beam ('snow jet'). Subsequent measurements yielded the expected throughput of 50%. The values are shown in Table 1.5. The throughput is simply the ratio between the transmitted power and the injected power. The visibility is given as:

$$\text{Vis} = \frac{P_o - P_{\text{res}}}{P_o} \quad (1.6)$$

with P_o being the power of the reflected light with the cavity off-resonant and P_{res} the reflected light power on resonance. The reflected power in the resonant case has three sources:

- a) Some of the TEM₀₀ mode at the resonance frequency is reflected because of imperfect impedance matching;
- b) Higher-order modes are reflected almost completely when the cavity is aligned properly;
- c) Phase modulation sidebands at RF frequencies that are not resonant in the cavity.

The finesse of MC1 has been estimated with a very simple measurement of the amplitude transfer function of the cavity: A signal was connected to the power modulation input of the slave-laser pump diodes to generate amplitude modulation. By sweeping this signal in frequency and measuring the light amplitude in transmission of MC1, the cavity pole could be determined. Unfortunately, a resonance in the slave laser distorts the amplitude modulation signal at 50 kHz. Therefore, the result of the measurement is only an estimate. The resulting value of 2700 is much larger than the expected 1800, indicating that the mirror properties given by the manufacturer are not correct. The finesse for MC2 has not been measured directly; instead, it has been estimated from the specifications in combination with the values measured for throughput and visibility.

Mode cleaner	Finesse	Throughput	Visibility
MC1	2700	80%	94%
MC2	1900	72%	92%

Table 1.5: Measured optical parameters of the mode cleaners. Finesse values are estimated, see text.

1.3.6 Mechanical setup of the suspension system

The sensitivity of gravitational-wave measurements would be severely limited by any residual position fluctuation of the mirrors. Therefore, the mirrors are suspended as pendulums inside an ultra-high vacuum system. This system reduces coupling of acoustic excitation and prevents a contamination of the optical surfaces. Main noise sources that move the mirrors include thermal and seismic noise.

Seismic noise comprises all mechanical fluctuations of the mirror mount. In most cases, these are due to seismic motion of the ground, vibrations of mechanical devices and acoustic influences. A good method for decreasing the effects of seismic noise is suspending

the mirrors on springs or as pendulums. Springs and pendulums are harmonic oscillators that efficiently isolate the suspended mass from movements of the suspension point for Fourier frequencies above their resonance frequency f_0 . For small disturbances and $f \gg f_0$, the transfer function of a simple pendulum can be written as:

$$\frac{x_{\text{mass}}}{x_{\text{susp}}} = \frac{f_0^2}{f_0^2 - f^2} \quad (1.7)$$

with x_{mass} being the change in position of the suspended mass and x_{susp} the change in position of the suspension point.

Thermal noise is a general term used for the fluctuations of the surface and the index of refraction of a solid body at a finite temperature. The fluctuation-dissipation theorem states that statistical fluctuations are linked to dissipations in the body. One can show that a material with low mechanical losses (high quality factor) shows lower thermal noise (except at the Fourier frequencies of the mechanical resonances). Therefore, the mirrors are made of a material with a high quality factor Q . Also, the suspension has to be designed for low mechanical loss, e.g. from shear or friction. The main optics in GEO 600 are fused-silica mirrors, monolithically suspended, with an estimated quality factor of up to $Q = 10^8$.

Mirror suspension

Figure 1.10 shows a vacuum tank of the mode-cleaner section with a mirror suspended as a double pendulum by steel wires. All mode-cleaner mirrors that are on the path of the main beam are suspended as shown. The main optics of the Michelson interferometer are suspended as triple pendulums. The residual motion of the mirrors is strong around the mechanical resonances of the pendulum. In order to reduce this motion, an electronic feedback loop with shadow sensors and coil-magnet actuators is located at the intermediate mass to damp the main pendulum resonances. The bandwidth of this so-called *local control* ranges from 0.3 Hz to 3 Hz. The quality factor of the undamped motion has been measured to be $Q \approx 10^5$, and the quality factor with damping by the local control is $Q \approx 3.5$ [Gossler]. The computed lowest resonances of the double pendulum are given in Table 1.6.

The actuators of the local control can also be used to move and orientate a mirror like a marionette, and thus align the optical system. In addition, the local control is used to apply slow feedback with a large dynamic range to compensate for slow drifts.

Mode	Frequency [Hz]
Longitudinal, Tilt	0.6, 1.3, 1.6, 2.3
Sideways, Roll	0.6, 1.5, 15, 34.5
Rotation	0.7, 2.0
Vertical	11.8, 30.1

Table 1.6: *The lowest resonance frequencies of a double-pendulum suspension.*

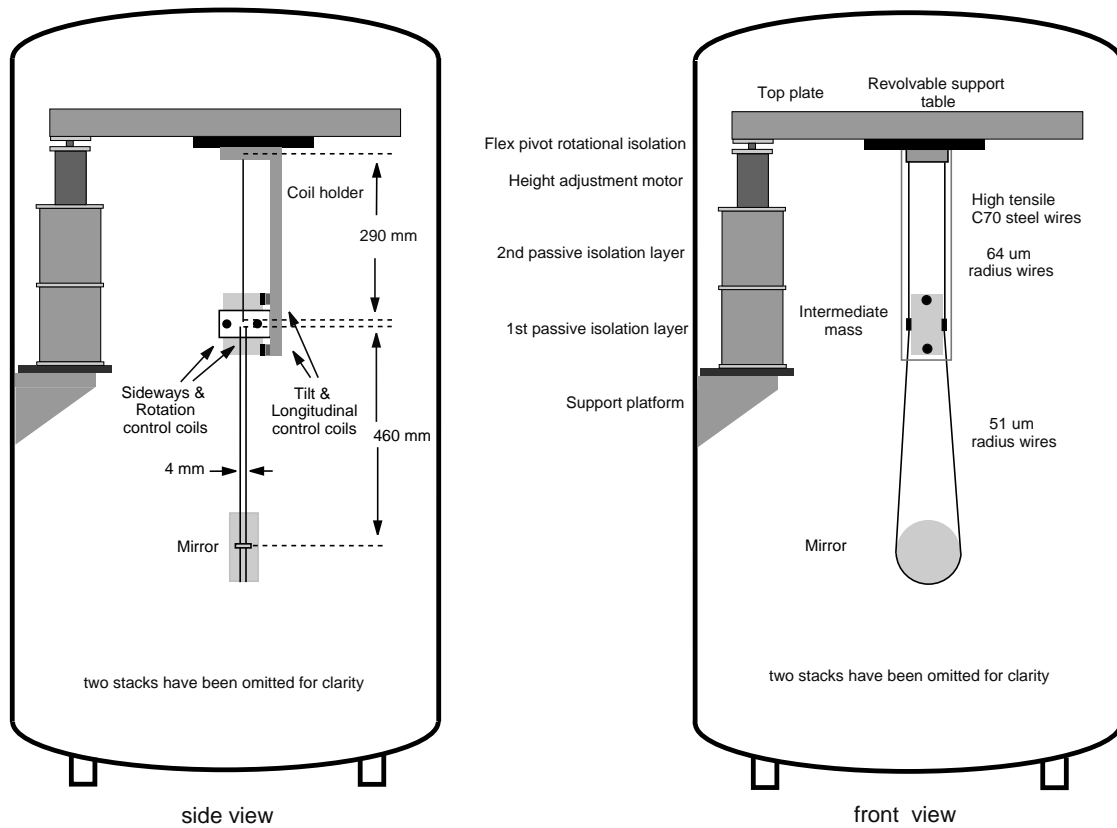


Figure 1.10: Design of the suspension of the double pendulums for the mode-cleaner mirrors. The diameter of the vacuum tank is 1 m.

1.4 Michelson interferometer

The Michelson interferometer is the principal measurement device of all interferometric gravitational-wave detectors to date. This interferometer is sensitive to changes in the arm-length difference. For the current earthbound detectors, the sensitivity is proportional to the length of the interferometer arms. The GEO 600 detector has a geometric arm length of ≈ 600 m. The optical path is folded once inside each arm to obtain a total optical path length for each arm of ≈ 2400 m. This is not precisely equivalent to a 1200 m long Michelson interferometer because the folding mirrors introduce extra noise; still, the sensitivity is improved by at least a factor of $\sqrt{2}$ compared with a simple 600 m long interferometer. Folding the arms of the interferometer has another advantage: the end mirrors of the Michelson interferometer can be located close to the beam splitter. This allows an installation of the control electronics in a single place without the need to send electronic signals over long distances.

GEO 600 uses the Dual-Recycling technique [Meers88, Strain91, Heinzl98] to enhance the sensitivity of the Michelson interferometer. Dual Recycling is a combination of Power

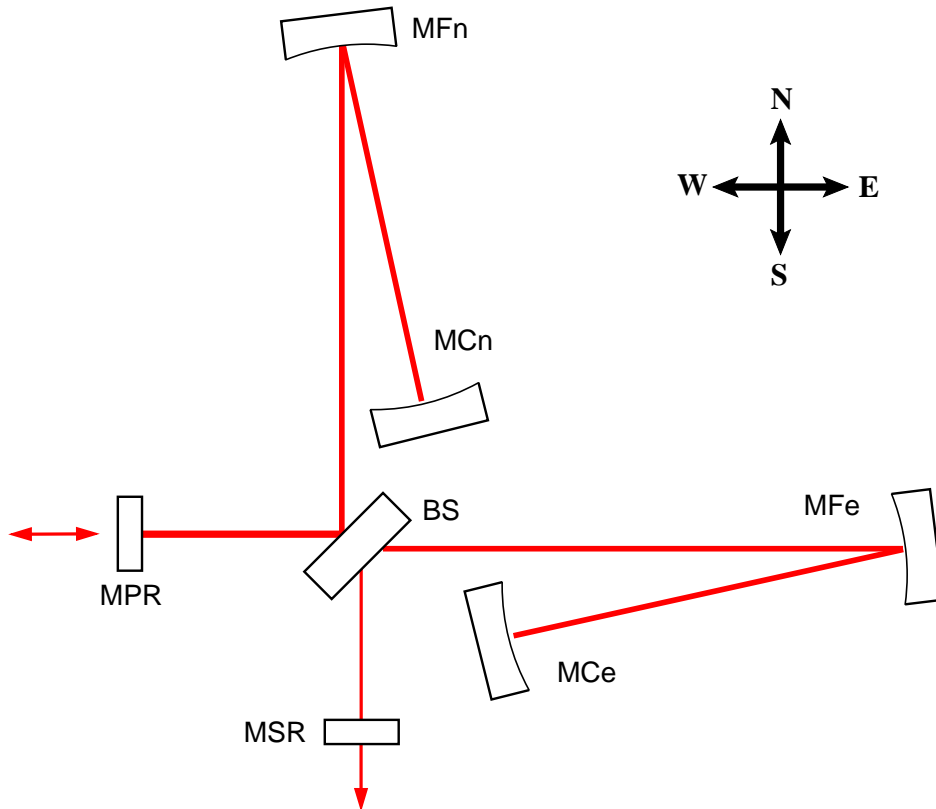


Figure 1.11: Simplified schematic of the Michelson interferometer. The beam enters the interferometer from the west through the Power-Recycling mirror (MPR) and is split at the main beam splitter (BS). Each arm of the interferometer is folded once by the folding mirrors (MF_n and MF_e). The folding is vertical, illustrated above as an horizontal setup. The end mirrors are MC_n and MC_e. The beam leaves the Michelson interferometer at the west and the south ports. The main output is the south port with the Signal-Recycling mirror (MSR).

Recycling [Drever, Schnier97] and Signal Recycling. With the light power of currently available lasers, the sensitivity in the measurement band is limited by shot noise. Both recycling schemes are able to improve the signal-to-noise ratio with respect to the shot noise; they improve the *shot-noise-limited sensitivity*.

Power Recycling: In the currently operating gravitational-wave detectors, the shot-noise-limited sensitivity can be improved by increasing the laser power in the interferometer arms. The signal-to-noise ratio is proportional to the square root of the light power [Mizuno95]. For very large light power, the quantum fluctuations of the light will be also seen as another noise source, the radiation pressure noise. The first generation of interferometric detectors, however, will not be limited by radiation pressure noise in the measurement band. The next generation is being designed for an optimum power with

respect to shot noise and radiation pressure noise. The required power is very large, in the order of 10^6 Watts. No currently available laser can provide this amount of continuous power with the desired stability. Power Recycling is a simple method for increasing the light power inside the Michelson interferometer: With the Michelson interferometer operating at the dark fringe, the main part of the light power injected into the west port also leaves the interferometer at the west port; the Michelson interferometer thus behaves like a mirror. When an extra mirror, the *Power-Recycling mirror* (MPR), is placed into the west port (see Figure 1.11), it forms a cavity together with the Michelson interferometer. This *Power-Recycling cavity* can be understood as a simple Fabry-Perot cavity, provided the Michelson interferometer is considered ideal and stable. Inside the cavity the light power is resonantly enhanced. The possible power enhancement is limited by optical losses inside the Michelson interferometer. With the power transmittance of the Power-Recycling mirror being 1000 ppm, we expect to realise a power enhancement of approximately 2000.

Signal Recycling: A passing gravitational wave creates phase-modulation sidebands inside the Michelson interferometer that are leaving the interferometer at the south port. If a mirror is placed into the south port (the *Signal-Recycling mirror*, MSR), these signal sidebands are reflected back into the interferometer. Because of its symmetry the Michelson interferometer can be described as a single mirror with respect also to the south port, too. In fact, another Fabry-Perot-like cavity is formed, the *Signal-Recycling cavity*. The signal sidebands are resonantly enhanced in the Signal-Recycling cavity. This enhancement results in a larger amplitude of the signal sidebands outside the Signal-Recycling cavity, i. e., on the photo diode, because the sidebands are created within the cavity (see [Heinzl99] for a detailed description of the optical properties of a two-mirror cavity with respect to Dual Recycling). The signal enhancement is proportional to the inverse square root of the bandwidth of the Signal-Recycling cavity. Signal Recycling decreases the bandwidth of the detector while improving the sensitivity within the bandwidth of the Signal-Recycling cavity. In addition, the Signal-Recycling cavity can be tuned easily so that the maximum enhancement is set to a user-defined Fourier frequency (signal frequency), see Chapter 3. This setup, which makes the detector a tunable narrow-band antenna, is called *detuned Signal Recycling* [Freise00].

1.4.1 Optical layout

A schematic drawing of the optical layout of the Michelson interferometer is shown in Figure 1.11. Figures 1.12, 1.13 and 1.15 show sections of the CAD drawing representing the Michelson interferometer.

From the second mode cleaner the beam travels north and enters the vacuum tank (TCIb, see Figure 1.12) holding a beam director (BDIPR) and the Power-Recycling mirror (MPR). Next to MPR, the reaction mass is shown; it is used for applying feedback to the mirror. The mode matching of the beam to the Power-Recycling cavity is done by three lenses: the output coupler of the second mode cleaner (MMC2b, see Figure 1.6) is

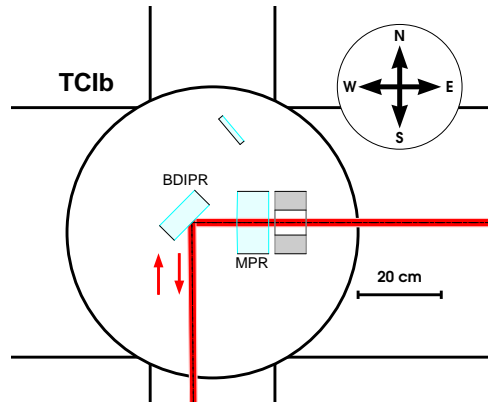


Figure 1.12: Input tank (TCIb) with a beam director (BDIPR) and the Power-Recycling mirror (MPR). The beam coming from the mode cleaner section (from south) is injected into the Michelson interferometer by BDIPR. The reaction mass used to apply a force to MPR is located east of the mirror; the beam is passed through a circular hole with a diameter of 65 mm.

concave-convex and serves as a lens. In addition, a small lens (LPR) is mounted on MU3. And finally, the Power-Recycling mirror is convex-flat, forming a collecting lens.

The beam enters the Michelson interferometer through the Power-Recycling mirror MPR. The reflected beam is used for the frequency control loop of the Power-Recycling cavity. It is reflected back into MU3 (see Figure 1.6) and directed out of the vacuum system by the northern Faraday isolator (FIPRb). Figure 1.14 shows the detection optics on the breadboard west of the mode cleaner section: the beam coming back from the Power-Recycling cavity reaches the breadboard via a lens, a periscope, an attenuator and a further periscope. These optical components are used to transform beam height, size and polarisation into practical values. The beam is split and detected on two quadrant cameras. The cameras are of the same type as those of the MC control loops. The so-called near-field camera (PDPR) functions as sensor for the Pound-Drever-Hall control loop for stabilising the laser light to the Power-Recycling cavity. In addition, the signals from PDPR and the signals from the so-called far-field camera (PDPRf) are used for the automatic alignment system.

The beam transmitted through MPR travels east towards the beam splitter (BS). It passes through a hole in the reaction mass of the Power-Recycling mirror. The hole has a diameter of 65 mm, while the beam has a diameter of less than 20 mm at that position. Figure 1.13 shows the section of the optical layout with the central vacuum tank (TCC), holding the main beam splitter, and the two *inboard* tanks (TCE and TCN) with the *end mirrors* (MCE and MCN). The beam transmitted through the beam splitter passes below MCE down the 600 m long vacuum tube. In another tank (TFE), the *folding mirror* (MFE) reflects the beam back towards the center. The beam hits the end mirror MCE 25 cm above the optical axis at the beam splitter. The end mirror is hit at normal incidence so that the light is reversed. Similarly, the beam reflected at the beam splitter travels north and is then directed up and back to the center by the folding mirror (MFN). The

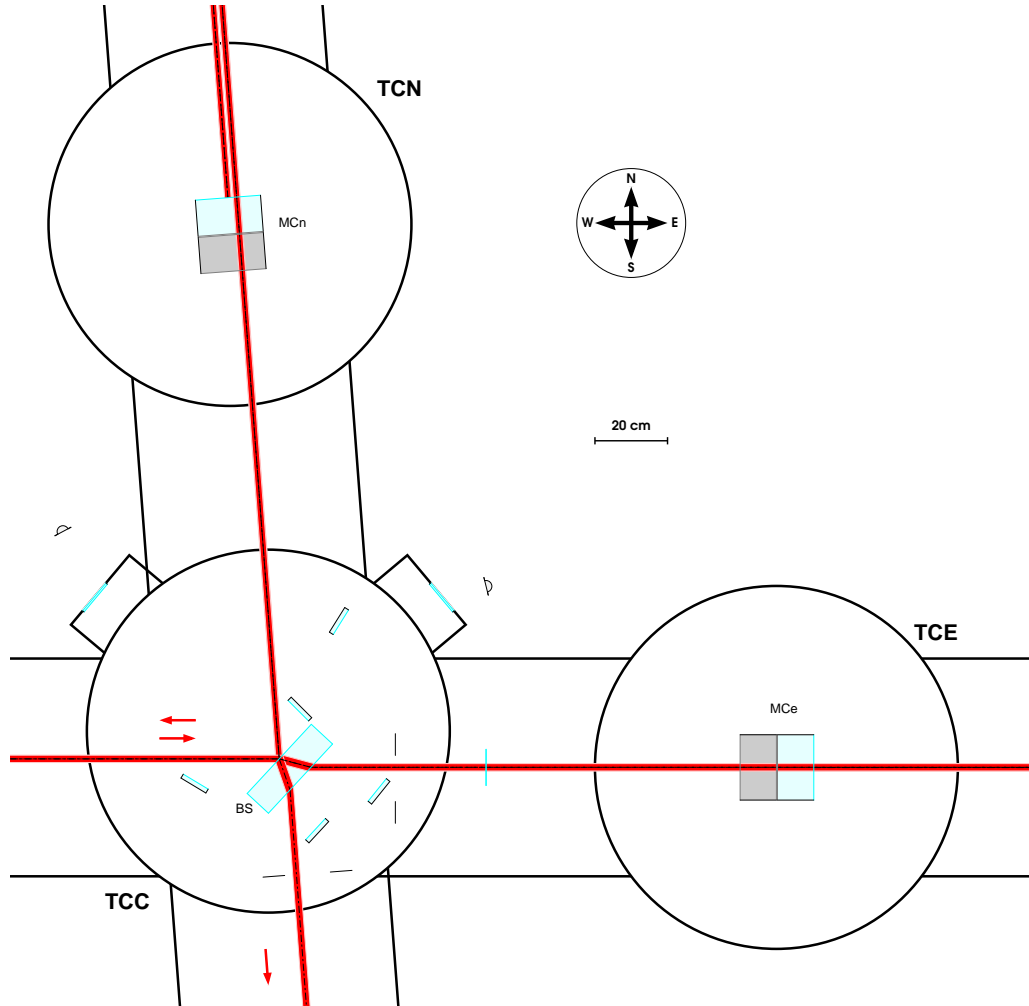


Figure 1.13: Section from the CAD drawing (Appendix A) with the central section of the Michelson interferometer. Only the main beam is shown: it approaches the beam splitter (BS) from the west and is split into two beams that travel along the 600 m long vacuum tubes. At 600 m, folding mirrors MF_n, MF_e (not shown) direct the beams back towards the central section. In the inboard tanks (TCN, TCE) the beams hit the end mirrors (MC_n, MC_e) 25 cm above the optical axis at the beam splitter and are reversed in their paths. The beams coming back from the interferometer arms are superimposed at the beam splitter and leave the interferometer through the west and the south ports. In this figure, the beams generated by the residual reflection at the back surface of the beam splitter have been omitted for clarity.

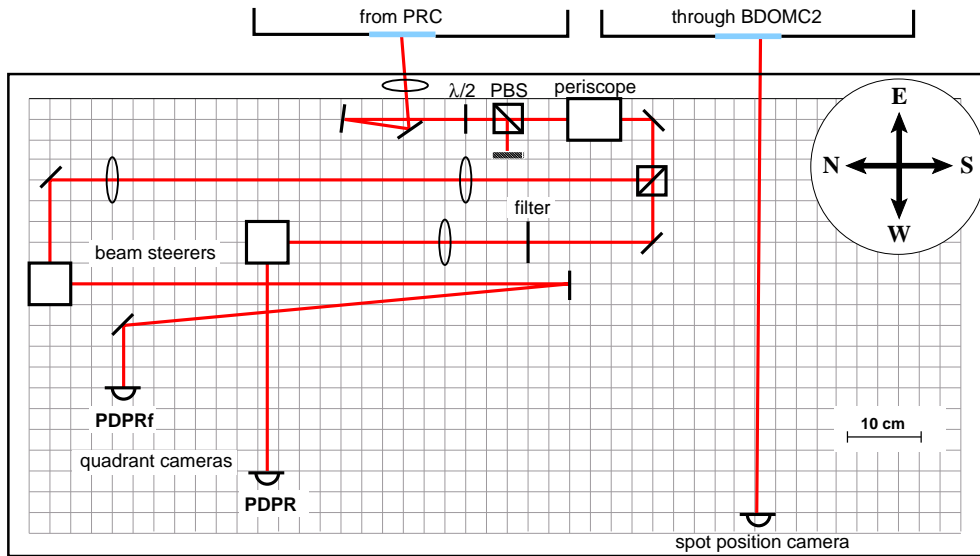


Figure 1.14: Breadboard located west of the mode-cleaner vacuum tank (TCMb). The beam coming back from the Power-Recycling cavity (PRC) is first passed through a lens, a periscope, an attenuator and a periscope to condition the beam for proper handling. The beam is then split and detected by two quadrant cameras. The so-called near-field camera (PDPR) is used for the length and frequency control. In addition, the signals from the two cameras are used for automatically aligning the mirrors of the Power-Recycling cavity. The lenses and beam steerers in front of the cameras are necessary for properly detecting the signals of the automatic alignment system.

retro reflection at the end mirror MC_n reflects the beam back towards the beam splitter. The reaction masses, used for applying feedback to the end mirrors for controlling the Michelson interferometer, are located directly behind the end mirrors.

The beams coming back from the interferometer arms are superimposed at the beam splitter and leave the interferometer to the west and south ports. The operating point of the GEO 600 Michelson interferometer is the dark fringe at the south port so that most of the light power is directed towards the west. The light fields that carry the signal, however, are leaving the Michelson interferometer through the south port, the main output port of the interferometer. Figure 1.15 shows the south port of the Michelson interferometer with the Signal-Recycling mirror (MSR) and the output optics. Next to the recycling mirror, the reaction mass for the length control of the Signal-Recycling cavity is shown. Three beam directors (BDO1, BDO2, BDO3) are used to inject the beam into the *output mode cleaner* (OMC), see Section 1.5; BDO1 is a spherical mirror that transforms the beam size for mode matching. The output mode cleaner is a small, rigid triangular cavity that rejects residual light in higher-order modes. The beam transmitted through OMC is then detected by a high-power photo diode (PDO) located outside the vacuum on an optical table, the so-called *detection bench*. The optical setup on the detection bench is more complicated than indicated in Figure 1.15, as it is still subject to changes.

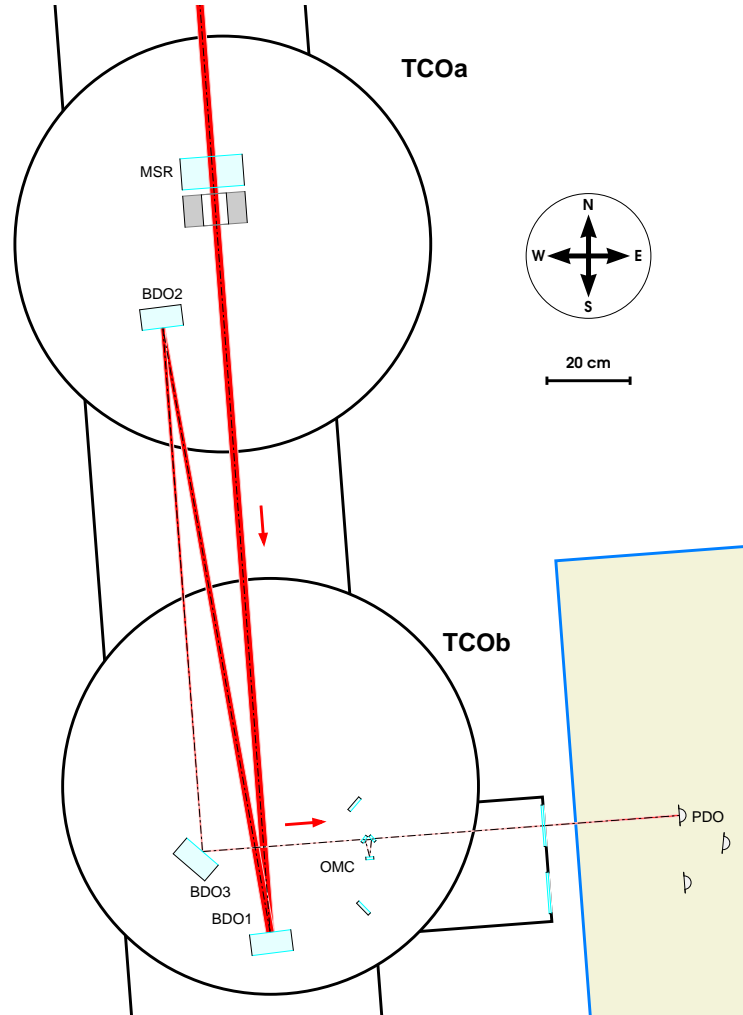


Figure 1.15: The output optics of the interferometer: the light from the beam splitter passes south through the Signal-Recycling mirror (MSR). Three beam directors (BDO1, BDO2, BDO3) are used to mode-match the beam to the output mode cleaner (OMC). That mode cleaner is designed to filter the beam from contributions in higher-order modes (mainly second-order modes originating from a thermal lens in the beam splitter). Finally, the beam leaves the vacuum and is detected by a high-power photo diode (PDO). The photo diode is mounted on an optical table, the detection bench. The optical components on the detection bench have been omitted because the setup is still subject to changes.

1.4.2 Interferometer design

The Dual-Recycled Michelson interferometer consists of three different types of optical components: The main mirrors (end mirrors and folding mirrors), the beam splitter and the recycling mirrors. The main mirrors and the beam splitter are suspended as triple pendulums. The Signal-Recycling mirror is also suspended as a triple pendulum with a similar suspension system as that of the main optics, with the difference that it does not have a monolithic stage (see below). The Power-Recycling mirror is suspended as a double pendulum, with a suspension very similar to the suspension system of the mode-cleaner mirrors.

This section gives the specified parameters for the optical components of the Michelson interferometer. During the commissioning of the detector we used so-called *test optics* that are similar to the final optics but with relaxed specifications. By using test optics, we were able to test the installation process without the risk of damaging or contaminating expensive high-quality optics.

The triple suspension of the main optics uses a monolithic lower stage only for the final optics; wire slings are used for the test optics. In the following, both the parameters of the final optics and of the currently installed test optics are given. Please note that during the on-going development, different sets of test optics might be installed.

Final optics: The main mirrors are fused-silica cylinders with a diameter of 180 mm. They are 100 mm thick and weigh 5.6 kg. The coating of the front surface is highly reflective with a power transmittance of ≈ 50 ppm. The back surfaces are coated for anti-reflection. A wedge of 1 mrad is used to avoid the etalon effect. The designed radius of curvature is 600 m for the end mirrors and 640 m for the folding mirrors. With the end mirror being approximately 600 m away from the folding mirror, the folded arms are thus insensitive to misalignments of the folding mirrors.

The beam splitter is a fused-silica cylinder. It is 80 mm thick with a diameter of 260 mm and weighs 9.34 kg. The front coating is designed to have a power transmittance of $T = 51.4\%$. The back surface has an anti-reflective coating. It is specified to have a power reflectance of less than 50 ppm. The slight asymmetry of the power splitting guarantees that some light will be leaving the Michelson interferometer through the west port while the Michelson interferometer is not controlled, even when the west port is at the dark fringe. This allows to stabilise the laser frequency to the Power-Recycling cavity with a free Michelson interferometer, which is important for the lock acquisition process [Heinzel99].

The beam splitter was made from a special type of fused silica with low absorption (Suprasil 311 SV by Heraeus) to minimise the thermal lens induced by absorbed laser light. The absorption in the beam-splitter substrate has been measured to be less than 0.5 ppm/cm.

The main optics are to be suspended with a monolithic suspension [Barr]: the intermediate mass of the respective triple pendulum is also made of fused silica. The mirror (or the beam splitter) is connected to the intermediate mass by fused-silica fibers that are welded to small pieces of fused silica, which in turn are contacted to the substrate using the silicate-bonding technique [Gwo]. The intermediate mass, the fibers and the mirror thus form a monolithic piece of fused silica. The mechanical quality factor of such a suspension system can be extremely high [Willems]. The final folding mirrors with monolithic suspension have been in place for more than a year. Measurements of the violin modes of the monolithic suspension indicate a quality factor of $Q \approx 10^8$. The end mirrors and the beam splitter are still test optics, suspended in wire slings.

The Power-Recycling mirror is 75 mm thick and has a diameter of 150 mm. It weights 2.9 kg and is suspended as a double pendulum similar to that of the mode-cleaner mirrors. The front surface is flat with a highly reflective coating; the power transmittance coefficient is designed to be $T = 1000$ ppm. The back surface has an anti-reflective coating and is convex with a radius of curvature of $R_C = 1.87$ m (specification).

The design of the Signal-Recycling mirror is similar to that of the Power-Recycling mirror except that both surfaces of the mirror are flat. The power transmittance of the Signal-Recycling mirror is a critical parameter for optimising the sensitivity of a Dual-Recycled interferometer. The first test of the setup with Signal Recycling will make use of a mirror with $T = 1\%$. In the future, other mirrors with a higher reflectance may be used (up to $R = 99.9\%$). The reaction mass located after the Signal-Recycling mirror has a hole with a diameter of 65 mm for the output beam to pass.

	MPR (waist)	end mirror	folding mirror
test optics	11.7 mm	9.7 mm	20.9 mm
final optics	8.9 mm	8.2 mm	24.7 mm

Table 1.7: Typical beam radii of the eigen-mode in the Power-Recycling cavity for test optics and final optics (the effects of the thermal lens have been ignored) [Winkler].

Test optics: The main test mirrors of the Michelson interferometer have the same size as the final mirrors. They were delivered with slightly incorrect radii of curvature. Later on, a corrective coating was applied. The resulting radii of curvature were $R_C \approx 710$ m for the folding mirrors and $R_C \approx 600$ m for the end mirrors. This results in a different beam size in the Power-Recycling cavity and therefore in a different mode matching for the Power-Recycling cavity (see Table 1.7). In addition, the corrective coating decreases the optical quality of the mirrors (the power transmittance increases towards the edge of the mirrors by ≈ 10 to 20 ppm/cm). It was possible, however, to perform the scheduled experiments with the test interferometer.

The Power-Recycling test mirror has a power transmittance of $T \approx 1.4\%$. The coating is not uniform; the power transmittance increases towards the edge of the mirror by ≈ 700 ppm/cm.

round-trip length	2394 m
FSR	125.25 kHz
FWHM	30 Hz
finesse	4500
beam waist w_0	9 mm
Rayleigh range z_R	240 m
Guoy phase	320°
mode separation	110 kHz

Table 1.8: Typical parameters of the Power-Recycling cavity. The parameters that refer to the beam shape and the finesse depend on the power at the beam splitter (see text). The parameters of the Signal-Recycling cavity differ slightly from the parameters of the Power-Recycling cavity because of a 9 cm larger round-trip length.

The test beam splitter is 235 mm in diameter, and 80 mm thick. It weighs approximately 7.6 kg. The fused silica of the test beam splitter (SV 312) is expected to have a slightly higher absorption than that of the final beam splitter. The anti-reflective coating was found to be worse than specified. Measurements indicate a power reflectance of ≈ 1000 ppm.

1.4.3 Optical properties

The beam waist of the eigen-modes of the Power-Recycling cavity is located at the flat surface of the Power-Recycling mirror. Other parameters of the eigen-modes inside the Power-Recycling cavity depend on the light power because of the thermal lensing in the beam splitter substrate (see below). Table 1.8 shows typical parameters of the Power-Recycling cavity. The parameters of the Signal-Recycling cavity are very similar; only the round-trip length is 9 cm larger, and the derived parameters differ accordingly.

The absorption inside the beam splitter creates a so-called *thermal lens* in the substrate. The resulting change in the beam parameters depends on the chosen design:

- a) Symmetric: The initial design of the optical layout included a so-called *compensation plate*. A compensation plate is a fused-silica cylinder identical to the beam splitter except that the coating of the front surface is anti-reflective, too. The compensation plate is placed into the north arm close to the beam splitter (here into TCC) so that the beam paths in the east and north arm both include a similar path through a fused-silica substrate. Thus, the effect is symmetric, and the interference contrast at the beam splitter is largely insensitive to the thermal lens. The beam parameters of the eigen-mode of the Power-Recycling cavity, however, change with the light power in the interferometer.
- b) Asymmetric: Recent research on thermo-refractive noise indicates that the extra noise introduced by a compensation plate results in a poorer sensitivity [Cagnoli]. Therefore, in the current design the compensation plate has been omitted. In this case, the thermal lens in the beam splitter affects only the east arm so that the beam sizes of the returning beams are not perfectly matched.

round-trip length	100.1 mm				
FSR	3 GHz				
FWHM	101 MHz				
finesse	30				
beam waist w_0	120 μm				
Rayleigh range z_R	42 mm				
Guoy phase (tangential)	100°				
mode separation	830 MHz				
TEM order	1	2	3	4	5
power suppression	210	350	90	45	320

Table 1.9: The designed optical parameters of the output mode cleaner. The parameters were computed for a radius of curvature of $R_C = 85$ mm for the curved mirror. The maximum possible suppression with this mode cleaner would be ≈ 360 .

Theoretical analysis predicts that the mismatch in the current design leads to a considerable fraction of the light power leaving the interferometer through the south port. Without Signal Recycling this extra loss mechanism would limit the power enhancement. FFT simulations indicate that only a light power of less than 3 kW at the beam splitter can be reached [Schilling02]. Signal Recycling, however, reduces the power loss considerably: first of all, the highly reflective Signal-Recycling mirror in the south port reduces the amount of light power that actually leaves the interferometer. In addition, the Dual-Recycling cavity shows an effect similar to the mode cleaning, the so-called *mode-healing*: the resonance condition inside a cavity is different for the different TEM_{nm} modes. The recycling cavities are designed to be resonant for a TEM_{00} mode of the input light. The light that is directed south because of the mismatch of the beam sizes at the beam splitter can be described well by second-order modes (TEM_{nm} modes with $n+m=2$). The Dual-Recycling cavity in GEO 600 is designed in such a way that the second order modes are suppressed. The FFT simulations show that with Signal Recycling and an input power of 5 W, the power at the beam splitter is approximately 10 kW, which is equivalent to the specified power enhancement of 2000. The beam sizes in the two arms are expected to be slightly different: directly after the beam splitter, the beam sizes are 8.8 mm in the north arm and 10.6 mm in the east arm. The beam size of the beam at the Power-Recycling mirror is ≈ 9.8 mm, which is 1 mm larger than the beam size calculated without a thermal lens.

1.5 Output mode cleaner

The possible asymmetry in the interferometer arms (see above) and imperfect radii of curvature of the interferometer mirrors cause a considerable fraction of power leaving the interferometer in second-order modes. This light does not contain any gravitational-wave signal. Therefore, an output mode cleaner is used to filter the beam before it is detected

by the high-power photo diode (PDO). The output mode cleaner is designed to yield a good (close to optimum) suppression for second-order modes. It is constructed as a small rigid cavity with a triangular beam path (see Figure 1.16). The round-trip length is approximately 10 cm. Table 1.9 shows the optical parameters of the cavity. The cavity will be suspended as a single pendulum in a vacuum tank (TCOb). After passing the output mode cleaner, the beam leaves the vacuum system towards the detection bench, where it is finally detected by a high-power photo diode.

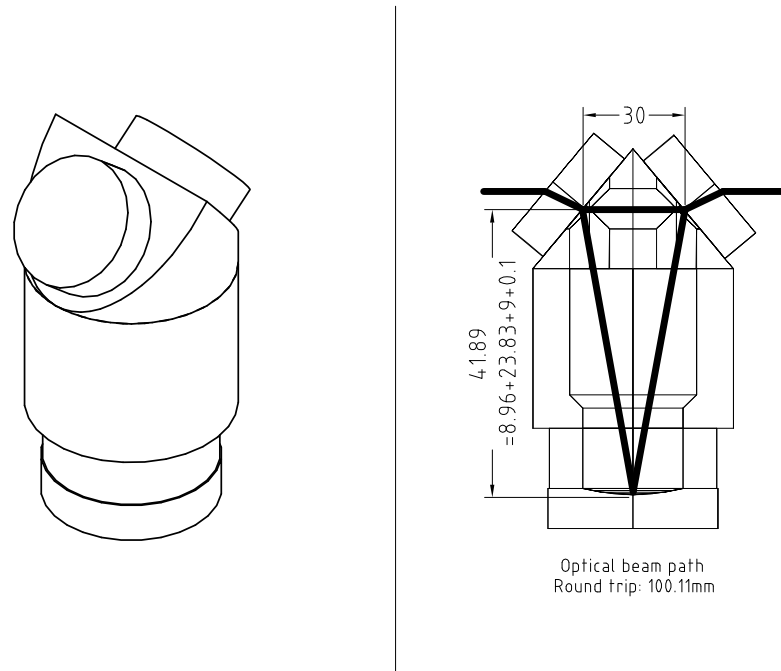


Figure 1.16: Schematic view of the output mode-cleaner design. It is a triangular ring cavity formed by three mirrors that are bonded to a rigid spacer.

Chapter 2

The laser frequency stabilisation for GEO 600

2.1 Introduction

A Michelson interferometer becomes insensitive to frequency fluctuations of the injected laser light when both interferometer arms have exactly the same length. It is then called a *white-light interferometer*. However, deviations from the operating point or imperfect optics would still lead to a false signal due to frequency fluctuations of the light. In GEO 600, the Schnupp modulation method [Schnupp] is used for controlling the Michelson interferometer. Schnupp modulation requires a phase modulation to be applied to the laser light before it enters the interferometer. This is done with an electro-optic modulator positioned in front of the Power-Recycling mirror. The modulator creates a pair of phase-modulation sidebands at an RF frequency (the modulation frequency) used to generate an error signal for the Michelson interferometer operation point. If the Michelson interferometer is set to be insensitive to frequency fluctuations, phase modulation is also not passed to the main output but reflected back towards the input (west) port. A small arm-length difference is necessary for the Schnupp modulation sidebands to reach the south output port where the error signal for the Michelson interferometer length control is detected. The arm-length difference defines a coupling factor for laser frequency noise into the gravitational-wave signal. The specifications for the laser frequency noise can be deduced from the desired sensitivity. Figure 2.1 shows the requirements for the frequency noise.

The laser frequency requirements can be met by using a very stable laser source and by further stabilising the laser light to a reference with active control. For laser frequency stabilisation one usually employs rigid cavities (so-called *reference cavities*) that provide a stable reference through their resonance frequency, i. e., their geometric length. A typical design for a reference cavity uses mirrors that are rigidly mounted (e. g., optically contacted) to a spacer made of material with a very low thermal expansion coefficient (Zerodur, Invar, ULE). The optical components thus form a very compact and mechanically stable device. In addition, these cavities should be positioned in vacuum and in an environment with stabilised temperature.

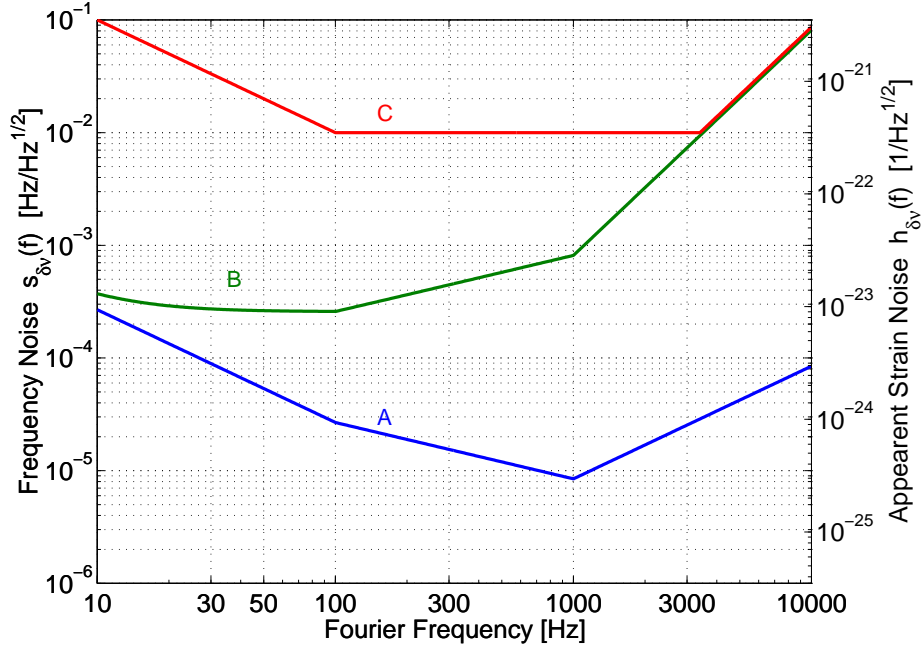


Figure 2.1: Requirements for the frequency noise of the laser system for GEO 600 [Brozek]. The three curves show the frequency-noise limit for various points inside the optical system: Graph A gives the frequency-noise limit at the beam splitter of the Michelson interferometer and graph B shows the limit for the light entering the Power-Recycling cavity. Graph C refers to the old design for a frequency stabilisation with a rigid reference cavity. It shows an assumed limit for such a laser system.

The first design concept for the frequency stabilisation for GEO 600 included such a reference cavity. During the implementation and characterisation of the frequency stabilisation, we decided to omit the reference cavity and use the suspended cavities of the mode cleaners as references. This resulted in a much simpler control scheme. For Fourier frequencies at which we expect to measure gravitational waves (the so-called *measurement band* from 50 Hz to 1500 Hz), the suspended cavities provide good references because of their excellent seismic suspension system. Rigid cavities provide a better reference at low frequencies. As the frequency stability at low frequencies is not very demanding, however, a simple control system can be used instead¹. The current design uses a stable electronic clock (GPS-controlled Rubidium oscillator) as reference for low frequencies. A sideband transfer method is used to control the length of the cavities with respect to the oscillator frequency.

¹ At Fourier frequencies above and below the measurement band the frequency fluctuations do not couple directly into the main interferometer output. It is desirable, however, to also minimise frequency fluctuations in these frequency bands: Second-order effects can shift frequency noise from higher or lower frequencies to the measurement band. In a well designed interferometer, these couplings are typically much smaller than the direct coupling of frequency fluctuations.

2.2 Frequency-noise specification

The computed specifications for the frequency stability are shown in Figure 2.1. The respective analysis was based on the expected sensitivity limits as known in 1999. The plot shows three graphs that give the computed limits for the frequency noise at different locations inside the optical system. Graph A shows the frequency-noise limit at the main beam splitter. The right axis gives the apparent strain amplitude and the left axis the corresponding frequency noise. The coupling of the frequency noise into the output signal of the Michelson interferometer was computed for an arm-length difference of 12 cm. Graph A was set to be a factor of 10 below the expected thermal noise.

Graph B shows the frequency-noise limit for the light entering the Power-Recycling cavity, which is expected to have a bandwidth (FWHM) of approximately 20 Hz so that the frequency noise is filtered as:

$$\tilde{x}_A(f) = \frac{10}{\sqrt{100 + f^2}} \tilde{x}_B \quad (2.1)$$

The frequency noise limit shown in graph C is of no importance for this work. It refers to an old design of the frequency stabilisation.

Recent research on thermal noise [Cagnoli] indicates that the thermal noise will limit the sensitivity of GEO 600 at higher strain amplitudes. A computation of the expected frequency-noise limit as of date is given in Section 3.3.5.

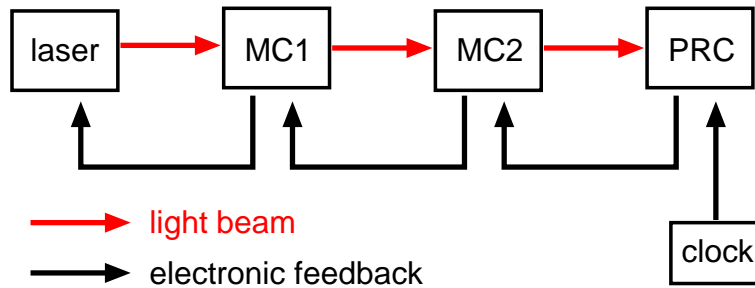


Figure 2.2: The basic control concept of the laser frequency stabilisation for GEO 600: The laser light is passed through two mode cleaners (MC1, MC2) and injected to the Power-Recycling cavity (PRC). Pound-Drever-Hall control systems are used to control the lengths of the mode cleaners and the laser frequency sequentially: The length of MC2 follows the length of the PRC, the length of MC1 follows the length of MC2 and the laser frequency follows the length of MC1. Thus, the laser frequency is resonant in all three cavities with the PRC as reference. In addition, the length of the Power-Recycling cavity is stabilised at low frequencies against a stable oscillator (clock).

2.3 Concept of the length and frequency control

Appendix B provides some general information about control loops, including the definitions of some expressions used to describe and characterise the control loops in the following sections.

The conceptual design of the frequency stabilisation is shown in Figure 2.2, whereas Figure 2.3 shows a diagram of the optical layout with the components of the respective control loops. The descriptions of the control system will be given in the order of the lock acquisition process:

1. At first, the slave laser is injection-locked to the master. The injection lock will not be described here. We regard the slave laser as a simple amplifier because its frequency will rigidly follow the frequency of the master laser. Feedback for changing the laser frequency can thus be applied to the master laser.
2. The laser light has to be passed through MC1. In other words, we have to lock the laser to the mode cleaner (or vice versa). The frequency of the laser is stabilised to the length of MC1 with a Pound-Drever-Hall control loop. The first mode cleaner experiences no control at that point. Its length is changing freely, and the control loop will change the laser frequency accordingly. Thus, the laser is locked to MC1, and the light will be transmitted through the mode-cleaner cavity.
3. Now, the light is to be passed through the second mode cleaner by also using a Pound-Drever-Hall loop. The frequency of the light reaching MC2 is stabilised to the length of MC2. Since the frequency of the laser light follows the length of MC1, this can be done by changing the length of MC1. In addition, there is the so-called *Bypass*, which is a high-passed feedback directly to the laser, allowing the control

loop to be build with a much higher control bandwidth. When this control loop is in operation, the *pre-stabilised* light reaches the main interferometer. The laser frequency noise for Fourier frequencies in the measurement band is determined by the mode-cleaner cavities. The mirrors of the mode cleaner are suspended as double pendulums to decouple the seismic motion from the mirrors (see Section 1.3.6). The transfer function of the pendulums (from suspension point to suspended mass) is $T_P \approx 1$ up to the first resonance frequency (≈ 1 Hz) and then falls with $1/f^4$. Therefore, the suspended cavities provide stable references for higher Fourier frequencies; however, they are noisy at and below the pendulum resonance frequencies. Consequently, the frequency fluctuations of the light stabilised to the mode cleaners will be lower than the fluctuations of the free-running laser frequency at high frequencies. At low frequencies, however, the laser frequency noise will be larger than that of the free-running laser.

4. The Power-Recycled Michelson interferometer is very similar to a simple cavity when the Michelson interferometer is on its operating point, the dark fringe. Therefore, another Pound-Drever-Hall control loop can be used to lock the laser light to the Power-Recycling cavity. The length of MC2 is changed accordingly by feeding back to one of its mirrors. For high-frequency actuation, an electro-optical modulator in front of the Power-Recycling cavity is used.
5. The control sidebands for the PRC control are generated in front of MC2. A deviation of the modulation frequency from the free spectral range of MC2 generates an error signal (in the light reflected by MC2) proportional to the length change of MC2 with respect to the RF sidebands. The modulation frequency is generated by a stable oscillator (which is locked to the GPS system). Thus, this error signal can be used to stabilise the laser frequency at low frequencies. The length of the Power-Recycling cavity is changed accordingly by feeding back to the Power-Recycling mirror. The corresponding control loop is called *DC loop*.

When all three Pound-Drever-Hall loops are working, the laser frequency follows the length of the free Power-Recycling cavity. The mirrors of the Power-Recycling cavity have a very good seismic suspension so that the absolute frequency stability at higher frequencies (above 50 Hz) should be excellent. At the resonance frequencies of the pendulums (between 0.3 Hz and 4 Hz), the length fluctuations can be significantly larger. Also, drifts at very low frequencies may be quite large. The DC loop prevents those by controlling the length of the Power-Recycling cavity at low frequencies. This guarantees that the laser frequency and the cavity lengths are fixed and the optical transfer functions (for example, for the modulation sidebands) are constant with time.

2.4 Pound-Drever-Hall control loops

Almost all feedback loops for length and frequency control use the Pound-Drever-Hall scheme [Drever83], which is a very useful method for stabilising a laser frequency to an optical cavity (or vice versa). Figure 2.4 shows the control loop design of the Pound-Dre-

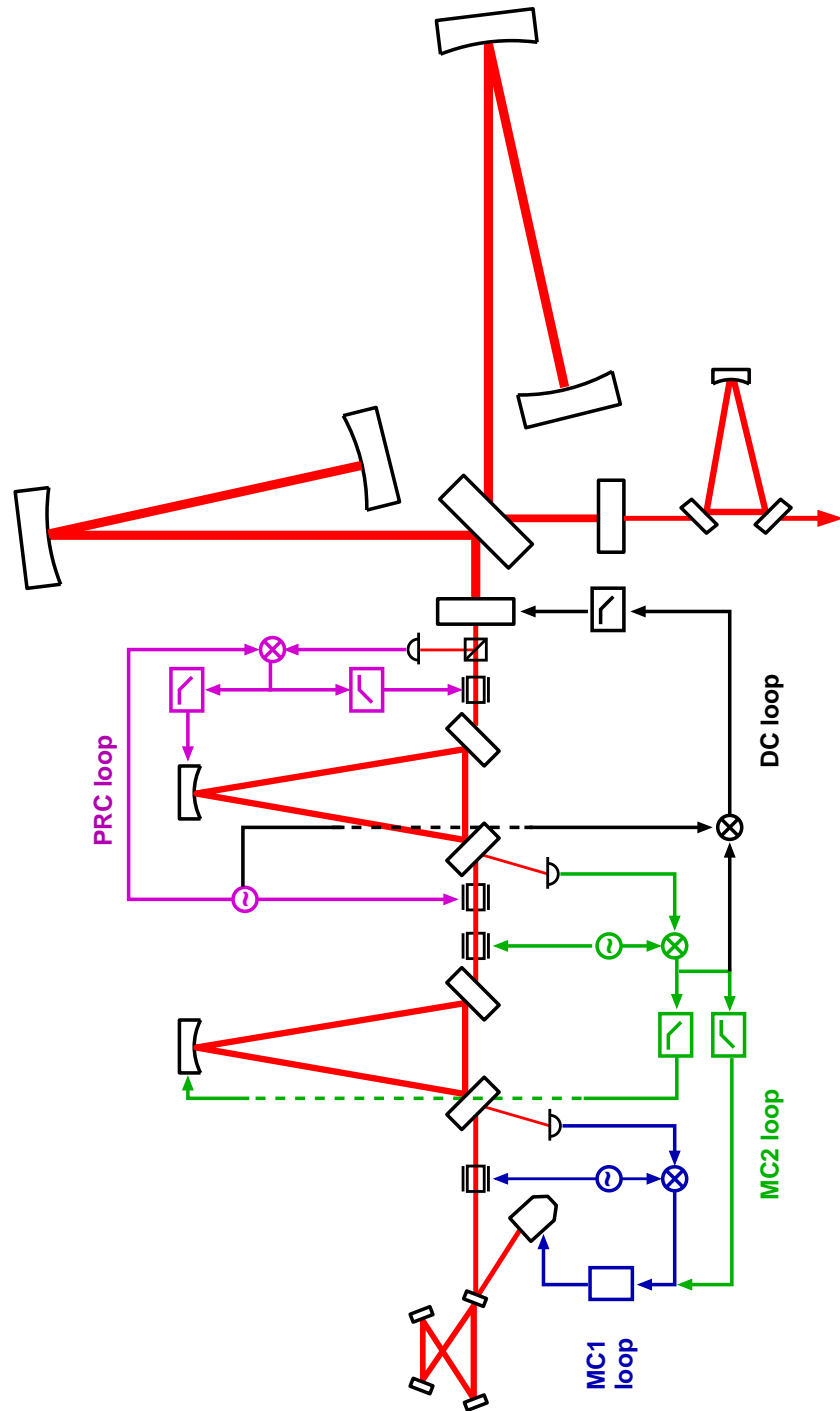


Figure 2.3: The optical layout of GEO 600 with the control loops of the length- and frequency-control system: Three Pound-Drever-Hall loops are used to sequentially control the laser frequency and the length of the mode-cleaner cavities. The DC loop is used to stabilise the length of the PRC against a GPS-locked oscillator for very low frequencies.

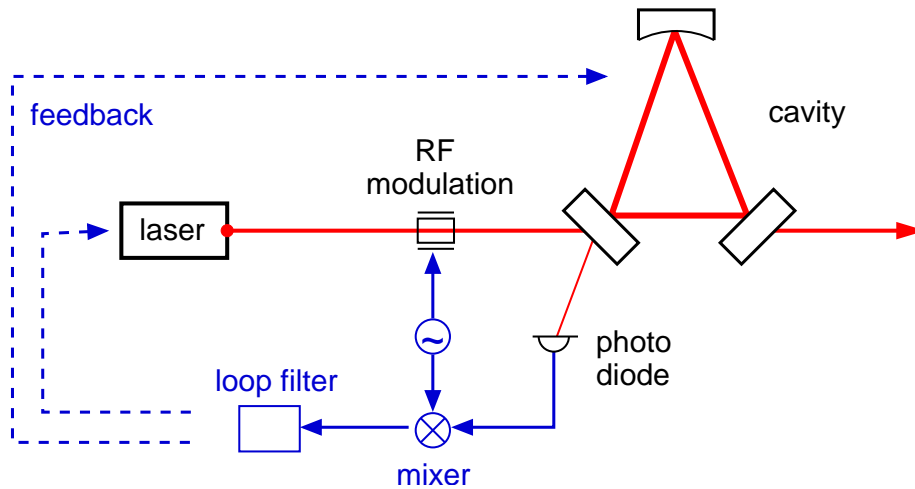


Figure 2.4: The layout of a typical Pound-Drever-Hall control loop. The light from the laser is modulated in phase at an RF frequency, the light reflected from the cavity is detected by a photo diode and demodulated by a mixer. An electronic filter generates a feedback signal that can either be applied to the laser frequency or to the cavity length.

ver-Hall scheme. The laser light is phase-modulated at an RF frequency before entering the cavity. The light reflected by the cavity is detected with a photo diode and demodulated at the RF modulation frequency. The resulting error signal is passed through an electronic loop filter and fed back either to the laser frequency or to the cavity length. The control loops used in the frequency stabilisation are of a very similar type and use similar components. In this section, the general features of the common components will be described, whereas the following sections deal with the different implementations.

Many aspects of modulation and demodulation in this context are described in [Heinzel99], and the analytic expression of a Pound-Drever-Hall error signal can be found in [Jennrich].

2.4.1 Quadrant cameras

The sensor generating the required error signal is one of the critical subsystems of every control loop. The noise suppression of a well-designed control loop is limited by the sensor noise. In the case of a Pound-Drever-Hall loop, the sensor for the laser frequency consists of the cavity, the modulation-demodulation electronics and the photo diode that detects the light reflected from a cavity.

The photo diodes used for the frequency stabilisation in GEO 600 provide a multitude of signals for various purposes. The diodes together with the electronic circuit are called *quadrant cameras*. Each of these cameras uses a Centrovision QD50-3T split photo diode. Table G.1 in Appendix G lists the specifications for that type of diode. These diodes have four separate areas (90° sectors of a circular diode, commonly called quadrants) that can

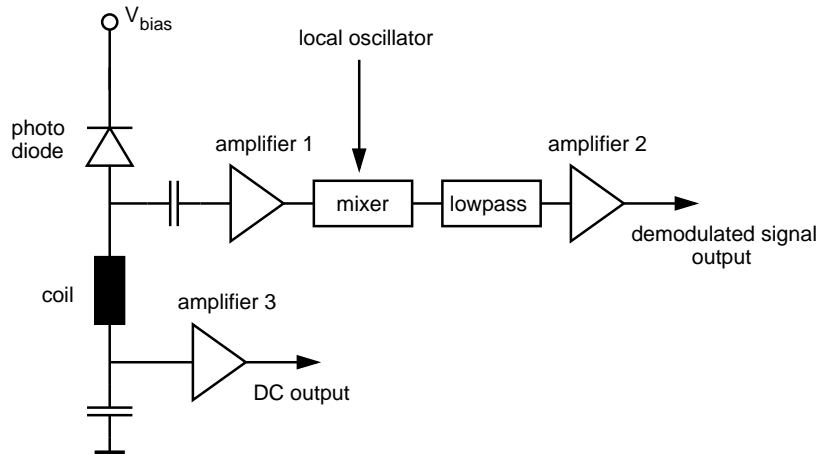


Figure 2.5: Simplified diagram of the electronics connected to each quadrant of the photo diode.

be read out independently. Each quadrant is connected to a similar electronic network. Figure 2.5 shows the schematic layout of the electronic circuit for one quadrant. A coil is put in series with the quadrant to form a resonant circuit with the capacitance of the diode. The resonance of this circuit is designed to match the frequency of the modulation sidebands. Such a photo diode is commonly described as *tuned* because it has the maximum sensitivity in a narrow, adjustable frequency band. The reverse bias voltage is applied to decrease the capacitance and the rise time of the diode, allowing for a high sensitivity at RF frequencies. The optimum bias voltages have been determined experimentally for each modulation frequency. A detailed explanation of this type of photo-diode electronics can be found in [Heinzel99].

The resonance circuit allows to amplify the signal around the modulation frequency. This signal is then passed via a capacitor and amplifier 1 to a mixer. Only the high-frequency component reaches the mixer and is demodulated at the modulation frequency. The output is then low-passed and amplified again (amplifier 2).

In addition, each quadrant is connected to a trans-impedance amplifier circuit used to extract the signal at low frequencies (< 1 MHz): Amplifier 3 converts the photo current into a voltage proportional to the light power. This signal is also called *DC output* of the quadrant.

In other words, each camera provides two signals per quadrant and, in total, eight output signals. These signals are not used independently; instead, sums and differences of these signals are produced electronically. The sum of the four low-frequency outputs is called *visibility*. If the detected laser beam fits completely onto the diode, the DC output is proportional to the amount of light reflected from the cavity and thus allows to compute the visibility for the cavity (the ratio of the light power entering the cavity to the power impinging onto the cavity). The sum of the four demodulated signals is used for length and frequency control. The sum signal presents the *error point* of the control loop that

uses the respective camera as a photo detector. Some of the various possible difference signals are used for the automatic alignment system [Grote02]. With respect to the bandwidth of the control loops, the transfer functions of all camera signals are flat and can be described by a simple gain factor.

2.4.2 Piezo-electric transducer

In simple terms, piezo-electric material relates mechanical stress to an electric charge on the surface. A block of piezo-electric material will stretch or shrink when an electric voltage is applied (or, if the material is extended or compressed, an electric voltage is produced). The change in size of such a *piezo-electric transducer* (PZT) is proportional to the applied voltage. This makes a PZT a convenient mechanical actuator. The only drawback of using PZTs are their mechanical resonances. As such a resonance creates large structures in the transfer function from applied voltage to length change, it is difficult to use a PZT in a control loop with a unity-gain frequency close to a resonance frequency.

Like permanent magnets, piezo-electric crystals have to be ‘prepared’ in order to show a macroscopic effect. The various sectors of anisotropic electric polarisation are aligned by stretching the crystal while a high DC voltage is applied. This procedure is called *polling*. A large reverse voltage can undo the polling. Therefore, PZTs should be used with uni-polar signals (bi-polar signals can be made uni-polar by adding a proper DC offset).

Two PZTs are used in the GEO 600 laser system. The first PZT changes the frequency of the master laser. It is mounted on top of the master-laser crystal and changes the optical path length as a result of stress-induced birefringence. It is the main feedback actuator of the frequency stabilisation. The second PZT serves as a mount for a mirror of the slave laser and thus changes the length of the slave-laser cavity. This PZT is used for controlling the injection lock of the slave laser.

2.4.3 Pockels cells

All electro-optic modulators used in GEO 600 are so-called *Pockels cells*. The electro-optical or Pockels effect is an anisotropic change in the index of refraction proportional to an external electric field. Several transparent materials with a large electro-optical effect are available and can be used to change the phase of a passing light field. Along one axis of the anisotropic crystal, the change in refractive index can be described as:

$$\Delta n = pE \tag{2.2}$$

with p being a material constant (with respect to light with a certain wavelength). The electro-optic modulators described in this work use Lithium Niobate (LiNbO_3) for which the change of the index of refraction along the extraordinary axis is:

$$\Delta n = \frac{n_e^3 r_{33}}{2} E \tag{2.3}$$

with n_e being the undisturbed index of refraction along the extraordinary axis and r_{33} the proper element of the electro-optic tensor.

The electrical contact consists either of metal plates or of metallic layers coated to two sides of the crystal. The phase change per applied electric voltage then depends on the geometry of the crystal, i. e., on the ratio between length along the optical axis d and thickness D (distance between the electric contacts). For example, the half-wave voltage at which the phase change is exactly $\lambda/2$ can be written as:

$$V_\pi = \frac{D}{d} \frac{\lambda}{n_e^3 r_{33}} \quad (2.4)$$

An electro-optic modulator can be used as a fast phase corrector. The phase change of the light can also be understood as a frequency change. In fact, a small phase modulation at a frequency ω_m with modulation index m_φ is equivalent to a frequency modulation at that frequency with the modulation index $m_\omega = m_\varphi \omega_m$. Thus, the transfer function of the Pockels cell used as an actuator for the laser frequency rises proportional to frequency.

Electrically, a Pockels cell is mainly a capacitor. With typical crystal sizes (determined by optical requirements) the half-wave voltage is usually hundreds of Volts. The output impedance of the necessary voltage amplifier generates a low pass with the capacitance of the Pockels cell. This gives an upper limit for the usage of this type of electro-optic modulators in control loops. When the Pockels cells are used for applying a fixed modulation frequency, a resonance circuit can be used to drive the modulator.

The modulator used as fast actuator for the laser-frequency control loop is a New Focus 4004. The technical data of this modulator is shown in Table G.2. This type of modulator is very small, which allows a low half-wave voltage of only 210 V. The aperture of 2 mm restricts its use to small beam sizes.

All modulators located in the vacuum are custom-made. They are positioned on so-called *mounting units* (see Section 1.3.3). Each mounting unit houses two Lithium Niobate crystals (8 mm x 8 mm x 35 mm) that can be used independently. With $n_e = 2.165$ and $r_{33} = 30.8 \cdot 10^{-12}$, the half-wave voltage computes to $V_\pi \approx 790$ V per crystal.

2.4.4 Coil-magnet actuator

All main interferometers and cavities in GEO 600 use suspended mirrors. The mode-cleaner mirrors and the Power-Recycling mirror are suspended as double pendulums, and the main optics of the Michelson interferometer and the Signal-Recycling mirror are suspended as triple pendulums. We use different techniques to apply a force to suspended mirrors:

- **Coil-magnet actuators with a fixed reference:** Three magnets are glued to the mirrors. Force can be applied with three coils attached to a holder that is fixed to the bottom of the vacuum tank. This method is only used for alignment control of beam directors.

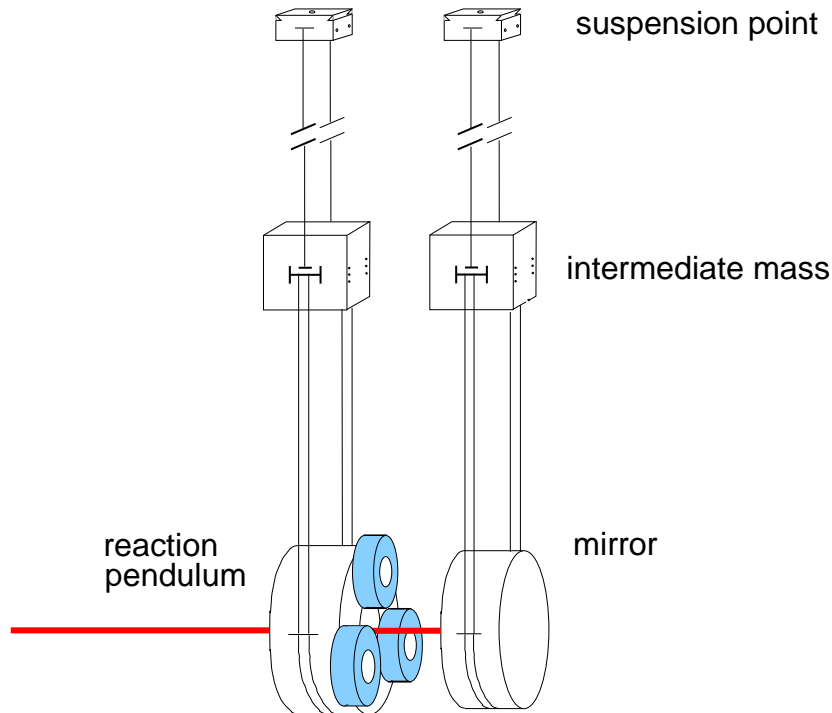


Figure 2.6: Schematic drawing of a mirror suspended as a double pendulum and a reaction pendulum with three coils. Opposite of each coil, a magnet is glued to the mirror.

- Coil-magnet actuators with a suspended reference:** A so-called *reaction mass*, an aluminium body with the same mass as the respective mirror, is suspended some millimeters behind (or in front of) the mirror, see Figure 2.6. The reaction mass holds three coils that are used to apply force to three magnets attached to the mirror. This form of actuation is used for controlling the mode cleaner lengths (via a reaction pendulum at each b mirrors) and the length of the recycling cavities (reaction masses at MSR and MPR). The main optics of the Michelson interferometer use a reaction mass at the intermediate stage, i. e., the force is applied to the intermediate mass.
- Electrostatic actuation:** For the main interferometer mirrors a reaction pendulum like the one described above is used, but the force is applied via an electrical field. In this case, the reaction mass is a fused-silica cylinder with a metallic comb-like structure coated onto it. This comb is used as a capacitor. The mirror, which is only approximately 3 mm away, can be understood as a dielectricum in the electric field of the capacitor. When a voltage is applied to the capacitor, the mirror experiences a force parallel to the field gradient and towards the maximum of the electric field. Therefore, only attractive forces can be generated. The mirror can be moved almost proportional to an applied control signal when a static DC offset voltage is applied to the capacitor coating in addition to the signal. This kind of actuator is used for the end mirrors of the Michelson interferometer with the triple suspension:

The lower mass of the reaction pendulum is used to apply a force directly to the respective mirror.

- **Coil-magnet actuators at the intermediate mass:** All suspended mirrors have a so-called *local-control system*. This is an electronic feedback loop used to actively damp the main pendulum resonances. The feedback is applied via coil-magnet actuators to the intermediate mass of double pendulums or to the top mass of triple pendulums. The coils are attached to a rigid structure that is connected to the top structure of the suspension, and the magnets are attached to the intermediate mass (see Figure 1.10).

It is possible to control the position of the mirror by applying a DC current to these actuators. This type of feedback is used by other control loops to compensate for slow drifts.

The mode-cleaner length and frequency control uses the coil-magnet actuators with a reference pendulum to feed back to one mirror of each mode cleaner for controlling the mode-cleaner lengths. Figure 2.6 shows a schematic diagram of a mirror suspended as a double pendulum with a reaction pendulum next to it.

The reaction pendulum is exactly matched to the mirror pendulum with respect to the masses, the mass distribution and, therefore, the pendulum resonance frequencies. Using the coil-magnet actuators, a force can be applied to the mirror. In order to convert a sinusoidal force with a constant amplitude into a mirror motion, we have to take into account the pendulum's equation of motion. A single pendulum with a sinusoidal force applied to the mass is described as a driven oscillator. From simple mechanics we know that for Fourier frequencies much lower than the resonance frequency ω_0 , the amplitude of motion of the mass is approximately $F/(M\omega_0^2)$ with F as the applied (small) force and m the mass of the mirror. For frequencies much larger than the resonance frequency, the amplitude can be approximated to $F/(M\omega^2)$ with ω being the angular frequency of the applied force.

The main longitudinal resonance frequency of the mode-cleaner pendulums is at approximately 1 Hz. Therefore, the actuator can only be used efficiently in a limited frequency range. In our case, the frequency range is smaller than 10 kHz, limited by the maximum force of the coil-magnet actuators.

2.5 Laser and first mode cleaner

Figure 2.7 shows the control loop for stabilising the master-laser frequency to the first mode cleaner (MC1 loop). A standard Pound-Drever-Hall scheme is used: The optical cavity of the mode cleaner is used as a frequency discriminator. The amplitude and phase of the light reflected from the cavity depend on the difference between the laser frequency and the longitudinal eigen-frequency of the cavity. The Pound-Drever-Hall method uses phase-modulation sidebands to detect the phase change of the reflected carrier light on a photo diode. The modulation frequency for the control of MC1 is 25.2 MHz, and it is

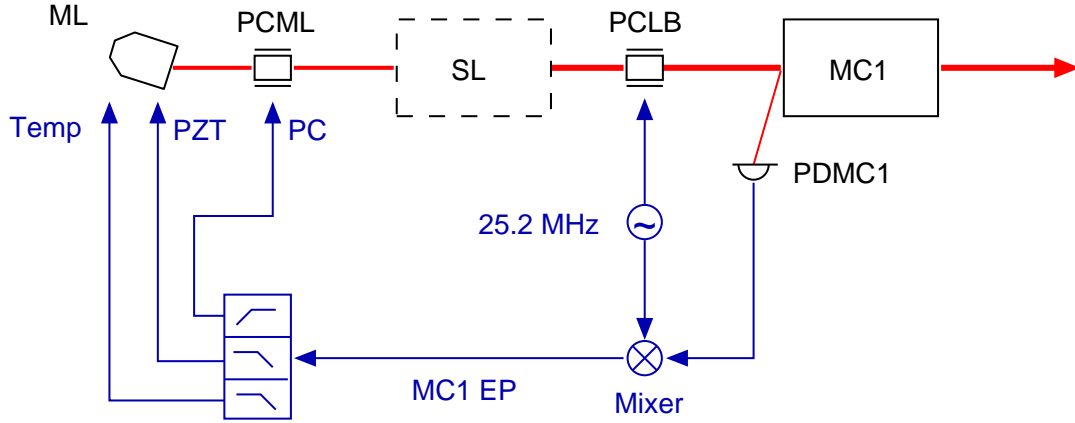


Figure 2.7: The control loop for stabilising the laser frequency to the resonance frequency of the first mode cleaner. The Pound-Drever-Hall signal is generated with a 25.2 MHz phase modulation. The feedback is split into three paths: the high-frequency component is fed back to a Pockels cell (PCML) and for frequencies below 15 kHz the feedback is applied via a PZT to the master-laser crystal. In addition, the signal is fed back to the temperature control of the master-laser crystal for very low frequencies (<0.5 Hz).

applied with PCLB in front of MC1. The light reflected by the input mirror (MMC1a) is detected by the photo diode PDMC1. The signal is then demodulated at 25.2 MHz with a mixer to generate the Pound-Drever-Hall error signal. The output of the mixer is the *error point* of the control loop (MC1 EP).

When the laser frequency is close to the cavity resonance, the error signal is given by:

$$x_{\text{MC1EP}} \approx C (f_{\text{Laser}} - N \cdot \text{FSR}_{\text{MC1}}) \quad (2.5)$$

with C being a constant, f_{Laser} the laser frequency, FSR_{MC1} the free spectral range of the MC1 cavity and N an integral number. In the following, $f_{\text{MC1}} = N \cdot \text{FSR}_{\text{MC1}}$ will be called *resonance frequency* of MC1 for simplicity.

This error signal is then passed through an electronic filter in which the signal is split into three feedback paths. The main feedback path is to the PZT mounted on top of the laser crystal. By applying a voltage to the PZT, the optical path length inside the laser crystal and thus the laser frequency can be changed effectively (2.28 MHz/V). Due to the mechanical resonances of the PZT, the high-frequency part of the feedback is split off and fed back to a fast phase shifter (PCML). The third feedback path is used to increase the dynamic range at very low frequencies: by feeding back to the temperature control of the master-laser crystal, the length of the crystal can be changed; this length change corresponds to a frequency change of 5.36 GHz/V. The main purpose of this temperature feedback is to compensate for slow drifts of large amplitude.

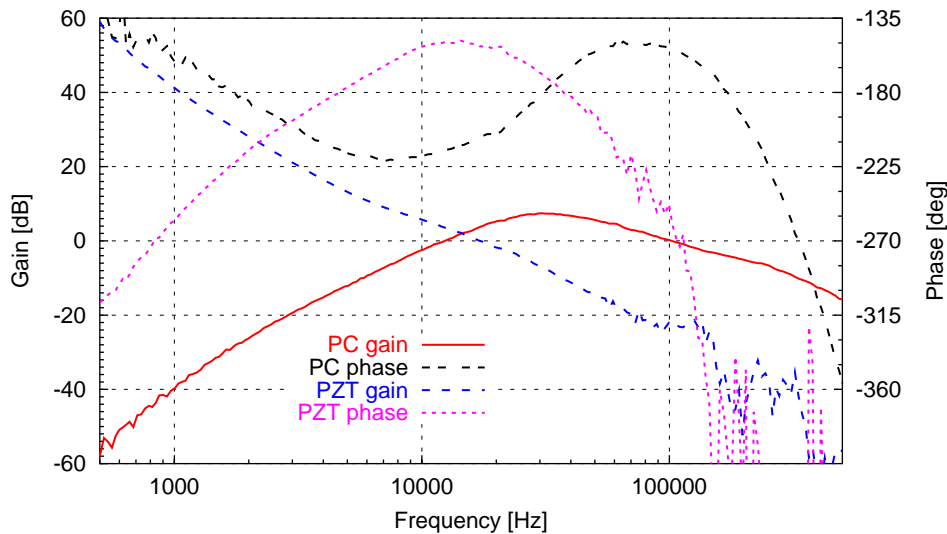


Figure 2.8: Closed-loop transfer functions of the PZT and PC feedback path, according to a measuring method as described in Appendix B.5 (please note that this does not represent the typical measurement of the open-loop gains of the two paths). The crossing between the two gains at 15 kHz marks the crossover frequency. The unity-gain frequency can be read as ≈ 100 kHz from the point where the PC gain crosses 0 dB.

2.5.1 Servo design

The open-loop gain is designed to have exactly one unity-gain point at approximately 100 kHz. Details of the loop filter electronics are provided in Appendix G.3. Figure 2.8 shows two measured closed-loop transfer functions of the MC1 control loop (see Appendix B.5 for a definition of this type of closed-loop measurements). The closed-loop transfer function for the two different feedback paths were measured with both feedback signals connected. To obtain the two graphs, the source signal (which is necessary for generating a transfer function) was added first to the PZT feedback path and then to the PC feedback path. The crossover frequency can be read from the plot as the frequency at which the two amplitudes are equal (≈ 15 kHz). In addition, the unity-gain frequency can be estimated to be at approximately 100 kHz where the PC feedback path crosses 0 dB. The crossover frequency to the temperature feedback has not been determined experimentally but is expected to be approximately 0.5 Hz.

The Pound-Drever-Hall error signal is valid only when the laser frequency is close to the resonance frequency of the cavity. Therefore, care has to be taken that this condition be fulfilled when the loop is closed. The process of closing such a loop in a way that a stable operation at the designed operating point is achieved is called *lock acquisition* (see Section 2.8.1).

For the lock acquisition of the MC1 loop, a ramp signal is applied to the master PZT. This sweeps the laser frequency over a wide range (greater than a free spectral range of the mode cleaner). The resonance frequency of the mode cleaner is changing only slowly compared to the induced sweep of the laser frequency so that at some point the laser light will become resonant in the MC1 cavity. At that time, the servo of the loop is switched on. Experience has shown that it is not necessary to change the loop gain for the lock acquisition. After the loop has been closed for some seconds, an extra integrator is switched on to increase the loop gain at low frequencies.

2.5.2 Error-point spectrum

Measuring the error-point spectrum \tilde{x}_{MC1EP} yields the deviation of the laser frequency from the cavity resonance frequency (also called *frequency fluctuations* in the following):

$$\tilde{x}_{\text{MC1EP}}(f) = C \cdot \frac{\tilde{f}_1(f)}{\sqrt{1 + (2f/\Delta f_{\text{MC1}})^2}} \quad (2.6)$$

with

$$f_1(t) = f_{\text{Laser}} - f_{\text{MC1}} \quad (2.7)$$

as the deviation of the laser frequency from the MC1 resonance frequency. The tilde denotes that the variable is a function of the Fourier frequency, and it is connected to the signal in the time domain via the Fourier transformation:

$$\begin{aligned} \tilde{x}_{\text{MC1EP}} &= \tilde{x}_{\text{MC1EP}}(f) = \text{FT} \{x_{\text{MC1EP}}(t)\} \\ \tilde{f}_1 &= \tilde{f}_1(f) = \text{FT} \{f_1(t)\} \end{aligned} \quad (2.8)$$

The difference between the laser frequency and the cavity resonance can be a good measure of the frequency noise of the laser. If, for example, the cavity were absolutely stable ($f_{\text{MC1}} = \text{const.}$), the fluctuations would be equal to the frequency noise of the laser frequency ($f_1 = f_{\text{laser}}$). This is also a good approximation of the fluctuations in real cavities with a non-zero length fluctuation, provided the laser frequency noise is still larger than fluctuations of the resonance frequency:

$$\begin{aligned} \tilde{f}_1^2 &= \tilde{f}_{\text{Laser}}^2 + \tilde{f}_{\text{MC1}}^2 \\ &\approx \tilde{f}_{\text{Laser}}^2 \quad \text{for} \quad \tilde{f}_{\text{Laser}} \gg \tilde{f}_{\text{MC1}} \end{aligned} \quad (2.9)$$

For the mode-cleaner cavities, the largest longitudinal motion of the suspended mirrors is at the pendulum resonance frequencies; at higher Fourier frequencies, the length fluctuations are expected to be very small because of the excellent seismic isolation.

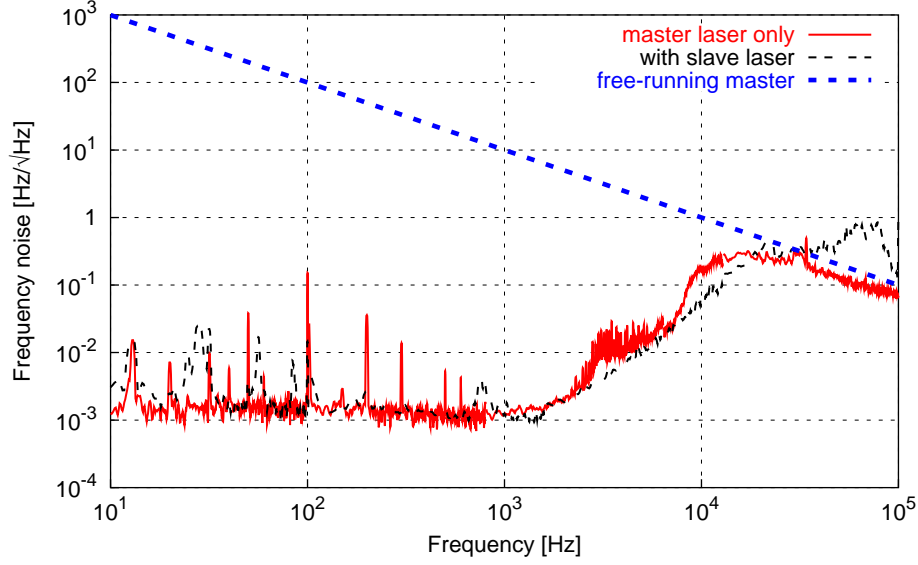


Figure 2.9: Error-point spectrum for the frequency stabilisation of the laser frequency to the first mode cleaner. One curve shows the in-loop frequency-noise spectrum for the system when the light from the master laser has been injected directly into MC1. This is compared to the full system with the slave laser in place. The system had not been changed otherwise. In addition, the theoretical prediction of the frequency noise of an un-stabilised (free-running) master laser is plotted.

The error-point spectrum is proportional to a spectrum of the frequency fluctuations multiplied by a one-pole low pass at the cavity pole frequency. The low pass is the characteristic transfer function of a Fabry-Perot cavity:

$$G_{\text{cavity}}(f) = \frac{1}{\sqrt{1 + \left(\frac{2f}{\Delta f}\right)^2}} \quad (2.10)$$

This transfer function describes the passive filtering of amplitude or frequency fluctuations of a light field that is resonant in the cavity. Thus, the frequency fluctuations of the light field inside the cavity can be described as:

$$\tilde{f}_{\text{cavity}} = G_{\text{cavity}}(f) \cdot \tilde{f}_{\text{Laser}} \quad (2.11)$$

Figure 2.9 shows the error-point spectrum for MC1. For comparison, the theoretically predicted frequency noise of a free-running master laser is plotted. It is expected to be [Brozek]:

$$\tilde{f}_{\text{ML}} \approx \frac{10^4}{f} \text{ Hz}/\sqrt{\text{Hz}} \quad \text{for } 1 \text{ Hz} < f < 100 \text{ kHz} \quad (2.12)$$

For Fourier frequencies below 1 kHz, the measured in-loop frequency noise is in the order of 1 mHz/ $\sqrt{\text{Hz}}$, which corresponds to a frequency noise suppression of, for example, 120 dB at 100 Hz.

During the installation of the frequency-control system, the slave laser was not yet available. Instead, the light from the master laser was injected directly into the mode cleaners. When the slave laser was added to the optical path, the electronic control systems were not changed. Figure 2.9 shows the error-point spectra of the MC1 control loop for these two experimental setups. The graph with the error-point spectrum for the system with the slave laser in place shows that the basic performance of the system did not change. The noise performances of the two control loops are very similar. Only at frequencies of 20 to 60 kHz do the mechanical resonances of the slave laser PZT give rise to some additional noise. In addition, the graph for the system with the slave laser shows less noise between 1 kHz and 10 kHz. This was achieved independently of the laser system by reducing the coupling of electronic noise into the loop-filter electronics.

Out-of-loop measurement

A measurement of the absolute frequency noise of the laser stabilised to the first mode cleaner must use an independent reference. The second mode cleaner provides a reference that is independent, except for possible common mode effects. Such effects may arise because the mirrors of both mode cleaners are suspended from the same top structures. Seismic motion that excites the mirrors of the cavities can induce a common mode motion that would not be detectable by using MC2 as reference.

For this measurement, the frequency of the light leaving MC1 was stabilised to MC2 (see next section) with a very low control bandwidth ($f_{\text{ug}} \approx 300$ Hz). For Fourier frequencies above the unity-gain frequency, the control loop for MC2 does not change the laser frequency at all so that the error point spectrum of the MC2 control loop shows the frequency noise:

$$\tilde{x}_{\text{MC2EP}} = C \cdot \tilde{f}_2 G_{\text{MC2}}(f) \quad \text{with} \quad f_2 = f_{\text{LP}} - f_{\text{MC2}} \quad (2.13)$$

with f_{LP} being the laser frequency passed through the first MC1. The passive filtering by the MC1 cavity can be described as:

$$\begin{aligned} \tilde{f}_{\text{LP}} &= \tilde{f}_{\text{Laser}} \left(1 + \left(\frac{2f}{\Delta f_{\text{MC1}}} \right)^2 \right)^{-1/2} \\ &= \tilde{f}_{\text{Laser}} G_{\text{MC1}}(f) \end{aligned} \quad (2.14)$$

and thus:

$$\tilde{x}_{\text{MC2EP}} = C \cdot \sqrt{\left(\tilde{f}_{\text{Laser}} G_{\text{MC1}}(f) \right)^2 + \tilde{f}_{\text{MC2}}^2} \cdot G_{\text{MC2}}(f) \quad (2.15)$$

Figure 2.10 shows a comparison of the in-loop measured frequency noise to the out-of-loop measurement. The in-loop measurement has been multiplied by $G_{\text{MC2}}(f)$ for better comparison. Above 5 kHz the resulting noise density is equal to the out-of-loop noise. Below 5 kHz the frequency noise differs from the in-loop measurement.

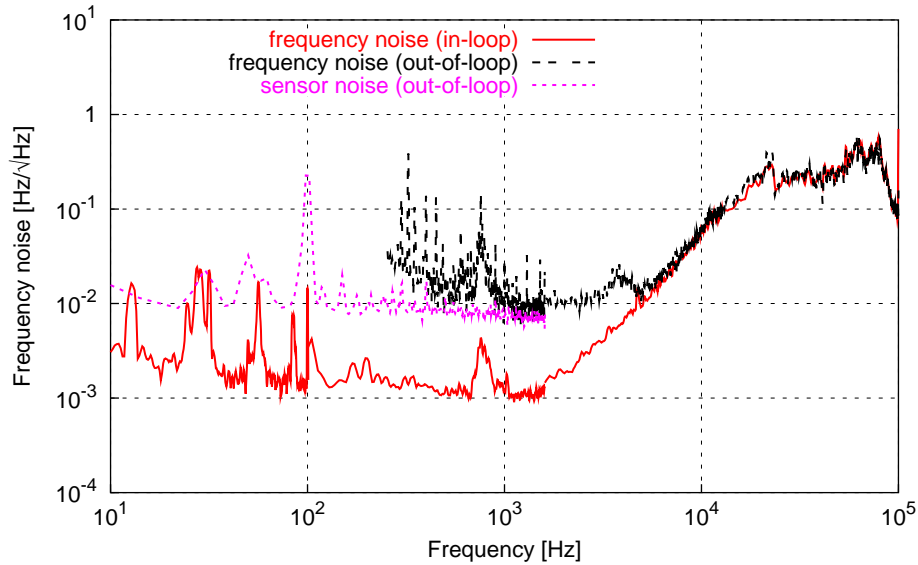


Figure 2.10: Out-of-loop measurement of the frequency noise of the MC1 control loop (the in-loop measurement has been multiplied by a one-pole low pass with the MC2 cavity pole for better comparison). Note that these measurements were made with the slave laser in place.

The out-of-loop frequency noise cannot be smaller than the sensor noise of the loop (at frequencies with loop gain greater than 1). At frequencies below 5 kHz, the frequency noise seems to be almost limited to $10 \text{ mHz}/\sqrt{\text{Hz}}$ by sensor noise. The noise of the quadrant camera and mixer is plotted as sensor noise in Figure 2.10. The sensor noise is electronic noise; we estimated that a shot-noise-limited performance can be achieved by increasing the light power on the photo diodes by a factor of five. This is not necessary, however, for achieving the specified frequency stability for GEO 600 (see below).

The measurement could only give information about the out-of-loop frequency noise above 300 Hz; in this frequency region, the achieved frequency stability is slightly better than that in previous results of an experiment with rigid cavities [Brozek].

Feedback signal

Figure 2.11 shows the feedback signal to the PZT in comparison to the expected free-running noise of the master laser (see Equation 2.12). For frequencies above 5 Hz, the measurement agrees very well with the expected noise of the master laser. For lower frequencies, the additional noise shows that the mode-cleaner cavity is dominant over the laser noise. This is expected because the motion of the mirrors around the resonance frequencies is large. The feedback to the PZT is a good measure of the length fluctuations of the MC1 cavity because the root-mean-square values of both signals are equally dominated by the mirror movements at the pendulum resonances. From the PZT feedback we

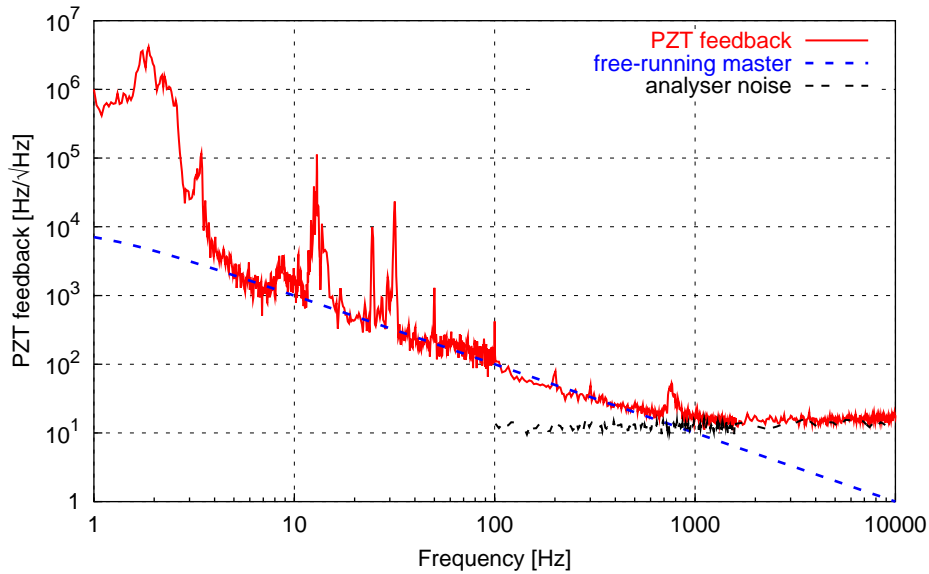


Figure 2.11: Feedback signal to the PZT compared to the expected frequency noise of a free-running master laser.

have estimated a typical fluctuation of the mirror position of $x_{\text{rms}} \approx 100$ nm. This value has also been confirmed by other measurements.

The features between 10 Hz and 40 Hz have been identified as motions of the mode-cleaner mirrors: a mechanical resonance of a connecting vacuum tube (13 Hz), the frequency of a Scroll pump connected to the mode cleaner vacuum system (24.5 Hz), and an undamped bounce mode of the double pendulums (≈ 30 Hz). A peak at 822 Hz shows another mechanical disturbance: the turbo-molecular pump connected to the mode-cleaner section is operated at that frequency.

2.5.3 Calibration of frequency-noise measurements

The measured error signals initially have the units $\text{V}/\sqrt{\text{Hz}}$. Calibration measurements are needed to determine the conversion factor for computing the frequency noise in $\text{Hz}/\sqrt{\text{Hz}}$.

All frequency-noise measurements were calibrated with the same method: For one subsystem of the loop, usually the actuator, a calibration factor C_1 in Hz/V has to be determined by an independent measurement. If the transfer functions of the several subsystems are known, a new calibration factor for the measurement point can be computed. In most cases, not all the transfer functions are known. Then a test signal at a fixed frequency is injected into the loop at that point of the electronics where the signal for the noise measurement is extracted. The test signal then propagates through the loop, and it can be measured at the (independently) calibrated point of the loop. This simple method provides the necessary transfer function for computing C_1 .

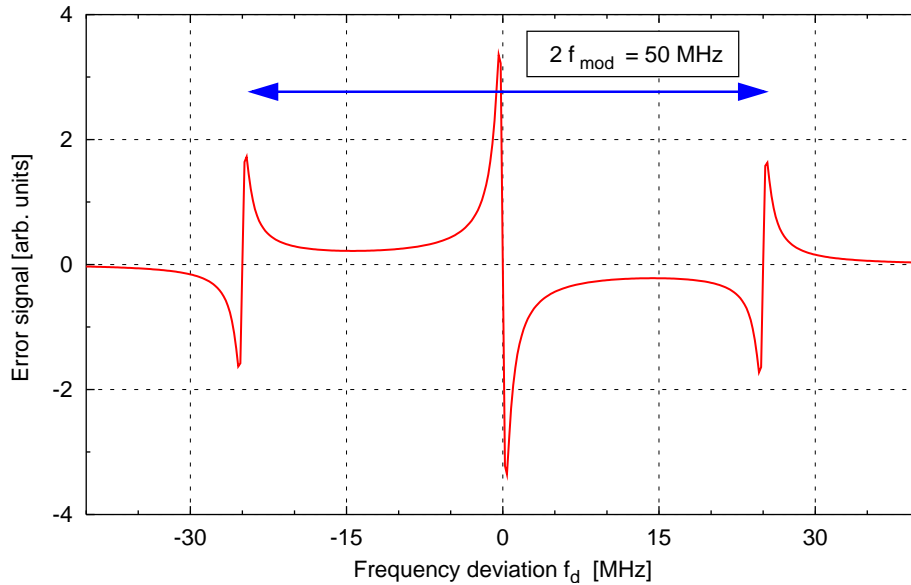


Figure 2.12: Example of a Pound-Drever-Hall error signal as a function of the frequency difference between the cavity resonance and the laser frequency. The symmetric features around the center peak are located at the modulation frequency, in this example at 25 MHz.

All frequency noise measurements shown here are calibrated against the PZT in the master laser. The calibration factor of that PZT of $C_{\text{PZT}} = 2.28 \pm 0.01$ MHz/V has been measured² in the following experiment: the light from the master laser was injected into a small, rigid, triangular cavity (a so-called *pre-mode cleaner*). A Pound-Drever-Hall error signal was generated by modulating the laser light in front of the cavity and by demodulating the reflected light. The error signal is proportional to f_d , the deviation of the laser light from the cavity resonance. The shape of the signal as a function of f_d is well known (Figure 2.12 shows an example). It has three prominent features: one large peak at $f_d = 0$ and two slightly smaller peaks when the frequency difference is equal to the modulation frequency $f_d = \pm f_{\text{mod}}$. The cavity is assumed to be rigid and stable so that the resonance frequency will change only slowly. When a ramp signal is applied to the PZT, the laser frequency is swept linearly and, at some point, becomes resonant in the cavity. If the ramp is fast enough, the frequency change induced by the ramp will dominate any random fluctuations of the laser frequency. With the known gradient of the ramp (Volts per second) one can derive the voltage needed to shift the frequency, for example, from $f_d = -f_{\text{mod}}$ to $f_d = +f_{\text{mod}}$. By repeating this measurement a number of times, an accurate calibration factor for the PZT can be obtained.

² The master laser was exchanged recently, and the calibration factor is likely to be different for the new PZT.

2.5.4 ‘Current lock’: Feeding back to the pump diode current

A new feedback technique for diode-pumped solid-state lasers has been developed in our group [Willke00]. It has been shown previously that a correlation exists between the power of the laser pump field and the laser frequency. The principle idea behind the new control concept is to use this correlation to act on the laser frequency. In practice, the current of the pump diodes is changed by the control loop. Therefore, this technique is called *current lock*. The current lock unifies the control of the laser frequency and of the laser power. It is expected to have advantages over the traditional feedback techniques if the frequency noise and the amplitude noise derive mainly from the power noise of the laser pump diodes. Another advantage is that the mechanical actuation by a PZT can be omitted. The PZT in the GEO 600 master laser, for example, induces complex mechanical deformations of the laser crystal in addition to the ideal actuation process.

The control electronics for stabilising the laser frequency to MC1 include a second, separate set of filters that can be used for a current lock of the master laser to MC1. With the current lock, the current of the pump diodes of the master laser replace the PZT as an actuator. The rest of the servo design is not changed. The filters have been adjusted so that the lock techniques could be exchanged by setting a jumper in the servo electronics and connecting the respective feedback signals. Measurements show that the current lock in this particular case gives exactly the same performance as the conventional method with feedback to the PZT. This proves that the current lock is a robust technique that can be used with good performance. However, in a straightforward implementation the expected advantages were not found. It is expected that a better understanding of the noise sources will allow to optimise the performance.

2.6 Second mode cleaner

The second mode cleaner is very similar to the first one. Therefore, plant and sensor of the control loop for MC2 (MC2 loop) are basically identical to that of the MC1 loop. Only the actuators and the electronic filters are different. The frequency of the light leaving MC1 is to be locked to the length of the second mode cleaner. Consequently, the length of MC1 has to be changed by the MC2 control loop.

Figure 2.13 shows a schematic drawing of the control loop for the second mode cleaner. Again, the control scheme is the Pound-Drever-Hall method. A modulator (PCMC2), placed between MC1 and MC2, creates phase-modulation sidebands at 13 MHz. The photo diode (PDMC2) detects the light reflected from MC2. The signal is then demodulated at 13 MHz. The loop filter splits the signal into a low-frequency part and a high-frequency part. The low-frequency signal (frequencies below 1 kHz) is sent to a coil-magnet actuator that can move the mirror MMC1b, thereby changing the length of the first mode-cleaner cavity. The actuation on a suspended mirror works well for low frequencies, but the gain falls with $1/f^2$ for higher frequencies. In order to get a high

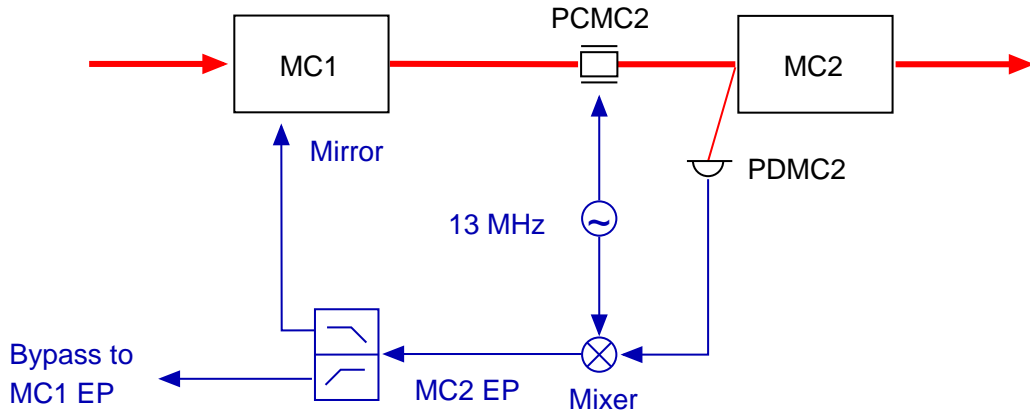


Figure 2.13: The control loop for stabilising the light leaving MC1 towards MC2. The Pound-Drever-Hall signal is created with a 13 MHz modulation. The light reflected from MC2 is detected by photo diode PDMC2 and demodulated at 13 MHz. The feedback signal is split into two paths: the low-frequency feedback acts on the lengths of the MC1 cavity, whereas the high-frequency part (*Bypass*) is injected into the MC1 error point, directly changing the frequency of the laser.

control bandwidth, the high-frequency signal is fed back directly to the master laser. This feedback path is called *Bypass*; in fact, the signal is added into the error point of the MC1 control loop. This forces the master-laser frequency to fluctuate with respect to the resonance of the first mode cleaner (at high frequencies); fluctuations with respect to the second mode cleaner, however, are reduced.

2.6.1 Servo design

The control loop is designed to have a unity-gain frequency of approximately 20 kHz when the high-frequency feedback (*Bypass*) is switched on. It is, however, possible to lock the second mode cleaner with the slow feedback (MMC1b) only, and the primary lock acquisition is more reliable if only the slow feedback is on. The low open-loop gain of the slow feedback provides a loop filter that is more robust during the first seconds after acquisition when the feedback signal might temporarily saturate the electronic filters. When the system has been in lock for a while, the feedback signals decrease to a lower level (given by the differential length fluctuations of the mode cleaner cavities). Then the *Bypass* and two integrators are switched on. This increases the gain and the frequency-noise suppression for Fourier frequencies below 10 kHz. The crossover frequency is at approximately 1 kHz. Figure 2.14 shows the closed-loop transfer functions of the MC2 loop measured during the four sequential states of the lock acquisition:

1. MMC1b feedback only: The high-frequency feedback is disconnected. The control loop is stable with a low unity-gain frequency, here ≈ 1 kHz. The lowest possible unity-gain frequency with this loop is approximately 300 Hz.

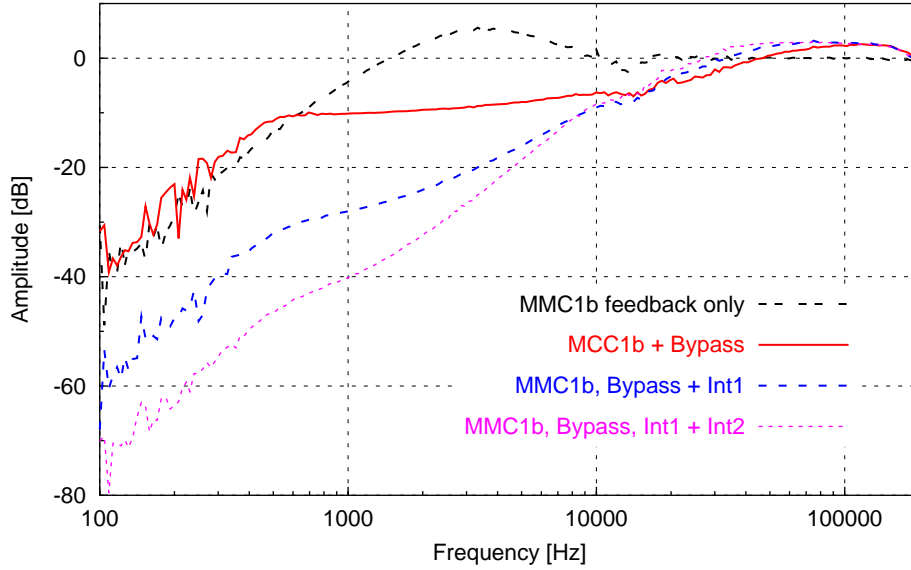


Figure 2.14: Closed-loop transfer functions of the MC2 loop. The closed-loop transfer function was measured for four different states of the control loop (see text).

2. Both feedback paths (MMC1b, Bypass) are connected: The unity-gain frequency is now at approximately 20 kHz, but the gain at low frequencies is still similar to that of the previous state.
3. and 4. Integrators are switched on: The high bandwidth allows to add extra integrators to the loop to increase the gain at low frequencies.

Details of the electronic implementation of this loop filter can be found in Appendix G.

2.6.2 Error-point spectrum

The in-loop frequency noise of the MC2 loop is shown in Figure 2.15. At Fourier frequencies below 7 kHz, the in-loop frequency noise is $\approx 1 \text{ mHz}/\sqrt{\text{Hz}}$. A comparison of the in-loop noises of the two mode-cleaner loops shows that the plateau at low frequencies is at the same level but extends to higher frequencies in the case of the MC2 loop.

It was not possible to do a similar out-of-loop measurement for the MC2 loop as described for the MC1 loop. The respective measurement requires the frequency of the light leaving MC2 to be stabilised to the Power-Recycling cavity with a low unity-gain frequency. This could not be done with the necessary stability. Instead, the out-of-loop noise in Figure 2.15 has been computed from the Power-Recycling cavity error point: in the case of an ideal loop, the error point spectrum is determined by the spectrum of the disturbances and the open-loop gain:

$$\tilde{x}_{\text{PRCEP}} = \frac{\tilde{f}_2 G_{\text{PRC}}}{1 - H_{\text{PRC,open-loop}}} \quad (2.16)$$

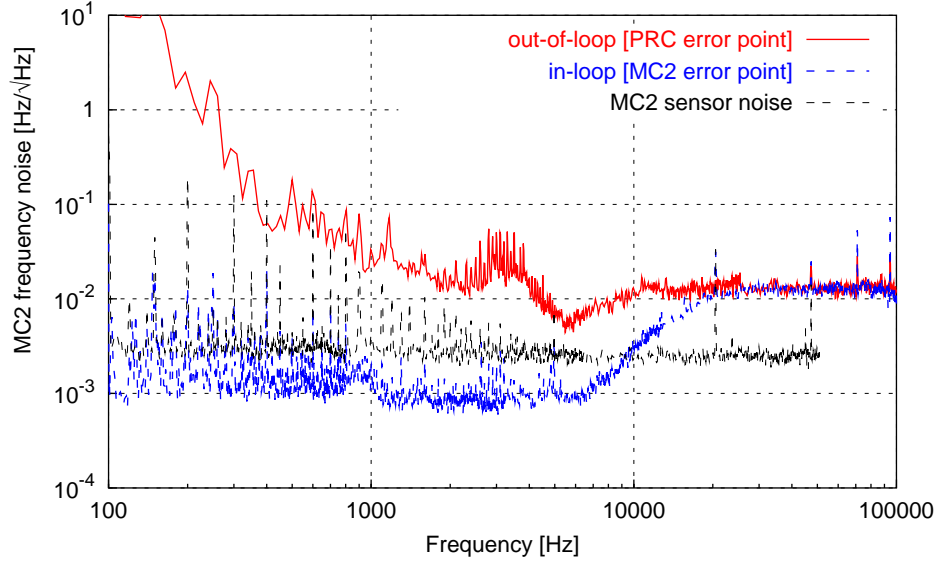


Figure 2.15: Error-point measurements of the frequency stabilisation of the laser frequency to MC2. One plot shows the in-loop frequency noise spectrum. In addition, the out-of-loop noise computed from the PRC error-point signal is plotted. The third plot shows the sensor noise of the MC2 photo diode (PDMC2).

with $f_2 = f_{LP2} - f_{PRC}$ as the deviation of the frequency of the light leaving MC2 (f_{LP2}) and the resonance frequency of the Power-Recycling cavity (f_{PRC}). The relative length fluctuations of the Power-Recycling cavity are 300 times smaller because of the greater cavity length. Therefore, the following approximation can be made:

$$\tilde{f}_2 \approx \tilde{f}_{LP2} \quad (2.17)$$

Thus, the out-of-loop noise, in this case the difference between the frequency of the light leaving MC2 and the resonance frequency of the Power-Recycling cavity, can be estimated as follows:

$$\tilde{f}_{LP2} \approx C \tilde{x}_{PRCEP} \cdot \frac{1 - H_{PRC,open-loop}}{G_{PRC}} \quad (2.18)$$

As the two mode-cleaner cavities are similar, it is expected that the MC2 loop cannot achieve a better out-of-loop performance than the MC1 loop. The steep rise of the noise with decreasing frequency is not equivalent to the expected length fluctuations of the MC2 cavity. We believe that the error signal of the Power-Recycling cavity is contaminated with electronic noise. In this case, Equation 2.18 does not hold and the top graph in Figure 2.15 does not represent the out-of-loop noise; this is to be investigated.

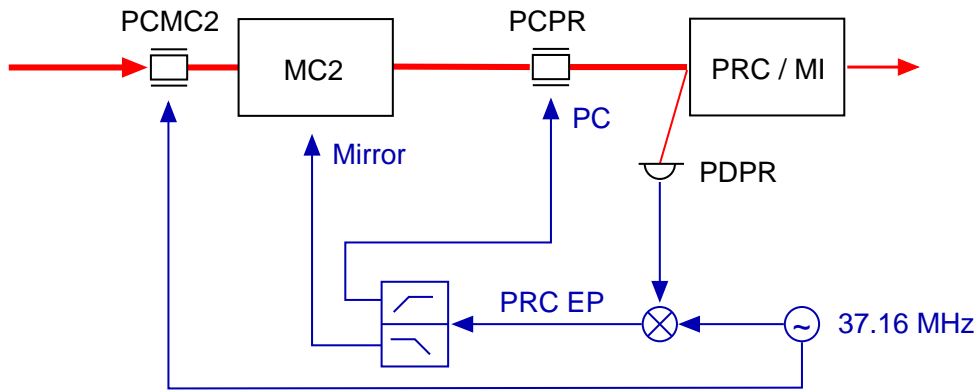


Figure 2.16: The control loop for stabilising the frequency of the light leaving MC2 to the length of the Power-Recycling cavity: The modulation sidebands are generated in front of MC2 (PCMC2). The modulation frequency is equal to the free spectral range of MC2 (≈ 37.16 MHz) so that the sidebands pass MC2 without being attenuated. The feedback is split in a way that the low-frequency part acts on the length of the MC2 cavity and the high-frequency part is sent to a fast phase shifter (PCPR).

2.7 Power-Recycling cavity

The Power-Recycled Michelson interferometer behaves like a Fabry-Perot cavity for the incoming light when the Michelson interferometer is held on the dark fringe. This is still true when Signal Recycling is used. Therefore, the Power-Recycled Michelson interferometer is commonly called *Power-Recycling cavity* (PRC). The Power-Recycling cavity is the reference for the laser frequency during normal operation of the GEO 600 detector. A Pound-Drever-Hall control scheme is used to stabilise the frequency of the light leaving the mode cleaners to the Power-Recycling cavity (PRC loop).

The concept of the control loop is shown in Figure 2.16. The light reflected from the Power-Recycling mirror (MPR) is detected with a photo diode (PDPR), demodulated and passed through an electronic filter. In this case, the electro-optic modulator (PCMC2), which generates the control sidebands, is not positioned directly in front of the Power-Recycling cavity but in front of MC2. The modulation frequency is adjusted to be exactly at the free spectral range of the MC2 cavity (≈ 37 MHz). Thus, the control sidebands are resonant in the MC2 cavity and consequently pass it without being attenuated.

The feedback signal is split into its high- and low-frequency parts. The low-frequency signal is fed back to MMC2b to change the length of the second mode cleaner. The high-frequency component is applied to an electro-optic modulator (PCPR) positioned in front of the Michelson interferometer and serving as a fast phase corrector.

Figure 2.17 shows the closed-loop transfer function of the PRC control system. When the measurement was done, the unity-gain frequency was approximately 20 kHz. The maximum unity-gain frequency for which a stable operation of the loop could be achieved is ≈ 40 kHz. The prominent features around 4 kHz and 7 kHz cannot be understood from

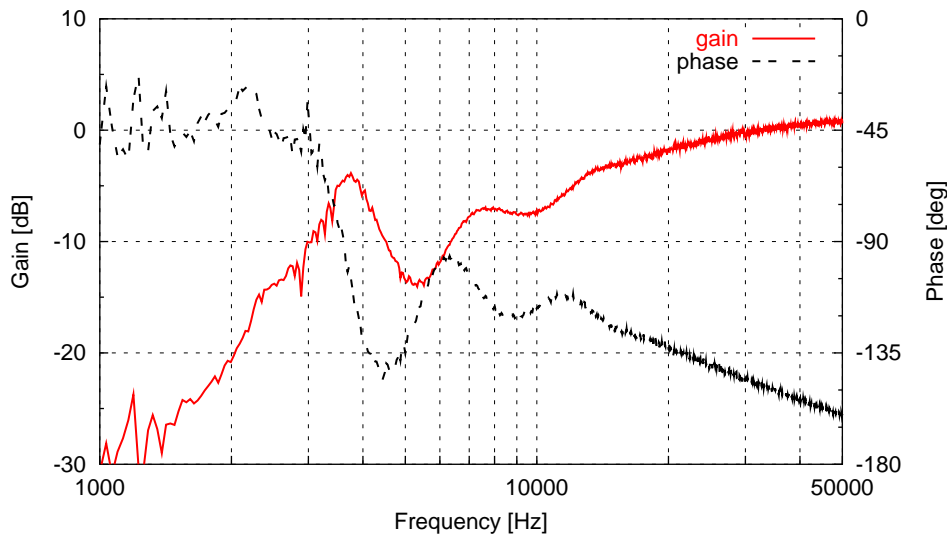


Figure 2.17: Closed-loop transfer function of the PRC loop. The unity-gain frequency is at approximately 20 kHz. The phase margin at that frequency shows that the overall gain can be further increased.

the design of the control loop and have to be investigated. The crossover frequency is at approximately 1 kHz, similar to the MC2 loop.

2.7.1 The ‘1200 m experiment’

By the beginning of 2001, the mode-cleaner section had been completed and in continuous operation for more than one year. Both cavities were automatically aligned, and the lock acquisition of the length-control loops was fully automated (see Section 2.8). We thus had a stable input beam for performing experiments with the optics of the main interferometer.

The so-called ‘1200 m experiment’ [Freise02] was an intermediate experiment for finalising and testing the laser frequency stabilisation. A 1200 m long Fabry-Perot cavity was created by installing the Power-Recycling mirror and the mirrors of one interferometer arm whilst leaving out the beam splitter. The optical parameters of this cavity are similar to the Power-Recycled cavity. In fact, this Fabry-Perot cavity resembles the Power-Recycled Michelson interferometer with a perfect Michelson interferometer being rigidly held on the dark fringe. Therefore, the cavity was well suited to install and test the final control systems of the frequency stabilisation. The advantage of this intermediate step was that it allowed to finalise the frequency-control system independently of the complex lock acquisition of the recycled Michelson interferometer. Figure 2.18 shows the control system for the frequency stabilisation as it was used for stabilising the laser light to the 1200 m long cavity.

In addition, this experiment was the first test of a large-scale optical system and gave us the opportunity to gather experience with many new components, such as the triple pendulum suspension of the main mirrors.

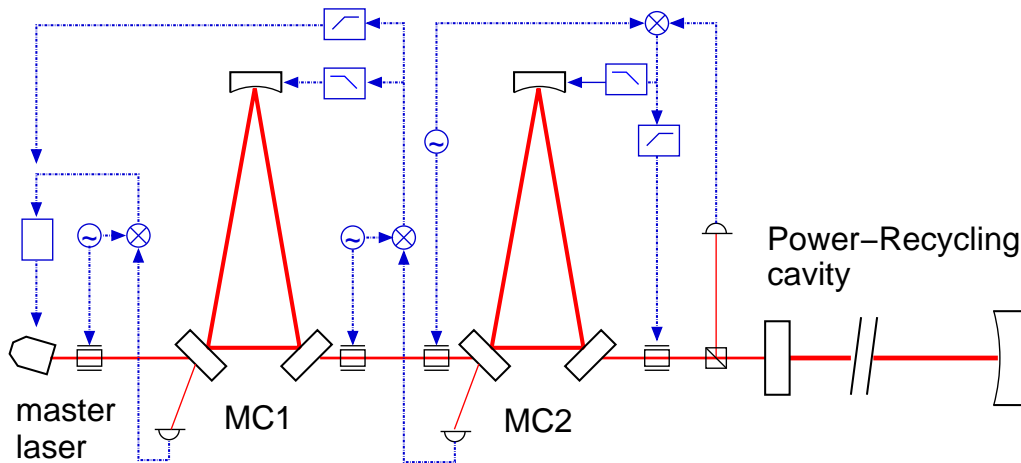


Figure 2.18: The frequency stabilisation system as used with the 1200 m long cavity in January 2001. The light of the master laser is filtered by two mode cleaners and injected into the 1200 m long Fabry-Perot cavity formed by the Power-Recycling mirror and the two mirrors of the folded east arm of GEO 600.

Fringes

In interferometry, the term *fringes* is often used to describe a striped beam pattern in the output of an interferometer. Throughout this work, the term *fringe* does not refer to a geometric pattern. Instead, it is used to indicate the change of the light power in an interferometer (or cavity) output from bright to dark and back (or vice versa) as a function of time.

A fringe in the light reflected from a cavity indicates that the frequency of the impinging light field is close to the resonance frequency of the cavity. If the laser frequency and the cavity have not been stabilised, the shape of the fringes can be used to extract information about the optical system.

The three mirrors of the 1200 m long cavity were without any automatic alignment control and thus had to be aligned manually for every experiment. When a reasonably good alignment was established, one could observe fringes in the light reflected from the long cavity. A numerical simulation was used to fit a model function to a measured time series of the reflected light power of the 1200 m long cavity (Figure 2.19). The simulation works in the time domain and calculates the dynamic changes of the light power inside a cavity after an incident laser beam comes into resonance with the cavity. In our case, the cavity is assumed to be rigid, while the frequency of the incoming beam is subject to a sweep (the effect is the same as for a cavity with moving mirrors that is illuminated by a light source with fixed frequency [Lawrence]). This assumption can be made because the relative stability of the 1200 m long cavity is much better than that of the mode cleaners that determine the frequency stability of the injected light. The particular fringe shown in Figure 2.19 was chosen because it could be modelled with a simple linear frequency sweep.

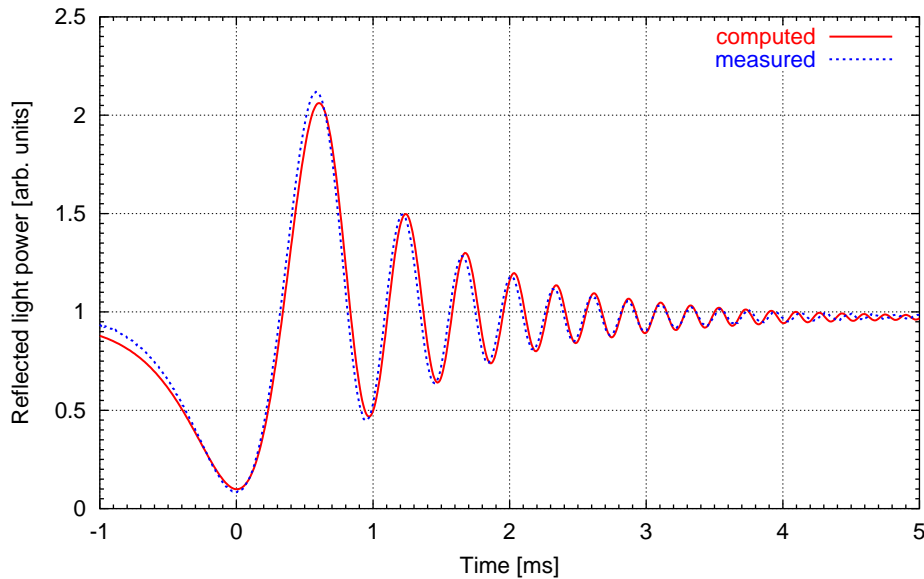


Figure 2.19: Measured fringe of the 1200 m long cavity compared to the result of a numerical simulation. The measurement shows a fringe that is typical with respect to the speed and amplitude. This particular fringe was chosen for its undisturbed shape. The simulation gives a finesse of 300 for the 1200 m long cavity and a velocity of 20 nm/s for the relative motion of the MC2 mirrors.

The parameters of the fitted model function showed that the finesse of the cavity (with that particular alignment) was 300 and the speed of the mirrors of the second mode cleaner was 20 nm/s. In other words, the PRC loop has to acquire lock in some milliseconds. The low first minimum of the ringing in Figure 2.19 shows that the mode matching is better than 90%. The finesse of 300 corresponds to a loss inside the cavity of 0.7%.

Lock acquisition

Figure 2.20 shows the feedback signals of the PRC loop during lock acquisition. The servo loop was closed automatically at the minimum of a fringe at time zero. It can be seen that the cavity acquired lock in 2 ms and stayed in lock while a residual motion of the mirrors damped out quickly. For lock acquisition the loop gain is reduced. When the lock has been established, the gain is slowly increased to the specified value and an extra integrator is switched on to increase the gain at low frequencies.

Long-term operation

The automation of the lock acquisition of this control loop was installed and worked reliably. Without an alignment control of the cavity mirrors, the continuous lock durations were limited by alignment drifts. However, we still achieved continuous lock periods of

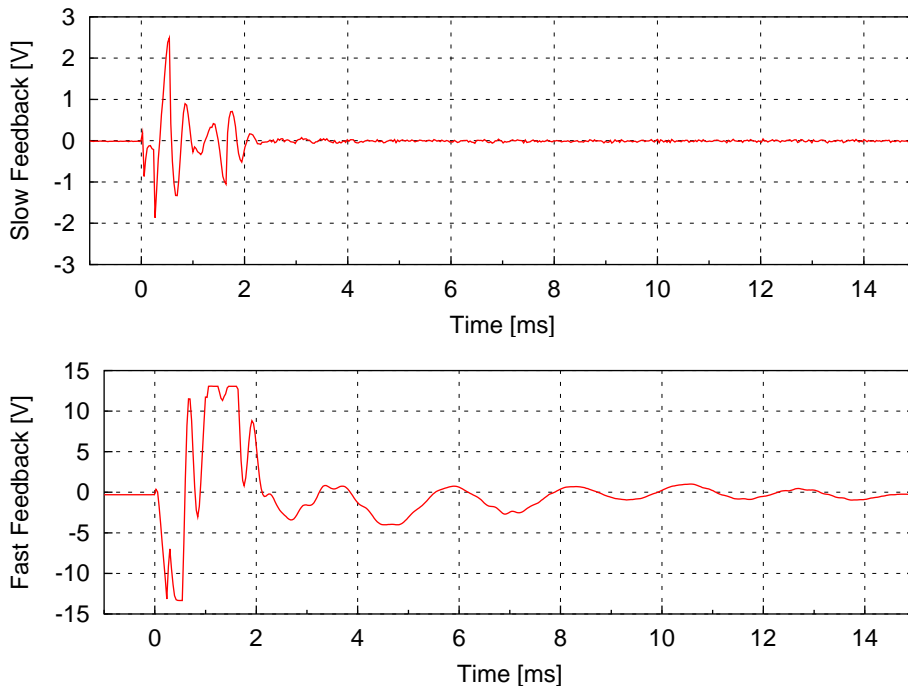


Figure 2.20: Time series of feedback signals of the control system for the 1200 m long cavity during lock acquisition. The servo was closed at time zero.

up to 10 hours, and the automation was able to re-lock the cavity over periods of up to 36 hours before the mirrors had to be realigned. For comparison, the laser and mode cleaner systems that were under automated alignment control [Grote02] typically achieved continuous lock times of 48 hours.

2.7.2 Error-point spectrum

For the GEO 600 detector in its final state, the required frequency stability inside the Power-Recycling cavity will be $30 \mu\text{Hz}/\sqrt{\text{Hz}}$ at 100 Hz, which corresponds to a frequency stability of $300 \mu\text{Hz}/\sqrt{\text{Hz}}$ at 100 Hz for the injected light. The objective of the intermediate experiment described here was to achieve an in-loop frequency noise at this level. Figure 2.21 shows the in-loop noise (i.e., the error-point spectrum) of the control loop for the 1200 m long cavity and the sensor noise of that loop. It can be seen that the goal mentioned above is met.

2.7.3 Power-Recycled Michelson interferometer

As of summer 2001, all main optics of the Michelson interferometer had been installed so that the Power-Recycled Michelson interferometer was in place. Except for the folding mirrors, test optics were used. The test optics are less expensive because the optical

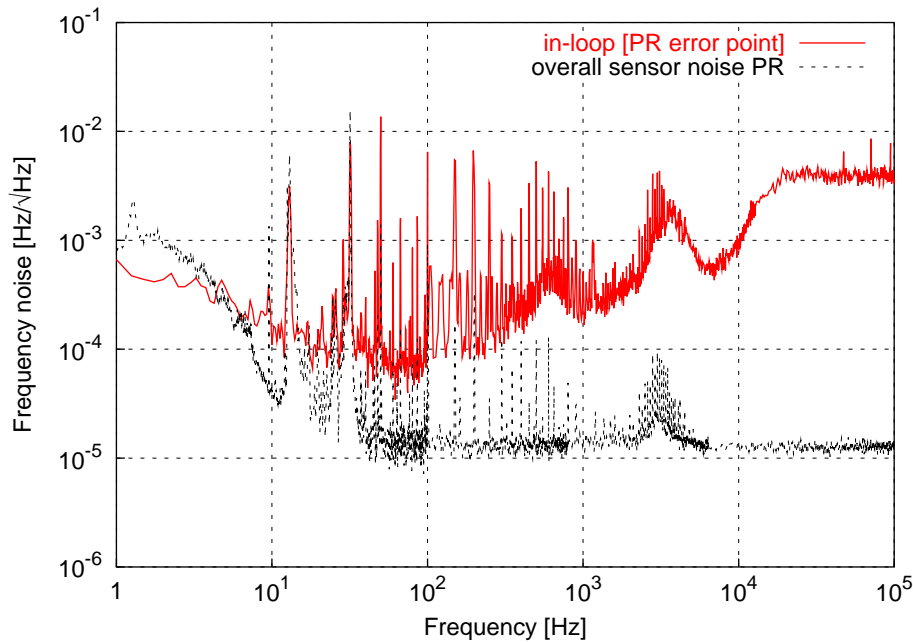


Figure 2.21: *In-loop frequency noise of the control loop of the 1200 m long cavity (PRC loop): approx. $100 \mu\text{Hz}/\sqrt{\text{Hz}}$ at 100 Hz.*

quality is slightly lower than that of the final optics. The use of test optics allowed us to test the installation procedure without the risk of damage to or contamination of the final optics.

The Power-Recycled Michelson interferometer has two longitudinal degrees of freedom, the Michelson-interferometer operating point (differential arm length) and the length of the Power-Recycling cavity (common arm length and the distance between the Power-Recycling mirror and the beam splitter). The error signals for each degree of freedom depend strongly on the state of the other. Figure 2.22 shows the schematic layout of the control loop for the Michelson-interferometer operating point. Schnupp modulation is used to generate phase-modulation sidebands [Schnupp]. These have to be resonant in the Power-Recycling cavity to enter the interferometer. The signal is detected in the south port by the main photo diode (PDO), and the feedback is applied to the end mirrors.

In order to lock the Michelson interferometer, the Power-Recycling cavity is stabilised first. A slight asymmetry in the power splitting of the beam splitter guarantees that some light is always reflected back to the input (west) port, even if the Michelson interferometer is on the bright fringe for the south port. Thus, an error signal for the Power-Recycling cavity can be generated while the Michelson interferometer is not yet controlled. The experience with the 30 m prototype interferometer in Garching [Heinzel98] showed that this locking hierarchy works reliably. To compensate for the variable reflectance of the Michelson interferometer (when the interferometer is not yet locked to the dark fringe), an automatic gain control has been added to the servo system for the Power-Recycling cavity.

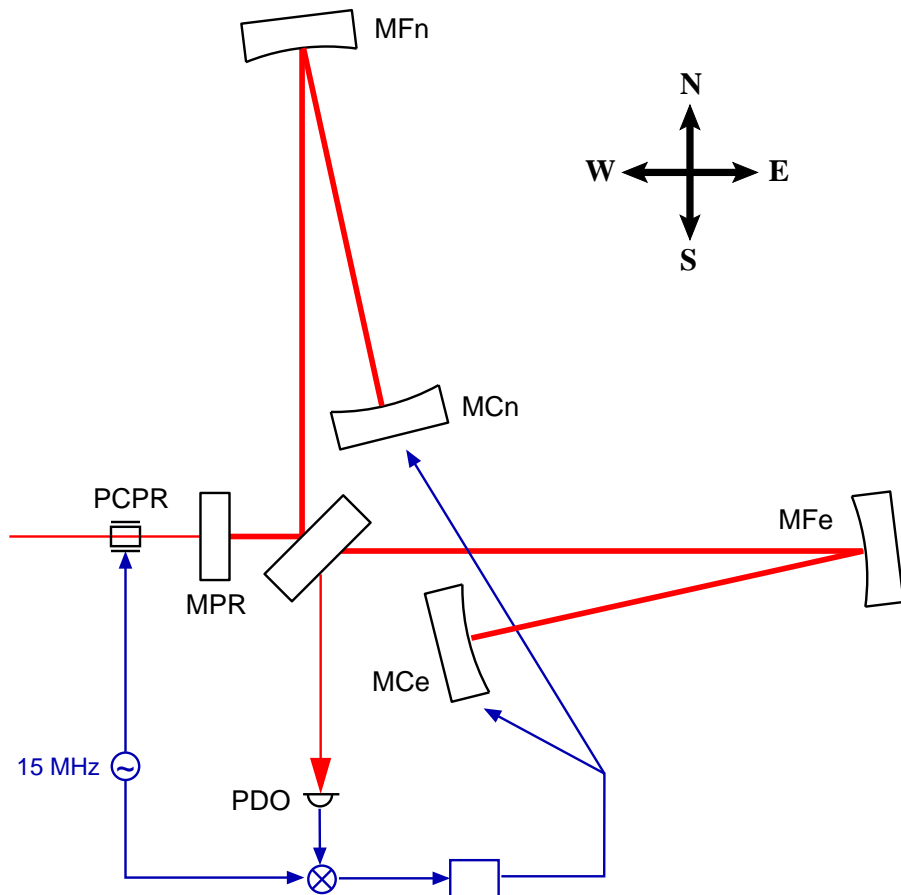


Figure 2.22: Control loop for the Michelson-interferometer operating point. Schnupp modulation is used to generate the phase-modulation sidebands. The error signal is derived using the photo diode in the south port (PDO) and a mixer. The feedback is applied differentially to the end mirrors (MCn, MCE) of the Michelson interferometer.

To reduce the low-frequency fluctuations of the laser frequency during the lock-acquisition process of the PRC loop, we use an extra control loop. The purpose of this loop is to speed up the lock-acquisition process. The fluctuations of the pre-stabilised light at low frequencies are determined by the length fluctuations of the mode cleaners. The resonance frequency of the Power-Recycling cavity shows fluctuations that are approximately 300 times smaller because of the longer cavity. Therefore, a lower (root-mean-square) deviation of the laser frequency from the PRC resonance can be achieved when the laser frequency is stabilised against a reference showing low fluctuations at low frequencies.

The length of the master-laser crystal is a convenient and sufficiently stable reference at low frequencies. We simply use the available feedback signal to the master-laser PZT as an error signal for stabilising the length of the second mode cleaner to the length of the master-laser crystal. This control loop is called *acquisition DC lock*. The control bandwidth is limited to frequencies below 10 Hz.

The observed fringes of the Power-Recycling cavity are much slower when the acquisition DC lock is switched on and the lock acquisition of the PRC loop is almost instantaneous. After successful lock acquisition, the acquisition DC lock is switched off.

Except for the acquisition DC lock and the automatic gain control, the control system has not been changed since the ‘1200 m experiment’. The PRC control loop can provide a stable lock while the Michelson interferometer changes a number of times between dark fringe and bright fringe. During this time, the Michelson-interferometer error signal allows the lock acquisition of the Michelson interferometer.

Long-term performance

In summer 2002, the international network of interferometric gravitational-wave detectors performed a continuous test operation in which five interferometers participated. The so-called S1 run was scheduled from August 23 to September 9. Table 2.1 shows the duty cycle of the optical subsystems of GEO 600 during that time period. The duty cycle is defined as the amount of time (on one day) during which the subsystem was locked. The maintenance periods in which the systems were deliberately disturbed were not subtracted. The longest continuous lock of all systems lasted more than 120 hours, proving the robustness and stability of the analogue control loops. In addition, little human interaction was necessary during the test run (and none during periods of normal operation). Thus, the automatic control systems worked reliably.

day	23.08	24.08 - 27.08	28.08	29.08	30.08	31.08	01.09
MC1	100%	100%	99.93%	99.96%	99.91%	100%	100%
MC2	100%	100%	99.91%	99.95%	99.88%	100%	100%
PRC	99.98%	100%	99.87%	99.94%	99.84%	100%	100%
MI	98.79%	100%	99.84%	99.90%	99.81%	99.97%	100%
day	02.09	03.09 - 05.09	06.09	07.09	08.09	09.09	
MC1	99.04%	100%	99.13%	100%	99.75%	99.94%	
MC2	98.86%	100%	98.82%	100%	99.62%	99.91%	
PRC	98.79%	100%	97.81%	100%	99.05%	99.76%	
MI	98.72%	100%	90.12%	100%	93.71%	99.72%	

Table 2.1: Duty cycle of the optical systems of GEO 600 during the S1 test run in summer 2002. The longest continuous lock of all systems lasted more than 120 hours.

2.7.4 Higher-order mode effects

One major difference between a Fabry-Perot cavity and the Power-Recycled Michelson interferometer is that the Michelson interferometer is not a perfect mirror, even if held

on the dark fringe. In the case of GEO 600 with test mirrors, the radii of curvature of the end mirrors were not perfectly matched. This results in an imperfect interference when the beams are superimposed at the beam splitter so that a considerable amount of light is converted into second-order modes and leaves the interferometer through the south port. The shape of the beam that leaves the south port is commonly described as a ‘sombbrero mode’ (see top center graph in Figure 2.23). In addition, any misalignment of the Michelson interferometer mirrors results in more light being lost through the south port. The two following examples show that the influence of the beam shape on the length- and frequency-control signals of the Michelson interferometer cannot always be neglected.

Lock acquisition of the Michelson interferometer control

Figure 2.23 shows measured and computed signals for the Power-Recycled Michelson interferometer: The Power-Recycled cavity was locked and the Michelson interferometer was freely passing through dark fringes. Zero time indicates the center of the respective dark fringe. The left column shows three typical measured fringes; each graph shows the Michelson-interferometer error signal and the PRC visibility, respectively. It can be seen that the size of the center part of both signals strongly varies, whereas the signal shape far away from the center remains similar. The ‘double dip’ in the PRC visibility is due to the changing reflectance of the Michelson interferometer: It is really highly reflective only at the dark fringe so that the PRC becomes over-coupled as designed. If the Michelson interferometer is moving away from the dark fringe, its reflectance is decreased. At some point the PRC becomes impedance-matched where the visibility is maximised. By further decreasing the MI reflectance, the visibility also decreases; the cavity becomes under-coupled. Thus, a full fringe of the Michelson interferometer results in a double structure, as seen in Figure 2.23, with the dips indicating the impedance-matched states.

Numerical simulations with FINESSE (see Appendix E) have been used to understand the signal shapes. The right column in Figure 2.23 shows the computed signals. The parameters of the simulations were adjusted as follows: To obtain a computed dark-fringe pattern similar to the observed ones, the radius of curvatures of the end mirrors (which are not known accurately) were adjusted accordingly in the simulation. The computed MI error point and the PRC visibility signals matched the measured signals with the strong center very well (top graph in Figure 2.23). It turned out that the form of the computed signals could be matched to the measured signals by introducing a misalignment of the end mirrors into the simulation (Figure 2.23 middle and bottom).

These simulations show that the Michelson interferometer works as expected and that a good alignment of the interferometer mirrors is necessary for obtaining a proper error signal. In particular, the lock acquisition requires a well-aligned interferometer. In normal operation, the automatic alignment system guarantees an optimised alignment so that even after a short loss of lock, the alignment of the mirrors is still sufficient for a successful re-locking.

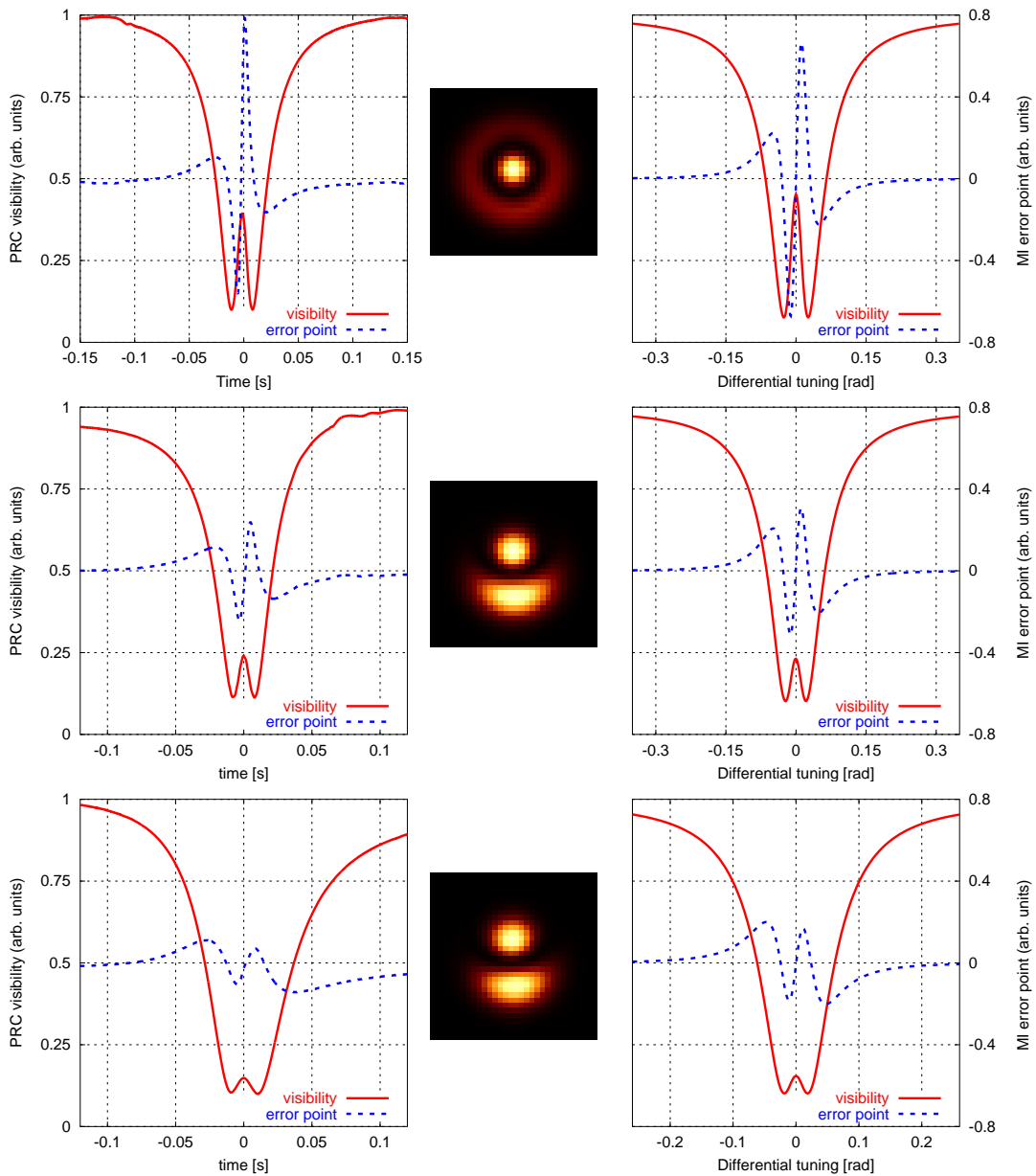


Figure 2.23: Measurement and simulation of Michelson-interferometer error signals: The left column shows measured signals for three typical fringes of the Michelson interferometer; each graph shows the MI error point and the PRC visibility while the Michelson interferometer passes through a dark fringe. The right column shows respective signals obtained by a FINESSE simulation (see Appendix E). From top to bottom, the simulations were done for increasing misalignments of the end mirrors ($0.2\ \mu\text{rad}$, $3\ \mu\text{rad}$ and $4\ \mu\text{rad}$). The center column shows the corresponding dark fringe pattern computed by the simulation.

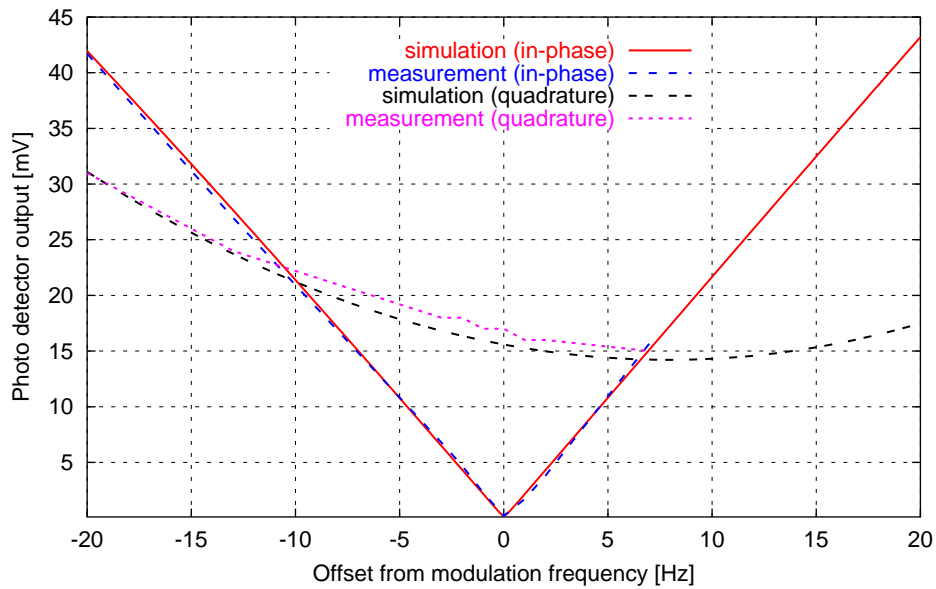


Figure 2.24: Coupling of a frequency calibration peak into the error signal of the Michelson interferometer as a function of the detuning of the Schnupp modulation frequency.

Frequency-noise coupling

The coupling of laser frequency fluctuations into the main output signal of the Michelson interferometer can be measured by applying a so-called calibration peak: A known disturbance with fixed frequency and amplitude is added to the frequency-control loops to impose an oscillation on the laser frequency. Measurements of this ‘peak’ in the spectrum of the Michelson-interferometer error signal yield a factor for the frequency-noise coupling.

First measurements with the Power-Recycled Michelson interferometer indicated that the coupling was approximately 100 times higher than expected from a simple linear model. In order to investigate this result, the coupling of the frequency peak was looked at in more detail: the frequency coupling can be increased by detuning the Schnupp modulation frequency from the optimum (which in this case can be defined as the frequency with the minimum frequency coupling). Figure 2.24 shows the measured peak amplitudes (in Volts on the photo diode PDO) as a function of the Schnupp modulation frequency. The signal from PDO is demodulated by two mixers to obtain the in-phase and quadrature signal.

A FINESSE simulation was used to compute the same signals: The shape of the measured graph could only be modelled if the second-order modes were included in the simulation. The models restricted to TEM_{00} modes gave a much lower coupling, and the distribution of the signal into phase and quadrature signals was different. This indicates that the light directed towards the output port of the Michelson interferometer due to mismatched beam sizes dominates the frequency-noise coupling. With Signal Recycling, the final optics and the output mode cleaner in place, the second-order modes on the output photo diode will be greatly reduced and, in consequence, also the frequency-noise coupling.

2.7.5 DC loop

The Pound-Drever-Hall control loops described above use suspended cavities as frequency references. The suspended optical systems, however, are subject to large fluctuations at low frequencies. Therefore, an additional control loop, the so-called *DC loop*, will be implemented to add a stabilisation for low frequencies to the control scheme.

The current design of the DC loop uses a *sideband transfer method*: The modulator for generating the modulation sidebands of the PRC loop is positioned *in front* of MC2 so that the sidebands are passed through the second mode cleaner. This is possible if the modulation frequency is also resonant in MC2. It is designed to be exactly the frequency of the free spectral range of MC2, which is ≈ 37 MHz. The free spectral range of the mode cleaner is proportional to $1/l$, with l being the lengths of the MC2 cavity, which is rigidly coupled to the length of the Power-Recycling cavity by the PRC loop. A double demodulation of the light reflected from MC2 (at 13 and 37 MHz) generates an error signal proportional to the deviation of the free spectral range from the frequency of the modulation sidebands. This signal is low-passed and then fed back to the position of the Power-Recycling mirror. Thus, the length of the Power-Recycling cavity is stabilised to the 37 MHz oscillator for low frequencies (DC).

The oscillator, a Rubidium clock locked to a GPS reference, provides a very good stability at low frequencies. The DC loop automatically stabilises the length of the mode cleaners and the laser frequency at low frequencies by means of the Pound-Drever-Hall feedback loops. The DC loop is not yet completely implemented.

2.8 Remote control and automatic operation

For a continuous operation of the detector, it is desirable that the control loops of the mode cleaners and the Power-Recycling cavity can be controlled remotely. In addition, an automatic operation should be implemented so that the optical systems require no human interaction during normal operation. Such an automation system requires that a failure of a control loop to keep the optical system on its operating point is detected automatically and action is taken to regain a stable operation. For this purpose digital electronics and LabView control programs have been installed to supervise and control the analogue servo electronics.

The analogue electronics are housed in standard 19-inch 6HE modules. In each module a board with digital electronics is located next to the analogue loop filter electronics. It can control CMOS switches and digital potentiometers on the analogue board and provides AD converters to read data from the analogue electronics. The digital electronics are connected via a bus system to so-called *MCP computers*. The MCPs are standard PCs that run a dedicated LabView program for reading from and writing to the digital bus [Casey]. Several LabView programs are used to allow data exchange between the hardware.

During this work, special *virtual instruments* were developed. These virtual instruments provide a graphical user interface that allows to remote-control the analogue circuits of the frequency control loops. All main switches and potentiometers of the loop filters are controlled remotely.

In addition, the LabView programs can be switched to automatic operation in which the detector requires no user interaction. The virtual instruments used for the frequency stabilisation are described in Appendix H.

2.8.1 Lock acquisition

The automation of the frequency stabilisation is in fact an automation of the lock acquisition. Lock acquisition describes the method of closing a control loop in such a way that the system will be stable and at its operating point (the system is *locked*).

In many cases, the error signal is only valid for a specific parameter range. Therefore, a lock-acquisition scheme must be able to determine whether the error signal is valid so that the loop can be closed at the right time. In some cases, the useful parameter range is reached due to the fluctuation of the un-stabilised system. It may also become necessary to act on the system (decrease or increase the fluctuation) during the lock-acquisition phase to reach that parameter range.

Once the lock is acquired, the system may stay locked for a long time before the loop fails, for example, due to a temporary outside disturbance. Then the lock acquisition process has to be repeated. In this case, the procedure is as follows: While the analogue control loops are stable and the optical systems locked, the LabView programs only monitor several parameters but do not act. As soon as the monitored parameters indicate that one or more loops have failed, the LabView code will open the respective loops and initiate a new lock acquisition.

Pound-Drever-Hall loops

In order to acquire lock, a Pound-Drever-Hall loop must be closed when the cavity is close to the operating point. The operating point is reached when the incident light is resonant in the cavity. The photo diode of the Pound-Drever-Hall loop provides the visibility and error signals. Figure 2.25 shows an example of these signals as a function of the deviation of the laser frequency from the cavity resonance. When the cavity and the laser frequency are without control, the deviation will change randomly and, at some time, create the shown signal. This signal is called *fringe*: The visibility passes its minimum and the error signal shows a zero crossing. Both signals are used to determine when the cavity is close to its operating point and the loop can be closed.

A small visibility signal indicates that the laser frequency is *close* to a resonance. By comparing the signal to a pre-set threshold, the fringe is ‘detected’. The threshold for the visibility must not be set too small because the minimum of the visibility can vary, for

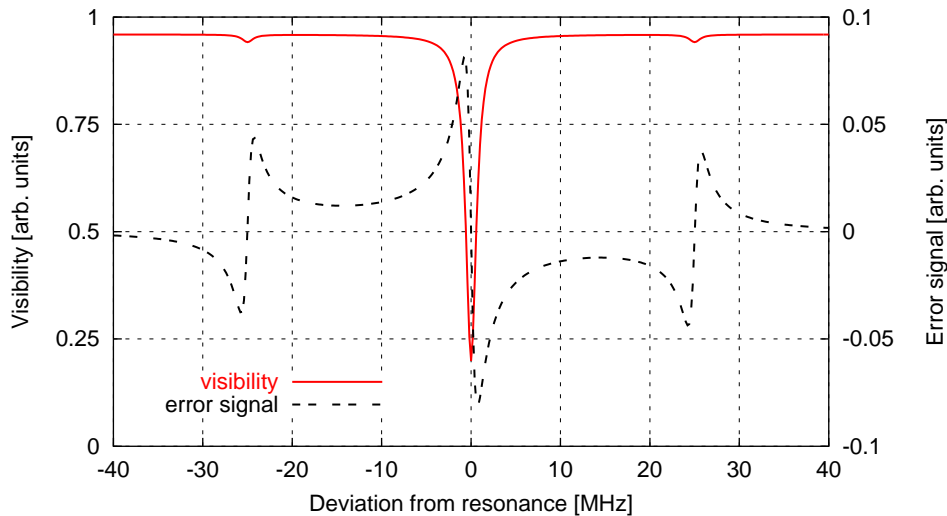


Figure 2.25: Example plots for the visibility and error signals of a Pound-Drever-Hall sensor when the incident light passes over a cavity resonance. This center structure is called fringe, the features at ± 25 MHz are caused by the phase-modulated sidebands (modulation frequency is 25 MHz).

example, because of the alignment of the cavity mirrors. During a fringe the error signal of the Pound-Drever-Hall loop is valid, and the zero crossing of the error signal indicates that the laser frequency is exactly on resonance. This is not affected by fluctuations of other parameters so that a very low threshold value for the error signal can then be used to exactly determine the time when the operating point is reached and the loop can be closed.

This method is used for all three Pound-Drever-Hall loops in this work (MC1 loop, MC2 loop, PRC loop). The necessary functions are implemented in analogue electronics. Comparators are used to compare the visibility and the magnitudes of the error signals to thresholds set by the LabView virtual instruments.

The LabView control programs can initiate the lock acquisition by setting the *Acquire status bit* to ON. Based on a simple logic the electronic decides when to close the loop: If the Acquire status is set to ON, the visibility is below the set threshold and the error signal is in the range defined by the threshold level; then the servo is switched on, i. e., the loop is closed. The loop stays closed until the Acquire status bit is set to OFF. Thus, if the loop fails, or the lock is not acquired, the analogue control cannot open the loop by itself. This has to be done by the LabView control programs.

In addition, the different loops include the following distinctive features:

- **MC1:** When the Acquire status bit for the MC1 loop is switched to ON, a ramp signal is applied to the PZT. The laser frequency is swept over a range greater than the free spectral range of MC1. This guarantees that, at some point, the laser light will be resonant in MC1.

- **MC2:** Both mode cleaner cavities have a low residual motion. Therefore, it can take minutes for a random drift to bring both mode cleaners to resonance simultaneously. In order to speed up the acquisition process, the following feature is used: Every time the Acquire status bit for the MC2 loop is set to ON, a very small step impulse is applied to the position of one mirror of the MC2 cavity. This has a similar effect as the ramp for MC1: It will move the mirror and thus change the resonance frequency of MC2.
- **PRC:** Experience has shown that the lock acquisition process is more reliable if the overall gain is decreased from the setting that is optimum with respect to noise suppression. Therefore, the gain is decreased (by the LabView automation) before the Acquire bit is switched to ON and increased as soon as the loop is closed.

2.8.2 Mode-cleaner control

The virtual instrument ‘automation MC1+2’ is used to control the analogue servo electronics for the control of MC1 and MC2. The graphical user interface (GUI) shows two ‘screens’ with the signals for visibility, the error-point signals and the feedback signals for both systems (see Appendix H for a screen-shot). In addition, there is a control section for each mode cleaner where the user can switch integrators or change gains. The virtual instrument can be used in a manual mode and for automated operation.

MC1: The following steps must be taken to switch on the control for the first mode cleaner:

- activate the feedback paths to the PZT, the EOM and to the laser temperature;
- switch off the integrators (during lock acquisition);
- set the gain and the thresholds for the visibility and the error signals;
- press the ‘Acquire’ button.

This starts the lock-acquisition function of the control electronics. If the loop is closed, the ‘Servo’ indicator will light up. If the lock acquisition was successful, the visibility signal should become small. In this case the integrators can be switched on. A high visibility signal indicates that the loop has failed to hold the system at the operating point. Then the acquire button has to be released to open the loop again.

If the program is switched to automatic mode, it follows the routine explained above. Three timers can be set by the user:

- Ramp timer: Number of seconds to wait for successful lock acquisition after Acquire was set to ON. If the acquisition fails, Acquire is set to OFF after the given time;
- Integrator timer: Number of seconds to wait before switching on the integrator after the lock has been established;
- Relax timer: Number of seconds to wait before setting Acquire to ON after it has been set to OFF.

MC2: The control for MC2 is similar. For starting the MC2 loop, the following steps must be taken:

- activate the feedback paths to the MMC1b mirror;
- switch off the feedback to the Bypass and the two integrators (during acquisition);
- set the gain and the thresholds for the visibility and error signals;
- press the Acquire button.

The lock acquisition is then handled by the analogue electronics. When the locked state has been reached, the Bypass feedback and the two integrators can be switched on.

In automatic mode, the virtual instrument performs the above steps automatically. The following timers can be set by the user:

- MC2 ON: Number of seconds to wait after MC1 is locked before Acquire for MC2 is set to ON.
- MC acquire: Number of seconds to wait before Acquire is switched OFF after Acquire has been switched to ON but no lock has been achieved.

2.8.3 Power-Recycling cavity control

The automation of the Power-Recycled Michelson interferometer is performed by a micro-controller that allows for a much faster switching than a LabView program. The virtual instrument ‘automation_PRC’ is still used for setting the overall gain and the thresholds for visibility and error point. The lock acquisition process is the same as for the mode cleaners. In addition, the acquisition DC lock is switched on during the lock acquisition process. After the locked state has been reached, the micro-controller takes over. In the future, this will probably be changed so that the micro-controller controls the lock-acquisition phase as well.

2.9 Automatic alignment system

The control loops described in this chapter are used to control the longitudinal degrees of freedom, i. e., the cavity and interferometer path lengths and the laser frequency. Thus, the positions of the mirrors on the optical axis are defined and controlled. An automatic mirror alignment system (or automatic alignment system) is used to control the remaining degrees of freedom, namely rotation and tilt of the mirrors [Heinzel99]. In order to achieve the designed sensitivity, the optical systems have to be aligned in a way that the beam axis and the axis of the cavity eigen-modes overlap. This *alignment* of the system has to be maintained over long stretches of time to allow continuous measurements. The automatic alignment system uses split photo diodes (quadrant cameras) and the so-called *differential wave-front sensing* scheme to generate error signals proportional to the misalignment of the beam axis with respect to the cavity or the interferometer. By rotating and tilting

the mirrors, the eigen-mode of the respective optical system is aligned to match the axis of the incoming beam. The control bandwidth of the alignment control loops is less than 50 Hz so that feedback cannot introduce noise in the measurement band. Furthermore, the automatic alignment system is completely automated, i. e., it is switched on and off automatically depending on the state of the longitudinal lock (the frequency stabilisation). Please see [Grote02] for a detailed description of the implementation of the automatic alignment system of GEO 600.

Chapter 3

Advanced interferometer techniques

3.1 Introduction

The Michelson interferometer is an optical instrument that can measure small changes in the differential optical length of the two arms. The sensitivity of the interferometer to gravitational waves can be improved by extending the optical setup. For example, Fabry-Perot cavities in the interferometer arms or recycling mirrors in the output ports can be used to enhance the sensitivity as they reduce the bandwidth of the detector or increase the light power stored in the interferometer.

The optical setup, including the mirror and beam splitter positions, the optical path lengths and the characteristics of the input light, is called *topology* of an interferometer. Changing the topology of the Michelson interferometer creates a new, different type of interferometer. Alternatively, so-called *advanced* interferometers can also be based on other interferometer types, for example the Sagnac interferometer [Shaddock]. The following sections describe Dual Recycling, an advanced technique based on the Michelson interferometer. In addition, the Xylophone interferometer that represents a possible extension of a Dual-Recycled system is introduced.

An analysis of interferometers with respect to the detection of gravitational waves includes a comparison of various topologies with the signal-to-noise ratio as the figure of merit. Such a comparison comprising various types of interferometers can be found in [Mizuno95]. To date, all large-scale interferometric gravitational-wave detectors are based on the Michelson interferometer. GEO 600 is the only project that uses an advanced technique (Dual Recycling) as the initial setup while other projects use a Michelson interferometer with cavities in the arms.

The next generations of interferometric detectors are already being planned or designed. The next step is to up-grade the detectors that use a Michelson interferometer having cavities in the arms by applying a technique similar to Dual Recycling: the so-called *Resonant Sideband Extraction* [Mizuno93, Heinzel96, Mason]. In addition, other comparable techniques are being investigated for possible use with gravitational-wave detectors, see [Mueller] for an example.

Future interferometric gravitational-wave detectors will possibly be built entirely with reflective optics (*all-reflective* interferometers) and use cryogenics to cool the main optics to reduce thermal and thermo-refractive noise. Such new interferometers provoke new challenges to the topology and configuration design.

3.1.1 Interferometer control

Any type of interferometric detector requires some active control to guarantee the stable and well-calibrated operation over long periods of time needed for the detection of gravitational waves. Control systems are used to stabilise various degrees of freedom of the interferometer such as optical path lengths and beam positions. In particular, the longitudinal degrees of freedom (mirror and beam splitter positions along the optical axis) have to be controlled with extreme accuracy. In the following, the setup of a particular control scheme for an interferometer is called *configuration*¹.

The main task in designing an interferometer configuration is the design of a suitable sensor or, in general, a sensing scheme. The generation of the required error signals is not straightforward: Advanced interferometers usually employ more mirrors or beam splitters than their better understood ancestors and therefore have more degrees of freedom. At the same time, they often provide only the same number of output signals as the basic interferometer. This is why the control of advanced interferometers requires sophisticated sensing schemes. Note that the difficulty lies not in generating error signals as such, but in finding independent signals for each degree of freedom.

Error signals for the interferometer control can be extracted from the optical system in various ways. One important issue in the design of a control system is the noise added to the detector by the control system. Therefore, the number of components added to the optical system for generating an error signal should be minimised. Any kind of interferometer provides a number of output ports in which the light amplitude and phase depend on the frequency of the injected light and on the various optical path lengths inside the interferometer. Usually, the dependence on the optical path lengths is different for the different output ports so that independent information about different degrees of freedom can be derived.

Heterodyne detection

The light phase cannot be detected directly by a photo detector. To extract phase information, the light field has to be superimposed with a second field. It is often convenient to have the second field independent of the interferometer; such a field is called *local oscillator*. The local oscillator presents a phase reference for the output field so that the beat signal changes in amplitude when the phase of the output field changes. One

¹ The terms *topology* and *configuration* are used to distinguish between the optical layout and the design of the interferometer control system because, generally, many different configurations can be used with a given interferometer topology. These two expressions are often used differently in other publications.

distinguishes between two methods, the *homodyne* detection in which the local oscillator has the same frequency as the output fields, and the *heterodyne* detection that uses a local oscillator with a different light frequency.

In a more general approach, the reference field does not have to be independent of the interferometer: in fact, the only requirement is that the reference field has a *different* phase dependence on the quantity to be measured compared with the output field. This can be achieved by passing a reference field with a frequency offset through the interferometer. In general, the phases of the two fields in the interferometer output depend differently on the optical path lengths so that the beat signal measured in an interferometer output can be used to extract phase information. This kind of reference field that takes the role of the local oscillator is called *control sideband* in the following. It is convenient to generate control sidebands by electro-optic modulators that always generate symmetric pairs of (phase-modulation) sidebands: Each pair consists of a *lower* sideband at $f = f_0 - Nf_{\text{mod}}$ and an *upper* sideband at $f = f_0 + Nf_{\text{mod}}$, with f_0 the frequency of the laser, f_{mod} the modulation frequency and N an integral number, also called the *order* of the pair of sidebands.

In GEO 600 we use heterodyne detection for all degrees of freedom of the recycled Michelson interferometer. In fact, seven light fields are present at the interferometer input: the laser light and three pairs of control sidebands.

3.1.2 Michelson interferometer

Figure 3.1 shows a simple Michelson interferometer held at the dark fringe; ideally, no laser light is directed towards the south port in this condition. The Michelson interferometer looks effectively like a mirror to injected light, for both the south and the west input port. The west port is used as the input port for the laser light.

Gravitational-wave signals

The effect of gravitational waves on the interferometer can be described as a phase modulation of the light in the interferometer arms. The gravitational wave thus generates *signal sidebands* at the signal frequency around the laser frequency. In the following, we assume for simplicity that the gravitational wave has the optimum polarisation (parallel to the arms of the Michelson interferometer) and the optimum direction of propagation (perpendicular to the interferometer plane).

The laser light, in the following called the carrier, is the reference frequency f_0 for the signal sidebands. The signal sidebands have a frequency offset of $\pm f_{\text{sig}}$.

Because of the quadrupole nature of the gravitational waves, the phase of the signal sidebands has an offset of 180° between the two interferometer arms. Therefore, the signal sidebands experience an interference condition at the beam splitter differing from that of the carrier field. In fact, they are directed towards the south port so that the

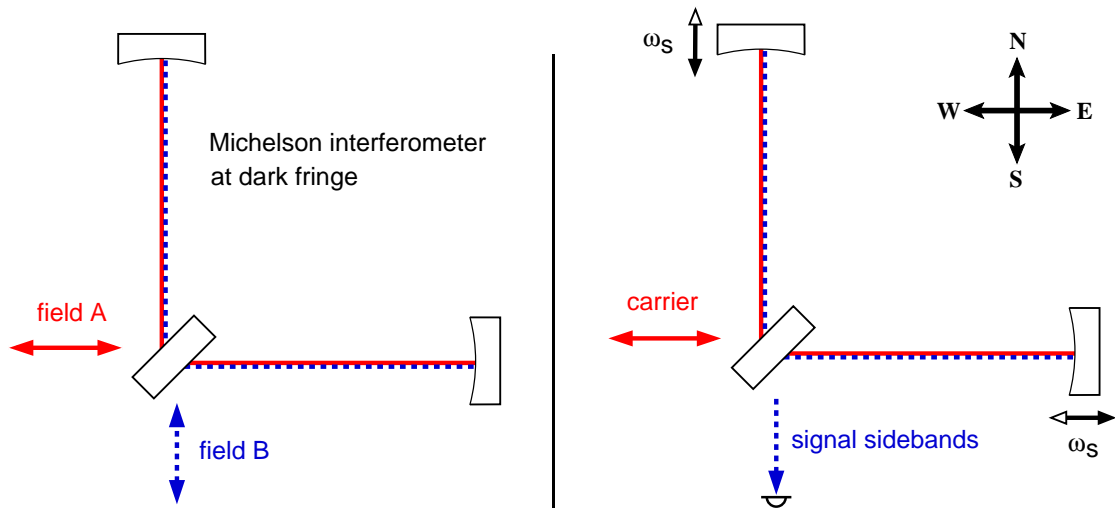


Figure 3.1: Michelson interferometer at the dark fringe: The west port is the input port for the laser light, the south port is held dark for the laser light, i. e., the laser light is reflected back towards the west port. Similarly, any light injected into the south port is directed back towards the south port; the Michelson interferometer essentially acts like a mirror with respect to injected light. The right graph shows the effect of a differential motion of the end mirrors (at frequency ω_s .) The modulation of the mirror position creates signal sidebands around the laser frequency. Because the modulation has a phase offset of 180° between the two arms, the signal sidebands experience opposite interference conditions with respect to the laser light and are directed towards the south port.

south port is the main output port of the Michelson interferometer in which the gravitational-wave signal is measured². Test signals similar to gravitational-wave signals can be introduced to the interferometer by differentially modulating the mirror positions.

3.1.3 Shot-noise-limited sensitivity

The quantum fluctuations of light are one of the main limiting noise sources of interferometric gravitational-wave detectors. The coupling of these fluctuations into the output signal of the detector is traditionally described by two separate effects³: *shot noise* and *radiation pressure noise*. Caves has shown that both noises can be understood as originating from vacuum fluctuations coupling into the dark port of the Michelson interferometer [Caves].

² This is not entirely correct because the signal sidebands have an absolute frequency differing from the carrier and are therefore in general not exactly at the ‘bright fringe’. For the Fourier frequencies of the expected gravitational waves, however, this effect can be neglected.

³ Recent research has pointed out that in some cases this description is not useful for explaining the effects of the quantum fluctuations on the sensitivity of the detector, see Section 3.1.4.

Shot noise: The detection of light power by a photo diode can be described as a photon-counting process, and the arrival time of photons (in a coherent state) can be modelled by a Poisson process. The ‘photon-counting error’ given by statistics produces a spurious signal in the detector output, which is described as shot noise⁴. The apparent change in the differential optical path length $2\Delta L$ due to shot noise can be written as a single-sided, linear spectral density [Rüdiger02]:

$$\widetilde{\delta L}_{\text{shot}}(f) = \sqrt{\frac{\hbar c}{\pi} \frac{\lambda}{\eta P}} \quad (3.1)$$

with P being the light power, η the quantum efficiency of the photo diode, $\hbar = h/2\pi$ Planck’s constant, λ the laser’s wavelength and c the speed of light. This shot noise is a so-called ‘white-noise’, i. e., the spectral density is independent of frequency. The spurious signal due to shot noise scales as $P^{-1/2}$ and thus can, in principle, be decreased by increasing the light power.

Radiation pressure noise: The suspended mirrors are subject to radiation pressure. The light in the interferometer arm results in an average constant force on the mirrors that changes the equilibrium position of the pendulums. Any change in light power will thus move the mirrors. The interference of the vacuum fluctuation with the laser light at the beam splitter leads to different light power fluctuations in the two interferometer arms and thus to a change in the differential optical path length. The spectral density of this change (for the GEO 600 configuration, including folded arms) can be written as [Harms]⁵:

$$\widetilde{\delta L}_{\text{rp}}(f) = \frac{20}{M f^2 c} \sqrt{\hbar \omega P} \quad (3.2)$$

with M being the mass of one mirror, ω the frequency of the laser light and f the signal frequency.

First-generation interferometric gravitational-wave detectors are not sensitive to radiation pressure noise because of the relatively low light power inside the interferometer. Second-generation detectors, however, are designed for much larger light power (up to 1 MW) so that these effects have to be taken into account.

Waste light: In a perfect Michelson interferometer held at the dark fringe, only the control and signal sidebands are present on the photo diode. Imperfect optics, however, generate a certain amount of ‘waste’ light that leaves the interferometer and hits the photo diode. This light does not carry any signal, but contributes shot noise.

⁴ The noise of randomly arriving particles can be visualised by shot clattering on a metal plate, hence the term ‘shot noise’.

⁵ The effects of radiation pressure noise on the beam splitter are not included in this equation.

The amplitudes of the signal sidebands are naturally very small. Therefore, the DC power on the photo diode is given by the power of the control sidebands (P_{csb}) and the power of the ‘waste’ light (P_{waste}).

The gravitational-wave signal in the output of the detector is proportional to the amplitude of the control sidebands and to the amplitude of the signal sidebands [Heinzel99]:

$$x_{\text{out}} \sim \sqrt{P_{\text{csb}}P_{\text{ssb}}} \quad (3.3)$$

The signal-to-noise ratio (SNR) with respect to shot noise is then proportional to:

$$\text{SNR}_{\text{shot}} \sim \frac{\sqrt{P_{\text{csb}}P_{\text{ssb}}}}{\sqrt{P_{\text{csb}} + P_{\text{waste}}}} \quad (3.4)$$

Theoretically, this SNR increases with increasing power in the control sidebands until the power of the waste light becomes much smaller than P_{csb} , i. e. $P_{\text{waste}} \ll P_{\text{csb}}$. Once this condition is fulfilled, the SNR is independent of the power of the control sidebands⁶. In practise, however, increasing the power of the control sidebands usually decreases the carrier power. Thereby, the signal sideband power and thus the sensitivity are reduced. Hence, the optimum setting of the control sideband power is usually close to that of the waste light power.

3.1.4 Quantum-noise correlations

Recent publications have pointed out that a distinction between shot noise and radiation-pressure noise does not provide a useful model for understanding the quantum noise of the light fields inside an interferometer with Signal Recycling or similar advanced techniques [Buonanno01, Buonanno02]. It turns out that in a Signal-Recycling interferometer the two noise sources are correlated so that an independent analysis cannot be performed. Currently, various approaches are underway to investigate and overcome the quantum noise in interferometry (see, for example, [Kimble]).

GEO 600 is the first interferometric gravitational-wave detector that uses Signal Recycling. The quantum noise in the GEO 600 configuration has been analysed recently [Harms]. The sensitivity of the detector with respect to quantum noise of the light differs from the results of a classic analysis. The significant differences, however, will be at frequencies below 100 Hz where GEO 600 is not likely to be limited by shot noise. Therefore, a classic analysis with respect to shot noise is sufficient to describe the main features of the GEO 600 detector. The sensitivity plots in this work are based on a simple, classic shot-noise analysis.

⁶ Please note that this is only correct for a ‘quadratic modulation’. For sinusoidal modulations, a higher modulation index results in extra carrier power being lost into higher-order modulation sidebands that do not contribute to the signal [Schilling].

3.2 Dual Recycling

The power in the signal sidebands is always much smaller than the power in the control sidebands (because of the small amplitude of the gravitational-wave signal); consequently, the signal sidebands do not contribute to the shot noise. Therefore, the sensitivity of the detector can be improved by enhancing the power in the signal sidebands. This can be achieved by increasing the light power in the arms or by increasing the interaction time of the gravitational wave with the light. In GEO 600 we use *Power Recycling* for enhancing the carrier power and *Signal Recycling* for increasing the signal interaction time. The combination of the two methods is called *Dual Recycling*. The concept of Dual Recycling has been proposed by Meers [Meers88], and it was also demonstrated first as a table-top experiment by the Glasgow group [Strain91]. Three table-top experiments in Hannover investigated various control methods for controlling a Michelson interferometer with signal recycling [Freise98, Barthel, Maaß]. Finally, the 30 m prototype interferometer in Garching was used to demonstrate Dual Recycling with a suspended interferometer and to design a control system suitable for the GEO 600 detector [Heinzel98, Heinzel99].

3.2.1 Power Recycling

Figure 3.2 shows a Michelson interferometer with Power Recycling. The Power-Recycling technique exploits the fact that the Michelson interferometer behaves like a mirror for injected light; the Power-Recycling mirror recycles the light from the bright fringe in the west port and then forms a cavity with the Michelson interferometer, the *Power-Recycling cavity*. The cavity is kept on resonance by a Pound-Drever-Hall method so that the carrier light is resonantly enhanced inside the cavity. The power of the phase-modulation sidebands is proportional to the carrier power. Hence, a greater carrier power results in a higher signal sideband power for a given gravitational-wave amplitude. Once created, the signal sidebands are not affected by Power Recycling because they are not present in the west port of the interferometer.

This method is very successful because it allows to increase the laser power without reducing the bandwidth of the detector or installing a larger laser. In addition, the filter effect of the Power-Recycling cavity reduces fluctuations in amplitude, frequency and geometry of the incoming light.

The maximally possible power enhancement is limited by losses in the interferometer:

$$\frac{P_{\text{cav}}}{P_{\text{in}}} = \frac{T_{\text{MPR}}}{(1 - a_{\text{loss}})^2} \quad (3.5)$$

where a_{loss} is the amplitude attenuation factor of one complete round-trip in the Power-Recycling cavity and T_{MPR} the power transmittance of the Power-Recycling mirror. The loss inside the cavity has two main origins: The finite reflectances of the mirrors and the imperfect interference of the superimposed beams at the beam splitter. The ratio of the maximum power in the west arm (Power-Recycling cavity) and the minimum power

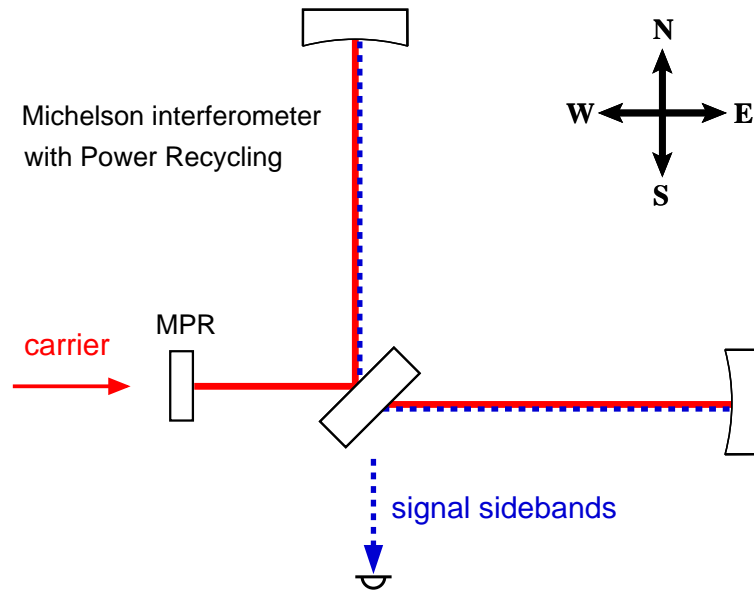


Figure 3.2: *Michelson interferometer with Power Recycling: The Power-Recycling mirror (MPR) in the west port recycles the light power reflected back from the Michelson interferometer. Together, the mirror and the interferometer form a cavity in which the carrier power is enhanced. The signal sidebands are not affected by the Power-Recycling mirror since they are not present in the west port.*

in the south port (dark fringe) is called *contrast* henceforth. In a perfect Michelson interferometer the contrast is infinity. In a real interferometer, the contrast is understood as the ratio of the experimentally achievable stable minima and maxima. Several effects degrade the contrast by increasing the amount of light leaving the interferometer through the nominally dark south port:

- modulation sidebands for heterodyne detection;
- fluctuations or deviations of the Michelson interferometer from its operating point due to limited performance of the control loop;
- asymmetric losses in the interferometer arms;
- wavefront mismatch of the returning beams at the beam splitter.

The power enhancement has natural limits, even with very small losses in the initial interferometer: the higher light power deposits energy inside the optical components, creating thermal lenses [Winkler91] (and therefore disturbing the properties of the optical systems) or possibly damaging the components. In addition, the SNR with respect to radiation pressure noise is approximately proportional to $P^{-1/2}$. Therefore, from a certain light power on, the detector sensitivity will be dominated by radiation pressure noise and degrade with further increasing light power.

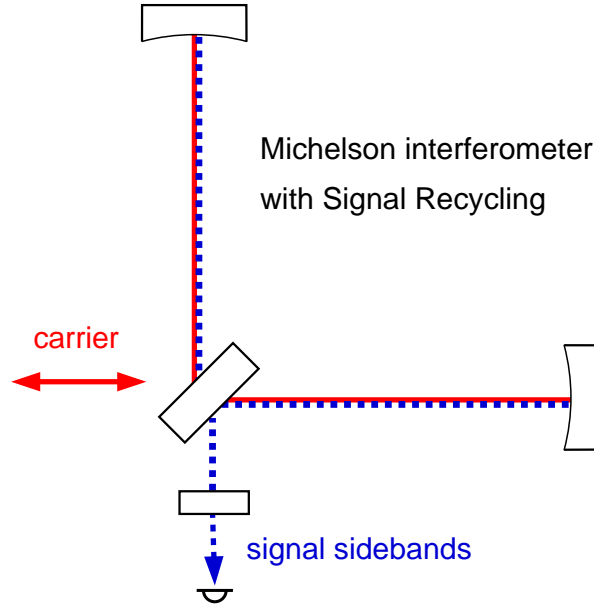


Figure 3.3: *Michelson interferometer with Signal Recycling: The Signal-Recycling mirror (MSR) recycles the signal sidebands in the south port. It forms a cavity with the Michelson interferometer in which the signal sidebands (or one of them) are resonant. Because the sidebands are created within this cavity, even their power outside the cavity, i. e., on the photo diode, is enhanced (see text).*

3.2.2 Signal Recycling

The power of the signal sidebands on the photo diode can be enhanced independently of the carrier light. Figure 3.3 shows a Michelson interferometer with Signal Recycling. The Signal-Recycling mirror (MSR) in the south port reflects the signal sidebands back into the Michelson interferometer. Again, the recycling mirror forms a cavity together with the Michelson interferometer, the Signal-Recycling cavity. The cavity is tuned to resonantly enhance the signal sidebands. At the same time, the power of the sidebands on the photo diode, i. e., *outside* the cavity, is also increased. This counter-intuitive effect is simply a result of the well-known equations for light fields inside a cavity, provided that the light source is *inside* the cavity (see, for example, Appendix D in [Heinzel99]).

Signal Recycling increases the shot-noise-limited sensitivity by reducing the bandwidth of the detector: Only signal frequencies that fall within the bandwidth of the Signal-Recycling cavity are enhanced. In practice, the Signal-Recycling cavity is set up in a way that the losses are considerably smaller than the power transmittance of the Signal-Recycling mirror, i. e., the cavity is *over-coupled*. In this case, the finesse of the cavity can be approximated as:

$$\mathcal{F} = \frac{2\pi}{T_{\text{MSR}}} \quad (3.6)$$

with T_{MSR} the power transmittance of the Signal-Recycling mirror. The power enhance-

ment of the signal sidebands outside the (over-coupled) cavity is given by:

$$\frac{P_{\text{ssb,SR}}}{P_{\text{ssb,noSR}}} = \frac{4}{T_{\text{MSR}}} \quad (3.7)$$

The sensitivity is proportional to the square root of the signal-sideband power. With the maximum detector bandwidth⁷ given as:

$$\Delta f_{\text{SRC}} = \frac{\text{FSR}_{\text{SRC}}}{\mathcal{F}} \quad (3.8)$$

with FSR_{SRC} being the *free spectral range* (FSR) of the Signal-Recycling cavity; we can write:

$$\text{SNR}_{\text{shot}} \sim \sqrt{\frac{1}{T_{\text{MSR}}}} \sim \frac{1}{\sqrt{\Delta f_{\text{SRC}}}} \quad (3.9)$$

with Δf_{SRC} being the bandwidth (FWHM) of the Signal-Recycling cavity. In the GEO 600 detector the free spectral range is determined by the optical path length of the interferometer arms, $\text{FSR}_{\text{SRC}} \approx 125$ kHz. Even if the gravitational-wave detector is used for a narrowband search, it must still have a sufficient bandwidth for *a priori* unknown deviations of the source from the expected signal frequency. Typical values for the GEO 600 detector are 100 Hz or 200 Hz. A bandwidth of 200 Hz corresponds to a Signal-Recycling mirror with a power transmittance of $T_{\text{MSR}} \approx 1\%$. The maximum signal enhancement in this case is $\sqrt{4/0.01} = \sqrt{400} = 20$.

The Signal-Recycling cavity and the Power-Recycling cavity share the Michelson interferometer; the theoretical limits of both cavities to the resonant enhancement are thus the same.

Tuned and detuned Signal Recycling

With the Power-Recycling cavity and the Michelson interferometer being at their nominal operating point, the resonance condition inside the Signal-Recycling cavity is determined by the position of MSR along the optical axis. Each microscopic position of MSR corresponds to a different Fourier frequency of maximum enhancement. Therefore, a change in the position of MSR is also called *tuning* or *detuning* of the mirror and thus of the detector. The tuning of a mirror is given in radian with 0 rad being the position (one of many possible ones) at which the carrier frequency is resonant in the Signal-Recycling cavity. One distinguishes between two modes of Signal Recycling:

Tuned recycling: The Signal-Recycling cavity is resonant for the carrier frequency f_0 . In this case, the bandwidth of the Signal-Recycling cavity spans positive and negative Fourier (signal) frequencies so that the detector bandwidth is only half the bandwidth of the Signal-Recycling cavity. At the same time, the detector bandwidth must be larger

⁷ The actual bandwidth depends on whether Signal Recycling is used in tuned or detuned mode, see next section.

than the Fourier frequency of the expected signal $\Delta f > 2f_{\text{sig}}$. Therefore, tuned recycling requires a large cavity bandwidth⁸.

Both signal sidebands are resonantly enhanced inside the cavity when the above conditions are fulfilled.

Detuned recycling: The Signal-Recycling cavity is resonant for $f_0 + f_{\text{sig}}$ (or $f_0 - f_{\text{sig}}$), i. e., the resonance of the cavity is centered on one of the signal sidebands. Thus, the bandwidth can be very small, in particular smaller than the signal frequency $\Delta f < f_{\text{sig}}$. In this case, only one signal sideband is resonant in the cavity. Consequently, the maximum signal amplification is a factor of two smaller compared with tuned Dual Recycling with a similar Signal-Recycling mirror (see Appendix F). On the other hand, the possibility of narrowing the bandwidth of the detuned detector allows to maximise the enhancement of the signal sideband by using a Signal-Recycling mirror with a higher reflectance.

In the case of detuned Signal Recycling, the detector bandwidth is given by the full bandwidth of the Signal-Recycling cavity.

3.2.3 Dual Recycling for GEO 600

The GEO 600 detector was designed to be used with tuned or detuned Dual Recycling. The tuned mode provides a good sensitivity over the full range of expected signal frequencies. Detuned Dual Recycling allows to achieve a better sensitivity, provided that the sensitivity is not limited by other noise sources. In the following, we assume that all noise sources except shot noise are small compared to the thermal noise (within the frequency range of interest > 50 Hz) so that the sensitivity of the detector can be computed from the thermal-noise and shot-noise spectral densities. The exact level or shape of the thermal noise is not known yet. Therefore, it is also not yet known at which frequencies detuned Dual Recycling offers a considerable improvement when compared with tuned Dual Recycling.

Detuned Dual Recycling, however, is a very flexible method that can be used for different modes of operation:

- a) A detector slightly detuned (to approximately 200 Hz) with a relatively high bandwidth (≈ 400 Hz). The detuning gives a good overlap of the spectral densities of the spurious signal due to shot noise and the ‘false signal’ due to thermal noise. This mode is comparable to tuned Dual Recycling with a broadband Signal-Recycling cavity.
- b) The Signal-Recycling cavity has a slightly smaller bandwidth (200 Hz) and is detuned to higher frequencies (approximately 400 Hz to 800 Hz). The bandwidth

⁸ The tuned mode of Dual Recycling is sometimes called ‘broadband’ because it is typically used with a cavity of large bandwidth. Similarly, the detuned mode is sometimes referred to as ‘narrowband’. Throughout this document, however, the terms *broadband* and *narrowband* refer to the bandwidth only, and never to the tuning of the cavity.

results in a slightly better sensitivity around these frequencies. Still, the bandwidth is large enough to search for unknown signals.

- c) The Signal-Recycling cavity has a relatively narrow bandwidth (< 100 Hz) and is detuned to higher frequencies (above 700 Hz). The lower thermal noise makes a drastic reduction of shot noise a reasonable goal, albeit only in a very narrow band. This mode can be used for dedicated searches when the frequency of the expected signal is known *a priori*.

Figure 3.4 shows the sensitivity limits of the GEO 600 detector with respect to thermal noise and shot noise for three typical modes of operation: The ‘tuned’ plot shows the optimised setup for broadband operation. The Signal-Recycling mirror has a power reflectance of $R = 0.97$, and the bandwidth of the Signal-Recycling cavity is given as:

$$\Delta f_{\text{SRC}} \approx \frac{\text{FSR}_{\text{SRC}}(1 - 0.97)}{2\pi} \approx 600 \text{ Hz} \quad (3.10)$$

In the case of tuned recycling, only half of the cavity bandwidth can be used for detection (only positive signal frequencies) so that the detector bandwidth is ≈ 300 Hz. Here, the sensitivity at frequencies below 300 Hz is limited by thermal noise. The two plots for detuned Dual Recycling show the optimised setup using the two most likely detuning modes. With a Signal-Recycling mirror with $R = 0.99$, the bandwidths of the Signal-Recycling cavity and of the detector are ≈ 200 Hz. This lower bandwidth allows to approximately reach the thermal noise in a frequency range between 400 Hz and 700 Hz.

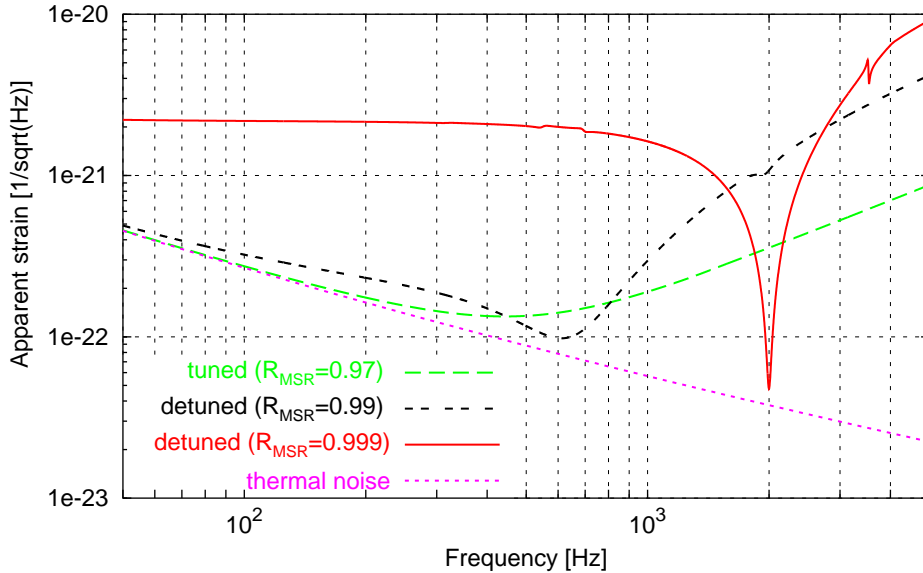


Figure 3.4: Example sensitivity plots for different Dual-Recycling modes: Three plots show the total of thermal noise and shot noise (thermal noise alone is shown for comparison). The tuned and the two detuned modes represent typical modes of operation of the GEO 600 detector.

Finally, the second plot of a detuned mode shows a narrowband setup with a Signal-Recycling mirror with $R = 0.999$. For frequencies above 800 Hz, this setup can provide the maximally possible sensitivity of the GEO 600 detector.

The GEO 600 detector can easily be set up for any of these modes: The detuning can be changed by adjusting some parameters of the control systems⁹. We expect to be able to tune the detector during normal operation without losing lock of the system. In order to change the *bandwidth* of the Signal-Recycling cavity, however, the Signal-Recycling mirror would have to be replaced. However, instead of using simple mirrors, one can also use a thermally tunable etalon as a Signal-Recycling mirror [Strain]. In this case, the reflectance of the etalon and thus the detector bandwidth can be changed easily with a temperature control system.

3.2.4 Interferometer control

The Dual-Recycled Michelson interferometer has three degrees of freedom: First, the length of the Power-Recycling cavity:

$$L_{\text{PRC}} = L_{\text{W}} + (L_{\text{E}} + L_{\text{N}})/2 \quad (3.11)$$

with L_{W} , L_{E} , L_{N} the lengths of the west, east and north arm respectively. Second, the operating point of the Michelson interferometer (differential arm length):

$$\Delta L = L_{\text{E}} - L_{\text{N}} \quad (3.12)$$

and third, the length of the Signal-Recycling cavity:

$$L_{\text{SRC}} = L_{\text{S}} + (L_{\text{E}} + L_{\text{N}})/2 \quad (3.13)$$

with L_{S} as the length of the south arm.

The length of the Power-Recycling cavity is used as reference for the laser frequency stabilisation (see Chapter 2) and is stabilised against a DC reference only at low frequencies (see Section 2.7.5). The length of the Power-Recycling cavity is assumed to be stable and independent of the other degrees of freedom. This is a good approximation in the steady state when all control loops are working. For the lock acquisition process, this approximation is, however, not valid.

The following sections describe the configuration of GEO 600 with respect to the error signals for controlling the Michelson interferometer and the Signal-Recycling mirror. The *MI loop* is used to maintain the dark-fringe operating point. A second control loop, the *SR loop*, is used to control the length of the Signal-Recycling cavity. Error signals for both degrees of freedom are obtained with the so-called *Schnupp modulation* technique.

⁹ In general, only the modulation frequency, the demodulation phase and the gain of the electronic servo have to be adjusted in order to tune the detector to a different frequency.

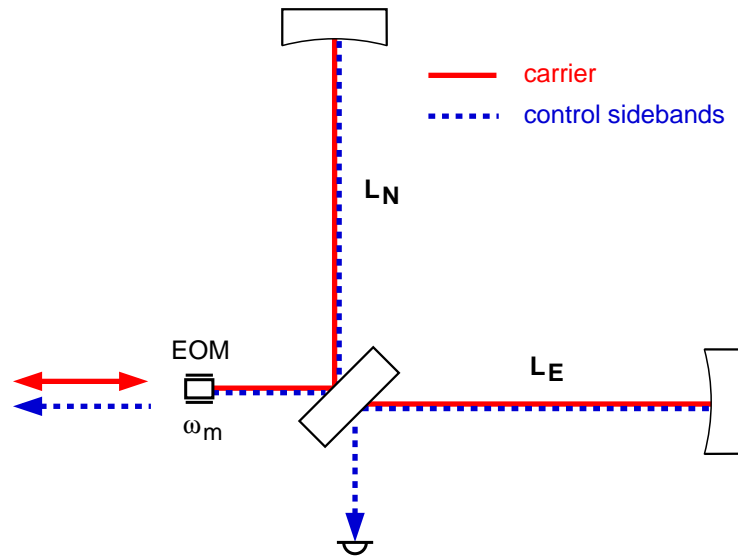


Figure 3.5: *Michelson interferometer with Schnupp modulation:* A pair of phase-modulation sidebands at frequency ω_m (control sidebands) is generated with an electro-optic modulator in the input port of the interferometer. In addition, the arm lengths of the Michelson interferometer are not equal ($L_N \neq L_E$) so that the dark fringe condition depends on the frequency of the input light. In general, a fraction of the control sidebands is directed back towards the west, and the other fraction is directed towards the south port. An error signal for the Michelson-interferometer differential arm length can, for example, be obtained by detecting the light in the south port and demodulating it at the modulation frequency. The signal has a zero crossing at the dark fringe for the carrier light, which is the desired operating point.

Schnupp modulation

The control method used in the GEO 600 detector has been originally proposed by Lise Schnupp [Schnupp]: The laser light is phase-modulated by an electro-optic modulator before it enters the interferometer¹⁰. This modulation (at an RF frequency) creates two control sidebands injected into the interferometer together with the carrier (see Figure 3.5). Schnupp modulation requires the arm lengths of the Michelson interferometer to be different so that the relative phase of the light fields returning from the interferometer arms depends on the frequency of the light. In particular, a Michelson interferometer that is at the dark fringe for the carrier light transmits a non-zero fraction of the control sidebands to the south port. The beat signal between the control sidebands and the carrier light leaking out of the Michelson interferometer generates a signal proportional to the deviation of the Michelson interferometer from the dark fringe. This error signal is used to control the differential position of the end mirrors. At the same time, it contains the gravitational-wave signal.

¹⁰ This method is also more generally known as ‘frontal’ or ‘pre-modulation’ method.

The Schnupp modulation method can also be used to generate error signals with respect to other degrees of freedom. In particular, the control signal for the Signal-Recycling mirror in GEO 600 is obtained by using an additional Schnupp modulation at a different modulation frequency.

Coupled four-mirror cavity

The Dual-Recycled Michelson interferometer can be described as a closed four-mirror cavity with a complex internal coupling. For the carrier and the signal sidebands, the coupling between the Power-Recycling cavity and the Signal-Recycling cavity is small because these light fields fulfil the dark-fringe operating condition. The Schnupp modulation sidebands, however, are designed not to be at the dark fringe in order to obtain a strong coupling between the cavities. In general, the terms Power-Recycling cavity and Signal-Recycling cavity do not make sense with respect to the control sidebands. Instead, the properties of the coupled four-mirror cavity have to be computed to understand the behaviour of the control sidebands.

The power of the control sidebands in the south port should be greater than the power of any waste light (as described in Section 3.1.3). In order to increase the power of the control sidebands, the modulation strength of the respective modulator must be increased. This, however, corresponds to less light power in the carrier field and hence yields a lower sensitivity of the detector. Therefore, the Schnupp modulation frequency has to be chosen such that the transmittance from the west port into the south port is maximised. This can be realised by selecting a modulation frequency that is approximately resonant in the four-mirror cavity.

Figure 3.6 shows the schematic configuration of the control system in the case of Dual Recycling. The length of the Power-Recycling cavity is assumed to be controlled by the frequency-stabilisation system. The differential arm length of the Michelson interferometer is controlled by the *MI loop*, and the length of the Signal-Recycling cavity is stabilised by the *SR loop*. Two modulators are used to create phase-modulation sidebands at ≈ 14.9 MHz for the MI loop and 9 MHz for the SR loop. These frequencies are chosen to approximately match a multiple of the free spectral range of the Power-Recycling cavity:

$$\begin{aligned} f_{\text{mod,MI}} &\approx 119 \cdot \text{FSR}_{\text{PRC}} \\ f_{\text{mod,SR}} &\approx 72 \cdot \text{FSR}_{\text{PRC}} \end{aligned} \tag{3.14}$$

The exact frequencies are chosen such that either both or one sideband of each pair of control sidebands is resonant in the Dual-Recycled Michelson interferometer: In general, the resonance conditions in the two recycling cavities are not identical. Figure 3.7 shows the resonance condition for an example setup in which the detector has been detuned to 500 Hz. The x-axis shows the modulation frequency as an offset to $f_{\text{mod,SR}} = 72 \cdot \text{FSR}_{\text{PRC}}$. The two graphs give the amplitudes of the upper and lower sidebands in the east arm of the Michelson interferometer. It can be seen that upper and lower sidebands

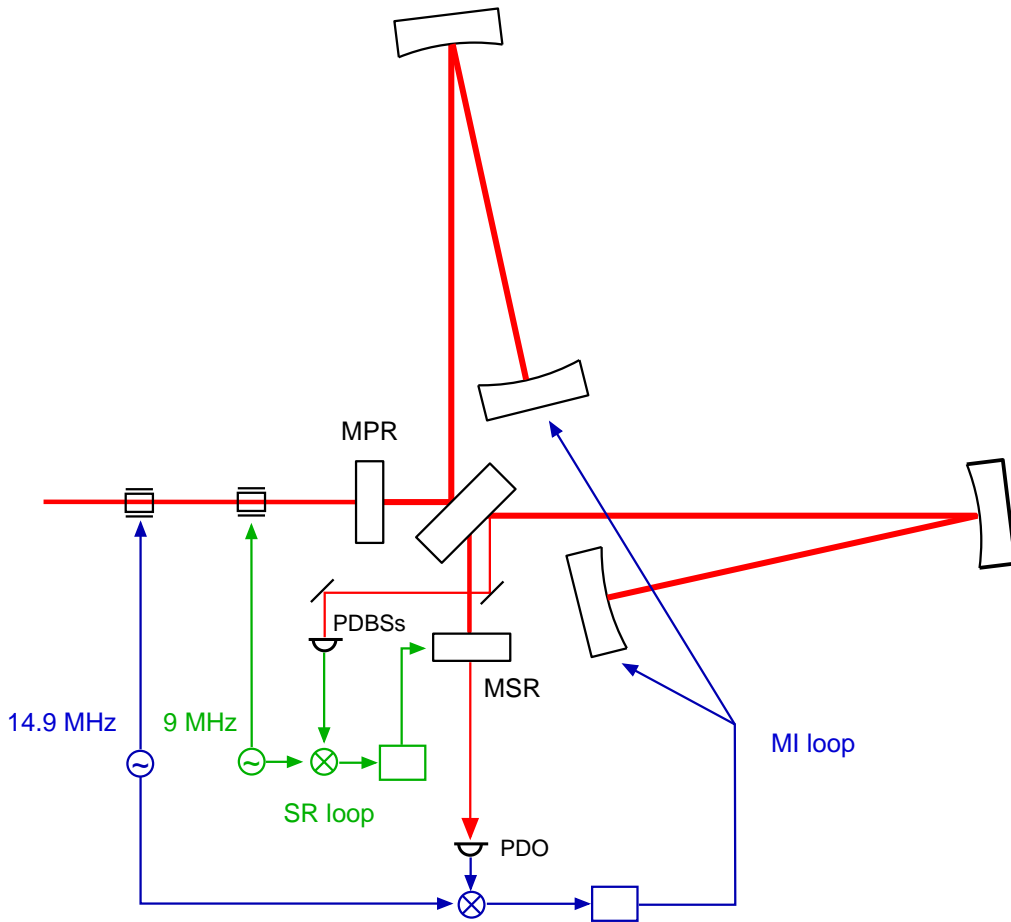


Figure 3.6: Control scheme of the Dual-Recycled Michelson interferometer: The laser light is phase-modulated before it enters the interferometer. Two pairs of control sidebands (at frequencies $f_{\text{mod,MI}} \approx 14.9$ MHz and $f_{\text{mod,SR}} \approx 9$ MHz) are created so that they are resonant in the recycled interferometer. The error signal for controlling the operating point of the Michelson interferometer (MI loop) is obtained by demodulating the signal of the main photo diode (PDO) in the south port (at $f_{\text{mod,MI}}$). Another photo diode (PDBSs) is used to detect the light reflected by the AR coating of the beam splitter; the photo diode signal is then demodulated at $f_{\text{mod,SR}}$ to generate the error signal for controlling the length of the Signal-Recycling cavity (SR loop).

cannot be maximised simultaneously and that none of the maxima occurs exactly at the 72th multiple of the free spectral range of the Power-Recycling cavity. In practice, the optimal Schnupp modulation frequency has to be found either experimentally or by using a simulation. The optimum modulation frequencies for two typical modes of the GEO 600 detector are given in Section 3.3.

The error signal for controlling the Michelson interferometer is obtained by demodulating the signal of the main photo diode in the south port with $f_{\text{mod,MI}}$. The signal for controlling the length of the Signal-Recycling cavity is obtained by demodulating the signal

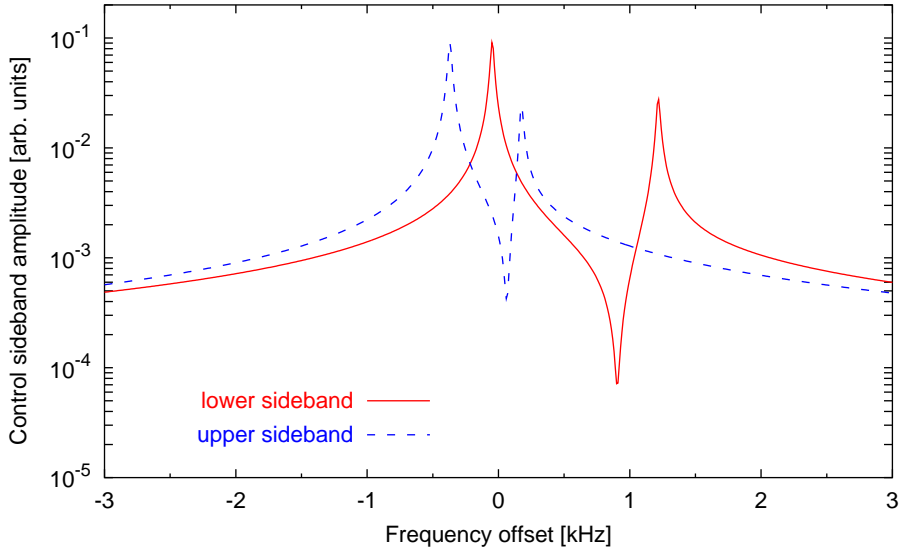


Figure 3.7: Resonance condition in the Dual-Recycled Michelson interferometer (detuned to 500 Hz): The plot shows the amplitude of the control sidebands (used in the SR loop) inside the Michelson interferometer as a function of the modulation frequency. The frequency is given as an offset to 9.018100 MHz, which is approximately 72 times the free spectral range of the Power-Recycling cavity. Because of the detuning, the upper and lower sidebands are not at resonance simultaneously, and no resonance appears exactly at a multiple of the free spectral range of the Power-Recycling cavity (the nearest peak is at -50 Hz).

of a second photo diode that detects the light reflected at the AR coating of the beam splitter, at the second modulation frequency $f_{\text{mod,SR}}$.

This control concept has been developed at the 30 m prototype interferometer in Garching. It was shown that suitable error signals can be derived and that a suspended Dual-Recycled Michelson interferometer can be operated in the tuned and detuned modes. A detailed description of the control concept and of the experimental demonstrations can be found in [Heinzel98, Heinzel99, Freise00]. In addition, an overview of the control configuration for Dual Recycling in GEO 600 is presented in [Heinzel02].

3.3 Simulating GEO 600 with Dual Recycling

In the following, numerical simulations with FINESSE (see Appendix E) are used to determine some of the optical parameters of the GEO 600 detector with respect to optimal performance of the interferometer in the detuned Dual-Recycling mode. For the first test of Dual Recycling, a Signal-Recycling mirror with $R_{\text{MSR}} = 0.99$ has been installed. This type of mirror gives a good sensitivity with a sufficiently large bandwidth. Later on, mirrors with higher reflectance of up to $R_{\text{MSR}} = 0.999$ may be used for dedicated narrowband searches.

The following simulations were done for two samples of SR mirrors: The first mirror has a reflectance of $R_{\text{MSR}} = 0.99$; the configuration using this mirror is referred to as ‘broadband’. The second mirror has a reflectance of $R_{\text{MSR}} = 0.999$ and the setup is called ‘narrowband’. These reflectances were chosen to represent both a typical bandwidth ($R_{\text{MSR}} = 0.99$) and the likely minimal bandwidth ($R_{\text{MSR}} = 0.999$).

The performance of GEO 600 in narrowband mode depends on the thermal noise limit. The current theoretical predication of the internal thermal noise limit is based on a quality factor of $Q = 5 \cdot 10^6$ for the mirrors (and the beam splitter). This Q factor has not yet been measured, and it might even be higher. In addition, the thermo-refractive noise, for example as shown in Figure 1.1, is based on recent research and must be understood as a worst-case limit only. Consequently, the optimum reflectance of the Signal-Recycling mirror for the narrowband mode is not yet known; a value of $R_{\text{MSR}} = 0.999$, however, represents a sensible upper limit because of the expected losses of ≈ 500 ppm inside the Michelson interferometer.

Unless otherwise noted, the following parameters are used in the simulation:

- Length of the west arm: $L_{\text{W}} = 1.145$ m, length of the south arm: $L_{\text{S}} = 1.235$ m; this results in a *cavity length difference* (length difference between the Signal-Recycling cavity and the Power-Recycling cavity) of $\Delta L_{\text{cav}} = 90$ mm.
- Length of the north arm¹¹: $L_{\text{N}} = 1195.579$ m, length of the east arm: $L_{\text{E}} = 1195.648$ m; this yields an arm-length difference of $\Delta L = 69$ mm, the average length is $\bar{L} = 1195.613$ m.
- From the lengths given above, the free spectral ranges of Power-Recycling and Signal-Recycling cavity can be computed as $\text{FSR}_{\text{PRC}} = 125251.9$ Hz and $\text{FSR}_{\text{SRC}} = 125242.5$ Hz.
- The power transmittance of the Power-Recycling mirror is $R_{\text{MPR}} = 0.999$. Assuming an over-coupled cavity, we get a cavity linewidth of $\Delta f_{\text{PRC}} \approx 20$ Hz. For the Signal-Recycling cavity, the linewidth is likewise $\Delta f_{\text{SRC}} \approx 20$ Hz for the mirror with $R_{\text{MSR}} = 0.999$ and $\Delta f_{\text{SRC}} \approx 200$ Hz for the mirror with $R_{\text{MSR}} = 0.99$.
- The power reflectance and transmittance of the beam splitter are $R_{\text{BS}} = 0.486$ and $T_{\text{BS}} = 0.514$, respectively; the second surface of the beam splitter is anti-reflection (AR) coated. This AR coating is assumed to have a power reflectance of $R_{\text{AR}} = 40$ ppm.
- The end mirrors have a power transmittance of $T = 50$ ppm. In addition to the given transmittance and reflectance, all surfaces (all mirrors and the beam splitter) are assumed to have a power loss of 30 to 50 ppm due to scattering and absorption in the coating.

¹¹ Please note that the geometric length of the interferometer arms in GEO 600 is ≈ 600 m. The arms are folded once so that the optical round-trip path length is ≈ 2400 m for each interferometer arm. In the simulation the arms can be unfolded and the distances from the beam splitter to the respective end mirror are used as the lengths of the interferometer arms.

- Two Schnupp modulation frequencies are present: The base frequency for the control of the Michelson interferometer is $f_{\text{mod,MI}} = 14.904976$ MHz, which is approximately 119 times the free spectral range of the Power-Recycling cavity. The second modulation is used for controlling the Signal-Recycling cavity. It is based on $f_{\text{mod,SR}} = 9.018130$ MHz. Usually, just the offset Δf_{mod} to the base frequency is given.

The control loops for the Michelson interferometer and the Power-Recycling cavity have finite gain and cannot completely remove random fluctuations. The residual disturbances are usually given as mirror displacements (root mean square). In the simulation, these deviations are represented by static offsets: The Michelson interferometer is arbitrarily set to have an offset of 10^{-11} m from the dark fringe, and the Power-Recycling cavity is assumed to have an offset of 10^{-12} m from the resonance condition. These offsets correspond to a deviation of the Michelson interferometer from the dark fringe of 60 and $6 \mu\text{rad}$ respectively, see Section E.2.4.

3.3.1 Detuning the Signal-Recycling mirror

The resonance frequencies in a simple Fabry-Perot cavity are multiples of the free spectral range $\text{FSR} = c/l$ with l being the optical path length of the cavity and c the speed of light. A displacement of one mirror by $\lambda/2$, corresponding to a detuning of $\phi = \pi$, will change the resonance frequency by one free spectral range. To detune the Signal-Recycling cavity by a given signal frequency f_{sig} , a detuning of the Signal-Recycling mirror by:

$$\phi_{\text{MSR}} = \pi \frac{f_{\text{sig}}}{\text{FSR}_{\text{SRC}}} = 25 \mu\text{rad} \cdot \left(\frac{f_{\text{sig}}}{1 \text{ Hz}} \right) \quad (3.15)$$

is required. The detuning can also be given as a mirror displacement:

$$\delta x_{\text{MSR}} = \frac{\lambda}{2\pi} \cdot \phi_{\text{MSR}} = 4.23 \text{ pm} \cdot \left(\frac{f_{\text{sig}}}{1 \text{ Hz}} \right) \quad (3.16)$$

A simulation of the GEO 600 configuration is shown in Figure 3.8. A differential signal is injected at the end mirrors of the interferometer¹², and the sum of the signal sideband amplitudes in the south port of the interferometer is plotted as a function of the detuning ϕ_{MSR} and the signal frequency f_{sig} . The linear fit in Figure 3.8 shows that this simple calculation agrees well with the simulation.

3.3.2 Error signal for controlling the Michelson interferometer

The error signal for the Michelson interferometer is obtained by demodulating the photo current from the photo diode in the south port with the MI modulation frequency. It can be measured as a function of time. Here, the error signals are analysed assuming a steady

¹² Signal injection refers to a differential modulation of the position of the end mirrors.

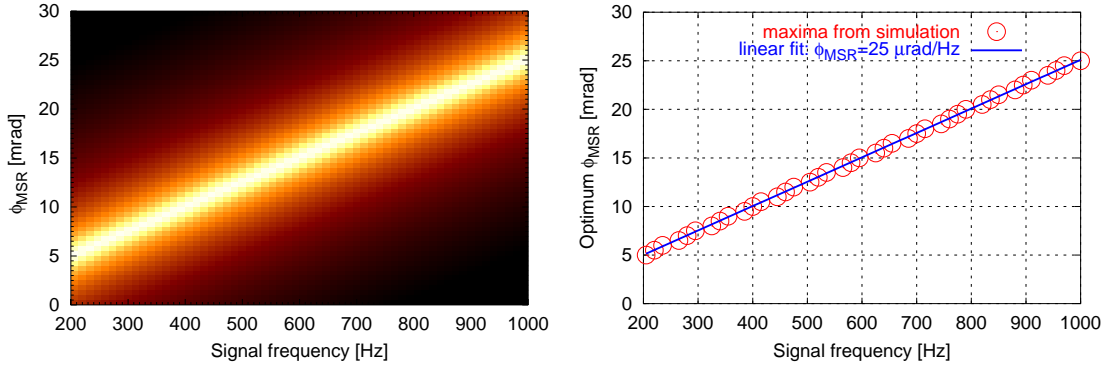


Figure 3.8: The power of the signal sidebands in the south port of the detector (gravitational-wave signal) is plotted as a function of the detuning of the Signal-Recycling mirror (ϕ_{MSR}) and the signal frequency (f_{sig}). The left graph shows a FINESSE simulation: bright areas indicate large amplitudes. The right graph shows the maxima from the left graph and a linear fit.

state. Thus, in the following simulations the error signal x_{EP} is defined as a function of a differential displacement x_{d} . The displacement is given as the distance between a mirror or beam splitter and its nominal position as defined by the desired operating point. In the case of the Michelson interferometer, the differential displacement gives the deviation from the chosen arm-length difference ΔL .

Figure 3.9 shows an example plot of a Michelson-interferometer error signal. The operating point is given as:

$$x_{\text{d}} = 0 \quad \text{and} \quad x_{\text{EP}}(x_{\text{d}} = 0) = 0 \quad (3.17)$$

The transfer function $T_{\text{opt},x_{\text{d}}}$ of the Michelson interferometer with respect to this error signal is defined by:

$$\tilde{x}_{\text{EP}}(f) = T_{\text{opt},x_{\text{d}}} T_{\text{det}} \tilde{x}_{\text{d}}(f) \quad (3.18)$$

with T_{det} as the transfer function of the sensor. In the following, T_{det} is assumed to be unity. At the zero crossing the slope of the error signal represents the magnitude of the transfer function for low frequencies:

$$\left. \frac{dx_{\text{EP}}}{dx_{\text{d}}} \right|_{x_{\text{d}}=0} = |T_{\text{opt},x_{\text{d}}}|_{f \rightarrow 0} \quad (3.19)$$

The quantity above will be called *error-signal slope* in the following. It is proportional to the so-called *optical gain* $|T_{\text{opt},x_{\text{d}}}|$, which describes the amplification of the gravitational-wave signal by the optical instrument.

The most difficult task in the analysis of a Dual-Recycling configuration is to understand the resonance conditions for control sidebands in the Dual-Recycled interferometer. The aim is to find an optical setup in which the throughput of the control sidebands (transmittance from the interferometer input to the main photo diode in the south port) is maximised for a broad range of detunings.

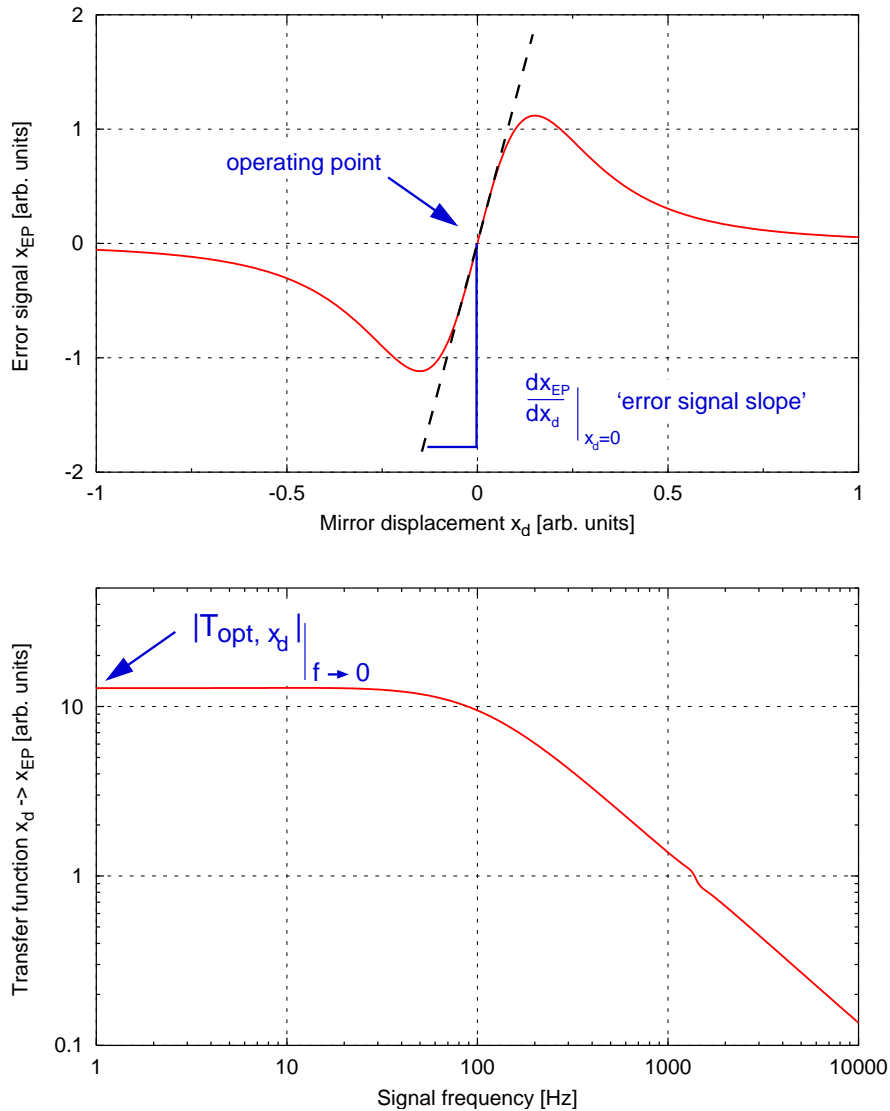


Figure 3.9: Example of an error signal: The top graph shows the electronic interferometer output signal as a function of the mirror displacement. The operating point is given as the zero crossing, and the error-signal slope is defined as the slope at the operating point. The bottom graph shows the magnitude of the transfer function mirror displacement \rightarrow error signal. The slope of the error signal (upper graph) is equal to the low frequency limit of the transfer function magnitude (see Equation 3.19).

3.3.3 Arm-length difference

Simulations of the 30 m prototype interferometer in Garching [Freise] show that the coupling of the Schnupp modulation sidebands depends mostly on the detuning of the Signal-Recycling mirror ϕ_{MSR} , the cavity length difference ΔL_{cav} and the frequency of

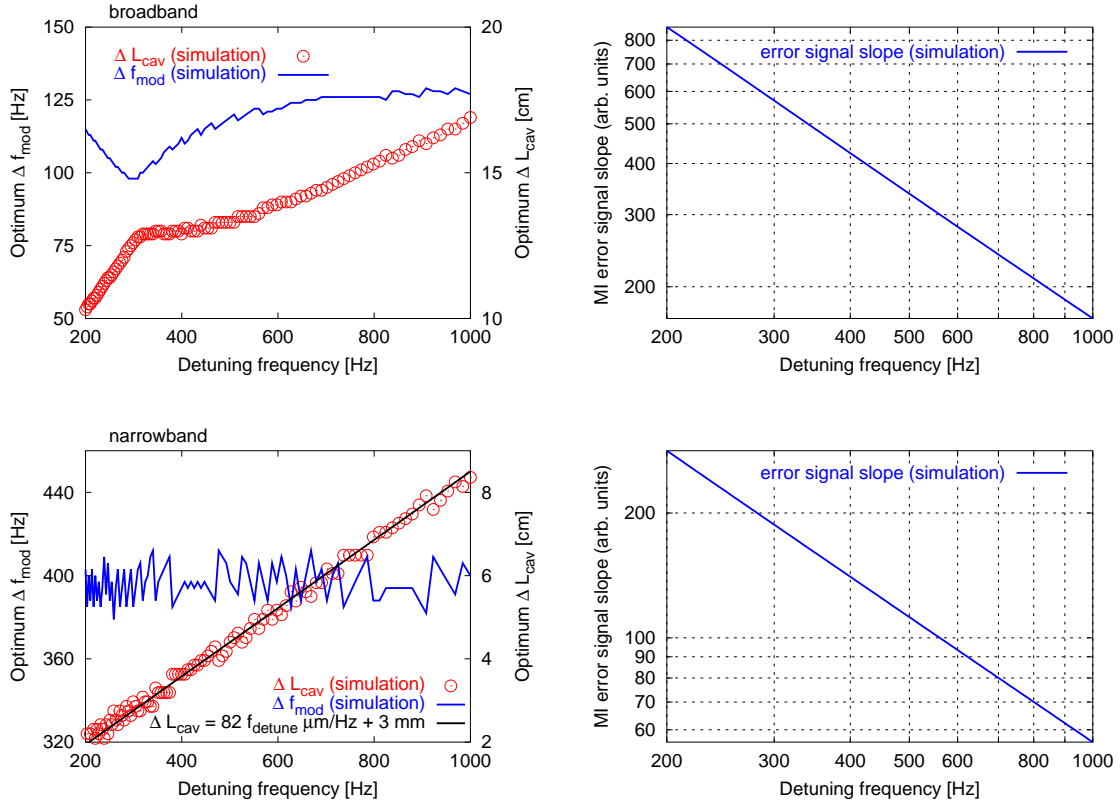


Figure 3.10: Optimisation of the MI error-signal slope. The top two graphs refer to the broadband mode, and the lower two graphs show the result for the narrowband mode. The Schnupp modulation frequency and the cavity length difference are varied in the simulation to find the maximum error-signal slope. The left graphs show the optimum parameters (the randomly varying values for the Schnupp modulation frequency are an artefact of the simple optimisation), the right graphs the corresponding slopes of the error signal at the operating point.

the Schnupp modulation sidebands f_{mod} . Figure 3.10 shows a numerical simulation for the GEO 600 configuration in broadband and narrowband modes. The frequency of the Schnupp modulation and the cavity length difference are varied independently for each detuning frequency from 200 to 1000 Hz. In practice, the Schnupp modulation can be varied easily, whereas it is difficult to change the cavity length difference without causing a large down time of the interferometer. Thus, we are looking for a cavity length difference that would allow a good performance for all detunings in both a narrowband and a broadband setup.

The straightforward optimisation shown in Figure 3.10 does not yield a clear optimum for the cavity length difference with respect to all detuning frequencies. Figure 3.11 shows the simulated slope of the error signal for three different fixed cavity length differences: The length difference of 5 cm would be a good compromise in the narrowband case, 13 cm was chosen as a possible solution in the broadband case, and 9 cm represents the average of those two values. The simulation shows that for the broadband mode the error-signal slope does not vary much with the arm-length difference: 13 cm and 9 cm are equally

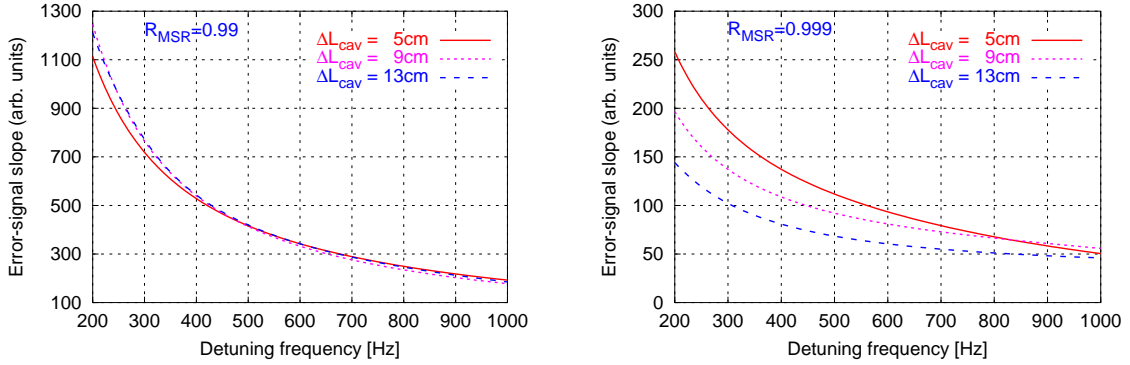


Figure 3.11: Error-signal slopes (MI loop) for three fixed cavity length differences. The Schnupp modulation frequency is always optimised. The left graph shows the result for broadband operation, the right graph gives the result for the narrowband case.

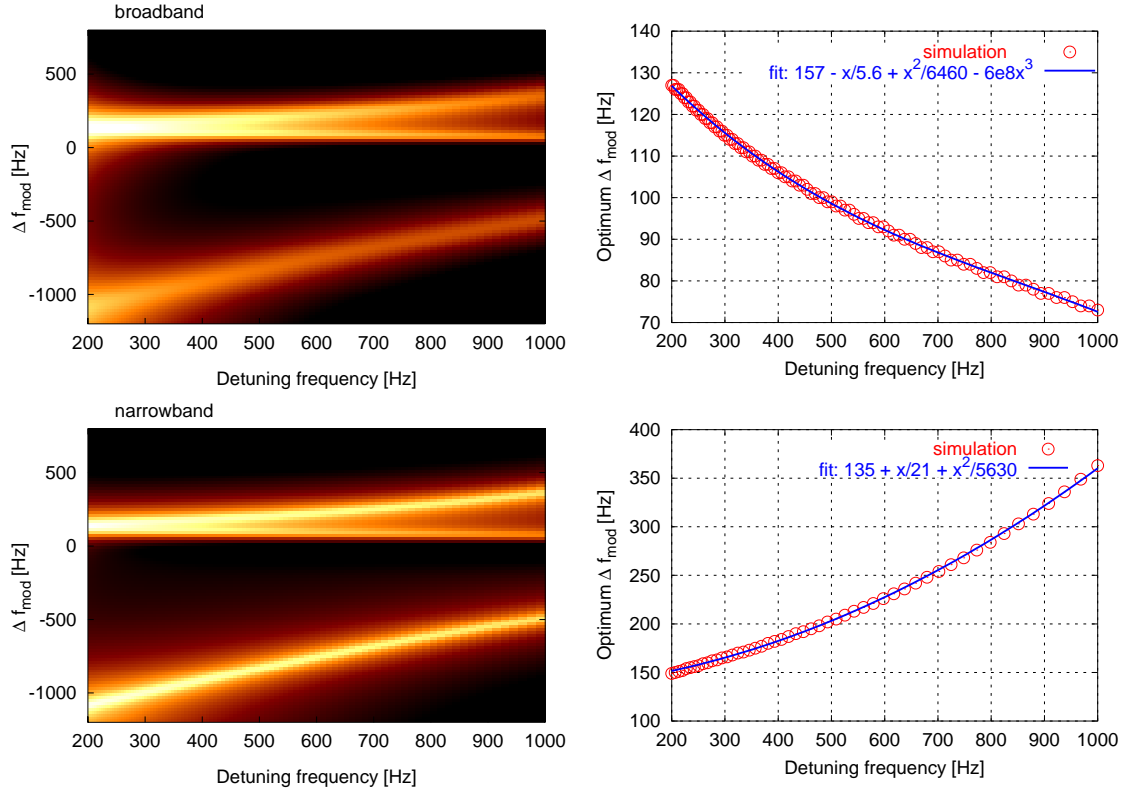


Figure 3.12: The optimum Schnupp modulation frequency (as an offset to 14.904976 MHz) for the MI loop as a function of the detuning frequency for a cavity length difference of 9 cm. The upper graphs refer to the broadband mode and the lower graphs to the narrowband mode. The left graphs show the error-signal slope, brighter areas indicate steeper slopes. The right plots give the maxima from the left plot and a non-linear fit.

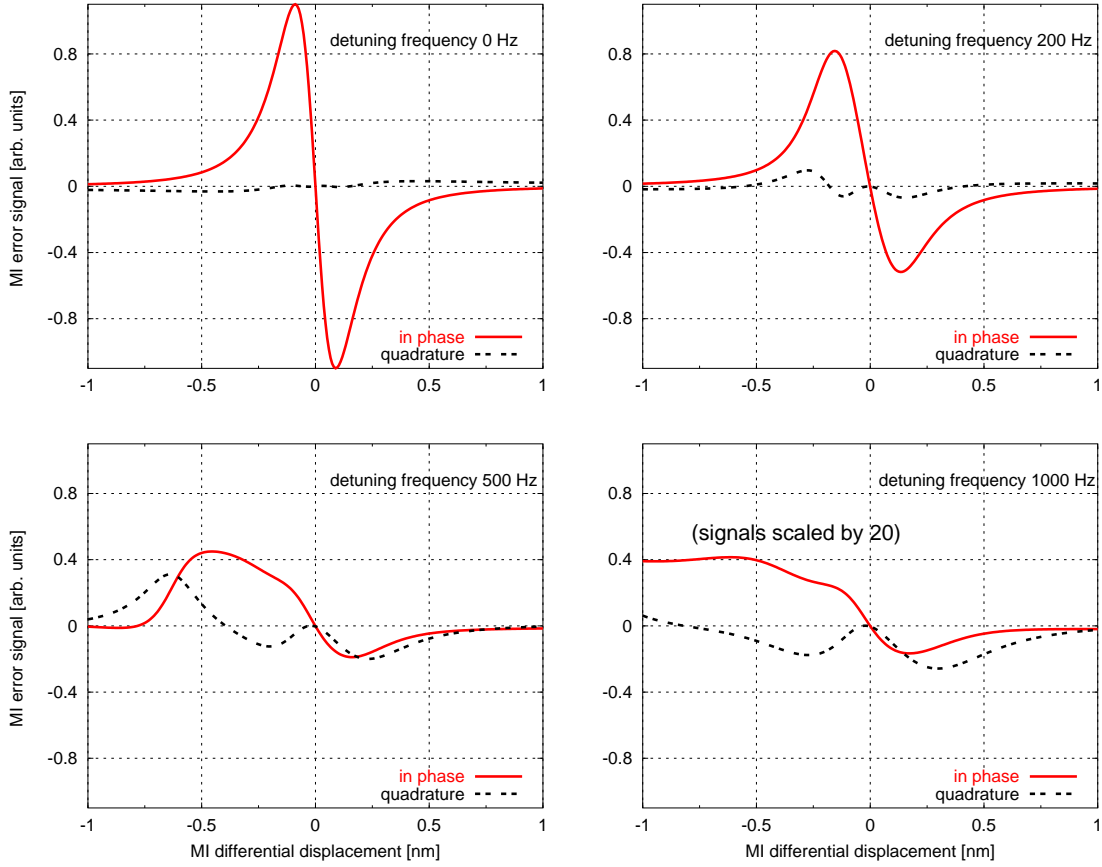


Figure 3.13: Error signals for controlling the Michelson interferometer: The error signals for the dark fringe operating point are computed using the optimised modulation frequencies from the previous simulations. The error signal becomes asymmetric with increasing detuning frequency but can still be used for control purposes because the zero crossing is well defined.

good and only 5 cm results in an approximately 10% lower value. For the narrowband case the situation is different: The error-signal slope is a factor of 6 smaller than in the broadband case and changes more strongly with the cavity length difference (note that the narrowband mode would mostly be used for large detuning frequencies, > 500 Hz).

The current design of the vacuum system and of the mechanical structure in the vacuum tank for the Signal-Recycling mirror (TCOa) results in a lower limit of 9 cm for possible cavity length differences. The results of the aforementioned simulations show that this value would allow good performance of the detector in the most likely cases. All following simulations thus use $\Delta L_{\text{cav}} = 9$ cm.

Figure 3.12 shows the simulated slope of the Michelson interferometer error signal for a cavity length difference of 9 cm. A non-linear fit to the maxima of the simulation yields an analytical model for the optimal Schnupp modulation frequencies for the narrowband and broadband mode, respectively. Figure 3.13 shows the corresponding error signals for four different tunings of the detector. In the case of tuned Signal Recycling, the

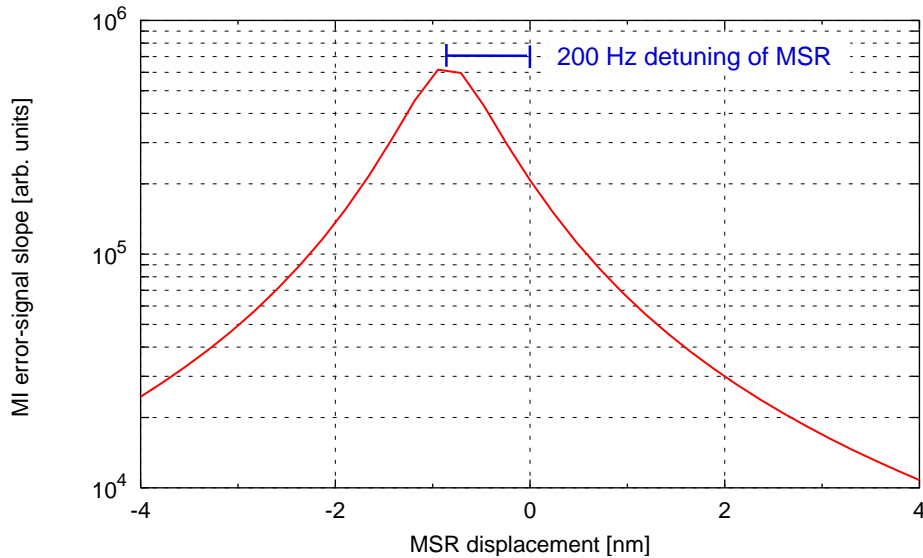


Figure 3.14: Error-signal slope of the MI loop as a function of the displacement of the Signal-Recycling mirror. Zero is defined as the detuned operating point (Signal-Recycling cavity detuned to 200 Hz). This maximum of the error-signal slope does not correspond to the operating point but to the position at which the Signal-Recycling cavity is resonant for the carrier.

error signal is symmetric with a well-defined zero crossing. If the detector is detuned the error signal becomes asymmetric. With increased detuning the error-signal slope becomes smaller and the asymmetry increases. These asymmetric error signals, however, still yield a single well-defined zero crossing at the operating point and are thus suitable for controlling the Michelson interferometer.

The dependence of the error-signal slope on the MSR detuning is shown in Figure 3.14: The Schnupp modulation frequency is optimised for a detuning of 200 Hz (which corresponds to a MSR displacement of ≈ 0.8 nm). The error-signal slope is plotted as a function of MSR displacement, assuming the Michelson interferometer to be tightly locked to the dark fringe. The maximum slope occurs when the Signal-Recycling cavity is in the ‘tuned’ state, even though the modulation has been optimised for a detuning. Figure 3.15 shows the error signals of the MI loop for larger displacements of the Signal-Recycling mirror.

The asymmetry of the optical gain of the MI loop with respect to the SR operating point is of no importance for the stable operation; however, it affects the lock acquisition process. A lock acquisition automation needs to determine the state of the uncontrolled interferometer. At least, it must be able to detect when random fluctuations put the interferometer close to the operating point. In a simple case, this can be done by monitoring several light powers and by comparing these signals with pre-defined threshold values (see Section 2.8.1 for an example). When these signals are asymmetric with respect to the operating point, this approach does not work. Possible lock acquisition schemes for Dual Recycling in the GEO 600 detector are currently being investigated.

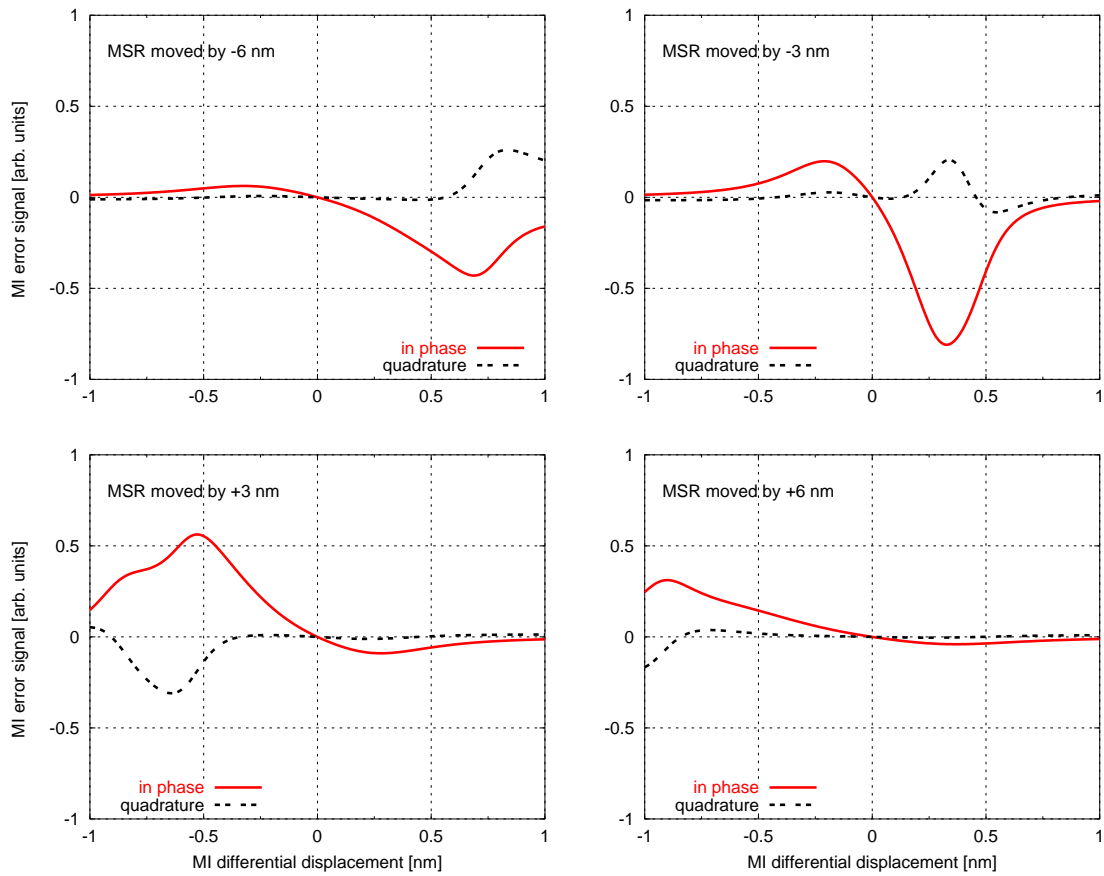


Figure 3.15: Error signals of the MI loop for four different MSR displacements. Here, the Michelson interferometer is at the dark fringe and the Signal-Recycling mirror is passing uncontrolled through its operating point (the displacements that correspond to operating points of detuned Signal Recycling are less than 4 nm).

3.3.4 Error signal for controlling the Signal-Recycling cavity

The microscopic position of the Signal-Recycling mirror defines the detuning of the detector. Required is an error signal for controlling the length of the Signal-Recycling cavity with a zero crossing at the desired detuning of the Signal-Recycling mirror.

The light power of the control sidebands is not directly related to the sensitivity of the detector (as opposed to the control sidebands of the MI loop). It is desirable, however, to maximise these control sidebands in order to increase the signal-to-noise ratio of the error signal and thus improve the noise performance and robustness of the SR control loop.

Simulations show that generating such an error signal is more complicated than for the MI loop. The main difference is that the zero crossing of the error signal strongly depends on the demodulation phase of the electronic mixer. Figure 3.16 shows the SR error signal as

a function of the detuning and the modulation frequency for four different demodulation phases. The borders between black and white areas represent zero crossings that mark possible operating points. In the control scheme for GEO 600, we use the zero crossings in the (lower) left area of the four graphs because they provide a steeper slope at the operating point.

It can be seen that the operating point moves with respect to the detuning when either the modulation frequency or the demodulation phase is changed. A simulation that yields an optimal modulation frequency must at the same time compute the optimal demodulation phase. It was not possible to find a simple algebraic dependence (like with the non-linear fit in the case of the MI loop) for the optimal values. Figure 3.17 shows the error signal for the Signal-Recycling mirror with an optimised Schnupp modulation frequency and demodulation phase for a detuning of 200 Hz. In addition, the error signals for slightly changed demodulation phases are shown. In practice, an alternating sequence of measurements and simulations will be necessary to determine the state of the detector and set the optimum parameters.

The error signals for controlling the Signal-Recycling mirror are strongly affected by the differential arm length of the Michelson interferometer. Figures 3.18 and 3.19 show SR loop error signals for a tuned and a detuned setup, respectively. The error signals are shown for different states of the Michelson interferometer: the dark fringe and small deviations from the dark fringe.

The Signal-Recycling error signal for tuned Dual Recycling develops a strongly reduced slope at the zero crossing when the Michelson interferometer is detuned from the dark fringe. In the case of detuned Dual Recycling, the zero crossing of the error signal is moved away from the nominal operating point if the Michelson interferometer is detuned from the dark fringe. In addition, an offset is introduced to the signal. As a consequence, the signal cannot be used to control the Signal-Recycling mirror. This shows that a lock acquisition process is unlikely to work for a detuning of 200 Hz. A lock acquisition of tuned Dual Recycling looks more promising. Another approach currently under investigation is to initially acquire lock for a strongly detuned operating point (for example, with a detuning of 20 kHz) and to then slowly change to the desired operating point while the interferometer is locked.

During a stable operation the deviations of the Michelson interferometer from the dark fringe are expected to be much smaller than those used in the simulations shown in Figure 3.19. Currently, we reach a deviation of approximately 10 pm (rms) and plan to achieve 1 pm [Grote] so that the Signal-Recycling cavity can also be used for a detuning frequency of 200 Hz. However, a strong coupling of the MI error signal into the SR error signal remains. The performance of the SR loop can be improved when a linear combination of the SR error signal and the MI error signal is used for controlling the Signal-Recycling mirror.

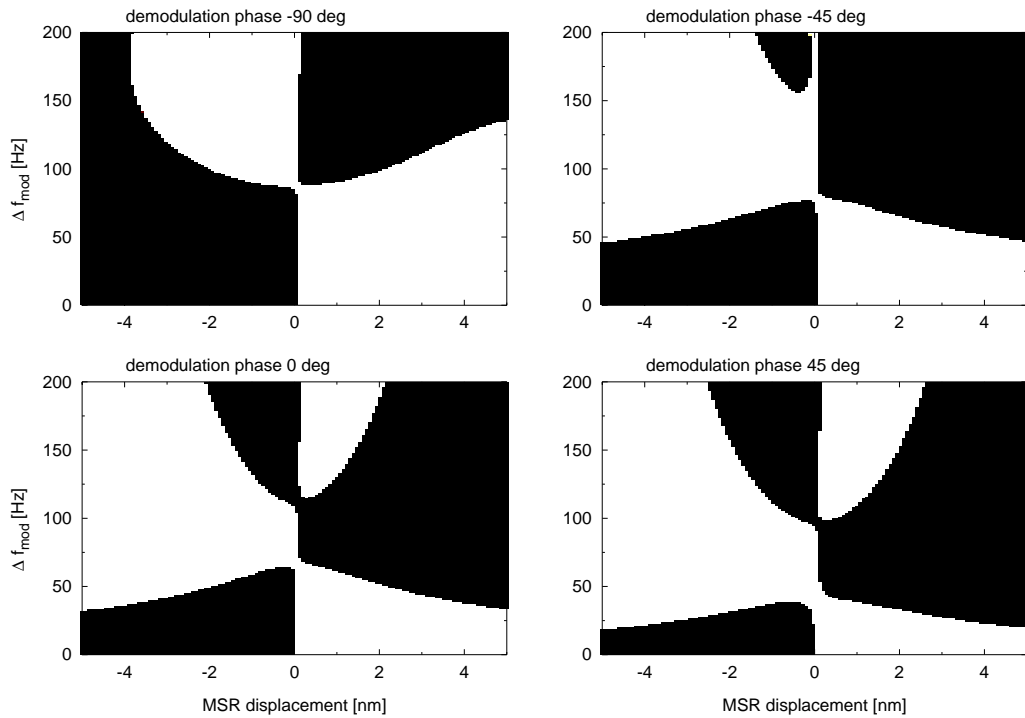


Figure 3.16: Error signal for controlling the Signal-Recycling cavity: The white areas indicate a positive, black areas a negative signal. The zero crossings, visible as the borders between black and white areas, define possible operating points. The modulation frequency is given as an offset to 9.018130 MHz. These graphs show that the operating point depends on the modulation frequency and the demodulation phase.

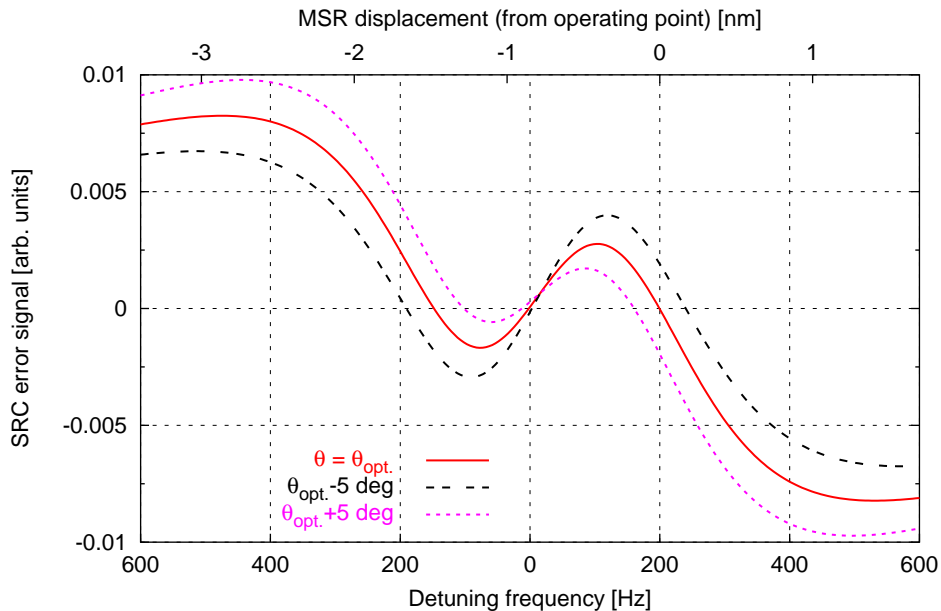


Figure 3.17: Error signal for the SRC control. The detuning is set to 200 Hz, the Schnupp modulation frequency is 9.018204 MHz. The plot shows the error signal for an optimised demodulation frequency and phase. In addition, two graphs for slightly different demodulation phases are shown.

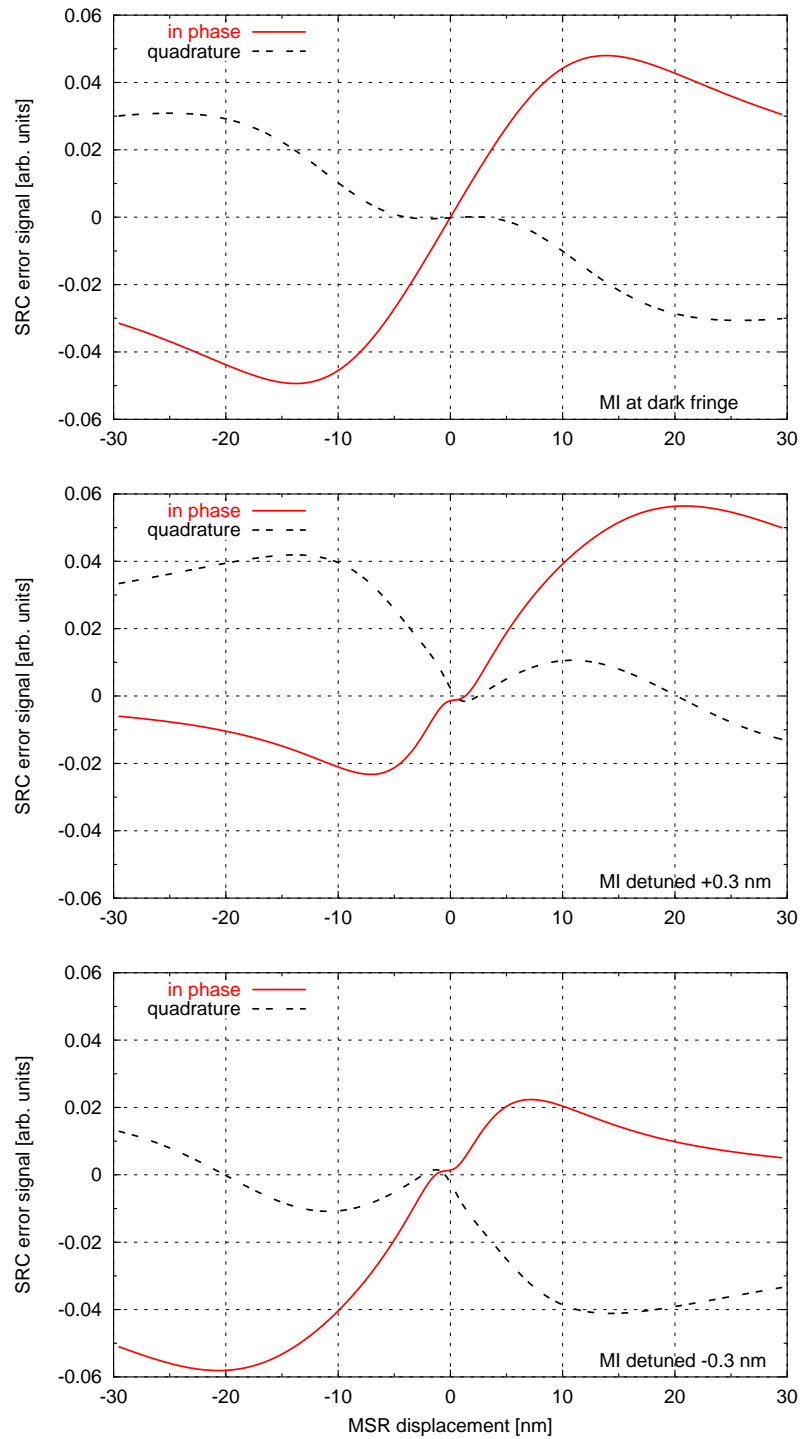


Figure 3.18: Error signal of the SR loop for tuned recycling. The three graphs show the error signal for different states of the Michelson interferometer: Even small deviations from the dark fringe result in a strongly reduced slope at the zero crossing.

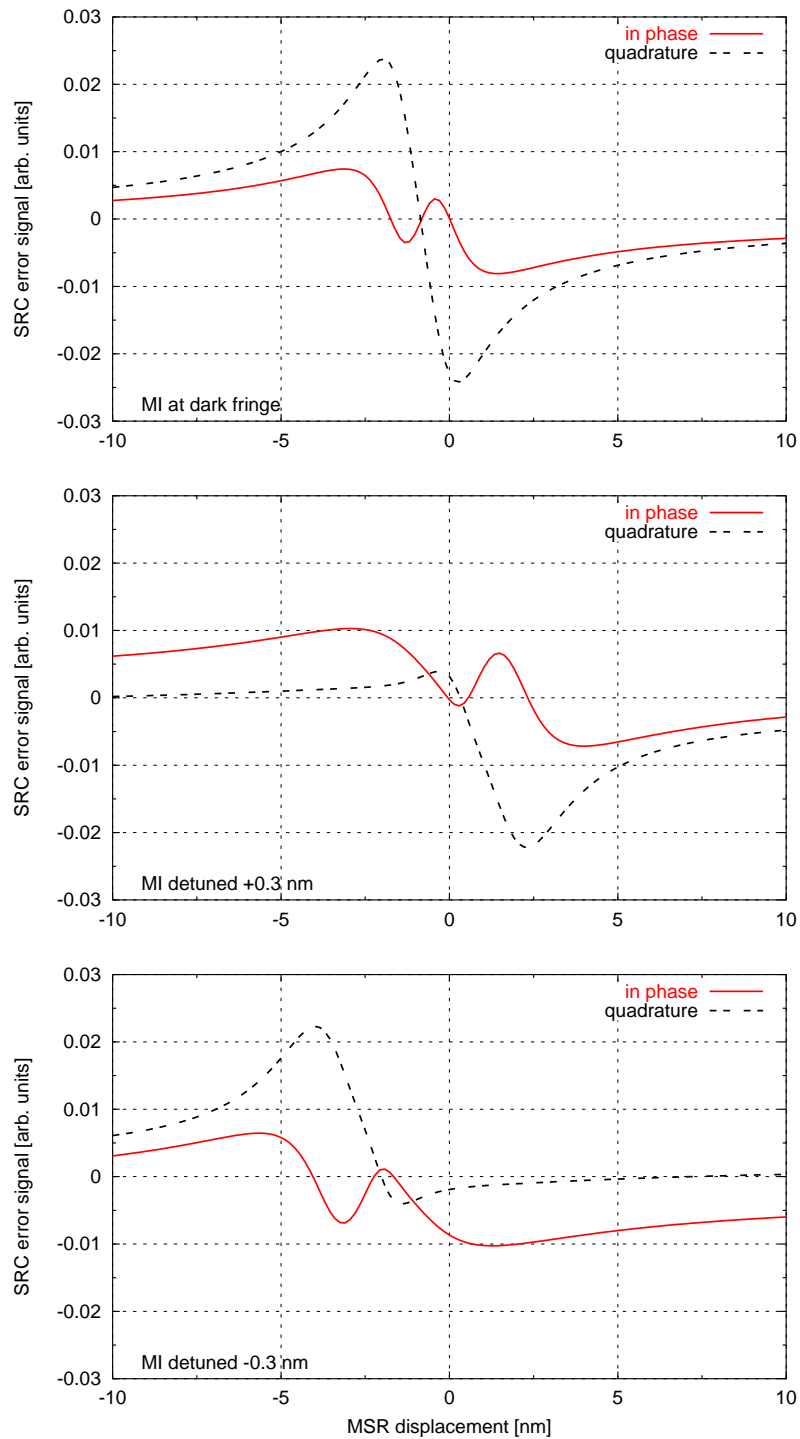


Figure 3.19: Error signal of the SR loop. The setup is optimised for a detuning of 200 Hz corresponding to a 0.8 nm displacement (in the above graphs zero displacement corresponds to this nominal detuning). The three graphs show the error signals for different states of the Michelson interferometer: Small deviations of the Michelson interferometer from the dark fringe move the zero crossing of the SR loop by a large amount. The error signal becomes unsuitable for a stable control.

3.3.5 Coupling of noise into the output signal

The figure of merit in designing an interferometric gravitational-wave detector is the signal-to-noise ratio (SNR). The sensitivity (defined as the signal amplitude that can be detected with unity SNR) must be extremely good to allow detection of the expected small signal amplitudes.

The maximum distance for a source to be detected can be computed from the sensitivity of the detector and the expected strength of a gravitational wave; the maximum distance is proportional to the detector sensitivity. If the sources are distributed uniformly in space, then the number of detectable sources is proportional to the cube of improvements in sensitivity. In addition, it makes a great difference whether a certain galaxy or galaxy cluster is within the detectable volume or not. These are the reasons why even a small improvement in the detector sensitivity can lead to a much greater chance of detecting gravitational waves.

Minimise the noise

A good SNR can especially be achieved by building the instrument in such a way that possible noise sources are either avoided or decoupled as much as possible from the measurement apparatus.

The possible noise sources can be divided into two classes. First, the noise sources that physically change the arm-length difference of the Michelson interferometer. For example, seismic noise that moves the vacuum tanks and thus the mirrors will be detected like a gravitational-wave signal. Therefore, the mirrors have to be isolated as much as possible from the motion of the vacuum tanks.

The second class of noise sources can be characterised by generating a spurious signal. Even though the arm-length difference of the Michelson interferometer does not change, the error signal indicates such a change. This kind of noise is often introduced via the control and feedback systems, depending in some way on the control topology. By choosing the right control method, especially for the Michelson interferometer, the influence of such noise can be reduced. It is crucial to carefully design and understand the control systems to avoid introducing noise via the feedback systems.

Sensitivity limits

In the following, the coupling of various optical noise sources into the output signal of GEO 600 is analysed. Limits for the respective noise magnitude are computed by comparing the effects of the noise signal on the interferometer output to those of the thermal noise. Thermal noise is expected to limit the sensitivity of the GEO 600 detector in the measurement band¹³ (see Figure 1.1). In the following, the thermal noise is therefore used as a reference, and the influence of other noise sources should be kept smaller.

¹³ The shot noise in Figure 1.1 may be larger than the thermal noise, but because of Signal Recycling the detector can always be tuned to be limited by thermal noise in a certain frequency band.

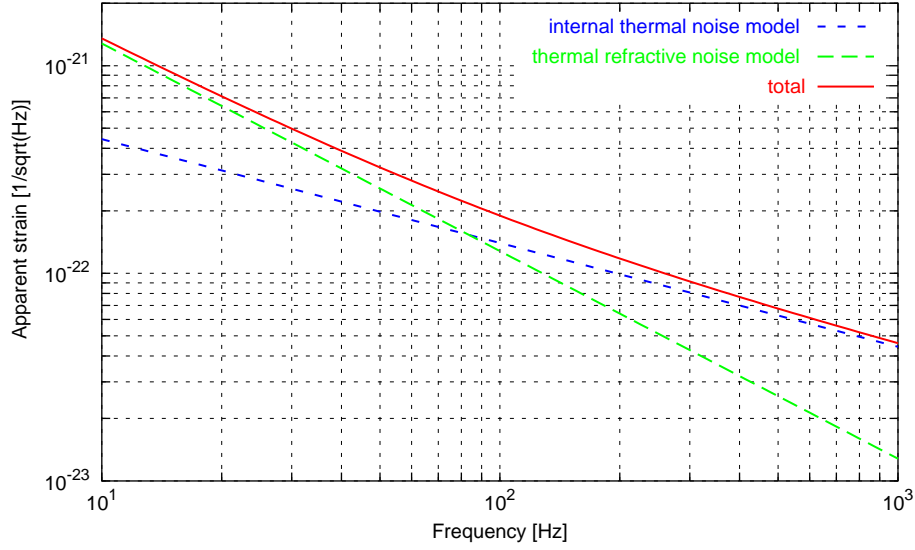


Figure 3.20: A simple mathematical model for the expected thermal-noise-limited sensitivity of GEO 600. The total thermal noise is the sum of the internal thermal noise that results in fluctuations of mirror surfaces and the thermo-refractive thermal noise that yields fluctuations in the index of refraction of the beam splitter.

The thermal noise shown in Figure 1.1 can be approximated by a model consisting of two contributions of different frequency response [Cagnoli]:

$$\tilde{h}_{\text{thermal}}(f) = \sqrt{\left(\frac{1.28 \cdot 10^{-20}}{\sqrt{\text{Hz}}} \left(\frac{f}{1 \text{ Hz}}\right)^{-1}\right)^2 + \left(\frac{1.4 \cdot 10^{-21}}{\sqrt{\text{Hz}}} \left(\frac{f}{1 \text{ Hz}}\right)^{-\frac{1}{2}}\right)^2} \quad (3.20)$$

The apparent strain sensitivity of this noise model is shown in Figure 3.20. A gravitational wave with a strain amplitude equal to $\tilde{h}_{\text{thermal}}$ would be detected with a SNR of unity.

If no signal is present and the thermal noise is the dominant noise source, the output signal of the detector will be given by the thermal noise spectral density multiplied by the transfer function of the interferometer. FINESSE can be used to compute the respective transfer functions; the output signal in Volt is shown in Figure 3.21. The unit Volt refers to a perfect photo detector and mixer: The quantum efficiency and the responsivity are unity, the mixer has a gain of unity, and the amplification in the photo diode electronics is also unity. All following graphs have been computed using the parameters of the GEO 600 detector with Dual Recycling as given in the beginning of Section 3.3.

The calculations are done for two envisaged Dual-Recycling settings: First, the broadband case with the reflectance of the Signal-Recycling mirror of $R_{\text{MSR}} = 0.99$. For matching the shot noise to the thermal noise, the detector is slightly detuned; in these simulations a detuning of 200 Hz is assumed. Second, the narrowband example that uses a Signal-Recycling mirror with $R_{\text{MSR}} = 0.999$ and a detuning of 500 Hz. The simulation uses geometric optics, i. e., higher-order modes of the laser beam are not taken into account.

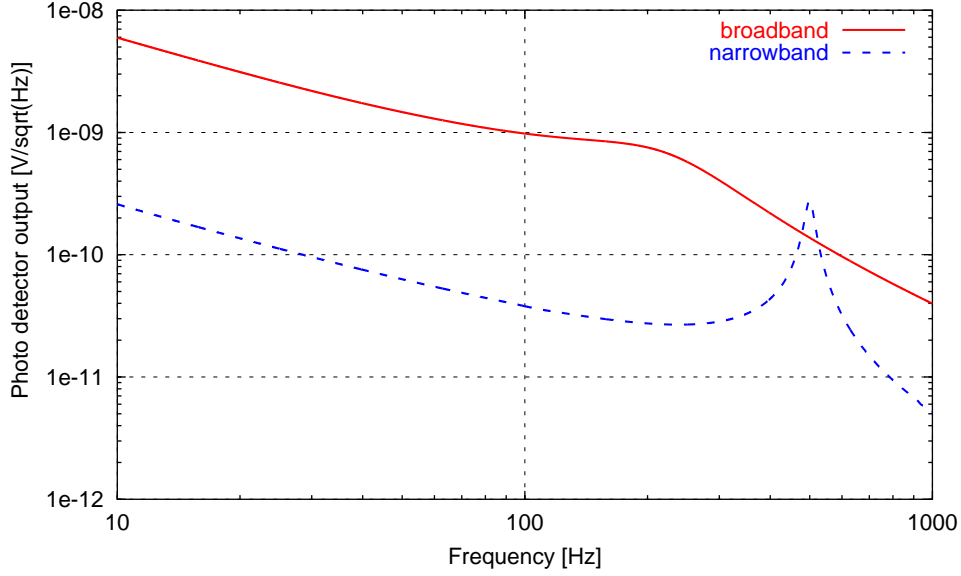


Figure 3.21: Detector output signal that corresponds to the thermal noise spectral density given in Equation 3.20.

The signal in Figure 3.21 represents the spectral density of the voltage at the photo detector output (after demodulation). It can be described as:

$$\tilde{O}_{\text{thermal}} = \tilde{h}_{\text{thermal}} T_{\text{opt,thermal}} T_{\text{det}} \quad (3.21)$$

with $T_{\text{opt,thermal}}$ being the optical transfer function *thermal noise* \rightarrow *interferometer output* and T_{det} the electrical transfer function *light power on photo detector* \rightarrow *mixer output* (here we assume for simplicity $T_{\text{det}} = 1\text{V/W}$). In the following, this output signal is compared to spurious signals generated in the same photo detector by other noise sources: For each noise source a transfer function *noise input* \rightarrow *detector output* is computed:

$$T_{\text{noise}} = T_{\text{opt,noise}} T_{\text{det}} \quad (3.22)$$

with $T_{\text{opt,noise}}$ as the optical transfer function from this noise input to the interferometer output.

Dividing $\tilde{O}_{\text{thermal}}$ by the computed transfer function yields the spectral density of the noise source (at the point where the noise enters the optical system), which corresponds to the equivalent apparent strain sensitivity of the thermal noise:

$$\tilde{x}_{\text{noise}} = \frac{\tilde{O}_{\text{thermal}}}{T_{\text{noise}}} = \tilde{h}_{\text{thermal}} \cdot \frac{T_{\text{opt,thermal}}}{T_{\text{opt,noise}}} \quad (3.23)$$

Consequently, such a spectral density of the respective noise source yields exactly the same output (spectral density) as the thermal noise. In order to compile a comprehensive noise budget, a requirement for the respective noise can be set by applying a safety factor to the computed noise spectral density. Please note that noise requirements are

often computed, and corresponding sensitivity curves plotted, assuming an independently optimised sensitivity for each Fourier frequency. The requirements derived in the following sections, on the other hand, represent two fixed experimental setups and thus refer to measurable spectral densities.

This analysis is limited as it computes only the linear coupling of each noise source into the main output signal. In reality, the noise may couple to the output in several ways. Furthermore, the analysis as described above does not show the dependence of the noise coupling on the parameters of the interferometer. It might be possible that the result strongly depends on a certain parameter, such as an optical path length or the deviation of the Michelson interferometer from the dark fringe. At least, a second analysis in which parameters are changed slightly should be performed in each case as a simple check. If the result changes notably a more detailed analysis is necessary.

This analysis does not take into account the demodulation phase. In some cases, the signal and the noise may appear in different quadratures so that a proper setting of the demodulation phase would reduce the influence of the noise. Detuned Dual Recycling, however, strongly couples the two quadratures so that the above effect is not expected to be significant.

Laser power noise

Power noise of the laser light couples into the output signal in various ways. Figure 3.22 shows the transfer function for amplitude fluctuations applied at the interferometer input (in front of the Power-Recycling mirror) to the interferometer output signal.

Figure 3.23 shows the respective requirement for the relative power noise. Note that the power noise spectral density must be *well below* the plotted graph to be insignificant with respect to the detector sensitivity.

Analyses of other coupling mechanisms of the power noise yield requirements of similar magnitude, see for example [Winkler02].

Laser frequency noise

The frequency fluctuations of the laser light can also create a ‘false signal’ in the main output of the Michelson interferometer. The direct coupling of the frequency noise into the interferometer signal is due to the finite arm-length difference. Figure 3.24 shows the transfer function from frequency noise to interferometer output signal and Figure 3.25 the derived frequency noise requirement.

The frequency-noise coupling in this simulation strongly depends on the arm-length difference and also on the deviation from the dark fringe. In general, any effect that directs carrier light into the south port increases the frequency-noise coupling, see for example Section 2.7.4.

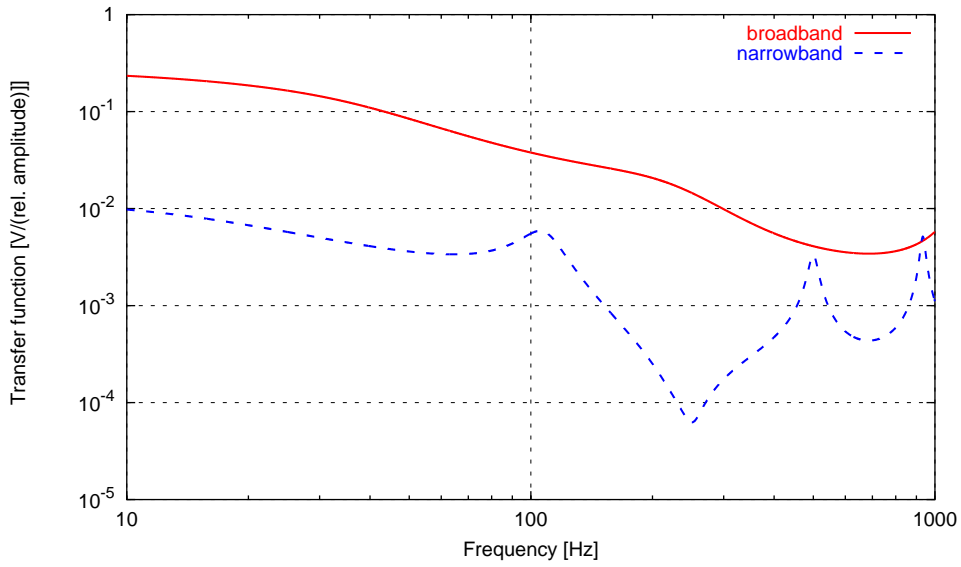


Figure 3.22: Computed transfer function laser amplitude fluctuations \rightarrow interferometer output.

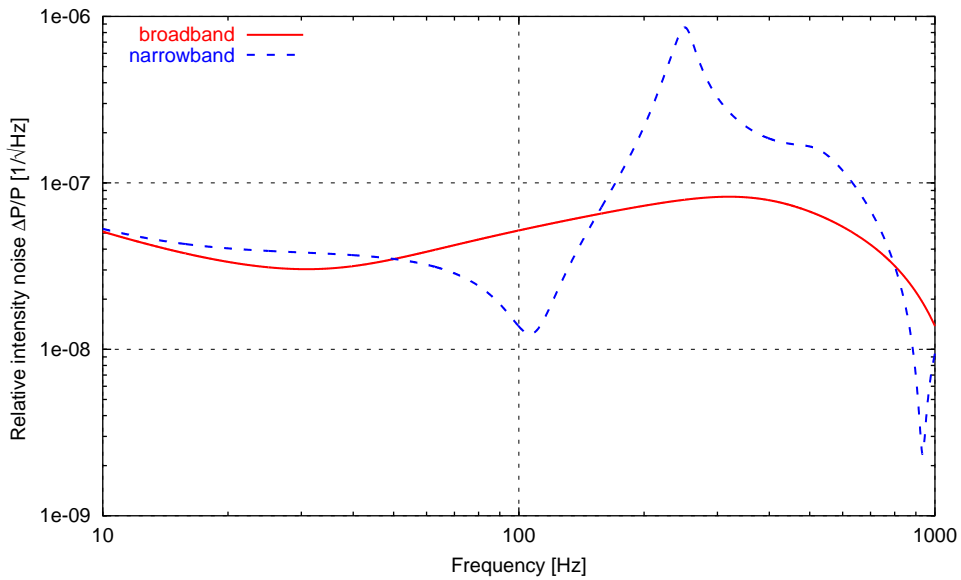


Figure 3.23: Computed relative power-noise requirement of the GEO 600 detector for a broadband and a narrowband mode.

This simulation yields a demanding requirement because of an assumed deviation from the dark fringe of ≈ 10 pm, which represents an experimentally derived parameter for the current Michelson interferometer with Power Recycling (i. e., the residual fluctuations due to the finite gain of the control loop). The dependence of the noise coupling on the deviation from the dark fringe is complicated and non-linear. If, for example, the deviation can be reduced as planned to 1 pm, the frequency-noise requirement is improved (i. e., relaxed) by a factor of ≈ 5 .

A comparison of the computed frequency-noise requirement with the current frequency stability of the GEO 600 laser system (see Figure 2.21) shows that the thermal-noise limit cannot be reached. Therefore, it is important further to improve the frequency stability and to minimise the deviation of the Michelson interferometer from the dark fringe. The control loops of the Power-Recycling cavity and of the Michelson interferometer have not yet been optimised with respect to the coupling of frequency noise. It is expected that a straightforward improvement of both loops allows to reduce the effect of the frequency noise below the thermal-noise limit.

Oscillator phase noise

The control system for the operating point of the Michelson interferometer uses a modulation scheme, i. e., at some point an RF phase modulation is applied to the laser light using an electro-optic modulator. The signal of the output photo diode is then demodulated (in an electronic mixer) by the same RF modulation frequency to generate the control signal.

The oscillator used to generate the RF frequency has, of course, a limited frequency stability. The fluctuations of the RF frequency can also be described as *oscillator phase noise*. A mathematical description of the effects of oscillator phase noise with respect to the phase modulation of a light field is given in Section E.2.8.

Using Equation E.62 we can compute a transfer function T_{ph} *oscillator phase noise* \rightarrow *main output signal* (shown in Figure 3.26) and consequently a requirement for the phase noise (shown in Figure 3.27). Figure 3.28 shows the measured phase noise of the HP 33120A signal generator used to generate the modulation frequencies for the MI and SR loops. The signal generator was set to 13 MHz and locked to a GPS reference during the measurement. It can be seen that the measured noise is considerably larger than the computed requirement.

Similar to the frequency noise, the tolerable oscillator phase noise also strongly depends on the arm-length difference and the deviation from the dark fringe. For the calculations a deviation of 10 pm was assumed. A smaller deviation relaxes the noise requirement; the dependence of the coupling on the deviation is non-linear. With a deviation from the dark fringe of 1 m the phase noise requirement is improved by a factor of ≈ 3 . Changing the arm-length difference changes the phase-noise requirement in a more complicated way. The best setup found yields a requirement that is a factor of ≈ 4 better than the one shown in Figure 3.27. Further investigations are necessary to reduce either the phase noise of the signal generator or the coupling of phase noise into the interferometer output signal.

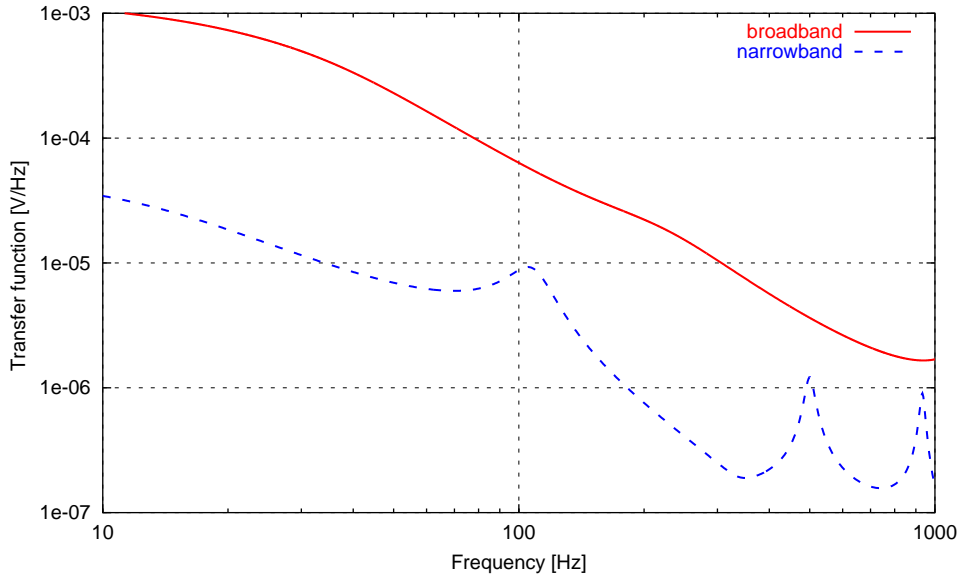


Figure 3.24: Computed transfer function frequency noise \rightarrow interferometer output.

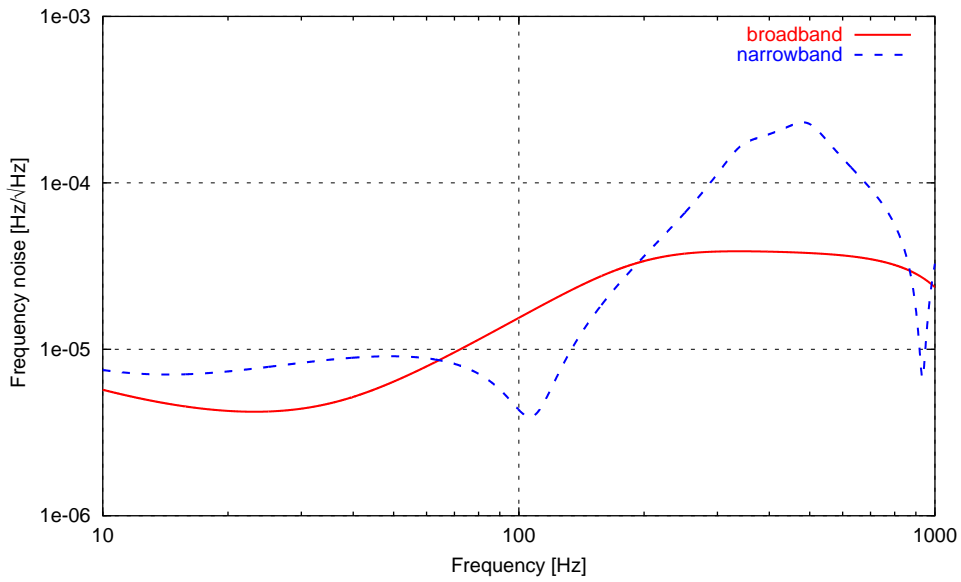


Figure 3.25: Computed frequency-noise requirement of the GEO 600 detector for a broadband and a narrowband mode.

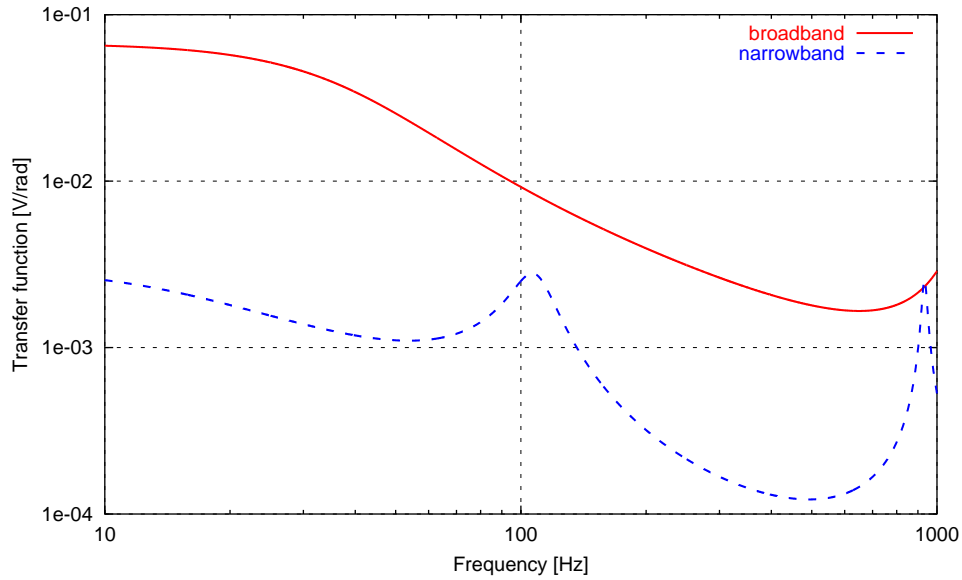


Figure 3.26: Transfer functions for oscillator phase noise \rightarrow main output for a broadband and a detuned case.

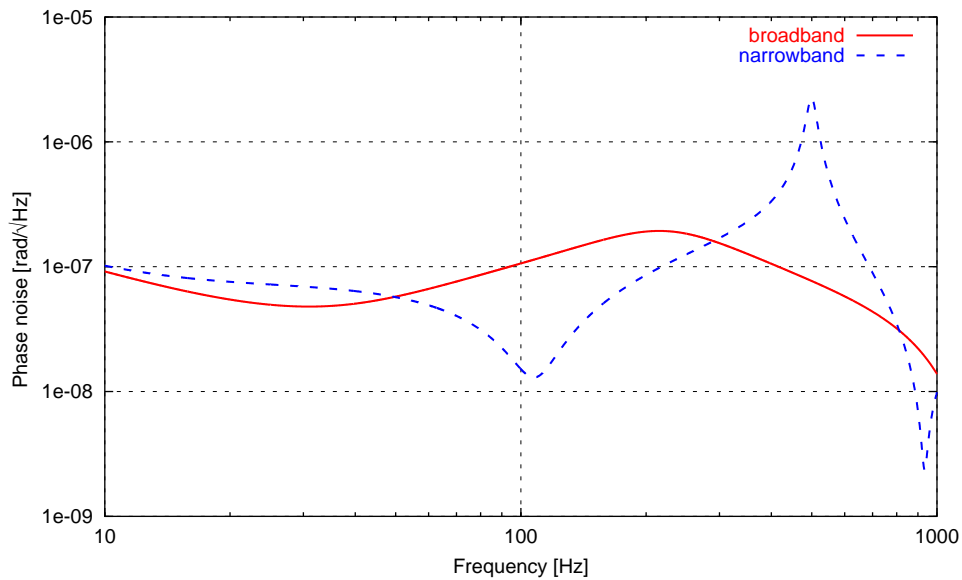


Figure 3.27: Computed requirement for the oscillator phase noise of the GEO 600 detector for a broadband and a narrowband mode.

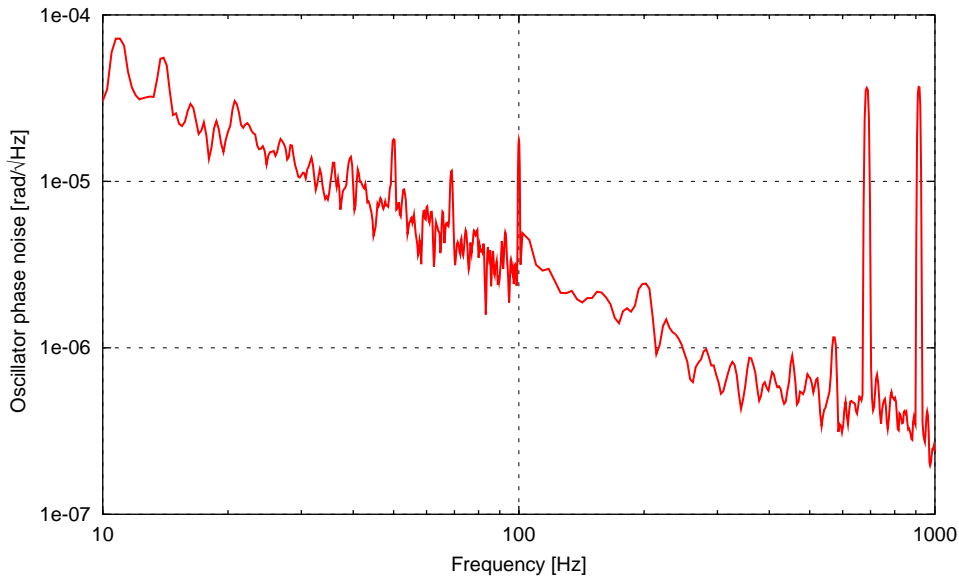


Figure 3.28: Phase noise of a HP 33120A signal generator at a modulation frequency of 13 MHz (locked to GPS reference).

3.4 The Xylophone interferometer

Jun Mizuno has presented a theorem [Mizuno95] claiming, in a simplified form, that the sensitivity of an interferometric gravitational-wave detector, integrated over frequency, only depends on the light energy in the interferometer arms. In other words, new interferometer topologies merely change the distribution of sensitivity with respect to Fourier frequency. This theorem has not yet been proven; nevertheless, the known interferometer topologies all match the theorem.

Provided that the theorem is correct, the best shape of the sensitivity would be a box: a constant sensitivity over the desired bandwidth and no sensitivity outside the bandwidth¹⁴.

Advanced optical techniques such as Signal Recycling change the shot-noise-limited sensitivity. The transfer function of the Michelson interferometer, and thus the sensitivity, is modified in two ways:

- a) The bandwidth is reduced with increasing maximum sensitivity;
- b) The center frequency of the sensitivity is tuned to a user-defined Fourier frequency.

The basic shape of the detector sensitivity, however, cannot be changed; it is defined by the Airy-function of the Signal-Recycling cavity (the resonant power enhancement in a Fabry-Perot cavity as a function of frequency).

¹⁴ If the apparent strain sensitivity of the limiting noise source, for example thermal noise, is not flat, then the optimum shape of the shot-noise-limited sensitivity would be a ‘matched’ box so that the shapes of the spectral densities of both noise sources are identical in the chosen bandwidth.

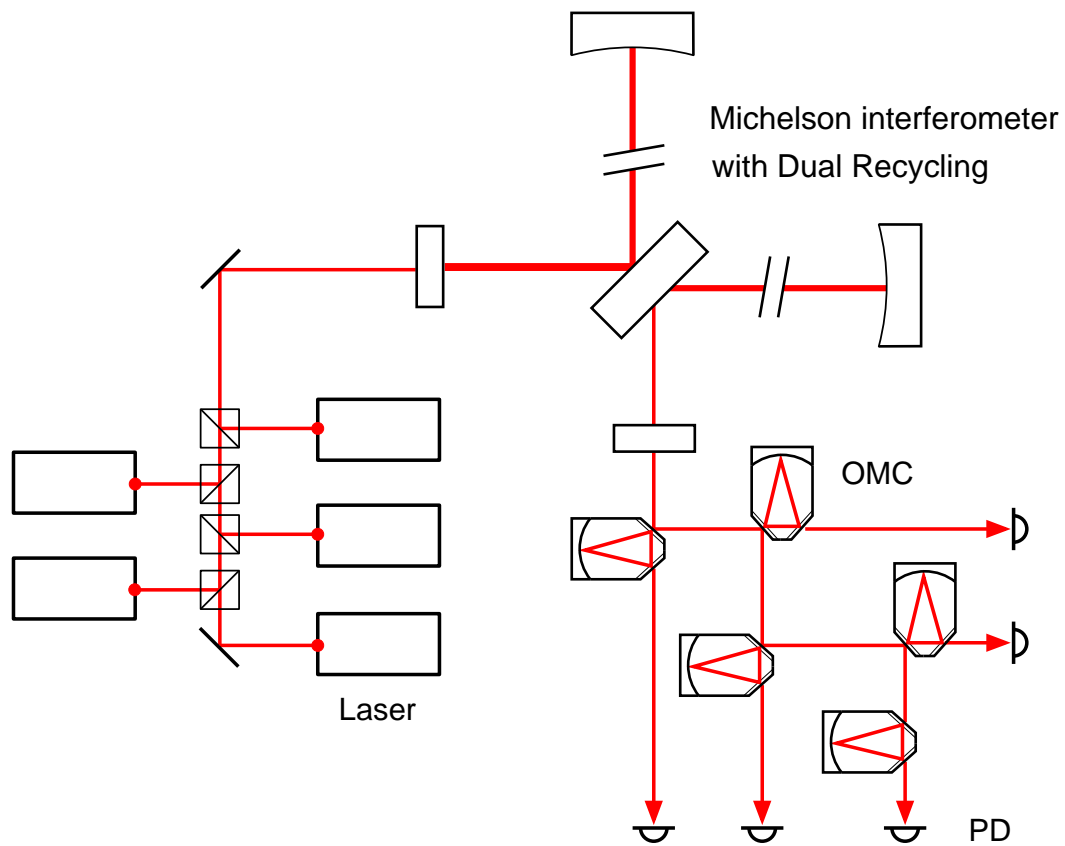


Figure 3.29: Optical layout of a Xylophone interferometer: A Michelson interferometer with Dual Recycling is equipped with five lasers. The lasers are set to different laser frequencies; the five beams are superimposed and injected into the Michelson interferometer. The light in the output port is divided with respect to the five different laser frequencies by five successive output mode cleaners (OMC) before the light is detected by five photo diodes.

The Xylophone interferometer represents an extension to the Dual-Recycled Michelson interferometer that allows to improve the shape of the shot-noise-limited sensitivity. The following sections present an analysis of a Xylophone based on the parameters of the Dual-Recycled GEO 600 detector.

3.4.1 Multiple colours

The basic idea behind the Xylophone interferometer is to operate a detuned, narrowband Dual-Recycled Michelson interferometer with several input lasers simultaneously. The same optical instrument yields a different center frequency of the sensitivity maximum for input beams with a different wavelength. The sensitivity of the detector is then given by the sum of the respective output signals. The overall sensitivities can be formed into

a designed shape by adjusting the maximum and the center frequencies of the sensitivity for each input light.

Figure 3.29 shows the schematic optical layout of a Xylophone interferometer. In this example, five lasers are used; they are set to different frequencies and the beams are superimposed¹⁵. Thus, the beam injected into the Michelson interferometer can be described as a *multi-colour beam*¹⁶.

The detuned Dual-Recycled Michelson interferometer with a single input beam at a fixed frequency can be described as follows:

- The interferometer is set to the dark fringe:

$$\Delta L = \frac{n_1 c}{2f_{\text{Laser}}} \quad (3.24)$$

with n_1 being an integral number, c the speed of light and f_{Laser} the frequency of the input light. A control loop for the differential arm length of the Michelson interferometer adjusts ΔL so that the above identity is maintained.

- The input light is resonant in the Power-Recycling cavity:

$$f_{\text{Laser}} = n_2 \cdot \text{FSR}_{\text{PRC}} \quad (3.25)$$

with n_2 being another integral number and FSR_{PRC} the free spectral range of the Power-Recycling cavity. The frequency stabilisation system controls the laser frequency so that this resonance condition is fulfilled.

- The Signal-Recycling cavity is assumed to be detuned to the signal frequency f_{det} . Thus, the resonance frequency of the Signal-Recycling cavity is given by:

$$f_{\text{Laser}} + f_{\text{det}} = n_3 \cdot \text{FSR}_{\text{SRC}} \quad (3.26)$$

The Signal-Recycling control loop maintains this resonance by adjusting the length of the Signal-Recycling cavity.

Figure 3.30 shows the light power in the south port of a simple Michelson interferometer with an arm-length difference of $\Delta L = 69$ mm as a function of the frequency of the injected light. The frequency is given as an offset to the base frequency for which the Michelson interferometer was set to be at the dark fringe. It can be seen that the dark fringe condition occurs periodically. In order to get from one dark fringe to the next, the frequency must be changed by:

$$\Delta f_{\text{Laser}} = \frac{c}{2\Delta L} \approx 2.176 \text{ GHz} \quad (3.27)$$

At the same time, the light is resonant in the Power-Recycling cavity at every multiple of the free spectral range. Therefore, it is always possible to find a light frequency

¹⁵ The method to superimpose the beams shown in Figure 3.29 is very simple but requires a lot of extra laser power that is then lost through the beam splitters. If the required extra power is not available, a more sophisticated scheme, as for the output optics, has to be used.

¹⁶ In reality, all lasers emit infrared light, and the differences in wavelength are very small (≈ 8 pm).

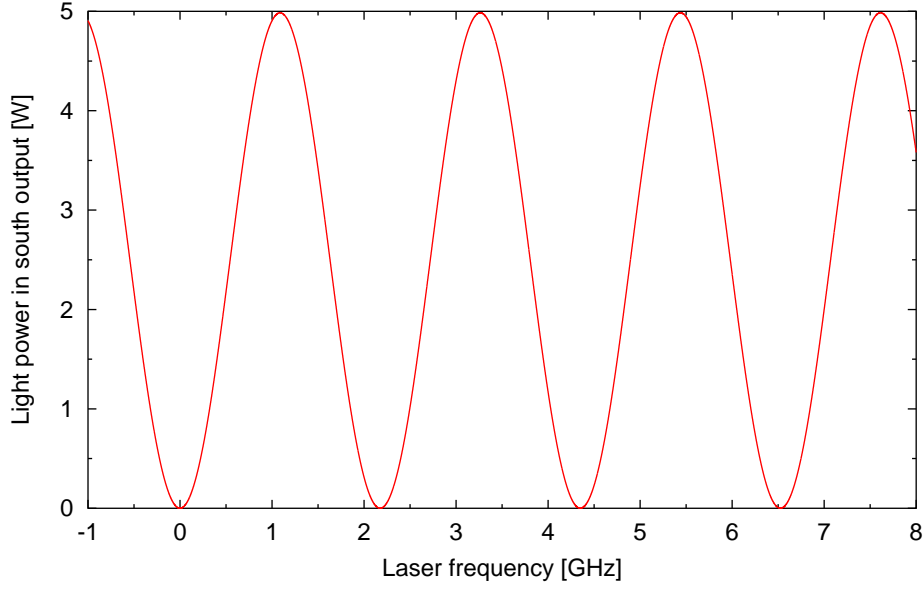


Figure 3.30: Light power in the south port of a simple Michelson interferometer with an arm-length difference of 69 mm as a function of the frequency of the input light. The frequency is given as the offset to a default frequency (≈ 281 THz) for which the interferometer has been adjusted to be at the dark fringe. The dark fringe condition occurs periodically as the frequency of the input light is changed.

(other than $\Delta f_{\text{Laser}} = 0$) at which the light is resonant in the Power-Recycling cavity and less than $0.5 \cdot \text{FSR}_{\text{PRC}} \approx 63$ kHz away from a dark fringe. A deviation of 63 kHz corresponds to a deviation of ≈ 20 pm and yields a strong coupling of frequency noise into the interferometer output signal (see Section 3.3.5). By carefully designing and setting the absolute length of the Power-Recycling cavity, this problem can be avoided.

Let us assume a second input light with the frequency set to be at the next dark fringe and resonant in the Power-Recycling cavity:

$$f'_{\text{Laser}} = f_{\text{Laser}} + n_4 \cdot \text{FSR}_{\text{PRC}} \quad \text{with} \quad n_4 \cdot \text{FSR}_{\text{PRC}} \approx 2.176 \text{ GHz} \quad (3.28)$$

The resonance of the Signal-Recycling cavity closest to the laser light frequency is given as:

$$(n_3 + n_5) \cdot \text{FSR}_{\text{SRC}} \quad (3.29)$$

By writing the detuning frequency of the Signal-Recycling cavity, given by Equation 3.26, as an offset to the new laser frequency we get:

$$\begin{aligned} f'_{\text{det}} &= (n_3 + n_5) \cdot \text{FSR}_{\text{SRC}} - f'_{\text{Laser}} \\ &= (n_3 + n_5) \cdot \text{FSR}_{\text{SRC}} - f_{\text{Laser}} - n_4 \cdot \text{FSR}_{\text{PRC}} \\ &= n_5 \cdot \text{FSR}_{\text{SRC}} - n_4 \cdot \text{FSR}_{\text{PRC}} + f_{\text{det}} \end{aligned} \quad (3.30)$$

Thus, the new detuning frequency is larger than the detuning frequency for the initial setup:

$$\Delta f_{\text{det}} = n_5 \cdot \text{FSR}_{\text{SRC}} - n_4 \cdot \text{FSR}_{\text{PRC}} \quad (3.31)$$

In other words, by using the unchanged Dual-Recycled Michelson interferometer with another light source that is shifted in frequency we can get the *same maximum sensitivity at a different Fourier frequency*.

If yet another input laser is added and its frequency set to be at the second dark fringe we get:

$$f''_{\text{Laser}} = f_{\text{Laser}} + 2n_4 \cdot \text{FSR}_{\text{PRC}} \quad \text{with} \quad 2n_4 \cdot \text{FSR}_{\text{PRC}} \approx 4.352 \text{ GHz} \quad (3.32)$$

and similarly:

$$\begin{aligned} f''_{\text{det}} &= (n_3 + 2n_5) \cdot \text{FSR}_{\text{SRC}} - f''_{\text{Laser}} \\ &= (n_3 + 2n_5) \cdot \text{FSR}_{\text{SRC}} - f_{\text{Laser}} - 2n_4 \cdot \text{FSR}_{\text{PRC}} \\ &= 2n_5 \cdot \text{FSR}_{\text{SRC}} - 2n_4 \cdot \text{FSR}_{\text{PRC}} + f_{\text{det}} \end{aligned} \quad (3.33)$$

and thus:

$$f''_{\text{det}} = 2\Delta f_{\text{det}} + f_{\text{det}} \quad (3.34)$$

Thus, the second laser, which is tuned to be on the second dark fringe, provides a sensitivity for which the center frequency of the maximum is shifted exactly twice as much as for the laser that is tuned to the first dark fringe.

In summary, if the input lights are set to be at the n -th dark fringe, the maximum of the sensitivity is shifted by $n \Delta f_{\text{det}}$. By using several input fields and adding the respective output signals, one can generate a comb-like detector sensitivity, provided that the bandwidth of the Dual-Recycled Michelson interferometer itself is small.

3.4.2 Sensitivity

Figure 3.31 shows such sensitivity for a Xylophone with five input lasers compared to an equivalent Dual-Recycled Michelson interferometer. Both examples are designed to have the same bandwidth of ≈ 200 Hz. A useful comparison between different interferometer types has to use the same total light power inside the interferometer [Mizuno95]. Here, a total power of 25 W was arbitrarily chosen. The Xylophone offers a more box-like sensitivity and increases the sensitivity in the detector bandwidth by a factor of ≈ 2 .

In this example, the five lasers were used with equal power. Different shapes can be modelled by using different output powers for the lasers. Figure 3.32 shows another example of a Xylophone interferometer sensitivity. In this case, the powers of the input lasers were scaled so that the sensitivity shows a slope (within the detector bandwidth). Such a shot-noise-limited sensitivity could be desirable for matching the shot noise to the spectral density of another noise source.

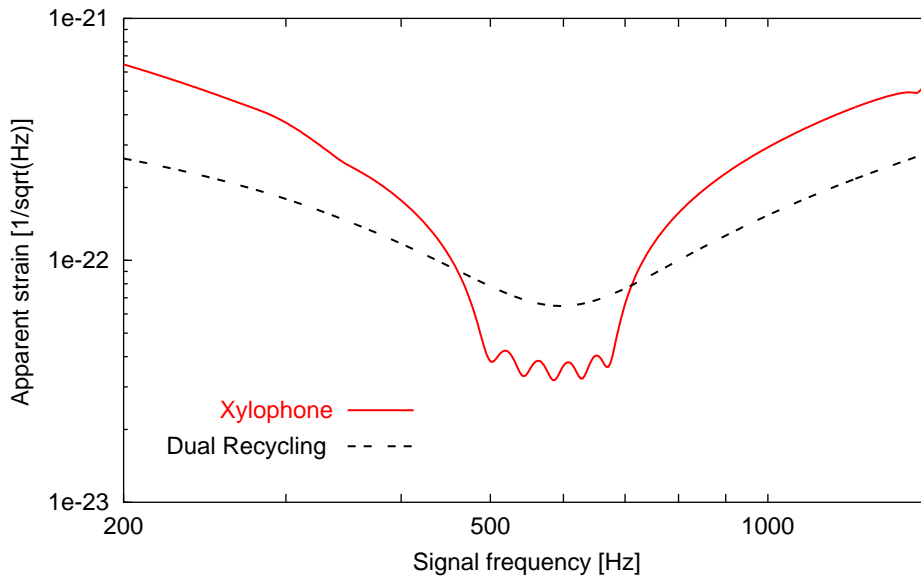


Figure 3.31: Shot-noise-limited sensitivity of a Xylophone interferometer compared to an equivalent Dual-Recycled interferometer. The bandwidths of both setups are approximately 200 Hz, and the total input light power is 25 W.

In principle, the sensitivity can be modelled into an arbitrary shape by using more lasers and a very small bandwidth of the Dual-Recycled Michelson interferometer. The losses inside the interferometer, however, create a lower limit for the bandwidth of Dual Recycling. In addition, the extra lasers and output mode cleaners require new control systems and are bound to add ‘technical’ noise to the system.

3.4.3 Additional control requirements

The basic control scheme used in the Dual-Recycled Michelson interferometer can also be used to control a Xylophone. However, some extra control loops are required. When a multi-colour beam is used, the control of the Dual-Recycled Michelson interferometer must be extended: because several light fields with different wavelengths are to be resonant in the cavities, the absolute lengths of the Power-Recycling cavity and the Signal-Recycling cavity must be set accurately. This requires extra sensors that create error signals with respect to the absolute lengths, and actuators with a large dynamic range.

In addition, the lasers have to be stabilised in frequency against each other, i. e., they must be phase-locked. These stabilisations must be included in the frequency stabilisation scheme and provide similar performance. Finally, the output mode cleaners must be held on resonance for the respective light field. The output optics in form of the output mode cleaners and photo diodes provide a challenge as they are bound to create more stray light.

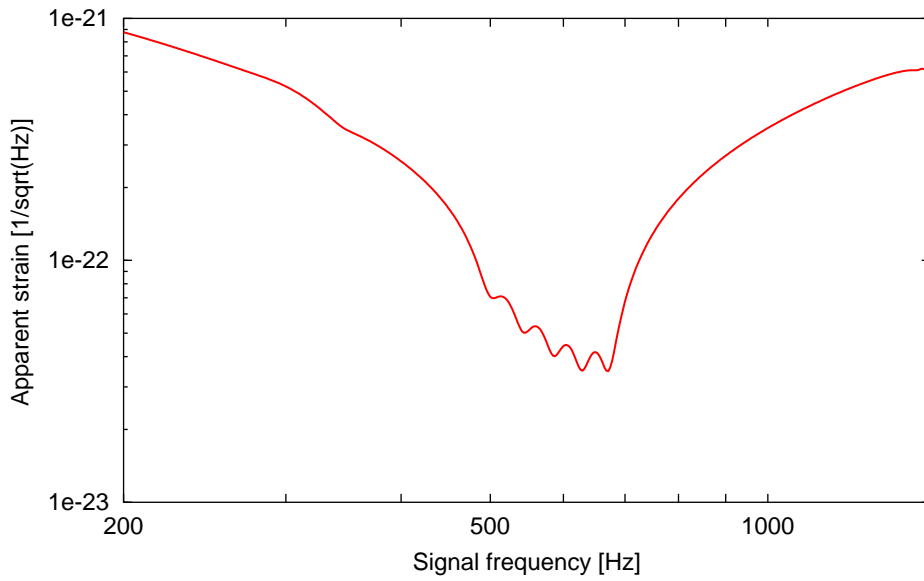


Figure 3.32: Example of a shot-noise-limited sensitivity designed to match another noise distribution (which, in this example, would be decreasing with frequency).

These additional requirements make the Xylophone a technically challenging project, but the extensions can probably be performed using techniques similar to those in Dual-Recycled systems, which will be well understood as soon as Dual Recycling has been installed and analysed in the GEO 600 detector. If the ‘technical’ noise sources, like stray light and laser frequency noise, can be suppressed, the Xylophone presents a simple and straightforward method for creating matched shapes for the detector sensitivity that provide the maximally possible shot-noise-limited sensitivity with respect to the chosen detector bandwidth and the total laser power.

Appendix A

The optical layout of GEO 600

The optical layout of GEO 600 is described in detail in Chapter 1. This appendix presents a CAD drawing of the detector. In addition, an input file for FINESSE with the optical components of GEO 600 is provided.

A.1 OptoCad drawing of GEO 600

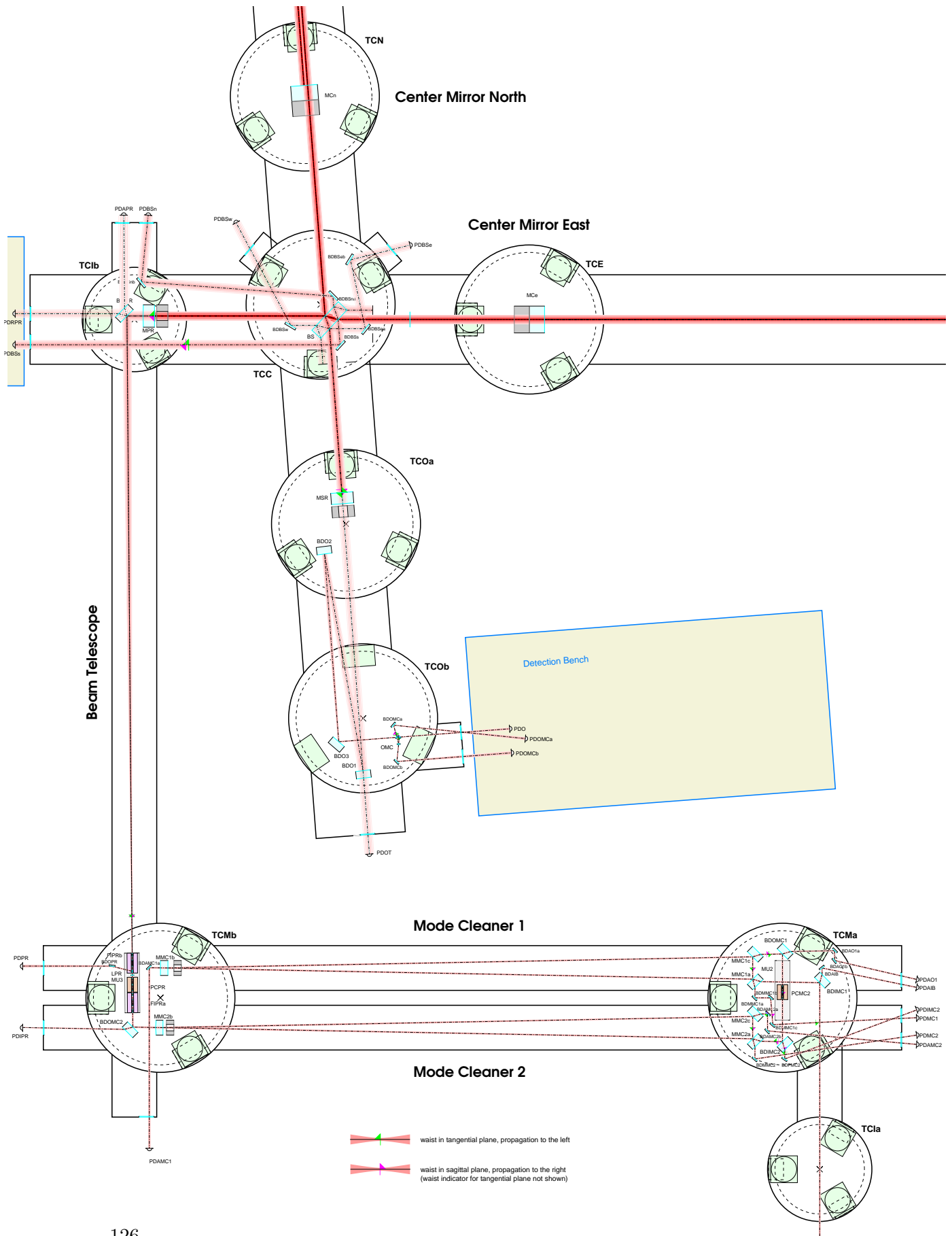
OPTOCAD is a computer program for tracing Gaussian beams through optical systems. It was written by Roland Schilling [[OPTOCAD](#)], who also maintains an input file for OPTOCAD containing the up-to-date parameters of the optical setup of GEO 600. This input file is used to plot the famous optical layout of GEO 600 (see next page for a section of that plot).

OPTOCAD automatically traces the laser beam through all given components and computes the parameters of the optical system (beam sizes, eigen-modes, mode-matching factors, etc.); optionally, it plots the beams and the optical components to a PostScript file. In addition, auxiliary components like vacuum tanks or labels can be added to the drawing.

The optical layout of GEO 600, as depicted on the next page, shows a to-scale schematic drawing of the optical systems. In the section shown here, the laser bench and the vacuum tanks with the folding mirrors (located 600 m away) have been omitted. The laser beam enters the vacuum system in the lower left corner of the drawing (at vacuum tank TC1a).

The existing systems are presented using measured data; not yet installed subsystems are shown using their designed parameters.

The OPTOCAD input file for GEO 600 is now also used as reference for parameters of the detector including mirror positions, beam sizes, cavity lengths or radii of curvature.



A.2 FINESSE input file with GEO 600 parameters

In collaboration with Roland Schilling, I created a similar input file for FINESSE (see Section E). This file is listed on the following pages; it contains the optical components of the input mode-cleaner section, the Dual-Recycled Michelson interferometer and the output mode cleaner. It can be used for various simulations of optical subsystems or the full GEO 600 detector.

```

#-----
# geo600_04.kat
#
# Input File for FINESSE (www.rzg.mpg.de/~adf)
# 25.08.2002 by Andreas Freise (freise@aei.mpg.de)
#-----
## Laser bench ##

# Laser
# (distances on laser bench up to MMC1a are only approximately)
l i1 14 0 nLaser
gauss beam_in i1 nLaser 1m -5.4
# beam size that fits into MC1, we assume "i1" includes the laser and
# mode matching lense as well as all the other components from the
# laser bench, except the modulator and the last table mounted mirror.

s s0 1 nLaser nEOM1in

## MU 1, modulation for PDH for locking laser to MC1
mod eom1 25M 0.1 1 pm 0 nEOM1in nEOM1out ## MC1 PDH locking frequency

s s1 1 nEOM1out nZ1
bs mZ 1 0 0 0 nZ1 nZ2 dump dump # the last table mounted mirror
s s2 2.86 nZ2 nBDIMC1a

##-----
## mode cleaners ##
#
# The mode cleaners are not adapted to fit the measured
# visibility, throughput or finesse. The specified values
# for the reflectivity and transmission of the mirrors were
# used instead.

## MC1
bs* BDIMC1 50 30 0 45 nBDIMC1a nBDIMC1b dump dump
s mc1_sin 0.45 nBDIMC1b nMC1in
bs* MMC1a 1778 56 0 44.45 nMC1in nMC1refl nMC1_0 nMC1_5
s mc1_s0 0.15 nMC1_0 nMC1_1
bs* MMC1b 35 68 0.0003 2.2 nMC1_3 nMC1_4 dump dump #3*10^-10m away from res.
attr MMC1b Rc 6.72
s mc1_s1 3.926 nMC1_4 nMC1_5
bs* MMC1c 1606 68 0 44.45 nMC1_1 nMC1_2 nMC1out dump

```

Appendix A The optical layout of GEO 600

```
s    mc1_s2 3.926 nMC1_2 nMC1_3

s    smcmc1 0.5 nMC1out nMU2in
## MU 2
mod  eom2 13M .1 1 pm 0 nMU2in nMU2_1      # MC2 PDH locking frequency
mod  eom3 37.16M .1 1 pm 0 nMU2_1 nMU2_2    # PR PDH locking frquency
isol  d1 0 nMU2_2 nMU2out                  # Faraday Isolator
s    smcmc2 0.5 nMU2out nMC2in

## MC2
bs*  MMC2a 1532 67 0 44.45 nMC2in nMC2refl nMC2_0 nMC2_5
s    mc2_s 0.15 nMC2_0 nMC2_1
# inner surface of MMC2b:
bs*  MMC2bi 1360 58 0 2.2 nMC2_3 nMC2_4 nMC2bi dump
attr MMC2bi Rc 6.72
s    mc2_s1 3.9588 nMC2_4 nMC2_5
bs*  MMC2c 114 62 0.0003 44.45 nMC2_1 nMC2_2 dump dump #3*10^-10m away from resonance
s    mc2_s2 3.9588 nMC2_2 nMC2_3

s    sMMC2b 0.05 1.44963 nMC2bi nMC2bo
# second surface of MMC2b:
m    MMC2bo 0 1 0 nMC2bo nMC2out
attr MMC2bo Rc 0.35

s    smcpr1 0.135 nMC2out nBDMC2a
bs*  BDMC2 50 30 0 45 nBDMC2a nBDMC2b dump dump

# Note:
# The length of 'smcpr2' and 'smcpr3' represent not the geometrical
# distance but the length of the space with respect to mode propagation.
# The values include the effects of the Faraday crystals and the
# modulator crystals which are not explicitly given here.

s    smcpr2 0.2825 nBDMC2b nMU3in

##-----
## MU 3
mod  eom4 9.018137M .3 2 pm 0 nMU3in nMU3_1    # Schnupp1 (SR control)
mod  eom5 14.904050M .5 2 pm 0 nMU3_1 nMU3_2    # Schnupp2 (MI control)
lens  lpr 1.8 nMU3_2 nMU3_3
# some rather arbitrary thermal lense for the isolators and the EOMs:
lens  therm 5.2 nMU3_3 nMU3_4
isol  d2 120 nMU3_4 nMU3out                  # Faraday Isolator

s    smcpr3 4.391 nMU3out nBDIPR1
bs*  BDIPR 50 30 0 45 nBDIPR1 nBDIPR2 dump dump
s    smcpr4 0.11 nBDIPR2 nMPRo

##-----
## main interferometer ##
##
## Mirror specifications for the _final_ optics are used.
##

# first (curved) surface of MPR
```

A.2 FINESSE input file with GEO 600 parameters

```

m   mPRo 0 1 0 nMPRo nMPRi
#attr mPRo Rc -1.867      # Rc as specified
attr mPRo Rc -1.85842517051051 # Rc as used in OptoCad (layout_1.41.ocd)
s   smpr 0.075 1.44963 nMPRi nPRo
# second (inner) surface of MPR
m*  MPR 1000 38 0. nPRo nPRi      # 1000ppm power recycling
#m  MPR 0 1 0. nPRo nPRi          # no power recycling

s   swest 1.145 nPRi nBSwest

## BS
##
##
##
##          nBSnorth      ,'-
##          |      +      '
##          |      ,      ':'
##          |      +i1      +
##  -----> ,:.- i2 ,'
##          + \ '-. +      nBSeast
##          , i3 \ , -----
##          +      \ +
##          , i4 .'
##          '-.      ..
##          '-. , |nBSsouth
##          -      |
##          |
##          |

bs  BS 0.4859975 0.5139975 0.0 42.834 nBSwest nBSnorth nBSi1 nBSi3
s   sBS1a 0.041 1.44963 nBSi1 nBSi1a
# here thermal lens of beam splitter (Roland Schilling: f about 1000m for 10kW at BS)
lens bst 1k nBSi1a nBSi1b
s   sBS1b 0.050 1.44963 nBSi1b nBSi2
s   sBS2 0.091 1.44963 nBSi3 nBSi4
bs  BS2 40u 0.99995 0 -27.9694 nBSi2 dump nBSeast dump      # 40ppm AR coating
bs  BS3 40u 0.99995 0 -27.9694 nBSi4 dump nBSsouth dump      # 40ppm AR coating

## north arm
s snorth1 598.5682 nBSnorth nMFN1
bs* MFN 50 10 0.0 0.0 nMFN1 nMFN2 dump dump
attr MFN Rc 640
s snorth2 597.0108 nMFN2 nMCN1
m* MCN 50 10 0.0 nMCN1 dump
attr MCN Rc 600

## east arm
s seast1 598.4497 nBSeast nMFE1
bs* MFE 50 10 0.0 0.0 nMFE1 nMFE2 dump dump
attr MFE Rc 640
s seast2 597.0663 nMFE2 nMCE1
m* MCE 50 10 0.0 nMCE1 dump
attr MCE Rc 600

## south arm

```

Appendix A The optical layout of GEO 600

```
s ssouth 1.103 nBSSouth nMSRi    # gives L_SRC-L_PRC= 0.09 m

m MSR 0.99 0.01 0.0 nMSRi nMSRo  # tuned recycling

##-----
## output optics

s sot1 1.990  nMSRo nOT1

bs BDO1 0.99 .01 0 2.869 nOT1 nOT2 nOTout dump
attr BDO1 Rc 6.3
s sot2 1.476  nOT2 nOT3
bs BDO2 1 0 0 2.8687 nOT3 nOT4 dump dump
s sot2 1.263  nOT4 nOT5
bs BDO3 1 0 0 45 nOT5 nOT6 dump dump
s sot3 0.393 nOT6 nMC3in

# output mode cleaner (OMC)
bs MMC3a .9 .1 0 50.8 nMC3in nMC3refl nMC3_1 nMC3_2
s mc3_s1 0.015 nMC3_1 nMC3_3
bs MMC3b .9 .1 0 -50.8 nMC3_3 nMC3_4 nMC3out dump
s mc3_s2 0.042555 nMC3_4 nMC3_5
bs MMC3c .999 .001 0 0 nMC3_5 nMC3_6 dump dump
attr MMC3c Rc 0.085
s mc3_s3 0.042555 nMC3_6 nMC3_2

##-----
## commands
maxtem 2
time
trace 6
phase 3
# MC1 cavity
cav mc1 MMC1a nMC1_0 MMC1a nMC1_5
# MC2 cavity
cav mc2 MMC2a nMC2_0 MMC2a nMC2_5
# PR cavity (north arm)
cav prc1 MPR nPRi MCN nMCN1
# PR cavity (east arm)
#cav prc2 MPR nPRi MCE nMCE1
# SR cavity (north arm)
cav src1 MSR nMSRi MCN nMCN1
# SR cavity (east arm)
#cav src1 MSR nMSRi MCE nMCE1
cav omc MMC3a nMC3_1 MMC3a nMC3_2

##-----
## Outputs
beam b1 nMSRo
xaxis b1 x lin -3 3 40
yaxis lin abs
```

Appendix B

Control loops

Control systems or control loops can be used for many different applications. Numerous types of control loops are known and described extensively in the literature, such as linear versus nonlinear, analog versus digital or even fuzzy control systems. This section describes some basic properties of a special kind of control loop, the analogue and linear system with negative feedback. The purpose of such a system is to keep a physical parameter as close as possible to a predefined value, which is often constant, in the presence of fluctuations of various origins that must be suppressed. In order to do so, this parameter is monitored continuously. When the parameter deviates from its pre-set value (the so-called *operating point*), a signal proportional to the deviation, the *error signal*, is generated and fed back via suitable filters to the system (with the opposite sign) to compensate for the deviation.

A feedback loop consists of the following subsystems:

- **Plant:** The physical system to be controlled by the feedback loop. Usually, the purpose of the feedback loop is to control only one parameter of the plant, which in itself might be a complex system.
- **Sensor:** A detector for the parameter to be controlled. It measures the deviation of the parameter from the operating point. The output of the sensor is called *error signal* (and the point where it is measured *error point*).
- **Servo:** In general, any kind of system that transforms the signal from the sensor into a feedback signal that can be fed back to the actuator. Its output is called *feedback signal*.
- **Actuator:** Attached to the plant or part of it. It is used to change the controlled parameter under command of the servo output.

The feedback loops discussed here concern optical systems. The plant is usually the laser or an interferometer. The sensor transforms an optical signal, such as a laser amplitude or the deviation between a laser frequency and a cavity resonance frequency, into an electrical signal. The loop filter is an analogue electronic circuit designed to generate the appropriate feedback signal. The output of the filter is connected to the actuator that changes a certain property of the optical system.

It often makes sense to consider the sensor and actuator as part of the plant because the signals between actuator and sensor are not electronic and, in most cases, very hard to measure independently. In the following, some simplified diagrams of feedback loops consist only of plant and filter. In these cases, sensor and actuator are understood as subsystems of the plant.

B.1 Open-loop gain

Any linear system can be characterised by its transfer function. Because of the linearity, it is sufficient to consider sinusoidal signals at a fixed frequency f . In control theory, three variables are used for the frequency, and it is important to keep them apart:

- the frequency f measured in Hz
- the angular frequency $\omega = 2\pi f$ measured in rad/sec
- the Laplace-variable $s = i\omega$

For a sinusoidal signal, input and output of the system can be written as:

$$\begin{aligned} In(t) &= \text{Re} \{A_0 \exp(i\omega t)\} \\ Out(t) &= \text{Re} \{A_1 \exp(i\omega t)\} \end{aligned} \quad \begin{array}{c} \text{In} \\ \longrightarrow \\ \boxed{\begin{array}{c} \text{System} \\ G \end{array}} \\ \longrightarrow \\ \text{Out} \end{array} \quad (\text{B.1})$$

The transfer function is the complex ratio (i.e., having both amplitude and phase information) between the output and the input signal as a function of signal frequency:

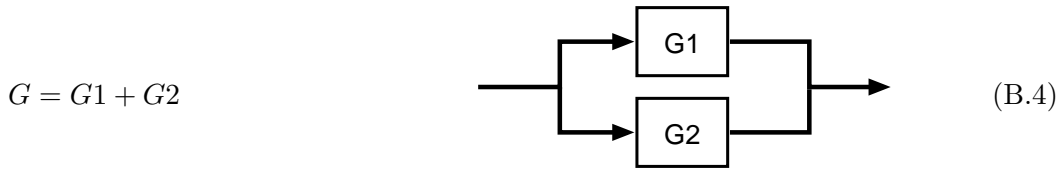
$$G(\omega) = \frac{Out(f)}{In(f)} \quad (\text{B.2})$$

In the following, this ratio is also called *open-loop gain*. In general, the functions In and Out can describe different physical parameters. For example, G may have the units of Volts per meter or Amperes per Volt.

Usually, a filter consists of several subsystems that can be considered separately. Sequential open-loop gains can be (complex) multiplied to get the overall open-loop gain:

$$G = G1 \times G2 \quad \begin{array}{c} \longrightarrow \\ \boxed{G1} \\ \longrightarrow \\ \boxed{G2} \\ \longrightarrow \end{array} \quad (\text{B.3})$$

In the case of split feedback paths, or if the loop has a split sensor, there are parallel subsystems. Then, the overall gain is the (complex) sum of the open-loop gains of the subsystems:

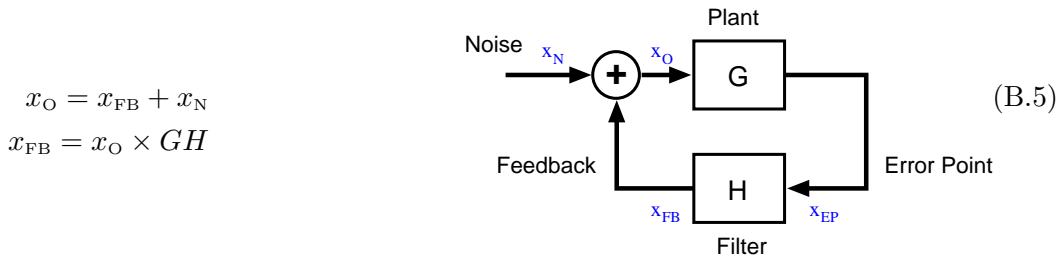


B.2 Closing the loop

A control loop is closed when all subsystems are connected sequentially in a circle and thus form a loop: The sensor is connected to the plant, its signal connected to the filter, and the filter generates the feedback signal that is connected to the actuator, which, in turn, changes the previously measured property of the plant.

To analyse the basic features of a closed loop, we assume that the loop is stable and working. How to build a stable loop and how to close it properly is discussed below (B.3).

The simplest closed feedback loop has two subsystems: the plant (G) and the filter (H). The open-loop gain of such a system is $G \cdot H$ (as a complex function of frequency). For analysing the properties of a closed loop, one has to inject a test signal (such as noise). The disturbances of the plant can be modelled best by adding the signal directly in front of the plant. The signals at every point in the loop can be computed by solving the following set of equations:



This yields:

$$x_O = \frac{1}{1 - GH} x_N, \quad x_{FB} = \frac{GH}{1 - GH} x_N \tag{B.6}$$

If the open-loop gain is larger than one ($|GH| \gg 1$), the injected noise is suppressed in x_O .

This can be understood by looking at a simple example. The parameter that should be controlled by the loop is x_O . It represents a physical parameter of the plant that can be changed by an actuator. Noise from outside the system will change the parameter x_O ; this effect is represented by the virtual adder in the figure above. In this example, the noise is simply a constant offset of $x_N = 1$. Let us assume that the gains of the plant and of the filter are 10 at DC ($G = 10, H = -10$).

Thus, the following signals exist inside the loop: When the loop is not closed, i. e., the feedback signal is not connected, we get:

- The offset at the plant is equal to the noise offset: $x_O = x_N = 1$.
- The error point is $x_{EP} = 10 x_O = 10$ and the feedback signal is $x_{FB} = -10 x_{EP} = -100$.

If the loop is closed and in stable operation, the signals inside the loop are as follows:

- Equation B.6 gives the output of the virtual adder as:

$$x_O = \frac{x_N}{1 - GH} = \frac{1}{1 + 10 \cdot 10} = \frac{1}{101} \quad (\text{B.7})$$

- This results in an error point signal of $x_{EP} = G x_O = 10/101$.
- The loop filter generates a feedback signal of $x_{FB} = H x_{EP} = -100/101$.
- Finally, checking that the signals at the virtual adder are correct:

$$x_O = x_{FB} + x_N = 1 - 100/101 = 1/101 \quad (\text{B.8})$$

This shows that the offset of x_O (as a result of the injected ‘noise’ offset x_N) is reduced approximately by the factor $|GH|$ when the loop is closed.

The term $1/(1 - GH)$ or in general $1/(1 - G_{\text{open-loop}})$ is also called *closed-loop gain*. Obviously, there is no fundamental limit for the suppression of noise that is added to the loop at that point. However, the noise is minimised only at the output of the (virtual) adder. In other words, although the noise is suppressed behind the noisy element, it is present with the full amplitude (and opposite sign) in front of the noisy element. For example, in the loop shown above, the feedback signal contains the noise (with opposite sign) in order to cancel the injected noise.

B.3 Stable loops

A feedback loop can be in one of three typical states:

- **Stable operation:** The plant is held at or close to the operating point, and any disturbance is suppressed by the open-loop gain. This state is often called *locked*: the system is *in lock* or *locked*.
- **Oscillation:** If the open-loop gain has not been designed properly (see below), the system may oscillate at a fixed frequency.
- **Free running (or not locked):** When the loop is not closed, the plant is described as *free* or *free running*. If the loop gain is too low, then the plant may also appear to be free even with the loop closed. This condition is defined as being *not locked*.

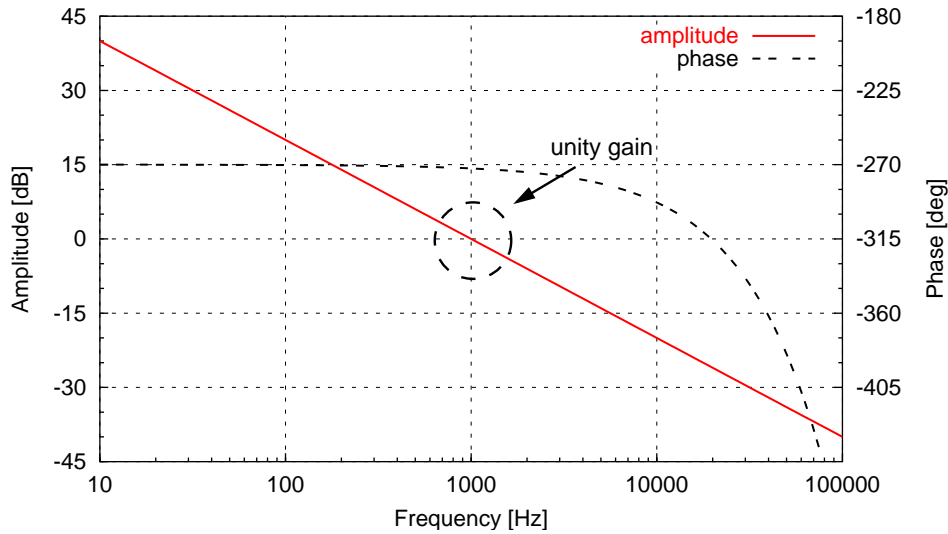


Figure B.1: Example open-loop gain of an unconditionally stable loop.

An extensive theoretical analysis of control loops and their design can be found in the literature. This section describes a simple approach sufficient for the type of control loops used in the described experiments. For a control loop to be stable, its open-loop gain has to fulfil the following criterion:

Whenever the amplitude of the open-loop gain is close to unity (unity gain), the respective phase must be larger than -360° (counting the phase at DC as -180°).

Otherwise, the denominator in Equation B.6 will approach zero and the loop becomes unstable.

The open-loop gain is a complex function of frequency. The frequencies at which the magnitudes of the open-loop gain are equal to one are called *unity-gain frequencies* or *unity-gain points*. Most loops have only one unity-gain point; in the case of multiple unity-gain points, the criterion above has to be matched for each of those.

An example of an open-loop gain of a simple control loop is shown in Figure B.1. It resembles an integrator with a time delay. At low frequencies, the phase is always larger than -360° so that the loop is stable. At high frequencies, the time delay yields a phase below -360° so that the maximum possible unity-gain frequency is less than 40 kHz. The loop remains stable when the overall gain is decreased; this kind of loop is called *unconditionally stable*.

Another typical example of an open-loop gain is shown in Figure B.2. Here, the phase drops below -360° at approx. 500 Hz and 40 kHz. If the overall gain is decreased, the unity-gain point moves down in frequency, and when it reaches 500 Hz the loop becomes unstable. This kind of loop is called *conditionally stable*.

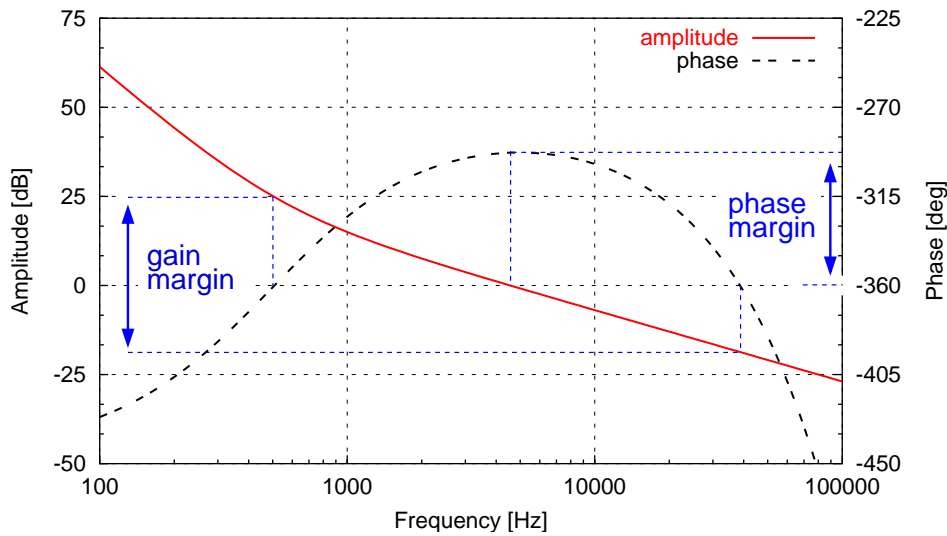


Figure B.2: Example of an open-loop gain of a conditionally stable loop. The difference between the phase at the unity-gain point and -360° is called phase margin. The difference between the maximum and minimum gain is called gain margin.

The difference between the minimum and the maximum possible overall gain is called *gain margin*. This number is an indicator of how sensitive the loop stability is with respect to changes in the overall gain. A small gain margin will probably cause the loop to become unstable after a while because of inevitable slow changes in the subsystems (for example, due to temperature changes).

The difference between the phase at the unity-gain point and -360° is called *phase margin*. It is sensible to design a control loop with a phase margin larger than 35° . All real components used to build the loop show low-pass effects or phase delays. Even in a careful design, some of these effects might have been neglected so that in reality the overall phase turns out to be more negative. A large phase margin at the design state allows for some ‘forgotten’ phase effects.

More complicated control loops may have an open-loop gain with several unity-gain points. Then, the criterion mentioned above must apply to every unity-gain point.

B.3.1 Performance limits

A loop can be used in stable operation if the open-loop gain is designed correctly. Still, there are a number of possible reasons for failure.

Low gain

Any deviation from the operating point is suppressed at best with the open-loop gain. If the open-loop gain is small or the noise too large, the control loop does not keep the plant at the operating point. This is, in principle, no failure of the loop as such but of the control system design.

Limited signal range

A stable loop can fail because of a special property of the plant. One can distinguish between at least two kinds of plants with the following properties:

- a) The sensor signal is always proportional to the deviation from the operating point;
- b) The sensor signal is only proportional to the deviation if the deviation is small compared to the full possible deviation.

Optical systems are mostly of the second type. These systems have the disadvantage that the control loop can only be stable when the deviation from the operating point is small. If the disturbance becomes too large, even the residual deviation can exceed the allowed range; typically, the signal becomes non-linear and the loop fails.

Sensor noise

The noise of the sensor limits the performance of the loop with respect to noise suppression. Here, the expression ‘sensor’ has to be understood in general terms as the method for extracting a signal. In some cases, the sensor as such cannot directly detect the physical property to be stabilised by the control loop. If this is the case, it is usually measured indirectly through another parameter. For example, in an optical system the sensor is commonly a photo detector. If we want to measure the phase of a light field, we have to build an interferometer that converts a phase change into a change in amplitude. Thus, the sensor is not only the photo detector itself but the interferometer plus the photo diode.

For the gravitational-wave detector GEO 600, the sensor noise is the sum of all noise signals that change the light power in the output of the Michelson interferometer. This noise cannot be removed by the loop controlling the arm length difference of the Michelson interferometer. Sensor noise, however, can often be reduced by other means, including a careful design of the system and an active suppression with independent control loops.

B.4 Closed-loop transfer function

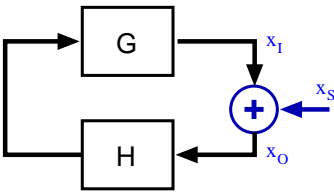
The design of a loop filter is difficult if the gain of the plant is not known. In many cases, it is possible to measure the transfer functions of some subsystems (sensor, actuator), but

not the gain of the complete plant. One likely reason could be that without a stabilising feedback loop, the plant fluctuates too much for a transfer function to be meaningful. For example, an optical cavity used as a frequency discriminator for measuring the frequency fluctuations of a light source is only linear in its response close to the resonance condition: the length of the cavity must be on resonance with the incoming light.

This problem can often be solved as follows: A simple filter (H) is designed so that the overall gain (GH) fulfils all criteria for a stable operation. Sometimes, an iterative process is needed to find the right filter gain.

Once the loop is closed and stable, one can measure the open-loop gain of the system. From the open-loop gain one can compute the exact transfer function of the plant. With this information, the filter can be improved for best performance. In the following, some methods for analysing closed loops are shown.

The following measurements make use of a network analyser¹: at some point, an adder is put into the loop so that a known disturbance (the source signal x_s) can be injected. At the same time, the electronic signal is measured at the other input of the adder (x_I) and/or at its output (x_O). This measurement yields the following result:

$$\begin{aligned}
 x_O &= x_I + x_s & \Rightarrow & \quad x_O = \frac{1}{1-HG} x_s \\
 x_I &= x_O HG & & \quad x_I = \frac{HG}{1-HG} x_s
 \end{aligned}$$

(B.9)

Figures B.3 and B.4 show the three different setups that can be used. A network analyser measures the quantity B/A as a function of frequency. In these examples, the open-loop gain of the system (HG) is given by Figure B.1. Figure B.3 shows two common ways of using the network analyser. The signal source of the network analyser is injected into the loop and at the same time connected to one input of the analyser. The top setup in Figure B.3 measures the following signal:

$$\frac{x_O}{x_s} = \frac{1}{1-HG} \tag{B.10}$$

The open-loop gain HG and thus G can be computed from this signal. Similarly, the lower setup in Figure B.3 yields:

$$\frac{x_I}{x_s} = \frac{HG}{1-HG} \tag{B.11}$$

¹ The measurements can also be performed similarly using an FFT spectrum analyser with two input channels.

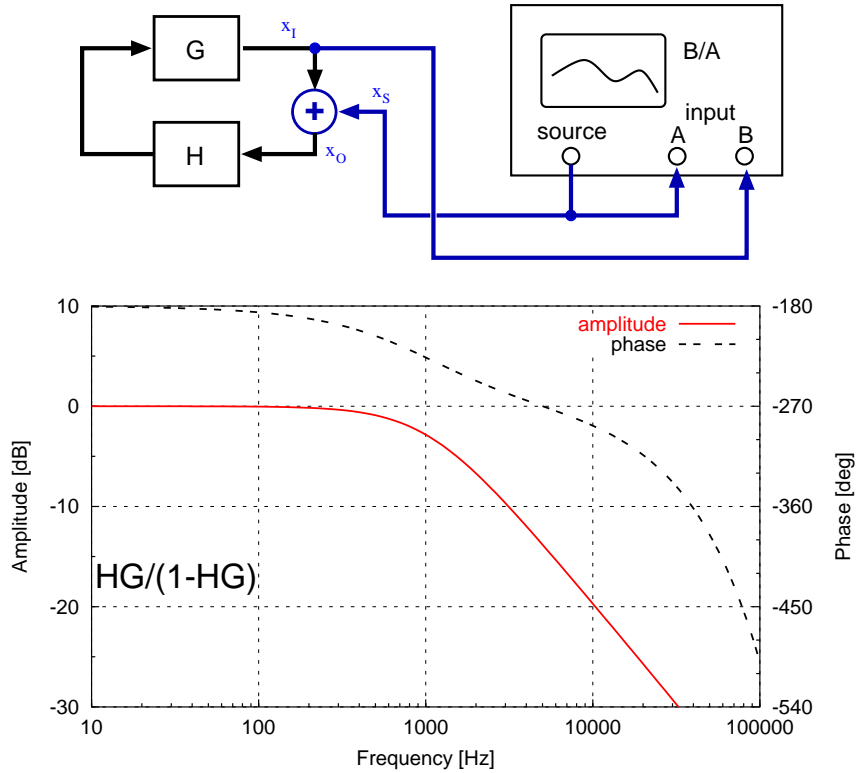
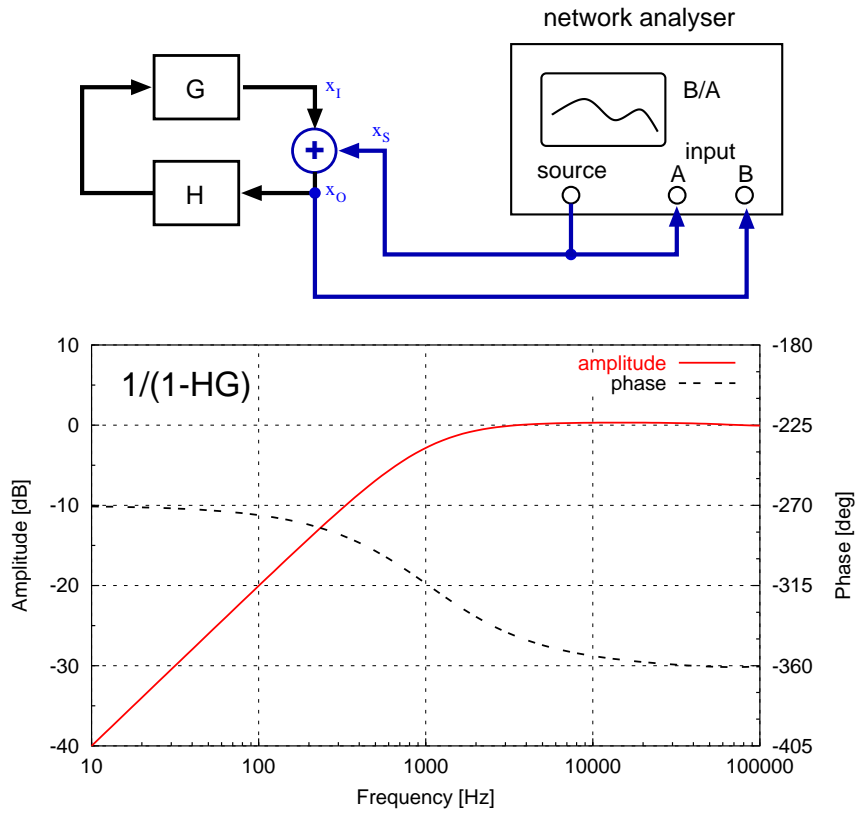


Figure B.3: Two possibilities of measuring closed-loop transfer functions with a network analyser.

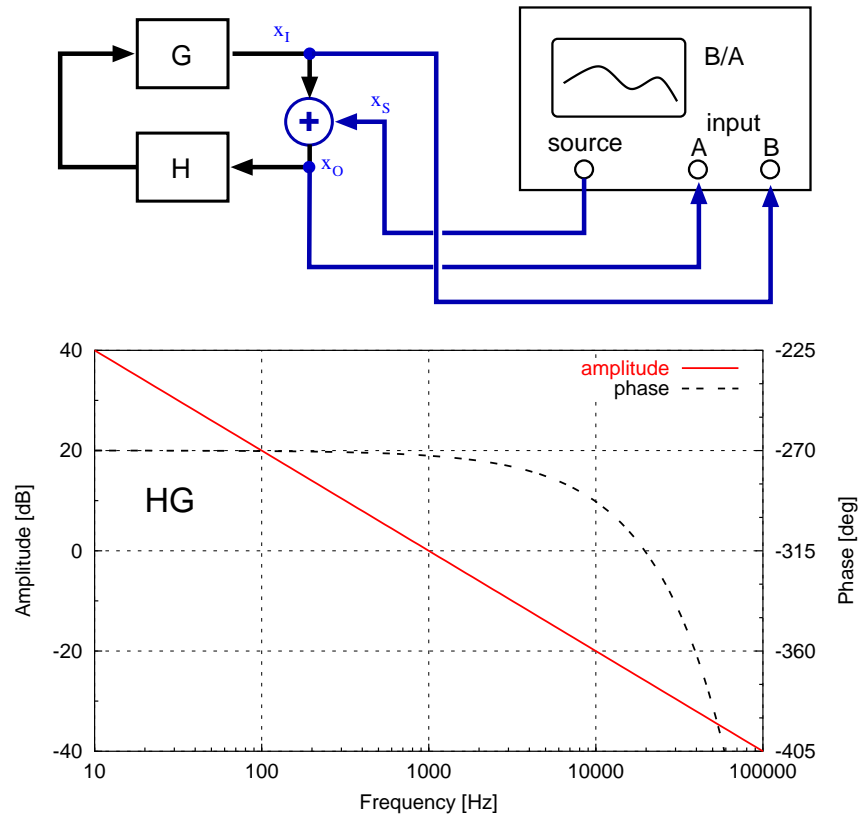


Figure B.4: Direct measurement of the open-loop gain in a closed loop.

If the two input channels of the network analyser can be accessed by the user, a direct measurement of the open-loop gain can be performed; Figure B.4 shows the respective setup. The source of the analyser is injected into the loop, and the second input of the adder and its output are connected to the two inputs of the analyser. The network analyser measures the quantity

$$\frac{x_I}{x_O} = HG \tag{B.12}$$

and thus directly the open-loop gain.

If H is not yet known or subject to changes, the feedback signal should be measured simultaneously so that H and G can be determined independently. If there are more subsystems for which the open-loop gains are unknown, more signals can be measured simultaneously (between the various subsystems). It is always possible to measure all necessary signals to determine all open-loop gains simultaneously by adding only one known signal at some point to the loop.

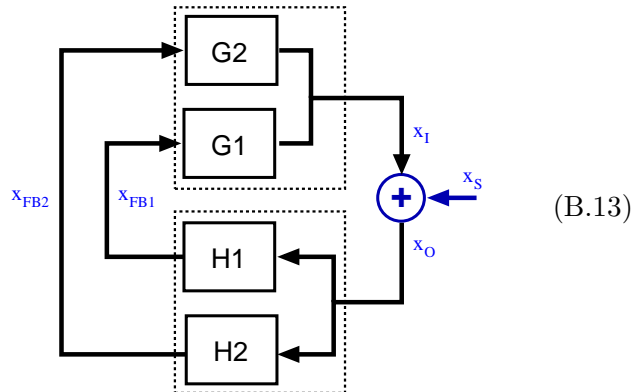
B.5 Split-feedback paths

Many control loops used in the GEO 600 detector have split-feedback paths. Usually, the feedback is divided according to Fourier frequency, because the various actuators have a limited frequency range. Split-feedback paths render the design and analysis of a feedback loop more complicated.

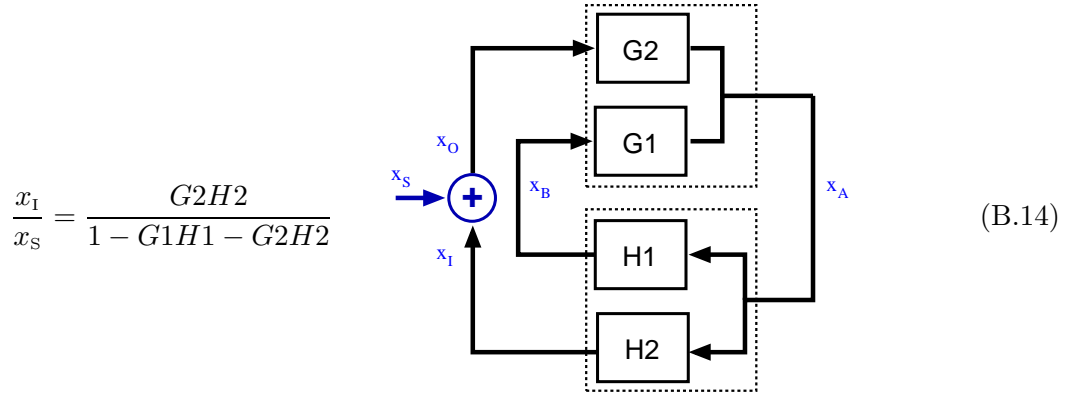
The point on the frequency axis where the magnitudes of the open-loop gains of two different feedback paths are identical is called *crossover*. The simplest possible crossover design includes one actuator for the low-frequency range and another for the high-frequency signals. At the crossover, the magnitudes of both open-loop gains are equal, and at lower frequencies the gain of the first actuator is higher than the gain of the second. Furthermore, in the high-frequency region the gain of the first actuator is low, whereas that of the second actuator is high.

The open-loop gain of the full loop can be measured as above and is simply:

$$G_{\text{open-loop}} = H_1G_1 + H_2G_2$$



The transfer functions can be determined using a network analyser as above. By placing an adder into one part of the loop and measuring the loop signals at various points, the transfer functions of all subsystems can be measured simultaneously. For example, adding the source signal into one of the feedback paths yields:



A useful variant of the above measurement can be used to simultaneously determine the crossover and unity-gain frequency in a common type of control loop. The respective control loop has to fulfil the following criteria for the following measurement to be useful:

- The feedback is split by frequency so that the high-frequency signals are sent to one actuator and the low-frequency signals to the other;
- The open-loop gain at the crossover frequency must be much larger than one.

This example is discussed for a loop that has one distinct unity-gain point and one crossover frequency. In this case, the unity-gain frequency and the crossover frequency can be estimated in a single measurement.

In order to determine the crossover frequency two measurements are usually performed: First, the adder for injecting the source is placed into the high-frequency feedback path:

$$\frac{x_{I2}}{x_{O2}} = \frac{G_2 H_2}{1 - G_1 H_1} \quad (B.15)$$

Second, a similar measurement in the low-frequency path yields:

$$\frac{x_{I1}}{x_{O1}} = \frac{G_1 H_1}{1 - G_2 H_2} \quad (B.16)$$

By comparing both results, one can determine the crossover frequency; the crossover is defined as $|G_1 H_1| = |G_2 H_2|$. With Equations B.15 and B.16 this yields:

$$\left| \frac{x_{I1}}{x_{O1}} \right| = \left| \frac{x_{I2}}{x_{O2}} \right| \quad (B.17)$$

The crossover frequency is defined as that frequency at which the magnitudes of both signals are equal.

If the open-loop gain at the crossover frequency is much greater than one ($|G_1 H_1| \gg 1$), the closed-loop measurements yield a magnitude of:

$$\left| \frac{G_1 H_1}{1 - G_2 H_2} \right| = \left| \frac{G_1 H_1}{1 - G_1 H_1} \right| \approx \frac{G_1 H_1}{G_1 H_1} = 1 \quad (B.18)$$

This shows that one of the closed-loop measurements is sufficient to measure the crossover frequency. In addition, at the unity-gain point the gain of the low-frequency path is usually much smaller than one so that we can approximate:

$$1 = G1H1 + G2H2 \approx G2H2 \quad \text{at the unity-gain frequency.} \quad (\text{B.19})$$

With Equation B.15, this yields:

$$\frac{x_{11}}{x_{O1}} = \frac{G2H2}{1 - G1H1} \approx \frac{G2H2}{1} \approx 1 \quad (\text{B.20})$$

as a result of the high-frequency path measurement at the unity-gain frequency. Thus, the crossover and unity-gain frequencies can be determined as those frequencies at which the high-frequency path measurement yields unity; an example of this measurement is given in Figure 2.8.

B.5.1 Measuring the performance of the loop

The aforementioned considerations show that for Fourier frequencies at a high open-loop gain ($G_{\text{open-loop}} \gg 1$) the following simple measurements can be made:

In-loop measurement of the residual noise: The residual noise can be measured by measuring the error point signal x_{EP} . This measurement is useful for testing the design of the control loop (the design of the open-loop gain). Please note that this kind of *in-loop* measurement cannot be used to determine the absolute noise performance of the plant.

Out-of-loop measurement of the residual noise: Let us suppose that the noise is added to the sensor signal, immediately after the plant. Then, the signal just after that point would again benefit most from the noise reduction, i. e., the error point would show low noise. In this case, however, the signal through the plant would still carry all the noise. In reality, noise adds to all signals of the loop. With a high loop gain, it is possible to suppress these noise signals in the error point signal. Sensor noise (and possibly noise added in the first stages of the filter), however, is not reduced and limits the performance of the plant. A so-called *out-of-loop measurement* in which the properties of the plant are measured against an independent reference is used to characterise the noise performance of a system.

The injected noise: It is difficult to design an electronic filter with a certain performance if the amplitude of the disturbances is not known. In this case, a simple feedback loop can be used to measure the disturbances because the feedback signal of the loop is a measure of the amplitude of the injected noise x_{N} .

Appendix C

Hermite-Gauss modes

The expression *mode* in connection with laser light usually refers to the eigen-modes of a cavity. Here, one distinguishes between longitudinal modes (along the optical axis) and transverse modes, the spatial distribution of the light beam perpendicular to the optical axis. In the following, we are looking at the spatial properties of a laser beam. A *beam* in this sense is a light field for which the power is confined in a small volume around one axis. Cavity eigen-modes provide a useful mathematical formalism for classifying a laser beam when the laser itself uses a stable cavity (as most stable cw lasers do).

A useful mathematical model for describing spatial properties of many laser beams are the Hermite-Gauss modes, which are the eigen-modes of a general spherical cavity (an optical cavity with spherical mirrors). The following section provides an introduction to Hermite-Gauss modes, including some useful formulas.

C.1 Gaussian beams

The so-called *Gaussian beam* often describes a simple laser beam in a good approximation. The Gaussian beam as such is the lowest-order Hermite-Gauss mode and will be described further on. The properties of a Gaussian beam are quite simple:

- The beam has a circular cross section
- the radial intensity profile of a beam with total power P is given by:

$$I(r) = \frac{2P}{\pi w^2(z)} \exp(-2r^2/w^2) \quad (\text{C.1})$$

with w the so-called *spot size*, defined as the *radius* at which the intensity is $1/e^2$ times the maximum intensity $I(0)$. This is, of course, a Gaussian distribution, hence the name Gaussian beam.

Such a beam profile (for a beam with a given wave length λ) can completely be determined by two parameters, the size of the minimum spot size w_0 (called *beam waist*) and the position z_0 of the beam waist along the z -axis. To characterise a Gaussian beam, some useful parameters can be derived from w_0 and z_0 . A Gaussian beam can be divided into

two different sections along the z -axis: a so-called *near field* (a region around the beam waist) and a *far field* (far away from the waist). The length of the near-field region is approximately given by the so-called *Rayleigh range* z_R . The Rayleigh range and the spot size are related by the following expression:

$$z_R = \frac{\pi w_0^2}{\lambda} \quad (\text{C.2})$$

With the Rayleigh range and the location of the beam waist, we can write the following useful expression:

$$w(z) = w_0 \sqrt{1 + \left(\frac{z - z_0}{z_R} \right)^2} \quad (\text{C.3})$$

This equation gives the size of the beam along the z -axis. In the far-field regime ($z \gg z_r, z_0$), it can be approximated by a linear equation:

$$w(z) \approx w_0 \frac{z}{z_R} \quad (\text{C.4})$$

The angle Θ between the z -axis and $w(z)$ in the far field is called *diffraction angle* and simply given by:

$$\Theta = \arctan(w_0/z_r) \quad (\text{C.5})$$

Another useful parameter is the *radius of curvature* of the wave front at a given point z . The radius of curvature describes the curvature of the ‘phase front’ of the electromagnetic wave (a surface across the beam with equal phase) at the position z . We get:

$$R_C(z) = z - z_0 + \frac{z_R^2}{z - z_0} \quad (\text{C.6})$$

For the radius of curvature we also find:

$$\begin{aligned} R_C &\approx \infty, & z - z_0 &\ll z_R && \text{(beam waist)} \\ R_C &\approx z, & z &\gg z_R, z_0 && \text{(far field)} \\ R_C &= 2z_R, & z - z_0 &= z_R && \text{(maximum curvature)} \end{aligned} \quad (\text{C.7})$$

C.2 Paraxial wave equation

An electromagnetic field (at one point in time and in one polarisation) in free space can in general be described by the following scalar wave equation [Siegman]:

$$[\nabla^2 + k^2] E(x, y, z) = 0 \quad (\text{C.8})$$

Two well-known exact solutions for this equation are the plane wave:

$$E(x, y, z) = E_0 \exp(-ikz) \quad (\text{C.9})$$

and the spherical wave:

$$E(x, y, z) = E_0 \frac{\exp(-i kr)}{r} \quad \text{with} \quad r = \sqrt{x^2 + y^2 + z^2} \quad (\text{C.10})$$

Both solutions yield the same phase dependency along an axis (here, for example, the z -axis) of $\exp(-i kz)$. This leads to the idea that a solution for a beam along the z -axis can be found in which the phase factor again is the same while the spatial distribution is described by a function $u(x, y, z)$ that is slowly varying with z :

$$E(x, y, z) = u(x, y, z) \exp(-i kz) \quad (\text{C.11})$$

Substituting this into Equation C.8 yields:

$$(\delta_x^2 + \delta_y^2 + \delta_z^2) u(x, y, z) - 2i k \delta_z u(x, y, z) = 0 \quad (\text{C.12})$$

Now we put the fact that $u(x, y, z)$ should be slowly varying with z in mathematical terms. The variation of $u(x, y, z)$ with z should be small compared to its variation with x or y . Also the second partial derivative in z should be small. This can be expressed as:

$$|\delta_z^2 u(x, y, z)| \ll |2k \delta_z u(x, y, z)|, |\delta_x^2 u(x, y, z)|, |\delta_y^2 u(x, y, z)| \quad (\text{C.13})$$

With this approximation, Equation C.12 can be simplified to the *paraxial* wave equation:

$$(\delta_x^2 + \delta_y^2) u(x, y, z) - 2i k \delta_z u(x, y, z) = 0 \quad (\text{C.14})$$

The Hermite-Gauss modes are exact solutions of the paraxial wave equation. The basic or ‘lowest-order’ mode of a *Gaussian beam* is given as:

$$u(x, y, z) = \left(\frac{1}{R_C(z)} - i \frac{\lambda}{\pi w^2(z)} \right) \cdot \exp \left(-i k \frac{x^2 + y^2}{2R_C(z)} - \frac{x^2 + y^2}{w^2(z)} \right) \quad (\text{C.15})$$

The solution of the paraxial wave equation given in Equation C.15 is only one part of an infinite set of solutions. In order to describe a complete set, we will introduce a more compact form of the above equations that makes use of the so-called *Gaussian beam parameter* q . The beam parameter is a complex quantity defined as:

$$\frac{1}{q(z)} = \frac{1}{R_C(z)} - i \frac{\lambda}{\pi w^2(z)} \quad (\text{C.16})$$

It can also be written as:

$$q(z) = i z_R + z - z_0 \quad \text{and} \quad q_0 = i z_R - z_0 \quad (\text{C.17})$$

Using this parameter Equation C.15 can be rewritten to:

$$u(x, y, z) = \frac{1}{q(z)} \exp \left(-i k \frac{x^2 + y^2}{2q(z)} \right) \quad (\text{C.18})$$

The complete set of solutions with respect to Equation C.18 is an infinite discrete set of modes $u_{nm}(x, y, z)$ with the indices n and m as *mode numbers*. The sum $n + m$ is called the *order* of the mode. These modes can be written as¹:

$$u_{nm}(x, y, z) = u_n(x, z)u_m(y, z) \quad \text{with} \quad (C.19)$$

$$u_n(x, z) = \left(\frac{2}{\pi}\right)^{1/4} \left(\frac{1}{2^n n! w_0}\right)^{1/2} \left(\frac{q_0}{q(z)}\right)^{1/2} \left(\frac{q_0 q^*(z)}{q_0^* q(z)}\right)^{n/2} H_n\left(\frac{\sqrt{2}x}{w(z)}\right) \exp\left(-i \frac{kx^2}{2q(z)}\right)$$

with $H_n(x)$ the Hermite polynomials of order n .

In some cases, it is convenient to write the Hermite-Gauss modes without the Gaussian beam parameter:

$$u_n(x, z) = \left(\frac{2}{\pi}\right)^{1/4} \left(\frac{\exp(i(2n+1)\Psi(z))}{2^n n! w(z)}\right)^{1/2} \times (C.20)$$

$$H_n\left(\frac{\sqrt{2}x}{w(z)}\right) \exp\left(-i \frac{kx^2}{2R_C(z)} - \frac{x^2}{w^2(z)}\right)$$

and for both transverse directions:

$$u_{nm}(x, y, z) = (2^{n+m-1} n! m! \pi)^{-1/2} \frac{1}{w(z)} \exp(i(n+m+1)\Psi(z)) \times (C.21)$$

$$H_n\left(\frac{\sqrt{2}x}{w(z)}\right) H_m\left(\frac{\sqrt{2}y}{w(z)}\right) \exp\left(-i \frac{k(x^2+y^2)}{2R_C(z)} - \frac{x^2+y^2}{w^2(z)}\right)$$

The latter form has the advantage of clearly showing the extra phase shift along the z -axis of $(n+m+1)\Psi(z)$, the so-called *Guoy phase*, see below.

C.3 Guoy phase shift

The full beam can be written as:

$$E(t, x, y, z) = \exp(i(\omega t - kz)) \sum_{n,m} a_{nm} u_n(x, z) u_m(y, z) \quad (C.22)$$

The shape of such a beam does not change along the z -axis (in the par-axial approximation). More precisely, the spot size and the position of the maximum intensity with respect to the z -axis may change, but the relative intensity distribution across the beam does not change its shape. The spatial distribution (u_n, u_m) depends on the parameter z but mainly gives rise to an extra longitudinal phase lag, the so-called *Guoy phase*. Compared to a plane wave, the Hermite-Gauss modes have a slightly slower phase velocity, especially close to the waist. The Guoy phase can be written as:

$$\Psi(z) = \arctan\left(\frac{z - z_0}{z_r}\right) \quad (C.23)$$

¹ Please note that this formula from [Siegman] is very compact. Since the parameter q is a complex number, the expression contains at least two complex square roots. The complex square root requires a different algebra than the standard square root for real numbers. Especially the third and fourth factors can *not* be simplified in any obvious way: $\left(\frac{q_0}{q(z)}\right)^{1/2} \left(\frac{q_0 q^*(z)}{q_0^* q(z)}\right)^{n/2} \neq \left(\frac{q_0^{n+1} q^{*n}(z)}{q^{n+1}(z) q_0^{*n}}\right)^{1/2} !$

And compared to the plane wave, the phase lag φ of a Hermite-Gauss mode is:

$$\varphi = (n + m + 1)\Psi(z) \quad (\text{C.24})$$

The characteristic parameters can also be given using the beam parameter q . The beam size:

$$w^2(z) = \frac{\lambda}{\pi} \frac{q^2}{\text{Re}\{q\}} \quad (\text{C.25})$$

The radius of curvature:

$$R_C(z) = \frac{q^2}{\text{Im}\{q\}} \quad (\text{C.26})$$

The Guoy phase:

$$\Psi(z) = \arctan\left(\frac{\text{Re}\{q\}}{\text{Im}\{q\}}\right) \quad (\text{C.27})$$

Appendix D

Mode cleaning

In this context, the name *mode cleaner* refers to the filter effect of spherical optical cavities. Passing a laser beam through such a cavity will possibly filter out higher-order modes¹. This mode-cleaning effect can be derived simply from the fact that the phase propagation in general is different for Hermite-Gauss modes with a different mode number. For example, a TEM₀₀ experiences a different change in phase as a TEM₁₀ while passing a geometric distance l (on the optical axis). This effect is related to the Guoy effect. The phase of a plane wave travelling a distance l (in vacuum) is given by:

$$\varphi_{\text{plane}} = -kl = -\frac{\omega l}{c} = -\frac{2\pi l}{\lambda} \quad (\text{D.1})$$

The phase of a light field in a TEM _{nm} mode after the same distance l (the wave is travelling from z_1 to z_2) is:

$$\varphi_{nm} = -kl + (n + m + 1) (\Psi(z_2) - \Psi(z_1)) \quad (\text{D.2})$$

with $\Psi(z)$ as the so-called *Guoy phase* given by:

$$\Psi(z) = \arctan\left(\frac{z - z_0}{z_R}\right) \quad (\text{D.3})$$

where z_0 is the position of the beam waist and z_R the Rayleigh range (see Appendix C).

Let us consider a cavity with a set of eigen-modes TEM _{nm} . To be on resonance, an eigen-mode has to also match the longitudinal resonance condition. The resonance condition for the electromagnetic field E_{cav} (of one eigen-mode) inside a simple two-mirror Fabry-Perot cavity can be expressed as:

$$E_{\text{cav}} = E_{\text{in}} \frac{i t_1}{1 - r_1 r_2 \exp(-i \varphi_{\text{rt}})} \quad (\text{D.4})$$

with E_{in} being the incident field and r_1, r_2, t_1, t_2 the amplitude coefficients for the reflection and transmission of the first and second mirror, respectively. φ_{rt} is the so-called

¹ In principle, also a higher-order mode can be passed while the zero-order mode and other higher-order modes are filtered out.

round-trip phase (the actual phase change of the light field after one complete round trip in the cavity).

The resonance condition of a cavity can be derived by maximising the intra-cavity field as a function of φ_{rt} . In order to maximise E_{cav} the phase factor in the denominator should be an integral multiple of 2π :

$$\varphi_{\text{rt}} = N 2\pi \tag{D.5}$$

Another common form of this equation is:

$$\varphi_{\text{rt}} = (q + 1) 2\pi \tag{D.6}$$

with q as the *longitudinal mode number*. The notation TEM_{nmq} can be used to uniquely define a laser beam with respect to a given cavity.

In a simple cavity, the round-trip phase is given by the round trip-length l of the cavity and the frequency of the light plus the Guoy phase:

$$\varphi_{\text{rt}} = -kl + (n + m + 1)\Psi_{\text{rt}} \tag{D.7}$$

For a given round-trip length and Guoy phase of the cavity, we can now compute the resonance frequency:

$$f_{\text{nm}} = \left(\frac{n + m + 1}{2\pi} \Psi_{\text{rt}} - (q + 1) \right) \frac{c}{l} \tag{D.8}$$

For the mode cleaning effect we are interested in the difference between the resonance frequencies for different mode numbers, sometimes called *mode separation*:

$$f_{\text{sep}} = f_{n+1,m} - f_{n,m} = \frac{\Psi_{\text{rt}}c}{2\pi l} \tag{D.9}$$

To summarise, laser light in Hermite-Gauss modes that travels along the z -axis experiences an extra phase shift compared to a plane wave, the Guoy phase shift. The extra phase scales linearly with the mode order $(n + m)$ and otherwise only depends on the beam parameter of the mode.

If we assume that, by design (and maintained by a control loop), the TEM_{00} is resonant in the cavity it fulfils the resonance condition:

$$\varphi_{\text{rt},00} = 2N\pi \tag{D.10}$$

and thus for higher-order modes we find:

$$\varphi_{\text{rt},nm} = 2N\pi + (n + m)(\Psi_{\text{rt}}) \tag{D.11}$$

In general, $\varphi_{\text{rt},nm}$ will not match the resonance condition, and thus the higher-order mode TEM_{nm} will not be resonant in the cavity. Therefore, such a mode will mostly be reflected and not transmitted by the cavity, i. e., the mode is filtered out on transmission. The

filter effect, of course, depends on the Guoy phase. From the properties of the Guoy phase shift we can see that the amount of extra phase shift depends on the beam parameter of the light beam which, in this case, is of course the beam parameter of the eigen-mode of the cavity. Thus, by carefully choosing the cavity geometry one can build a cavity with the desired Guoy phase. Equation D.11 clearly shows that it is impossible to design a cavity that gives maximum filtering for all higher-order modes. In practice, however, it is sufficient to suppress the first higher-order modes. The laser light usually does not have much power in modes with a large mode number. In addition, such modes have a larger beam size. Thus, they will experience much more losses inside the mode cleaner cavity if the mirrors are designed to fit (in size) the lowest-order mode.

Appendix E

Numerical analysis of optical systems

E.1 Introduction

The search for gravitational waves with interferometric detectors has led to a new type of laser interferometer: a long baseline Michelson interferometer with suspended mirrors and beam splitters. These instruments must provide an enormous sensitivity to function as gravitational-wave detectors.

Several prototype interferometers have been build during the last decades to investigate the performance of interferometers in detecting gravitational waves. The optical systems, Fabry-Perot cavities, a Michelson interferometer and combinations of both are in principle very simple and have been used in many fields of science for many decades. The sensitivity required for the detection of the expected small signal amplitudes of gravitational waves has put new constrains onto the design of laser interferometers. The work of the gravitational-wave research groups has led to a new exploration of the theoretical analysis of laser interferometers. Especially, the clever combination of known interferometers has produced new types of interferometric detectors that offer an optimised sensitivity for detecting gravitational waves.

This chapter describes a useful method for analysing optical systems. It allows to compute the frequency domain signals or the transfer functions of a linear optical system. The amplitudes of the electrical field inside an optical system can be computed as well as many output signals.

The analysis described here merely uses classic descriptions for optical components and light fields. Some aspects, especially the noise introduced by the quantum fluctuations of the light fields, cannot be explored using this concept as such. Nevertheless, this type of analysis is also a basis for more advanced analyses of detectors that make use of non-classic techniques.

E.1.1 Time domain and frequency domain analysis

The analysis of linear optical systems generally allows two approaches: First, the analysis in the frequency domain in which each parameter or signal is described as a function of

frequency, and second, the analysis in the time domain in which signals and parameters are time-dependent entities. In both cases, the mathematical description of the physical objects is basically the same. The difference lies in the way the coupling between local objects or fields is used to determine the state of the overall system.

Time domain

The time domain analysis can be used to describe the dynamics of a system. It is based on the assumption that all couplings inside the system can be described locally on a small time scale. The time scale, determined by a time step δt , is defined by the properties of the object of the analysis: The time step has to be set smaller than characteristic time constants of the physical system. If, for example, the dynamic power enhancement inside a Fabry-Perot cavity is to be computed, the time step must be smaller than the round-trip time $t_{\text{rt.}} = L_{\text{rt.}}/c$. In order to compute the time evolution of the system, an initial state is defined for $t = 0$ first. Next, the equations of motion are solved locally for each subsystem and the state of each subsystem is computed for $t = t + \delta t$. Thus, the state of the entire system is deduced considering local interactions. By continuously repeating the last step, the dynamic evolution of the system is derived. This method is very powerful but also very slow: The typical time steps δt are very small (10^{-6} to 10^{-10} seconds). In addition, the typical duration of a ‘virtual experiment’ (often extended further by the settling time of the systems) is in the order of seconds or even minutes. This results in an enormous number of necessary operations.

Frequency domain

The analysis in the frequency domain assumes the system to be in a steady state. In this case, all couplings can be described globally by one set of linear equations. The properties of the system are derived by solving the set of equations once. This method is much faster than the time domain analysis but has the disadvantage of not being able to compute any dynamic effects. It is possible, however, to analyse slow dynamic effects, i. e., when a parameter change can be approximated as a sequence of quasi-static processes. Signals are described with respect to the Fourier frequency. The assumption of a steady state allows oscillating signals at all Fourier frequencies, but it requires that their amplitudes, frequencies and phases are fixed.

An interferometric gravitational-wave detector should be as stable as possible during normal operation: In other words, any change in the parameters should be minimised. In many respects, the detector in normal operation can be assumed to be in steady state so that the frequency domain analysis can be used. The time domain analysis is commonly used for investigating the lock acquisition process or any other dynamic change in the optical system before a steady state of the normal operation has been achieved.

E.2 FINESSE, a numeric interferometer simulation

The work on the prototype interferometers has shown that the models describing the optical system become very complex even though they are based on simple principles. Consequently, computer programs were developed to automate the computational part of the analysis. To date, several programs for analysing optical systems are available to the gravitational-wave community [STAIC]. However, during the work on the Garching prototype interferometer (1998), the available programs were found to be slow and not very flexible. Gerhard Heinzel had the idea of using a numerical algorithm for a frequency domain simulation¹.

In consequence, FINESSE has been developed during this work [FINESSE]. The program was designed to be a fast and flexible tool for computing, for example, error signals, transfer functions and sensitivity curves. The user can build any kind of virtual interferometer using the following components:

- lasers, with user-defined power, wavelength and shape of the output beam;
- free spaces with arbitrary index of refraction;
- mirrors and beam splitters, with flat or spherical surfaces;
- modulators to change amplitude and phase of the laser light;
- amplitude or power detectors with the possibility of demodulating the detected signal with one or more given demodulation frequencies;
- lenses and Faraday isolators.

For a given optical setup, the program computes the light field amplitudes at every point in the interferometer assuming a steady state. To do so, the interferometer description is translated into a set of linear equations that are solved numerically. For convenience, a number of standard analyses can be performed automatically by the program, namely computing modulation-demodulation error signals and transfer functions. FINESSE can perform the analysis using geometric optics or Hermite-Gauss modes. The latter allows to compute the effects of mode matching and misalignments. In addition, error signals for automatic alignment systems can be simulated.

The possible applications of this program are too numerous to list. A detailed description of the program and the implemented physics can be found in the FINESSE manual. The mathematical formalism described in this chapter has been developed to be used within FINESSE. It presents a set of special mathematical tools based on a few well-known principles (see for example [Siegman]). The explanation given here is well suited for the use within a computer program, in some cases with special regard to the numeric nature of the code.

¹ The simulation of an optical system described by a set of linear equations poses a very similar problem as the analysis of linear electronic circuits. Thus, Gerhard Heinzel suggested to adapt the code of his program for analysing electronic circuits [LISO] for the analysis of optical systems.

E.2.1 Analysis of optical systems with geometric optics

The following sections describe a mathematical formalism based on geometric optics² only; however, it can be extended for more advanced analyses, for example, by including the description of a beam shape and position via Hermite-Gauss modes (see Section E.3).

This analysis is based on the principle of super-position of light fields: A laser beam can be described as the sum of different light fields. Possible degrees of freedom are:

- frequency
- geometrical shape
- polarisation

In the analysis of interferometric gravitational-wave detectors, the amplitudes and frequencies of light fields are of principal interest. The polarisation is neglected in the analysis given here, but the formalism can be extended to include the polarisation similarly to the extension with Hermite-Gauss modes.

E.2.2 Static response and frequency response

The optical system shall be modelled by one set of linear equations that describes the light field amplitudes in a steady state. When a vector of input fields is provided, the set of linear equations can be mathematically solved by computing a so-called solution vector that holds the field amplitudes at every component in the optical system.

The analysis provides information about the light field amplitudes as a function of the parameters of the optical system. Two classes of calculations can be performed:

- a) **Static response:** Computing the light field amplitudes as a function of a quasi-static change of one or more parameters of the optical components. For example, the amplitude of a light field leaving an interferometer as a function of a change in an optical path length. The settling time of the optical system can usually be estimated using the optical parameters. Parameter changes that are negligible during the settling time can be assumed to be quasi-static. In a well-designed optical system many parameter changes can be treated as quasi-static so that the static response can be used to compute, for example, the (open-loop) error signal of a control loop of the optical system.
- b) **Frequency response:** In general, the frequency response describes the behaviour of an output signal as a function of the frequency of a fixed input signal. In other words, it represents a transfer function; in this context, a transfer function of an optical system. The input signal is commonly the modulation of light fields at some point in the interferometer.

² The term 'geometric optics' is often used for the analysis of the position (and angle) of a ray propagating through an optical system. Here, the term is used to indicate an 'on axis' analysis, i. e., only the phase of the light field on the optical axis are of interest, not the location of the optical axis.

The frequency response allows to compute the optical transfer functions as, for example, required for designing control loops.

E.2.3 Description of light fields

A laser beam is usually described by the electric component of its electromagnetic field:

$$\vec{E}(t, \vec{x}) = \vec{E}_0 \cos(\omega t - \vec{k}\vec{x}) \quad (\text{E.1})$$

In the following calculations, only the scalar expression for a fixed point in space is used. The calculations can be simplified by using the full complex expression instead of the cosine:

$$E(t) = E_0 \exp(i(\omega t + \varphi)) = a \exp(i\omega t) \quad \text{with} \quad a = E_0 \exp(i\varphi) \quad (\text{E.2})$$

The real field at that point in space can then be calculated as:

$$\vec{E}(t) = \text{Re}\{E(t)\} \cdot \vec{e}_{\text{pol}} \quad (\text{E.3})$$

with \vec{e}_{pol} as the unit vector in the direction of polarisation.

Each light field is then described by the complex amplitude a and the angular frequency ω . Instead of ω , also the frequency $f = \omega/2\pi$ or the wavelength $\lambda = 2\pi c/\omega$ can be used to specify the light field. It is often convenient to define one *default frequency* (also called *default laser frequency*) f_0 as a reference and describe all other light fields by the offset Δf to that frequency. In the following, some functions and coefficients are defined using f_0 , ω_0 or λ_0 referring to a previously defined default frequency. The setting of the default frequency is arbitrary, it merely defines a reference for frequency offsets and does not influence the results.

The electric component of electromagnetic radiation is given in Volt per meter. The light power computes as:

$$P = \epsilon_0 c E E^* \quad (\text{E.4})$$

with ϵ_0 the electric permeability of vacuum and c as the speed of light. However, for more intuitive results the light fields can be given in converted units, so that the light power can be computed as the square of the light field amplitudes. Unless otherwise noted, throughout this work the unit of light field amplitudes is the square root of Watt. Thus, the power computes simply as:

$$P = E E^* \quad (\text{E.5})$$

E.2.4 Lengths and tunings

The Michelson interferometer in the GEO 600 detector uses three different types of light fields: The laser with a frequency of $f \approx 2.8 \cdot 10^{14}$ Hz, modulation sidebands used for

interferometer control with frequencies (offsets to the laser frequency) of $f \approx 30 \cdot 10^6$ Hz, and the signal sidebands at frequencies of 10 Hz to 1000 Hz.

The resonance condition inside the cavities and the operating point of an interferometer depend on the optical path lengths modulo the laser wavelength, i. e., for the light of a Nd:YAG laser, as it is used by GEO 600, length differences of less than $1 \mu\text{m}$ are of interest, not the absolute length. The propagation of the sideband fields depends on the much larger wavelength of the (offset) frequencies of these fields and thus often on absolute lengths. Therefore, it is convenient to split distances D between optical components into two parameters [Heinzel99]: One is the macroscopic ‘length’ L defined as that multiple of the default wavelength yielding the smallest difference to D . The second parameter is the microscopic *tuning* that is defined as the remaining difference between L and D . This tuning is usually given as a phase ϕ (in radian) with 2π referring to one wavelength³.

This convention provides two parameters that can describe distances with a markedly improved numeric accuracy. In addition, this definition often allows to simplify the algebraic notation of interferometer signals.

In the following, the propagation through free space is defined as a propagation over a macroscopic length L , i. e., a free space is always ‘resonant’, i. e., a multiple of λ_0 . The microscopic tuning appears as a parameter of mirrors and beam splitters. It refers to a microscopic displacement perpendicular to the surface of the component. If, for example, a cavity is to be resonant to the laser light, the tunings of the mirrors always have to be the same whereas the length of the space in between can be arbitrary.

E.2.5 Phase change on reflection and transmission

When a light field passes a beam splitter, a phase jump in either the reflected, the transmitted or both fields is required for energy conservation; the actual phase change for the different fields depends on the type of beam splitter (see [Rüdiger] and [Heinzel99]). In practice, the absolute phase of the light field at a beam splitter is of little interest so that for computing interferometer signals one can choose a convenient implementation for the relative phase. Throughout this work, the following convention is used: Mirrors and beam splitters are assumed to be symmetric (not in their power splitting but with respect to the phase change), and the phase is not changed upon reflection; instead, the phase changes by $\pi/2$ at every transmission.

Please be aware that this is directly connected to the resonance condition in the simulation: If, for example, a single surface with power transmittance $T = 1$ is inserted into a simple cavity, the extra phase change by the transmission will change the resonance condition to its opposite. Inserting a real component with two surfaces, however, does not show this effect.

³ Note that in some other publications π is used to refer to one wavelength instead.

E.2.6 Modulation of light fields

In principle, all parameters of a light field can be modulated. This section describes the modulation of the amplitude, phase and frequency of the light.

Any sinusoidal modulation of amplitude or phase generates new field components that are shifted in frequency with respect to the initial field. Basically, light power is shifted from one frequency component, the *carrier*, to several others, so-called *sidebands*. The relative amplitudes and phases of these sidebands differ for different types of modulation and different modulation strengths.

Phase modulation

Phase modulation can create a large number of sidebands. The amount of sidebands with noticeable power depends on the modulation strength (or depths) given by the *modulation index* m .

Assuming an input field:

$$E_{\text{in}} = E_0 \exp(i\omega_0 t) \quad (\text{E.6})$$

a sinusoidal phase modulation of the field can be described as:

$$E = E_0 \exp\left(i(\omega_0 t + m \cos(\omega_m t))\right) \quad (\text{E.7})$$

This equation can be expanded using the Bessel functions $J_k(m)$ to:

$$E = E_0 \exp(i\omega_0 t) \sum_{k=-\infty}^{\infty} i^k J_k(m) \exp(ik\omega_m t) \quad (\text{E.8})$$

The field for $k = 0$, oscillating with the frequency of the input field ω_0 , represents the carrier. The sidebands can be divided into *upper* ($k > 0$) and *lower* ($k < 0$) sidebands. These sidebands are light fields that have been shifted in frequency by $k\omega_m$. The upper and lower sidebands with the same absolute value of k are called a pair of sidebands of order k .

Equation E.8 shows that the carrier is surrounded by an infinite number of sidebands. However, the Bessel functions decrease for large k . Especially for small modulation indices ($m < 1$), the Bessel functions can be approximated by:

$$J_k(m) = \frac{1}{k!} \left(\frac{m}{2}\right)^k + O(m^{k+2}) \quad (\text{E.9})$$

In that case, only a few sidebands have to be taken into account. For $m \ll 1$ we can write:

$$E = E_0 \exp(i\omega_0 t) \times \left(J_0(m) - iJ_{-1}(m) \exp(-i\omega_m t) + iJ_1(m) \exp(i\omega_m t) \right) \quad (\text{E.10})$$

and with

$$J_{-k}(m) = (-1)^k J_k(m) \quad (\text{E.11})$$

we get:

$$E = E_0 \exp(i\omega_0 t) \left(1 + i \frac{m}{2} \left(\exp(-i\omega_m t) + \exp(i\omega_m t) \right) \right) \quad (\text{E.12})$$

as the first-order approximation in m .

Amplitude modulation

In contrast to phase modulation, (sinusoidal) amplitude modulation always generates exactly two sidebands. Furthermore, a natural maximum modulation index exists: The modulation index is defined to be one ($m = 1$) when the amplitude is modulated between zero and the amplitude of the unmodulated field.

If the amplitude modulation is performed by an active element, for example by modulating the current of a laser diode, the following equation can be used to describe the output field:

$$\begin{aligned} E &= E_0 \exp(i\omega_0 t) \left(1 + m \cos(\omega_m t) \right) \\ &= E_0 \exp(i\omega_0 t) \left(1 + \frac{m}{2} \exp(i\omega_m t) + \frac{m}{2} \exp(-i\omega_m t) \right) \end{aligned} \quad (\text{E.13})$$

However, passive amplitude modulators (like acousto-optic modulators or electro-optic modulators with polarisers) can only reduce the amplitude. In these cases, the following equation is more useful:

$$\begin{aligned} E &= E_0 \exp(i\omega_0 t) \left(1 - \frac{m}{2} \left(1 - \cos(\omega_m t) \right) \right) \\ &= E_0 \exp(i\omega_0 t) \left(1 - \frac{m}{2} + \frac{m}{4} \exp(i\omega_m t) + \frac{m}{4} \exp(-i\omega_m t) \right) \end{aligned} \quad (\text{E.14})$$

Frequency modulation

For small modulation indices phase modulation and frequency modulation can be understood as different descriptions of the same effect [Heinzel99]. With the frequency defined as $f = d\varphi/dt$ a sinusoidal frequency modulation can be written as:

$$E = E_0 \exp \left(i \left(\omega_0 t + \frac{\Delta\omega}{\omega_m} \cos(\omega_m t) \right) \right) \quad (\text{E.15})$$

with $\Delta\omega$ as the frequency swing (how *far* the frequency is shifted by the modulation) and ω_m the modulation frequency (how *fast* the frequency is shifted). The modulation index is defined as:

$$m = \frac{\Delta\omega}{\omega_m} \quad (\text{E.16})$$

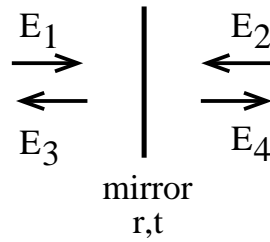


Figure E.1: Coupling of light fields at a simplified mirror.

E.2.7 Coupling of light field amplitudes

Many optical systems can be described mathematically using linear coupling of light field amplitudes. Passive components, such as mirrors, beam splitters and lenses, can be described well by linear coupling coefficients. Active components, such as electro-optical modulators cannot be described that easily. Nevertheless, simplified versions of active components can often be included in a linear analysis.

The coupling of light field amplitudes at a simple (perfect, flat, symmetric) mirror under normal incidence is shown in Figure E.1 and can be described as follows: There are two input fields, E_1 impinging on the mirror on the front surface and E_2 on the back surface. Two output fields are leaving the mirror, E_3 and E_4 . With the amplitude coefficients for reflectance and transmittance (r , t) the following equations can be composed:

$$\begin{aligned} E_3 &= rE_1 + itE_2 \\ E_4 &= rE_2 + itE_1 \end{aligned} \tag{E.17}$$

Possible loss is included in this description because the sum $r^2 + t^2$ may be less than one; see Section E.2.5 about the convention for the phase change.

The above equations completely define this simplified optical component. Optical systems that consist of similar components can be described by a set of linear equations. Such a set of linear equations can easily be solved mathematically, and the solution describes the equilibrium of the optical system: Given a set of input fields (as the ‘right-hand-side’ of the set of linear equation), the solution provides the resulting field amplitudes everywhere in the optical system. This method has proven to be very powerful for analysing optical systems. It can equally well be adapted to an algebraic analysis as to a numeric approach.

In the case of geometric optics, the light fields can be completely described by their complex amplitude and their angular frequency. The linear equations for each component can be written in the form of local coupling matrices in the format:

$$\begin{pmatrix} \text{Out1} \\ \text{Out2} \end{pmatrix} = \begin{pmatrix} a_{11} & a_{21} \\ a_{12} & a_{22} \end{pmatrix} \begin{pmatrix} \text{In1} \\ \text{In2} \end{pmatrix} \quad \begin{array}{c} \xrightarrow{\text{In1}} \\ \xleftarrow{\text{Out1}} \end{array} \left| \begin{array}{c} \xleftarrow{\text{In2}} \\ \xrightarrow{\text{Out2}} \end{array} \right. \quad (\text{E.18})$$

with the complex coefficients a_{ij} . These matrices serve as a compact and intuitive notation of the coupling coefficients. For solving a set of linear equations, a different notation is more sensible: A linear set of equations can be written in the form of a matrix that represents the interferometer: the *interferometer matrix* times the vector of field amplitudes (solution vector). Together with the so-called right-hand side vector that gives numeric values for the input field, the set of linear equation is complete:

$$\begin{pmatrix} \text{interferometer} \\ \text{matrix} \end{pmatrix} \times \begin{pmatrix} \vec{x}_{\text{sol}} \end{pmatrix} = \begin{pmatrix} \vec{x}_{\text{RHS}} \end{pmatrix} \quad (\text{E.19})$$

For the above example of the simple mirror the linear set of equations in matrix form looks as follows:

$$\begin{pmatrix} 1 & 0 & 0 & 0 \\ -a_{11} & 1 & -a_{21} & 0 \\ 0 & 0 & 1 & 0 \\ -a_{12} & 0 & -a_{22} & 1 \end{pmatrix} \times \begin{pmatrix} \text{In1} \\ \text{Out1} \\ \text{In2} \\ \text{Out2} \end{pmatrix} = \begin{pmatrix} \text{In1} \\ 0 \\ \text{In2} \\ 0 \end{pmatrix} \quad (\text{E.20})$$

Propagation through free space

The propagation of a light field through free space over a given length L (index of refraction n) can be considered as passing a component ‘space’. The component ‘space’ is specified by a macroscopic length as defined above.

$$\begin{pmatrix} \text{Out1} \\ \text{Out2} \end{pmatrix} = \begin{pmatrix} 0 & s_1 \\ s_2 & 0 \end{pmatrix} \begin{pmatrix} \text{In1} \\ \text{In2} \end{pmatrix} \quad \begin{array}{c} \xrightarrow{\text{In1}} \\ \xleftarrow{\text{Out1}} \end{array} \left[\begin{array}{c} \xleftarrow{\text{In2}} \\ \xrightarrow{\text{Out2}} \end{array} \right] \text{Space} \quad (\text{E.21})$$

The propagation only affects the phase of the field:

$$s_1 = s_2 = \exp(i\omega nL/c) = \exp(i(\omega_0 + \Delta\omega)nL/c) = \exp(i\Delta\omega nL/c) \quad (\text{E.22})$$

with $\exp(i\omega_0 nL/c) = 1$ following from the definition of macroscopic lengths (see above). The used parameters are the length L , the index of refraction n , ω as the angular frequency of the light field and $\Delta\omega$ as the offset to the default frequency.

Mirror

From the definition of the component ‘space’ that always represents a macroscopic length, follows the necessity to perform microscopic propagations inside the mathematical representation of the components *mirror* and *beam splitter*.

In this description the component mirror is always hit at normal incidence. Arbitrary angles of incidence are discussed for the component beam splitter, see below.

A light field E_{in} reflected by a mirror is in general changed in phase and amplitude:

$$E_{\text{refl}} = r \exp(i\varphi) E_{\text{in}} \quad (\text{E.23})$$

with r being the amplitude reflectance of the mirror and $\varphi = 2kx$ the phase shift acquired by the propagation towards and back from the mirror if the mirror is not located at the reference plane ($x = 0$).

The *tuning* ϕ gives the displacement of the mirror expressed in radian (with respect to the reference plane). A tuning of $\phi = 2\pi$ represents a displacement of the mirror by one carrier wavelength: $x = \lambda_0$. The direction of the displacement is arbitrarily defined as in the direction of the normal vector on the front surface.

If the displacement x_m of the mirror is given in meters, then corresponding tuning ϕ computes as follows:

$$\phi = kx_m = x_m \frac{\omega}{c} \quad (\text{E.24})$$

A certain displacement results in a different phase shifts for light fields with different frequencies. The phase shift a general field acquires at the reflection on the front surface of the mirror can be written as:

$$\varphi = 2\phi \frac{\omega}{\omega_0} \quad (\text{E.25})$$

If a second light beam hits the mirror from the other direction the phase change φ_2 with respect to the same tuning would be:

$$\varphi_2 = -\varphi$$

The tuning of a mirror or beam splitter does not represent a change in the path length but a change in the position of component. The transmitted light is thus not affected by the tuning of the mirror (the optical path for the transmitted light always has the same length for all tunings). Only the phase shift of $\pi/2$ for every transmission (as defined in Section E.2.5) has to be taken into account:

$$E_{\text{trans}} = i t E_{\text{in}} \quad (\text{E.26})$$

with t as the amplitude transmittance of the mirror.

The coupling matrix for a mirror is:

$$\begin{pmatrix} \text{Out1} \\ \text{Out2} \end{pmatrix} = \begin{pmatrix} m_{11} & m_{21} \\ m_{12} & m_{22} \end{pmatrix} \begin{pmatrix} \text{In1} \\ \text{In2} \end{pmatrix} \quad \begin{array}{c} \xrightarrow{\text{In1}} \\ \xleftarrow{\text{Out1}} \end{array} \left[\right] \begin{array}{c} \xleftarrow{\text{In2}} \\ \xrightarrow{\text{Out2}} \end{array} \quad (\text{E.27})$$

with the coefficients given as:

$$\begin{aligned} m_{12} &= m_{21} = it \\ m_{11} &= r \exp(i2\phi \omega/\omega_0) \\ m_{22} &= r \exp(-i2\phi \omega/\omega_0) \end{aligned} \quad (\text{E.28})$$

Beam splitter

A beam splitter is similar to a mirror except for the extra parameter α that indicates the angle of incidence of the incoming beams. Since, in this work, a displacement of the beam splitter is assumed to be perpendicular to its optical surface, the angle of incidence affects the phase change of the reflected light. Simple geometric calculations lead to the following equation for the optical phase change φ :

$$\varphi = 2\phi \frac{\omega}{\omega_0} \cos(\alpha) \quad (\text{E.29})$$

The coupling matrix has the following form:

$$\begin{pmatrix} \text{Out1} \\ \text{Out2} \\ \text{Out3} \\ \text{Out4} \end{pmatrix} = \begin{pmatrix} 0 & bs_{21} & bs_{31} & 0 \\ bs_{12} & 0 & 0 & bs_{42} \\ bs_{13} & 0 & 0 & bs_{43} \\ 0 & bs_{24} & bs_{34} & 0 \end{pmatrix} \begin{pmatrix} \text{In1} \\ \text{In2} \\ \text{In3} \\ \text{In4} \end{pmatrix} \quad \begin{array}{c} \text{In2} \downarrow \uparrow \text{Out2} \\ \xrightarrow{\text{In1}} \quad \diagdown \quad \diagup \quad \xleftarrow{\text{In3}} \\ \xleftarrow{\text{Out1}} \quad \diagup \quad \diagdown \quad \xrightarrow{\text{Out3}} \\ \text{In4} \uparrow \downarrow \text{Out4} \end{array} \quad (\text{E.30})$$

with the coefficients:

$$\begin{aligned} bs_{12} &= bs_{21} = r \exp(i2\phi\omega/\omega_0 \cos \alpha) \\ bs_{13} &= bs_{31} = it \\ bs_{24} &= bs_{42} = it \\ bs_{34} &= bs_{43} = r \exp(-i2\phi\omega/\omega_0 \cos \alpha) \end{aligned} \quad (\text{E.31})$$

Modulator

The modulation of light fields is described in Section E.2.6. A small modulation of a light field in amplitude or phase can be described as follows: A certain amount of light power is shifted from the carrier into new frequency components (sidebands). In general, a modulator can create a very large number of sidebands if, for example, the

modulator is located inside a cavity: On every round trip the modulator would create new sidebands around the previously generated sidebands. This effect cannot be modelled by the formalism described here.

Instead, a simplified modulator scheme is used. The modulator only acts on specially selected light fields and generates a well-defined number of sidebands. With these simplifications the modulator can be described as:

- an attenuator for the light field that experiences the modulation (at the carrier frequency);
- a source of light at new frequency (the sideband frequencies), see Section E.2.8.

All other frequency components of the light field are not affected by the modulator. The coupling matrix for the modulator is:

$$\begin{pmatrix} \text{Out1} \\ \text{Out2} \end{pmatrix} = \begin{pmatrix} 0 & e_{o21} \\ e_{o12} & 0 \end{pmatrix} \begin{pmatrix} \text{In1} \\ \text{In2} \end{pmatrix} \quad \begin{array}{ccc} \xrightarrow{\text{In1}} & \boxed{\phantom{\text{modulator}}} & \xleftarrow{\text{In2}} \\ \xleftarrow{\text{Out1}} & & \xrightarrow{\text{Out2}} \end{array} \quad (\text{E.32})$$

The coefficients for field amplitudes that are not affected by the modulator are simply:

$$e_{o12} = e_{o21} = 1 \quad (\text{E.33})$$

When the input field is a carrier field the coefficients are given as:

$$e_{o12} = e_{o21} = C \quad (\text{E.34})$$

with

$$C = 1 - \frac{m}{2}$$

(m is the modulation index `midx`) in the case of amplitude modulation and:

$$C = J_0(m)$$

for phase modulation.

Isolator (diode)

The isolator represents a simplified Faraday isolator: light passing in one direction is not changed, whereas the power of the beam passing in the other direction is reduced by a specified amount:

$$\begin{pmatrix} \text{Out1} \\ \text{Out2} \end{pmatrix} = \begin{pmatrix} 0 & d_{21} \\ d_{12} & 0 \end{pmatrix} \begin{pmatrix} \text{In1} \\ \text{In2} \end{pmatrix} \quad \begin{array}{ccc} \xrightarrow{\text{In1}} & \boxed{\phantom{\text{isolator}}} & \xleftarrow{\text{In2}} \\ \xleftarrow{\text{Out1}} & & \xrightarrow{\text{Out2}} \end{array} \quad (\text{E.35})$$

The coupling coefficients are:

$$\begin{aligned} d_{12} &= 1 \\ d_{21} &= 10^{-S/20} \end{aligned} \tag{E.36}$$

with S as the specified suppression given in dB.

Lens

A lens is assumed not to change the amplitude or phase of the light fields:

$$\begin{pmatrix} \text{Out1} \\ \text{Out2} \end{pmatrix} = \begin{pmatrix} 0 & 1 \\ 1 & 0 \end{pmatrix} \begin{pmatrix} \text{In1} \\ \text{In2} \end{pmatrix} \quad \begin{array}{c} \xrightarrow{\text{In1}} \\ \xleftarrow{\text{In2}} \\ \xleftarrow{\text{Out1}} \\ \xrightarrow{\text{Out2}} \end{array} \left(\text{Lens} \right) \tag{E.37}$$

E.2.8 Light sources

After the set of linear equations for an optical system has been determined, the input light fields have to be given by the user. The respective fields are entered to the so-called ‘right hand side’ (RHS) vector of the set of linear equations. The RHS vector consists of complex numbers that specify the amplitude and phase of every input field. Input fields are initially set to zero, and every non-zero entry describes a light source. The possible sources are lasers, modulators and ‘signal sidebands’.

Laser

The principal light sources are, of course, the lasers. They are simply specified by light power, frequency and phase. The phase is only of interest as a relative phase between several lasers.

Modulators

Modulators produce non-zero entries in the RHS vector for every modulation sideband that is generated. Depending on the order ($k \geq 0$) and the modulation index (m), the input field amplitude for amplitude modulation is:

$$a_{\text{in}} = \frac{m}{4} \tag{E.38}$$

and for phase modulation:

$$a_{\text{in}} = (-1)^k J_k(m) \exp(i\varphi) \tag{E.39}$$

with φ given as (Equation E.8):

$$\varphi = \pm k \cdot \left(\frac{\pi}{2} + \varphi_s \right) \quad (\text{E.40})$$

where φ_s is the user-specified phase from the modulator description. The sign of φ is the same as the sign of the frequency offset of the sideband. For ‘lower’ sidebands ($f_{\text{mod}} < 0$) we get $\varphi < 0$, for ‘upper’ sidebands ($f_{\text{mod}} > 0$) it is $\varphi > 0$.

Signal sidebands

The most complex input light fields are the signal sidebands. They can be generated by many different types of modulation inside the interferometer (signal modulation in the following). The components mirror, beam splitter, space, laser and modulator can be used as a source of signal sidebands. The Primarily, artificial signal sidebands are used as the input signal for computing transfer functions of the optical system. The amplitude, in fact the modulation index, of the signal is assumed to be much smaller than one so that the effects of the modulation can be described by a linear analysis. If linearity is assumed, however, the computed transfer functions are independent of the signal amplitude; thus, only the relative amplitudes of output and input are important, and the modulation index of the signal modulation can be arbitrarily set to one in the simulation.

In order to have a determined number of light fields, the signal modulation of a signal sideband has to be neglected. This approximation is sensible because in the steady state the signal modulations are expected to be tiny so that the second-order effects (signal modulation of the signal modulation fields) can be omitted.

Mirror: If a mirror position is modulated, then the reflected light will experience a phase modulation. The mirror motion does not change transmitted light. The relevant parameters are shown in Figure E.2. At a reference plane (the nominal mirror position when the tuning is zero), the field impinging on the mirror is:

$$E_{\text{in}} = E_0 \exp\left(i(\omega_c t + \varphi_c - k_c x)\right) = E_0 \exp(i\omega_c t + \varphi_c) \quad (\text{E.41})$$

If the mirror is detuned by x_t (here given in meters) then the electric field at the mirror is:

$$E_{\text{mir}} = E_{\text{in}} \exp(-i k_c x_t) \quad (\text{E.42})$$

With the given parameters for the signal frequency the position modulation can be written as $x_m = a_s \cos(\omega_s t + \varphi_s)$ and thus the reflected field at the mirror is:

$$E_{\text{refl}} = r E_{\text{mir}} \exp(i 2k_c x_m) = r E_{\text{mir}} \exp\left(i 2k_c a_s \cos(\omega_s t + \varphi_s)\right) \quad (\text{E.43})$$

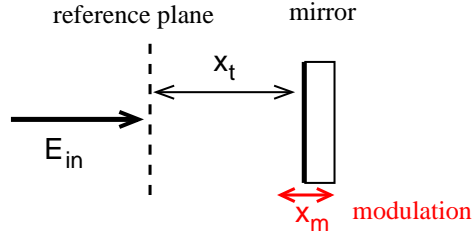


Figure E.2: Signal applied to a mirror: modulation of the mirror position

with $m = 2k_c a_s$ this can be expressed as:

$$\begin{aligned}
 E_{\text{refl}} &= r E_{\text{mir}} \left(1 + i \frac{m}{2} \exp \left(-i (\omega_s t + \varphi_s) \right) + i \frac{m}{2} \exp \left(i (\omega_s t + \varphi_s) \right) \right) \\
 &= r E_{\text{mir}} \left(1 + \frac{m}{2} \exp \left(-i (\omega_s t + \varphi_s - \pi/2) \right) + \right. \\
 &\quad \left. \frac{m}{2} \exp \left(i (\omega_s t + \varphi_s + \pi/2) \right) \right)
 \end{aligned} \tag{E.44}$$

This gives an amplitude for both sidebands of:

$$a_{\text{sb}} = r m/2 E_0 = r k_c a_s E_0 \tag{E.45}$$

The phase back at the reference plane is:

$$\varphi_{\text{sb}} = \varphi_c + \frac{\pi}{2} \pm \varphi_s - (k_c + k_{\text{sb}}) x_t \tag{E.46}$$

with the plus sign referring to the ‘upper’ sideband and the minus sign to the ‘lower’ sideband. As in FINESSE the tuning is given in degrees, i. e., the conversion from x_t to ϕ has to be taken into account:

$$\begin{aligned}
 \varphi_{\text{sb}} &= \varphi_c + \frac{\pi}{2} \pm \varphi_s - (\omega_c + \omega_{\text{sb}})/c x_t \\
 &= \varphi_c + \frac{\pi}{2} \pm \varphi_s - (\omega_c + \omega_{\text{sb}})/c \lambda_0/360 \phi \\
 &= \varphi_c + \frac{\pi}{2} \pm \varphi_s - (\omega_c + \omega_{\text{sb}})/\omega_0 2\pi/360 \phi
 \end{aligned} \tag{E.47}$$

For a nominal signal amplitude of $a_s = 1$, the sideband amplitudes become very large, for an input light at the default wavelength typically:

$$a_{\text{sb}} = r k_c E_0 = r \omega_c/c E_0 = r 2\pi/\lambda_0 E_0 \approx 6 \cdot 10^6 \tag{E.48}$$

Numerical algorithms have the best accuracy when the various input numbers are of the same order of magnitude, usually set to a number close to one. Therefore, the signal amplitudes for mirrors (and beam splitters) should be scaled: A natural scale is to define the modulation in radians instead of meters. The scaling factor then is ω_0/c , and with $a = \omega_0/c a'$ the reflected field at the mirror becomes:

$$\begin{aligned}
 E_{\text{refl}} &= r E_{\text{mir}} \exp \left(i 2\omega_c/\omega_0 x_m \right) \\
 &= r E_{\text{mir}} \exp \left(i 2\omega_c/\omega_0 a'_s \cos(\omega_s t + \varphi_s) \right)
 \end{aligned} \tag{E.49}$$

and thus the sideband amplitudes:

$$a_{\text{sb}} = r \omega_c/\omega_0 a'_s E_0 \quad (\text{E.50})$$

with the factor ω_c/ω_0 typically being close to one. The units of the computed transfer functions are ‘output unit per radian’; which are neither common nor intuitive. The inverse scaling factor c/ω_0 can be used to convert the result into the more common ‘per meter’.

When a light field is reflected at the back surface of the mirror, the sideband amplitudes are computed accordingly. The same formulas as above can be applied with $x_m \rightarrow -x_m$ and $x_t \rightarrow -x_t$, yielding the same amplitude as for the reflection at the front surface, but with a slightly different phase:

$$\begin{aligned} \varphi_{\text{sb,back}} &= \varphi_c + \frac{\pi}{2} \pm (\varphi_s + \pi) + (k_c + k_{\text{sb}}) x_t \\ &= \varphi_c + \frac{\pi}{2} \pm (\varphi_s + \pi) + (\omega_c + \omega_{\text{sb}})/\omega_0 2\pi/360 \phi \end{aligned} \quad (\text{E.51})$$

Beam splitter: Similarly to the mirror, a modulation of the position of a beam splitter creates phase-modulation sidebands in the reflected light. In fact, the same computations as for mirrors can be used for beam splitters. However, all distances have to be scaled by $\cos(\alpha)$, with α being the angle of incidence: Again, only the reflected fields are changed by the modulation, and the fields reflected at the front and back surface have different phases. The amplitudes and phase compute to:

$$\begin{aligned} a_{\text{sb}} &= r \omega_c/\omega_0 a_s \cos(\alpha) E_0 \\ \varphi_{\text{sb,front}} &= \varphi_c + \frac{\pi}{2} \pm \varphi_s - (k_c + k_{\text{sb}})x_t \cos(\alpha) \\ \varphi_{\text{sb,back}} &= \varphi_c + \frac{\pi}{2} \pm (\varphi_s + \pi) + (k_c + k_{\text{sb}})x_t \cos(\alpha) \end{aligned} \quad (\text{E.52})$$

Space: For interferometric gravitational-wave detectors, the ‘free space’ is an important component for injecting the signal: A passing gravitational wave modulates the optical path length of the space. A light field travelling along this ‘free space’ will thus be modulated in phase. The phase change $\varphi(t)$ accumulated over the full length is (see, for example, [Mizuno95]):

$$\varphi(t) = \frac{\omega_c n L}{c} + \frac{a_s \omega_c}{2 \omega_s} \sin\left(\omega_s \frac{n L}{c}\right) \cos\left(\omega_s \left(t - \frac{n L}{c}\right)\right) \quad (\text{E.53})$$

with L the length of the space, n the index of refraction and a_s the signal amplitude given as strain (h). This results in a signal sideband amplitude and phase of:

$$\begin{aligned} a_{\text{sb}} &= \frac{1}{4} \frac{\omega_c}{\omega_s} \sin\left(\omega_s \frac{n L}{c}\right) a_s E_0 \\ \varphi_{\text{sb}} &= \varphi_c + \frac{\pi}{2} \pm \varphi_s - (\omega_c + \omega_s) \frac{n L}{c} \end{aligned} \quad (\text{E.54})$$

Laser: The light from a laser can be modulated in amplitude, phase or frequency. For example, the frequency modulation of the laser is described as:

$$E = E_0 \exp\left(i\left(\omega_c t + a_s/\omega_s \cos(\omega_s t + \varphi_s) + \varphi_c\right)\right) \quad (\text{E.55})$$

The amplitudes of the signal sidebands are scaled with frequency as:

$$\begin{aligned} a_{\text{sb}} &= \frac{a_s}{2\omega_s} E_0 \\ \varphi_{\text{sb}} &= \varphi_c + \frac{\pi}{2} \pm \varphi_s \end{aligned} \quad (\text{E.56})$$

Signal modulations of amplitude and phase are computed accordingly.

Modulator: The formalism described here uses simplified modulators. Nevertheless, the component offers many parameters that could be modulated by an applied signal. Of particular interest is a phase modulation of the initial modulation frequency called RF frequency in the following to distinguish it from the signal modulation frequency. This can be understood as ‘phase noise’ of the oscillator that provides the RF modulation frequency.

Analysing the effects of oscillator phase noise on the interferometer output signal is useful for computing requirements for the oscillator with respect to a certain interferometer configuration. In Equation E.7 the phase of the RF modulation frequency was supposed to be zero and is not given explicitly. In general, the modulated light has to be written with a phase term:

$$E = E_0 \exp\left(i\left(\omega_0 t + m \cos\left(\omega_m t + \varphi_m(t)\right)\right)\right) \quad (\text{E.57})$$

Using Equation E.8 phase noise can be included as:

$$E = E_0 \exp(i\omega_0 t) \sum_{k=-N}^N i^k J_k(m) \exp\left(ik(\omega_m t + \varphi_m(t))\right) \quad (\text{E.58})$$

with N as the maximum order of modulation sidebands used in the simulation. A transfer function can be computed to investigate the coupling of $\varphi_m(t)$ to the output signal. The input signal is a cosine modulation at the signal frequency (ω_{noise}) applied to the phase of the RF modulation:

$$\varphi_m(t) = m_2 \cos(\omega_{\text{noise}} t) \quad (\text{E.59})$$

This results in the following field:

$$\begin{aligned} E = E_0 \exp(i\omega_0 t) \sum_{k=-N}^N i^k J_k(m) \exp(ik\omega_m t) \times \\ \sum_{l=-\infty}^{\infty} i^l J_l(k m_2) \exp(il\omega_{\text{noise}} t) \end{aligned} \quad (\text{E.60})$$

The extra modulation of φ_m thus adds extra sidebands to the light (they will be called ‘audio sidebands’ in the following since in most cases the interesting signal frequencies are

between DC to some kHz, whereas the RF modulation frequencies are very often in the MHz regime). The audio sidebands are generated around each RF modulation sideband. We are interested in the coupling of the audio sidebands to the interferometer output, because these sidebands will generate a false signal and therefore limit the sensitivity of the interferometer. For computing transfer functions, the amplitudes of the signal sidebands (here: modulation index of audio sidebands) are assumed to be very small so that only the terms for $l = -1, 0, 1$ in the second sum in Equation E.60 have to be taken into account and the Bessel functions can be simplified:

$$E = E_0 \exp(i\omega_0 t) \sum_{k=-N}^N i^k J_k(m) \exp(ik\omega_m t) \times \left(1 + i \frac{k m_2}{2} \exp(-i\omega_{\text{noise}} t) + i \frac{k m_2}{2} \exp(i\omega_{\text{noise}} t) + O((km_2)^2)\right) \quad (\text{E.61})$$

When the user-defined absolute phases and modulation amplitudes are included, the electric field leaving the modulator can be written as:

$$E = E_0 \exp\left(i(\omega_0 t + \varphi_0)\right) \sum_{k=-N}^N i^k J_k(m) \exp\left(ik(\omega_m t + \varphi_m)\right) \times \left(1 + i \frac{k m_2 a_s}{2} \exp\left(-i(\omega_s t + \varphi_s)\right) + i \frac{k m_2 a_s}{2} \exp\left(i(\omega_s t + \varphi_s)\right) + O((km_2)^2)\right) \quad (\text{E.62})$$

and with

$$E_{\text{mod}} = E_0 J_k(m) \quad (\text{E.63})$$

$$\varphi_{\text{mod}} = \varphi_0 + k\frac{\pi}{2} + k\varphi_m$$

the sideband amplitudes are:

$$a_{\text{sb}} = \frac{a_s k m_2}{2} E_{\text{mod}} \quad (\text{E.64})$$

$$\varphi_{\text{sb}} = \varphi_{\text{mod}} + \frac{\pi}{2} \pm \varphi_s$$

E.2.9 Detectors and demodulation

Solving the set of linear equations for a given optical setup and input fields yields light field amplitudes. Light fields cannot be detected directly; photo diodes are used instead to measure the light power. A photo diode converts the light power into a photo current. The photo diodes used in the GEO 600 project employ a trans-impedance amplifier to convert the photo current into an output voltage. When a modulation-demodulation control scheme is used, this voltage is further demodulated by an electronic mixer. Thus, the ‘output signal’ of an interferometer can be given in the following units:

- amplitude of a light field, here given in $[\sqrt{\text{W}}]$ (see Section E.2.3)
- power of a light field in $[\text{W}]$

- photo current proportional to light power in [A]
- electrical voltage proportional to photo current in [V]
- electrical voltage proportional to one frequency component of the photo current (mixer output) in [V]

The scaling factor from Watts of light power to Amperes of photo current (also called *responsivity*) is given as:

$$C_{\text{ampere}} = \frac{e \eta \lambda_0}{2\pi \hbar c} \left[\frac{\text{A}}{\text{W}} \right] \quad (\text{E.65})$$

with e the electron charge, η the quantum efficiency of the detector, \hbar Planck's constant and c the speed of light. λ_0 is the wavelength of the light fields⁴. The scaling factors for the trans-impedance amplifier and the mixer depend on the actual design of the electronic circuit. In the following, these scaling factors are ignored: signals for photo diodes are computed in Watts even if the output of a mixer is described.

In general, several light fields with different amplitudes, phases and frequencies will be present on a photo diode. The resulting light field in an interferometer output (i. e., on a photo diode) can be written as:

$$E = \exp(i\omega_0 t) \sum_{n=0}^N a_n \exp(i\omega_n t) \quad (\text{E.66})$$

with a_n as complex amplitudes. The frequency ω_0 is defined arbitrarily as the default laser frequency, and ω_n are offset frequencies to ω_0 (either positive, negative or zero). The advantage of this notation is that the various components are sorted according to their Fourier frequency (offset to ω_0).

Note that very often a slightly different representation is chosen:

$$E = \exp(i\omega_0 t) \left(b_0 + b_1 \exp(i\omega_1 t) + b_{-1} \exp(-i\omega_1 t) + \dots \right. \\ \left. + b_M \exp(i\omega_M t) + b_{-M} \exp(-i\omega_M t) \right) \quad (\text{E.67})$$

where ω_0 is the carrier frequency and $\omega_1, \omega_2, \dots > 0$ are the absolute frequency offsets of the (symmetric) sidebands. In a general approach, however, more than one carrier field might be present, and the sideband fields are not necessarily symmetric with respect to the carrier fields; therefore, Equation E.66 is to be preferred.

When the light field is given as in Equation E.66, the amplitude at a certain Fourier frequency ω_k can be computed as:

$$z = \sum_n a_n \quad \text{with} \quad \{n \mid n \in \{0, \dots, N\} \wedge \omega_n = \omega_k\} \quad (\text{E.68})$$

⁴ It is convenient to use only one wavelength even if several light fields with different wavelengths are present or sidebands are concerned. In most cases, the differences in λ are small so that the error is negligible.

The light power as detected by a photo diode is:

$$\begin{aligned}
 P &= E \cdot E^* = \sum_{i=0}^N \sum_{j=0}^N a_i a_j^* \exp(i(\omega_i - \omega_j)t) \\
 &= A_0 + A_1 \exp(i\bar{\omega}_1 t) + A_2 \exp(i\bar{\omega}_2 t) + \dots
 \end{aligned} \tag{E.69}$$

with A_i as light power sorted by the beat frequencies $\bar{\omega}_i$. In practice, one seldomly has to compute the light power as above. Certain subsets of the sum in Equation E.69 can be used instead. The two most common signals are the DC value (average power) and the power demodulated at a certain frequency (or demodulated sequentially at several frequencies).

The DC value: gives the average light power on the detector. It is the sum of all components (in Equation E.69) with no frequency dependence. The frequency dependence vanishes when ω_i equals ω_j and thus the exponent becomes zero. The output is a real number:

$$x = \sum_i \sum_j a_i a_j^* \quad \text{with} \quad \{i, j \mid i, j \in \{0, \dots, N\} \wedge \omega_i = \omega_j\} \tag{E.70}$$

A single demodulation can be described by a multiplication of the light power with the term $\cos(\omega_x + \theta_x)$ (with ω_x the demodulation frequency and θ_x the demodulation phase). Electronically, this represents a so-called mixer. The mixer has two inputs and one output. One input is connected to the photo diode, and the second input is connected to an oscillator that generates a harmonic signal at the demodulation frequency (at some demodulation phase). The harmonic signal for the second input of the mixer is also called *local oscillator*. Note that this *electrical* local oscillator is different from the *optical* local oscillator.

The input signal from the photo diode is:

$$S_0 = |E|^2 = E \cdot E^* = \sum_{i=0}^N \sum_{j=0}^N a_i a_j^* \exp(i(\omega_i - \omega_j)t) \tag{E.71}$$

The mixer multiplies both input signals. The output of an (ideal) mixer then is:

$$\begin{aligned}
 S_1 &= S_0 \cdot \cos(\omega_x + \theta_x) \\
 &= S_0 \frac{1}{2} (\exp(i(\omega_x t + \theta_x)) + \exp(-i(\omega_x t + \theta_x))) \\
 &= \frac{1}{2} \sum_{i=0}^N \sum_{j=0}^N a_i a_j^* \exp(i(\omega_i - \omega_j)t) \times \\
 &\quad \left(\exp(i(\omega_x t + \theta_x)) + \exp(-i(\omega_x t + \theta_x)) \right)
 \end{aligned} \tag{E.72}$$

With

$$\begin{aligned} A_{ij} &= a_i a_j^* \quad \text{and} \\ \exp(i\omega_{ij}t) &= \exp(i(\omega_i - \omega_j)t) \end{aligned} \quad (\text{E.73})$$

we can write:

$$\begin{aligned} S_1 &= \frac{1}{2} \left(\sum_{i=0}^N A_{ii} + \sum_{i=0}^N \sum_{j=i+1}^N \left(A_{ij} \exp(i\omega_{ij}t) + A_{ij}^* \exp(-i\omega_{ij}t) \right) \right) \times \\ &\quad \left(\exp(i(\omega_x t + \theta_x)) + \exp(-i(\omega_x t + \theta_x)) \right) \end{aligned} \quad (\text{E.74})$$

In most cases, only the low-frequency component of S_1 is used by applying a low pass filter:

$$\begin{aligned} S_{1,\text{LP}} &= \frac{1}{2} (A_{ij} \exp(-i\theta_x) + A_{ij}^* \exp(i\theta_x)) \\ &= \text{Re} \{ A_{ij} \exp(-i\theta_x) \} \\ &\quad \text{with } \{i, j \mid i, j \in \{0, \dots, N\} \wedge \omega_{ij} = \omega_x\} \end{aligned} \quad (\text{E.75})$$

The second quadrature may also be of interest. It can be obtained by using a second mixer with a local oscillator that has a 90° offset to the local oscillator of the previous one. This yields:

$$\begin{aligned} S_{1,\text{LP,quad}} &= \text{Re} \{ A_{ij} \exp(-i(\theta_x - \pi/2)) \} \\ &= \text{Re} \{ i \cdot A_{ij} \exp(-i\theta_x) \} \\ &= -\text{Im} \{ A_{ij} \exp(-i\theta_x) \} \\ &\quad \text{with } \{i, j \mid i, j \in \{0, \dots, N\} \wedge \omega_{ij} = \omega_x\} \end{aligned} \quad (\text{E.76})$$

The in-phase and quadrature signal can be understood as the real and imaginary part of a complex number:

$$z = A_{ij}^* \quad \text{with } \{i, j \mid i, j \in \{0, \dots, N\} \wedge \omega_{ij} = \omega_x\} \quad (\text{E.77})$$

A double demodulation is a multiplication with two local oscillators:

$$S_2 = S_0 \cdot \cos(\omega_x + \theta_x) \cos(\omega_y + \theta_y) \quad (\text{E.78})$$

This can be written as:

$$\begin{aligned} S_2 &= S_0 \frac{1}{2} (\cos(\omega_y + \omega_x + \theta_y + \theta_x) + \cos(\omega_y - \omega_x + \theta_y - \theta_x)) \\ &= S_0 \frac{1}{2} (\cos(\omega_+ + \theta_+) + \cos(\omega_- + \theta_-)) \end{aligned} \quad (\text{E.79})$$

and thus be reduced to two single demodulations. Again, only the low-frequency component shall be extracted. With Equation E.75 we get two complex numbers:

$$\begin{aligned} z1 &= A_{ij}^* \quad \text{with} \quad \{i, j \mid i, j \in \{0, \dots, N\} \wedge \omega_i - \omega_j = \omega_+\} \\ z2 &= A_{kl}^* \quad \text{with} \quad \{k, l \mid k, l \in \{0, \dots, N\} \wedge \omega_k - \omega_l = \omega_-\} \end{aligned} \quad (\text{E.80})$$

The demodulation phases are applied as follows to obtain a real output signal (two sequential mixers):

$$x = \text{Re} \{ (z1 \exp(-i\theta_x) + z2 \exp(i\theta_x)) \exp(-i\theta_y) \} \quad (\text{E.81})$$

A demodulation phase for the first frequency (here θ_x) must be given in any case. When a transfer functions is to be computed it is convenient to generate a complex output by omitting the second phase:

$$z = z1 \exp(-i\theta_x) + z2 \exp(i\theta_x) \quad (\text{E.82})$$

Multiple demodulations can also be reduced to single demodulations as above.

E.3 Transverse electromagnetic modes

The analysis with geometric optics as described above allows to perform a large variety of simulations. Some analysis tasks, however, include the beam shape and position, i. e., the properties of the field transverse to the optical axis. The effects of misaligned components, for example, can only be computed if beam shape and position are taken into account.

The following sections describe a straightforward extension of the above analysis using transverse electromagnetic modes (TEM): Hermite-Gauss modes are used to describe the geometrical properties of par-axial beams. A mathematical description of Hermite-Gauss modes can be found in Appendix C.

E.3.1 Electrical field with Hermite-Gauss modes

In the previous analysis, a laser beam was described in general by the sum of various frequency components of its electric field:

$$E(t, z) = \sum_j a_j \exp(i(\omega_j t - k_j z)) \quad (\text{E.83})$$

Now, the geometric shape of the beam is included by describing each frequency component by a sum of Hermite-Gauss modes:

$$E(t, x, y, z) = \sum_j \sum_{n,m} a_{jnm} u_{nm}(x, y) \exp(i(\omega_j t - k_j z)) \quad (\text{E.84})$$

Each part of the sum can be treated as an independent field that can be described using the equation for geometric optics with only two exceptions:

- The propagation through free space has to include the Guoy phase shift (see Appendix D);
- Upon reflection or transmission at a mirror or beam splitter the different Hermite-Gauss modes may be coupled (see below).

Gaussian beam parameters: As described in Appendix C, each set of Hermite-Gauss modes forms a complete and orthonormalised set of eigen-modes of a spherical cavity. The set of eigen-modes is characterised by the beam parameter q defined as:

$$q(z) = i z_R + z - z_0 \quad \text{and} \quad q_0 = i z_R - z_0 \quad (\text{E.85})$$

with z_R being the Rayleigh range and z_0 the position of the beam waist. Each beam segment, that is the beam in the component ‘free space’, can be described by one constant beam parameter q_0 . The beam parameter q_0 can be changed when the beam interacts with a spherical surface.

If the interferometer is confined to a plane, it is convenient to use two beam parameters, q_s for the sagittal plane and q_t for the tangential plane:

$$u_{nm}(x, y) = u_n(x, q_t) u_m(y, q_s) \quad (\text{E.86})$$

The transformation of the beam parameter can be performed by the so-called ABCD matrix-formalism [Siegman]. When a beam passes a mirror, beam splitter, lens or a free space, the beam parameter q_1 is transformed to q_2 . The transformation can be described by four coefficients commonly given as a matrix:

$$\frac{q_2}{n_2} = \frac{A \frac{q_1}{n_1} + B}{C \frac{q_1}{n_1} + D} \quad \text{with the coefficient matrix:} \quad M = \begin{pmatrix} A & B \\ C & D \end{pmatrix} \quad (\text{E.87})$$

with n_1 being the index of refraction at the beam segment defined by q_1 and n_2 the index of refraction at the beam segment described by q_2 . The ABCD matrices for the optical components used by FINESSE are given below.

Transmission through a mirror: A mirror in this context is a single, partly reflecting surface with an angle of incidence of 90° . The transmission is described as:

$$M = \begin{pmatrix} 1 & 0 \\ \frac{n_2 - n_1}{R_C} & 1 \end{pmatrix} \quad \begin{array}{c} \xrightarrow{q_1} \\ n_1 \end{array} \left. \vphantom{\begin{matrix} q_1 \\ n_1 \end{matrix}} \right\} \begin{array}{c} \xrightarrow{q_2} \\ n_2 \end{array} \quad (\text{E.88})$$

with R_C being the radius of curvature of the spherical surface. The sign of the radius is defined such that R_C is negative if the center of the sphere is located in the direction of

propagation. The curvature shown above (in Equation E.88), for example, is described by a positive radius.

The matrix for the transmission in the opposite direction of propagation is identical.

Reflection at a mirror: The matrix for reflection is given as:

$$M = \begin{pmatrix} 1 & 0 \\ -\frac{2}{R_C} & 1 \end{pmatrix} \quad \begin{array}{c} \mathbf{q}_1 \rightarrow \\ \mathbf{q}_2 \leftarrow \end{array} \quad \begin{array}{c} \text{---} \\ \text{---} \\ \text{---} \\ \text{---} \\ \text{---} \\ \text{---} \\ \text{---} \\ \text{---} \\ \text{---} \\ \text{---} \end{array} \quad (\text{E.89})$$

The reflection at the back surface can be described by the same matrix with $C \rightarrow -C$.

Transmission through a beam splitter: A beam splitter is understood as a single surface with an arbitrary angle of incidence α_1 . The matrices for transmission and reflection are different for the sagittal and tangential planes (M_s and M_t).

$$M_t = \begin{pmatrix} \frac{\cos(\alpha_2)}{\cos(\alpha_1)} & 0 \\ \frac{\Delta n}{R_C} & \frac{\cos(\alpha_1)}{\cos(\alpha_2)} \end{pmatrix} \quad \begin{array}{c} \mathbf{q}_1 \\ \alpha_1 \\ n_1 \end{array} \quad \begin{array}{c} \mathbf{q}_2 \\ \alpha_2 \\ n_2 \end{array} \quad (\text{E.90})$$

$$M_s = \begin{pmatrix} 1 & 0 \\ \frac{\Delta n}{R_C} & 0 \end{pmatrix}$$

with α_2 given by:

$$n_1 \sin(\alpha_1) = n_2 \sin(\alpha_2) \quad (\text{E.91})$$

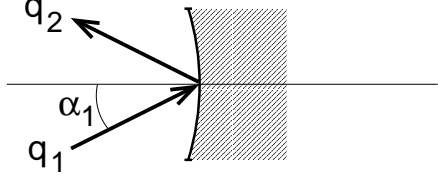
and Δn as:

$$\Delta n = \frac{n_2 \cos(\alpha_2) - n_1 \cos(\alpha_1)}{\cos(\alpha_1) \cos(\alpha_2)} \quad (\text{E.92})$$

If the direction of propagation is reversed, the matrix for the sagittal plane is identical and the matrix for the tangential plane can be obtained by changing the coefficients A and D as follows:

$$\begin{array}{l} A \rightarrow 1/A \\ D \rightarrow 1/D \end{array} \quad (\text{E.93})$$

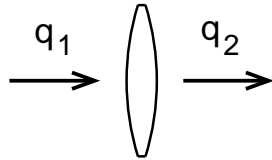
Reflection at a beam splitter: The reflection at the front surface of a beam splitter is given by:

$$M_t = \begin{pmatrix} 1 & 0 \\ -\frac{2}{R_C \cos(\alpha_1)} & 1 \end{pmatrix} \quad M_s = \begin{pmatrix} 1 & 0 \\ -\frac{2 \cos(\alpha_1)}{R_C} & 1 \end{pmatrix} \quad (E.94)$$


For the description of a reflection at the back surface the matrices have to be changed as follows:


$$R_C \longrightarrow -R_C \quad \alpha_1 \longrightarrow -\alpha_2 \quad (E.95)$$

Transmission through a thin lens: A thin lens transforms the beam parameter as follows:

$$M = \begin{pmatrix} 1 & 0 \\ -\frac{1}{f} & 1 \end{pmatrix} \quad (E.96)$$


with f as the focal length. The matrix for the opposite direction of propagation is identical.

Transmission through a free space: On propagation through a free space of the length L and index of refraction n the beam parameter is transformed as follows:

$$M = \begin{pmatrix} 1 & \frac{L}{n} \\ 0 & 1 \end{pmatrix} \quad (E.97)$$


The matrix for the opposite direction of propagation is identical.

E.3.2 Coupling of Hermite-Gauss modes

Let us assume two different cavities with different sets of eigen-modes. The first set is characterised by the beam parameter q_1 and the second one by the parameter q_2 . A beam with all power in the fundamental mode $TEM_{00}(q_1)$ leaves the first cavity and is injected into the second. Here, two ‘mis-configurations’ are possible:

- If the optical axes of the beam and the second cavity do not overlap perfectly, the setup is called *misaligned*
- If the beam size or shape of the beam at the second cavity does not match the beam shape and size of the (resonant) fundamental eigen-mode ($q_1(z_{\text{cav}}) \neq q_2(z_{\text{cav}})$), the beam is not *mode-matched* to the second cavity, i. e., there is a *mode mismatch*.

The above mis-configurations can be used in the context of simple beam segments. In the simulation, the beam parameter for the input light is specified by the user. Ideally, the ABCD matrices allow to trace a beam through the optical system by computing the proper beam parameter for each beam segment. In this case, the basis system of Hermite-Gauss modes is transformed the same way as the beam so that the coefficients a_{jnm} in Equation E.84 remain constant, i. e., the different modes are *not coupled*.

For example, an input beam described by the beam parameter q_1 is passed through several optical components, and at each component the beam parameter is transformed according to the respective ABCD matrix. Thus, the electric field in each beam segment is described by Hermite-Gauss modes based on different beam parameters, but the relative power between the Hermite-Gauss modes with different mode numbers remains constant, i. e., a beam in a TEM₀₀ mode is described as a TEM₀₀ mode throughout the full system.

In practice, it is usually impossible to compute proper beam parameters for each beam segment as above, especially when the beam passes a certain segment more than once. The most simple example is the reflection at a spherical mirror: The input beam shall be described by q_1 . From Equation E.89 we know that the proper beam parameter of the reflected beam is given as:

$$q_2 = \frac{q_1}{-2q_1/R_C + 1} \tag{E.98}$$

with R_C being the radius of curvature of the mirror. In general, we get $q_1 \neq q_2$ and thus two different ‘proper’ beam parameters for the same beam segment. Only a special radius of curvature would result in matched beam parameters ($q_1 = q_2$).

Coupling coefficients

The Hermite-Gauss modes are coupled whenever a beam is not matched to a cavity or to a beam segment or if the beam and the segment are misaligned. In this case, the beam has to be described using the parameters of the beam segment (beam parameter and optical axis). This is always possible because each set of Hermite-Gauss modes (defined by the beam parameter at a position z) forms a complete set. Such a change of the basis system results in a different distribution of light power in the (new) Hermite-Gauss modes and can be expressed by coupling coefficients that yield the change in the light power with respect to mode number.

Let us assume a beam described by the beam parameter q_1 is injected into a segment described by the parameter q_2 . The optical axis of the beam shall be misaligned: the coordinate system of the beam is given by (x, y, z) and the beam travels along the z -axis.

The beam segment is parallel to the z' -axis and the coordinate system (x', y', z') is given by rotating the (x, y, z) system around the y -axis by an angle γ . The coupling coefficients are defined as:

$$u_{n_1 m_1}(q_1) \exp(i(\omega t - kz)) = \sum_{n_2, m_2} k_{n_1, m_1, n_2, m_2} u_{n_2 m_2}(q_2) \exp(i(\omega t - kz')) \quad (\text{E.99})$$

with $u_{n_1 m_1}(q_1)$ as the Hermite-Gauss modes used to describe the injected beam and $u_{n_2 m_2}(q_2)$ as the ‘new’ modes that are used to describe the light in the beam segment.

Using the fact that the Hermite-Gauss modes u_{nm} are orthonormal, we can compute the coupling coefficients by the following convolution [Bayer-Helms]:

$$k_{n_1, m_1, n_2, m_2} = \exp\left(i 2kz' \sin^2\left(\frac{\gamma}{2}\right)\right) \iint dx' dy' u_{n_2 m_2} \exp(ikx' \sin \gamma) u_{n_1 m_1}^* \quad (\text{E.100})$$

These equations are very useful in the par-axial approximation as the coupling coefficients decrease with large mode numbers. In order to be described as par-axial, the angle γ must not be larger than the diffraction angle of the beam and the beam parameters q_1 and q_2 must not differ too much⁵.

The convolution given in Equation E.100 can directly be computed using numerical integration. In [Bayer-Helms], however, a different expression for these coupling coefficients is derived by using algebraic transformation; the convolution integrals are then expressed by simpler sums. This mathematical description of the coefficients has been implemented in FINESSE because it provides a numerically faster method than the direct numerical integration.

E.3.3 Misalignment angles at a beam splitter

The coupling of Hermite-Gauss modes in a misaligned setup as described above is defined by a misalignment angle. However, in the case of a beam splitter under arbitrary incidence the analysis of the geometry is complicated because it is commonly described in three different coordinate systems. Our discussion will be limited to the following setup: the beam travels along the z -axis (towards positive numbers) and a beam splitter (surface) is located at $z = 0$ and may be rotated around the y -axis by an angle α ($|\alpha|$ = angle of incidence). This shall be the ‘‘aligned’’ setup.

To describe a misalignment of the beam splitter, one usually refers to a coordinate system attached to the beam splitter. This coordinate system is called x', y', z' in the following and can be derived - in this case - by rotating the initial coordinate system by α around the y -axis. The misalignment can be quantified by two angles β_x, β_y that describe the rotation of the beam splitter around the x' -axis and the y' -axis, respectively. Rotation around the x' -axis is often called *tilt*, and rotation around the y' -axis just *rotation*. Whereas the initial rotation α may be large, the misalignment angles β_x and β_y are usually small.

⁵ A quantitative measure for the allowed mismatch in q_1 and q_2 can possibly be derived by comparing the respective beam sizes and diffraction angles.

In fact, most models describing the effects of misalignment are using approximations for small perturbations.

Here, we are interested in the exact direction of the reflected beam. The reflected beam, though, may be characterised in yet another coordinate system (x'', y'', z'') with the z'' -axis being parallel to the reflected beam. This coordinate system can be derived from (x, y, z) by a rotation of 2α around the y -axis. A misalignment of the beam splitter will cause the beam to also be misaligned. The misalignment of the beam is given by the two angles δ_x, δ_y that describe the rotation around the x'' -axis and the y'' -axis, respectively.

It can easily be shown that for $\beta_x = 0$, the misalignment of the beam is $\delta_x = 0$ and $\delta_y = 2\beta_y$. For normal incidence ($\alpha = 0$) we get a similar result for $\beta_y = 0$: $\delta_y = 0$ and $\delta_x = 2\beta_x$. For arbitrary incidence, the geometry is more complex. In order to compute the effect caused by a tilt of the beam splitter we need basic vector algebra. Please note that the following vectors are given in the initial coordinate system (x, y, z) . First, we have to compute the unit vector of the beam splitter surface \vec{e}_{bs} . This vector is rooted at $(0,0,0)$, perpendicular to the surface of the beam splitter and pointing towards the negative z -axis for $\alpha = 0$.

For $\alpha = 0$ this vector is $\vec{e}_{\text{bs}} = -\vec{e}_z$. Turning the beam splitter around the y -axis gives:

$$\vec{e}_{\text{bs}} = (\sin(\alpha), 0, -\cos(\alpha)) \quad (\text{E.101})$$

Next, the beam splitter is tilted by the angle β_x around the x' -axis. Thus, the surface vector becomes:

$$\vec{e}_{\text{bs}} = (\sin(\alpha) \cos \beta_x, -\sin(\beta_x), -\cos(\alpha) \cos \beta_x) \quad (\text{E.102})$$

In order to compute the unit vector parallel to the reflected beam, we have to ‘mirror’ the unit vector parallel to the incoming beam $-\vec{e}_z$ at the unit vector perpendicular to the beam splitter. As an intermediate step, we compute the projection of $-\vec{e}_z$ onto \vec{e}_{bs} (see Figure E.3):

$$\vec{a} = -(\vec{e}_z \cdot \vec{e}_{\text{bs}}) \vec{e}_{\text{bs}} = \cos(\beta_x) \cos(\alpha) \vec{e}_{\text{bs}} \quad (\text{E.103})$$

The reflected beam (\vec{e}_{out}) is then computed as:

$$\begin{aligned} \vec{e}_{\text{out}} &= -\vec{e}_z + 2(\vec{a} + \vec{e}_z) = 2\vec{a} + \vec{e}_z \\ &= (2 \cos^2(\beta_x) \cos(\alpha) \sin(\alpha), -2 \cos(\beta_x) \cos(\alpha) \sin(\beta_x), -2 \cos^2(\beta_x) \cos^2(\alpha) + 1) \\ &=: (x_o, y_o, z_o) \end{aligned} \quad (\text{E.104})$$

To evaluate the change of direction of the outgoing beam caused by the tilt of the beam splitter β_x , we have to compare the general output vector \vec{e}_{out} with the output vector for no tilt $\vec{e}_{\text{out}}|_{\beta_x=0}$. Indeed, we want to know two angles: the angle between the two vectors *in* the z, x -plane (δ_y) and the angle between \vec{e}_{out} and the z, x -plane (δ_x). The latter one is simply:

$$\sin(\delta_x) = 2 \cos(\beta_x) \cos(\alpha) \sin(\beta_x) = \cos(\alpha) \sin(2\beta_x) \quad (\text{E.105})$$

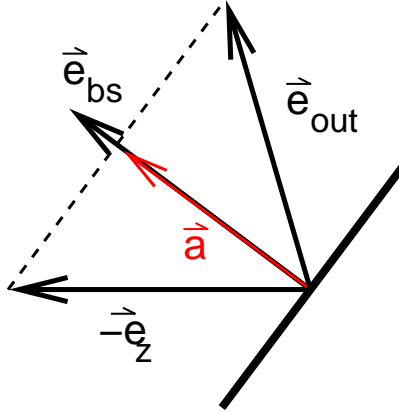


Figure E.3: Mirroring of vector $-\vec{e}_z$ at the unit vector of the beam splitter surface \vec{e}_{bs} .

For small misalignment angles ($\sin(\beta_x) \approx \beta_x$ and $\sin(\delta_x) \approx \delta_x$), Equation E.105 can be simplified to:

$$\delta_x \approx 2\beta_x \cos(\alpha) \quad (\text{E.106})$$

One can see that the beam is tilted less for an arbitrary angle of incidence than at normal incidence. An angle of 45° , which is quite common, yields $\delta_x = \sqrt{2}\beta_x$.

In order to calculate δ_y , we have to evaluate the following scalar product:

$$\begin{aligned} \vec{e}_{\text{out}}|_{y_o=0} \cdot \vec{e}_{\text{out}}|_{\beta_x=0} &= \sqrt{x_o^2 + z_o^2} \cos(\delta_y) \\ \Rightarrow \cos(\delta_y) &= \frac{-1}{\sqrt{x_o^2 + z_o^2}} (x_o \sin(2\alpha) + z_o \cos(2\alpha)) \end{aligned} \quad (\text{E.107})$$

This shows that a pure tilt of the beam splitter also induces a rotation of the beam. The amount is very small and proportional to $\sim \beta_x^2$. For example, with $\alpha = 45^\circ$ and $\beta_x = 1$ mrad, the rotation of the beam is $\delta_y = 60 \mu\text{rad}$. Figure E.4 shows the angles δ_x and δ_y as functions of α for $\beta_x = 1^\circ$.

In the case of $\beta_x \neq 0$ and $\beta_y \neq 0$, the above analysis can be used by changing α to $\alpha' = \alpha + \beta_y$.

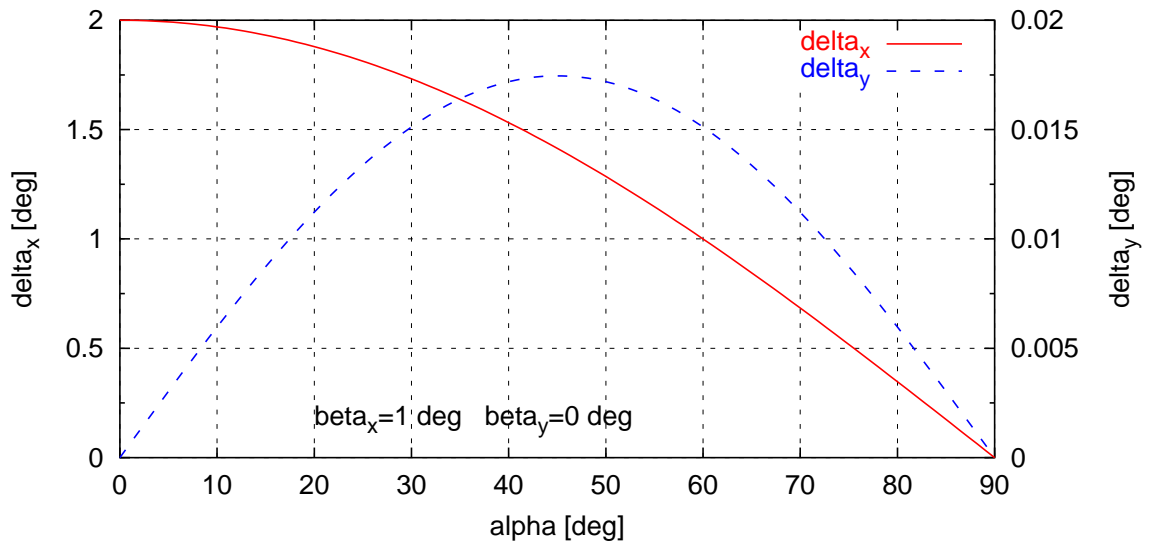


Figure E.4: Misalignment angles of a beam reflected by a beam splitter as functions of the angle of incidence α . The beam splitter is misaligned by $\beta_x = 1^\circ$ and $\beta_y = 0$.

Appendix F

A factor of two

The maximum signal-to-noise ratio (SNR) in tuned Signal Recycling is a factor of two larger than the maximum SNR in detuned Signal Recycling, assuming the same Signal-Recycling mirror and the sensitivity of the recycled Michelson interferometer to be limited by the shot noise of the control sidebands (see Section 3.2). This can be understood as follows: When the Signal-Recycling cavity is detuned by more than the bandwidth of the Signal-Recycling cavity, only one signal sideband is enhanced by the Signal-Recycling cavity. Thus, only half the signal amplitude is used in the detection process. In the following, a more quantitative analysis is given.

The light fields detected by the photo diode are called E_r (tuned case) and E_d (detuned case). The photo diode detects the light power proportional to $|E|^2$. We assume that only the two Schnupp modulation sidebands and the two signal sidebands are present. In general, for the light field at the photo diode we can write:

$$E = A_1 e^{i(\omega+\omega_m)t} + A_2 e^{i(\omega-\omega_m)t} + B_1 e^{i(\omega+\omega_s)t} + B_2 e^{i(\omega-\omega_s)t} \quad (\text{F.1})$$

The power is proportional to:

$$EE^* = A_1^2 + A_2^2 + B_1^2 + B_2^2 + I' + I'' \quad (\text{F.2})$$

with

$$\begin{aligned} I' &= A_1 A_2 (e^{2i\omega_m t} + e^{-2i\omega_m t}) + B_1 B_2 (e^{2i\omega_s t} + e^{-2i\omega_s t}) \\ I'' &= \left. \begin{aligned} &A_1 B_1 (e^{i(\omega_m - \omega_s)t} + e^{-i(\omega_m - \omega_s)t}) \\ &+ A_2 B_2 (e^{-i(\omega_m - \omega_s)t} + e^{i(\omega_m - \omega_s)t}) \end{aligned} \right\} = 2(A_1 B_1 + A_2 B_2) \cos(-) \\ &\quad \left. \begin{aligned} &+ A_1 B_2 (e^{i(\omega_m + \omega_s)t} + e^{-i(\omega_m + \omega_s)t}) \\ &+ A_2 B_1 (e^{-i(\omega_m + \omega_s)t} + e^{i(\omega_m + \omega_s)t}) \end{aligned} \right\} = 2(A_1 B_2 + A_2 B_1) \cos(+)$$

and

$$\begin{aligned} \cos(-) &= \cos((\omega_m - \omega_s)t) \\ \cos(+)&= \cos((\omega_m + \omega_s)t) \end{aligned}$$

Thus we get:

$$EE^* = A_1^2 + A_2^2 + B_1^2 + B_2^2 + 2(A_1B_1 + A_2B_2) \cos(-) \\ + 2(A_1B_2 + A_2B_1) \cos(+) + O(2\omega_w s) + O(2\omega_m)$$

For tuned Signal Recycling we can assume: $A_1 = A_2$ and $B_1 = B_2$. Therefore we get:

$$E_r E_r^* = 2A^2 + 2B^2 + 4AB (\cos(-) + \cos(+)) \\ = 2A^2 + 2B^2 + 8AB \cos(\omega_m t) \cos(\omega_s t)$$

That corresponds to a signal-to-noise ratio of:

$$\text{SNR}_r = C \cdot \frac{8AB}{\sqrt{2(A^2 + B^2)}} \quad (\text{F.3})$$

with C as a constant factor.

In the case of detuned Signal Recycling we can set $A_2 \approx 0$ and $B_2 \approx 0$ and get:

$$E_d E_d^* = A^2 + B^2 + 2AB \cos(-) \\ = A^2 + B^2 + 2AB (\cos(\omega_m t) \cos(\omega_s t) + \sin(\omega_m t) \sin(\omega_s t))$$

Demodulated at ω_m the result is a complex number including both quadratures referring to the signal frequency. With the used quadrature detection, the root mean square of real and imaginary parts gives a $\sqrt{2}$, and we get $2\sqrt{2}AB$ for the ω_m -dependant signal. The corresponding SNR is:

$$\text{SNR}_d = C \cdot \frac{2\sqrt{2}AB}{\sqrt{(A^2 + B^2)}} \quad (\text{F.4})$$

This confirms the intuitive factor of two:

$$\frac{\text{SNR}_r}{\text{SNR}_d} = \frac{8}{\sqrt{2} \cdot 2 \cdot \sqrt{2}} = 2 \quad (\text{F.5})$$

Appendix G

Electronics

G.1 Split photo diode

The quadrant cameras used in the Pound-Drever-Hall loops of the frequency stabilisation system (see Chapter 2, especially Section 2.4.1) use a Centrovision QD50-3T split photo diode. The photo diode consists of four independent sectors.

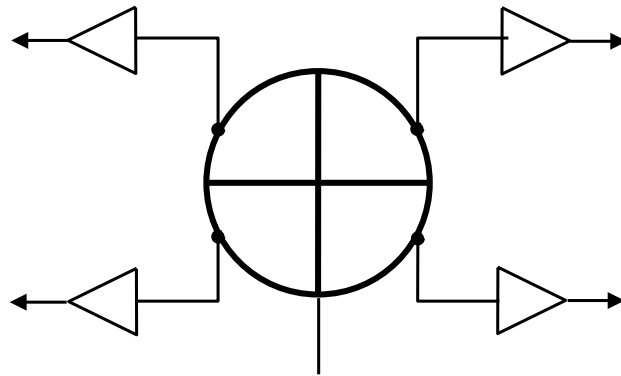


Figure G.1: Schematic diagram of the Centrovision QD50-3T photo diode: The sensitive area is split into four 90-degree sectors. Each sector provides an independent electronic signal.

active area	50 mm ²
diameter	8 mm
element separation	0.2 mm
dark current (max)	1 μ A
dark current (typ.)	70 n A
maximum reverse Voltage (V_r)	60 V
capacitance ($V_r = 0$ V)	75 pF
capacitance ($V_r = 60$ V)	8 pF
rise time (typ.)	12 ns
quantum efficiency @ 1064 nm	≈ 0.2 A/W

Table G.1: Specifications of the Centrovision QD50-3T photo diode [Centrovision].

G.2 Electro-optic modulator

The control loop that stabilises the laser frequency of the master laser to MC1 uses a New Focus 4004 electro-optic modulator as a fast phase corrector (see Section 2.4.3).

operating freq.	DC-100 MHz
material	LiTaO ₃
max. optical power	1 W/mm ²
aperture	2 mm
optical throughput	>93%
capacitance	20-30 pF
modulation depth	15 mrad/V
V_{π}	210 V

Table G.2: Specifications of the New Focus 4004 electro-optic modulator [New Focus].

G.3 Electronic filters

The following sections describe the design of the electronic filters for the MC1 loop, the MC2 loop and the PRC loop. Most of the filter electronics for the mode cleaners are located in two modules (A and B). The schematics of the electronic circuits in these modules are shown in Figures G.3 to G.7. These schematics show some electronic components not described here; they are optional parts of the loop filters and monitor signals connected to the digital electronics (the signal input of module A is shown in Figure G.5 top left).

In addition, the measured and calculated transfer functions of the MC1 filter electronics in modules A and B are shown in Figure G.2. The theoretical transfer functions were computed with a numeric simulation by Gerhard Heinzel [LISO]. The input file for LISO is given in Section G.3.3.

G.3.1 First mode cleaner (MC1)

The filter consists of the following elements (from signal input to output):

- Two switchable, cascaded, transient integrators (pole at 5 Hz, zero at 400 Hz, pole at 4 kHz and zero at 40 kHz).
- A digital potentiometer to adjust the overall gain.

Then the feedback is split into three paths:

The PZT feedback path consists of:

- An integrator (pole at 36 Hz, zero at 360 Hz).

- A high-voltage amplifier with an output of 0 to 300 Volts, the amplifier is also integrating (pole at 1 kHz, zero at 10 kHz).
- The PZT itself. A resistor and the capacitance of the PZT together with its connecting cable ($C=3.5$ nF) form a single pole low-pass at 1 kHz.

The PC (or EOM) feedback path is build of the following components:

- A passive high pass at 70 Hz.
- A complex active stage with a zero at 7 Hz, a double pole at 1 kHz and a zero at 33 kHz. This stage has a gain maximum of 37dB at 1 kHz.
- Another passive high pass at 70 Hz.
- A differentiator with a zero at 360 kHz and a pole at 7 MHz.
- A high voltage amplifier with an output of ± 200 V. The input stage of the amplifier is AC-coupled. The amplifier circuit is integrating with a pole at 3 kHz and a zero at 30 kHz.
- The Pockels cell (together with its connecting cable the capacitance is $C = 1.15$ nF) and the output network of the amplifier form a low pass with a pole at 27 kHz.

The temperature feedback has two sequential, switchable integrators with a pole at 5 mHz and a zero at 50 mHz each.

G.3.2 Second mode cleaner (MC2)

The filter consists of the following elements (from signal input to output):

- A digital potentiometer to adjust the overall gain via the LabView control program.
- A switchable transient integrator (pole at 1.8 kHz, zero at 18 kHz).
- A switchable integrator (pole at 1.1 kHz).

Then the feedback is split into two paths:

The Bypass feedback path; the signal is injected into the MC1 error point after passing the following components:

- A passive high pass at 3.4 Hz.
- A passive, transient low pass (pole at 700 Hz, zero at 1.4 kHz).

The MC1 (or MMC1b) feedback path uses the coil-magnet actuators to change the length of the MC1 cavity. The required filter electronics are located in a separate module (MC1 long.) described in [Skeldon]. The filters components include:

- Two sequential transient differentiators (zero at 5 kHz, pole at 50 kHz, and zero at 500 Hz, pole at 5 kHz).
- Five sequential Scultety filters (see below).

In addition, a current driver (or coil driver) is used to apply the signals to the coils of the actuator. The Scultety filters are adjustable notch filters that are required in the MC1 feedback to reduce the feedback at the frequencies of the internal mechanical resonances of the mirror. The resonance frequencies have been determined experimentally and the filters were tuned to the following frequencies: 25.6 kHz, 32.6 kHz, 35.8 kHz, 54.0 kHz, 60.5 kHz. In addition, the notch filters were adjusted to be as narrow as possible.

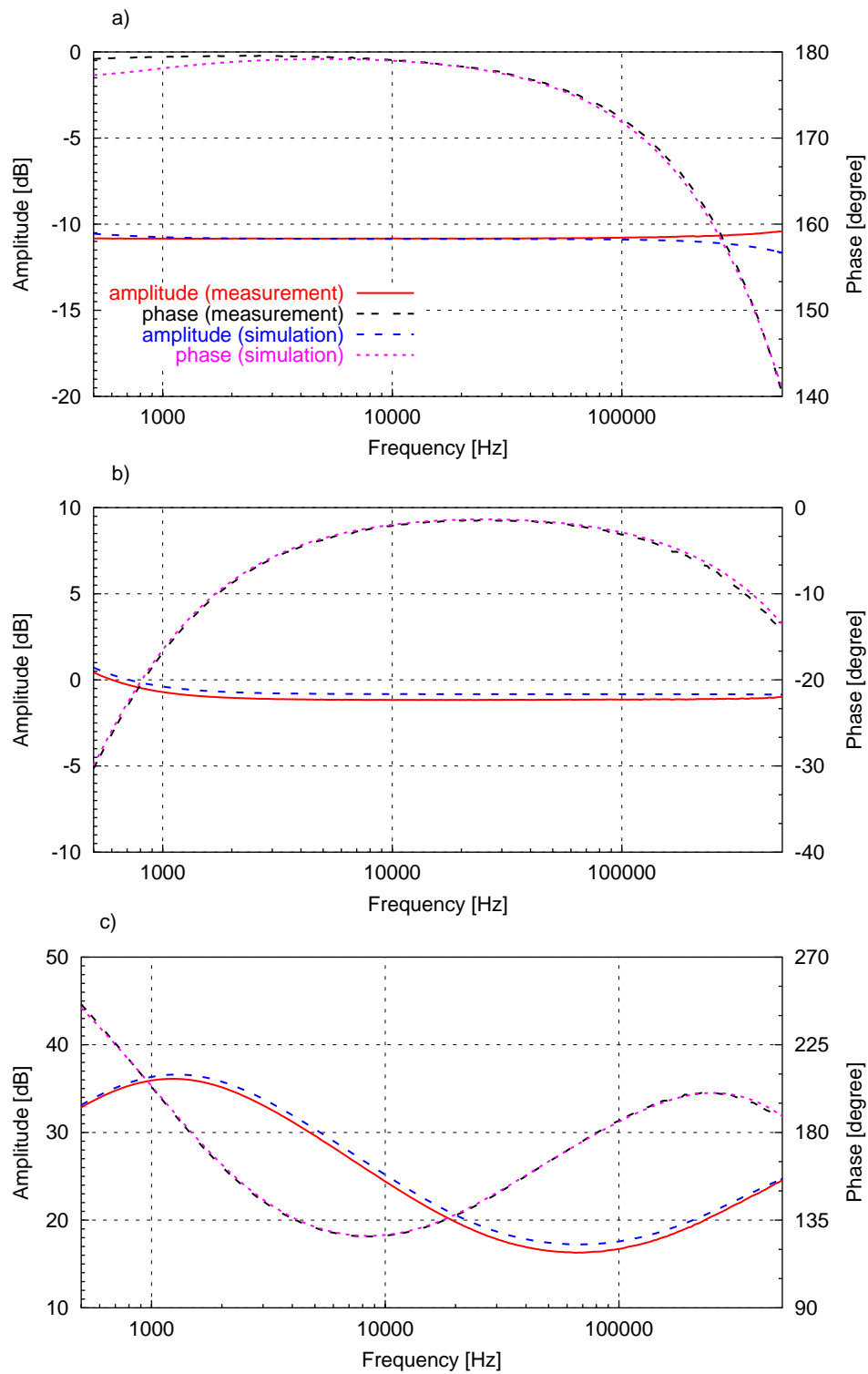


Figure G.2: MC1 filter electronics: a) transfer function from MC1 error point to Module A signal output (integrator switched off), b) MC1 transfer function of Module B signal input to PZT feedback output and c) transfer function of Module B signal input to EOM feedback output.

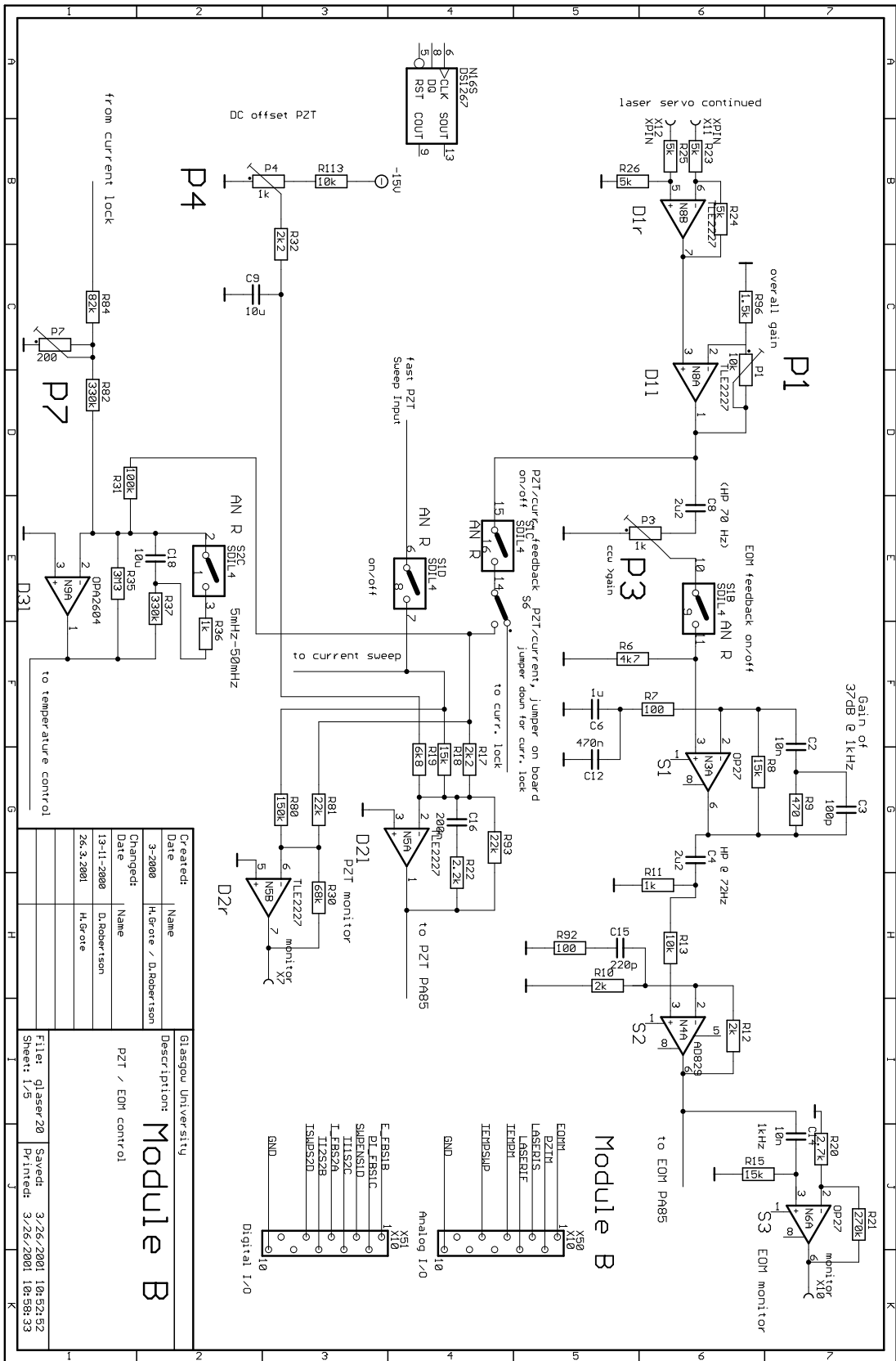


Figure G.3: Schematic drawing of the filter electronics for MC1 and MC2 (part 1 of 5).

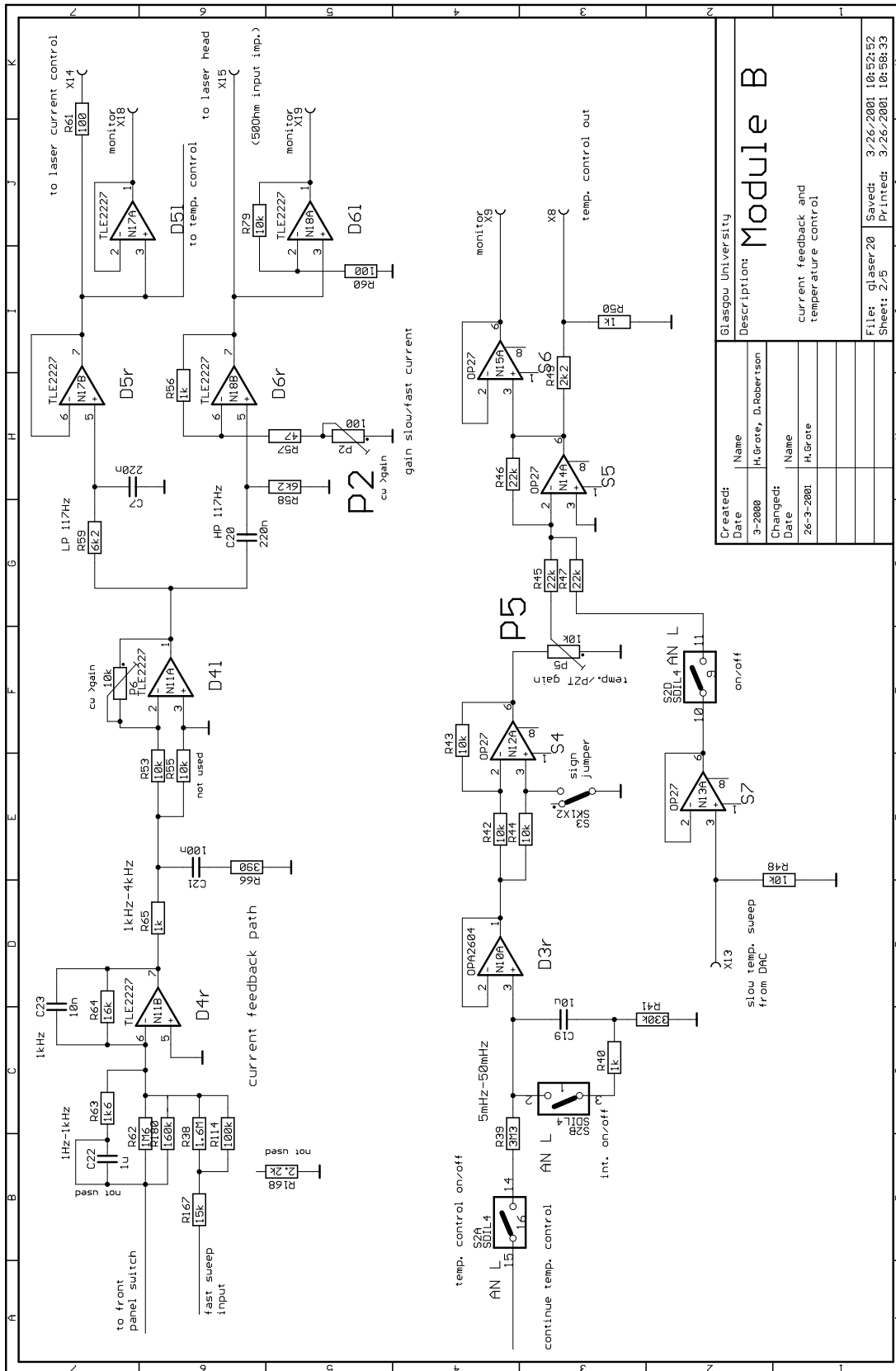


Figure G.4: Schematic drawing of the filter electronics for MC1 and MC2 (part 2 of 5).

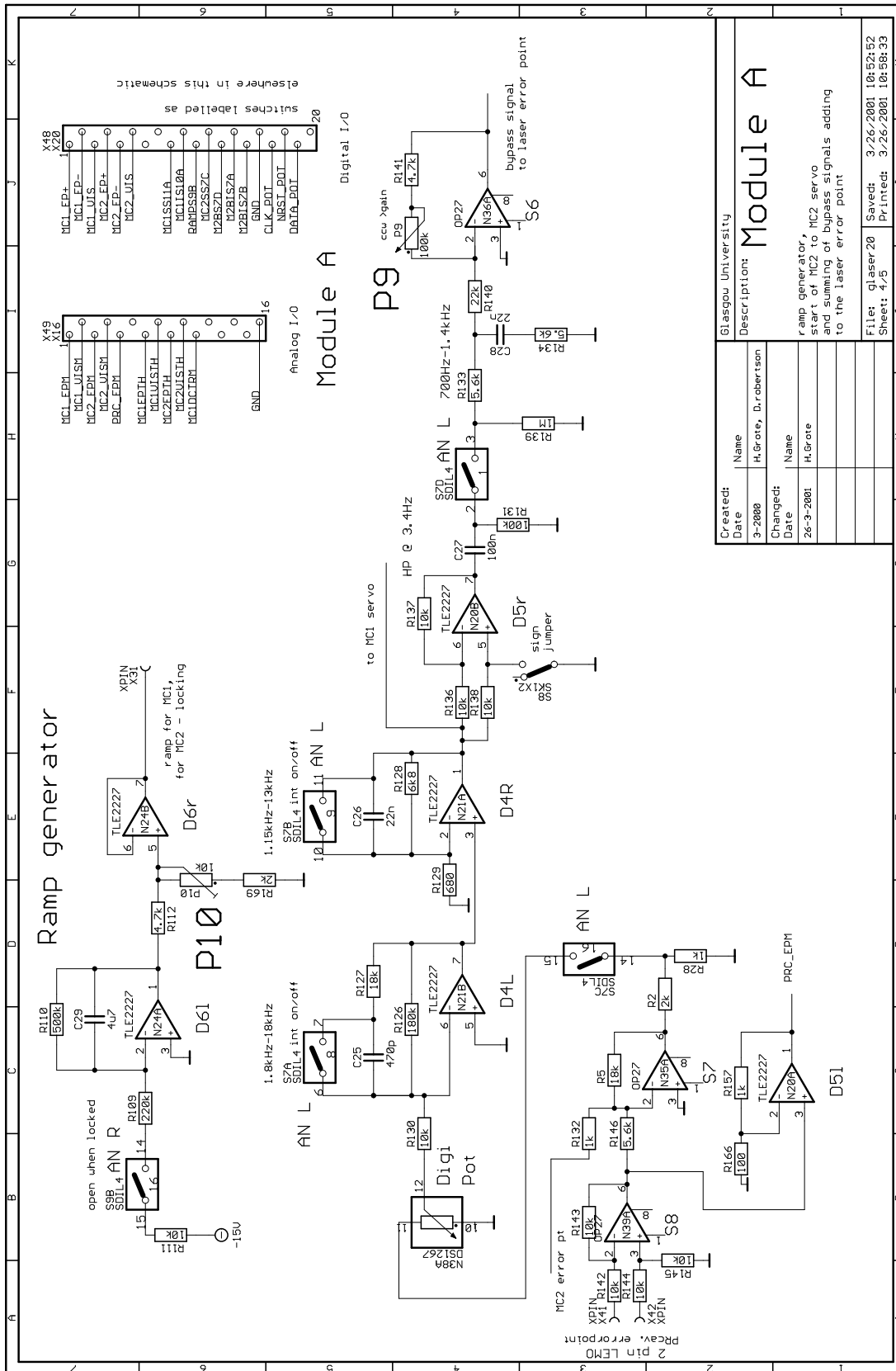


Figure G.6: Schematic drawing of the filter electronics for MC1 and MC2 (part 4 of 5).

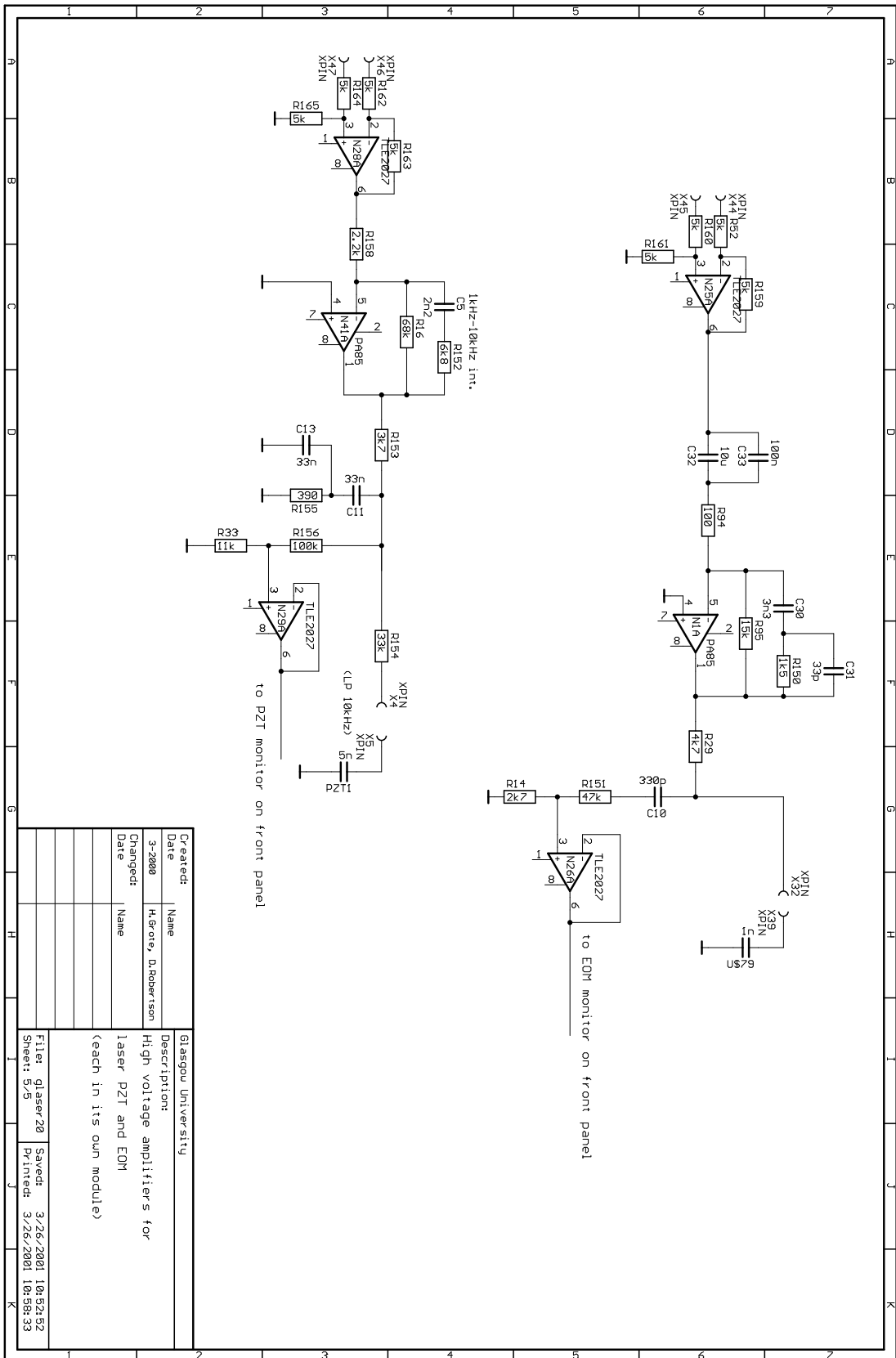


Figure G.7: Schematic drawing of the filter electronics for MC1 and MC2 (part 5 of 5).

G.3.3 Liso file for the MC1 and MC2 servo electronics

```

# LISO input file for MC1, MC2 servo electronics,
# Andreas Freise, 05.07.2002
#### Module A #####
# Differential receiver
#
#                               R76
#                               -----
#                               +-----| 10k |-----+
#                               |         '-----'         |
#                               |                             |
#                               R75 |         OP27           |
# *MODAIN* ----- | na1_m|'. |
# nain >-----| 10k |-----+-----+-----> *MODA1*
#           '=====|         | >-----+----->
# >-----| 10k |-----+ +,' na1_o
# gnd     '-----| na1_p|. '
#           R77   |         A_S1
#
#           .-.
#           |1| R78
#           |0|
#           |k|
#           '-,'
#           |
#           ===
r r75 10k nain na1_m
r r76 10k na1_m na1_o
r r77 10k gnd na1_p
r r78 10k na1_p gnd
op opa_s1 op27 na1_p na1_m na1_o

# First filter, switchable integrator (4kHz-40kHz),
# adds Signal + Bypass from MC2 + DAC Offset trimmer
#
#                               .===== Integrator On/Off
#                               | / |
#                               +-|-0 0-|+-
#                               | '===== |
#                               R69 |C24 |na22 R68
# *MODA1* ----- | , ,1.1n| -----
# >-----| 3.9k |-----+-----+-----| 4k |-----+
#           '-----| ' ' '-----' |
#           R148 ----- |C17 ,10n R67----- |
# >- - - -| 3.9k |-----+-----| 40k |-----+
# Bypass MC2 '-----| ' ' na23 '-----' |
#
#           R149 ----- | R54 -----
#           +-----| 27k |-----+-----| 3M |-----+
#           | | '-----| '-----' |
#           | |
#           .-. |
#           | na2_m|'. TLE2227 |
# R1 |2| | C1 +-----+ -'. |
# |7| --- | >-----+----->
# |k| --- 1u +-----+ +,' na2_o *MODA2*
# '-,' | | |. '

```

```

#           |           |           |           A_D21
# > - -+ ===           ===
# DAC offset
#
# Adding of Bypass signal ignored

r r69 3.9k na1_o na2_m
r rc24s 30 na2_m na22 # R of CMOS switch (for Integrator Off)
r r54 3M na2_m na2_o
c c24 1.1n na2_m na22
r r68 4k na22 na2_o
c c17 10n na2_m na23
r r67 40k na23 na2_o
c cinv 1p na2_m gnd # C to gnd due to CMOS switch
r r149 27k na2_m na24 # Add in DAC offset (0 V)
c c1 1u na24 gnd # "
r r1 27k na24 gnd #
op opa_d21 tle2227 gnd na2_m na2_o

# Servo On/Off, digi-pot for overall gain, test input
#
# *MODA2*
# >-----+          test input
#           |          >- - +
#           |          |
#           .-.          | R51
# R123 |2|          | ----- |R27 -----
#           |k| Servo +-| 33k |-+----| 33k |-----
#           | | On/Off '-----' | '-----' |
#           '-' .===== R34 | TLE2227 |
#           | | / | ----- |na3_m|'
# na31 +----|-0 0-|+ +-| 33k |-+-----+ -'. |
#           | '=====| | '-----' | >-----+----->
#           .-.          | |na32 +-----+ +,' nao *MODBIN*
# R147 |1|          .-. , ' | |.'
#           |k|          | , ' |          A_D2r
#           | |          , ' |          ===
#           '-'          x' | |
#           |          '-' Digi-Pot
#           |          |
#           ===          ===
#
# (test input ignored)

r r123 2k na2_o na31
r r147 1k na31 gnd
r rg1 0k na31 na32 # digipot
r rg2 10k na32 gnd # digipot
r ra1 33k na32 na3_m
r ra2 33k na3_m nao
op opa tle2227 gnd na3_m nao

#### Module B #####
# Differential receiver
#
# R24

```



```

#           |   | n   -----   | R8   -----   |
#           +-----+-----| 100 |-----+-----| 15k |-----+
#           nb32   '-----'   |   '-----'   |
#
#           EOM FB   |
#           (HP 70Hz)   0n/0ff   | nb3_m|'.   OP27   |
#           C8   .=====   +-----+ -'.   |
#           2u2, ,   | / |   |   >-----+----->
# >-----+-----| |---+   +-|-0 0-|-----+ +,' nb3_o   *MODB2*
##EOMFB*   ' ' | | '=====' |nb3_p|. '
#           | |   |   B_S1
#           .-. , '   .-.
#           P3 | , '   |4| R6
#           , ' |1   |k|
#           x' | |k   |7|
#           '- '   '- '
#           |   |
#           ===   ===

c c8 2.2u nb2_o nb34
r p3 .4k nb34 nb3_p # gain set to ~ 0.5
r p3b .6k nb3_p gnd
r r6 4.7k nb3_p gnd
r r7 100 nb3_m nb32
c c6 1.u nb32 gnd
c c12 470n nb32 gnd
r r8 10k nb3_m nb3_o # value in the schematic: 15k
c c2 10n nb3_m nb33
r r9 470 nb33 nb3_o
c c3 100p nb33 nb3_o
op opb_s1 op27 nb3_p nb3_m nb3_o

# Another filter (high pass)
#
#           ===   ===
#           |   |
#           .-.   .-.
#           R92 |1|   |2|R10
#           |0|   |k|
#           |0|   | |
#           '- '   '- '   R12
#           | 220p , |   -----
#           nb42   -----| |-----+-----+
#           C15 ' ' |   '-----'   |
#           |   |
#           |   |
#           (HP 72Hz)   | nb4_m|'.   AD829   |
#           C4   R13   +-----+ -'.   |
##MODB2* 2u2, , nb41   -----   | >-----+----->
# >-----+-----| |---+-----|10k |-----+ +,' nb4_o   *EOMHV*
#           ' ' |   '-----'   nb4_p|. '
#           |   |   B_S2
#           .-.
#           | |
#           R11 |1|

```



```

#      |M| R e5          ---
#      | |              --- 1n
#      '-'   Monitor out | C e5
#      +----->        |
#      .-.   ne_mon      ===
#      |1|
#      |0|
#      |k| R e6
#      '-'
#      |
#      ===
c c32 10u   nea1_o nea21
c c33 100n  nea1_o nea21
r r94 100   nea21 nea2_m
r r95 15k   nea2_m nea2_o
c c30 3.3n  nea2_m nea22
c c31 33p   nea22 nea2_o
r r150 1.5k nea22 nea2_o
op opea_2 pa85 gnd nea2_m nea2_o

r r29 5.1k nea2_o nea24
c ce4 180p nea2_o nea23
r re4 19.4k nea23 nea24

# eom, hv out
c ce5 1n nea24 gnd

# monitor output eom amp
r re5 1M nea24 nea_mon
r re6 10k nea_mon gnd

# PZT Feedback part
#
#                               200n   R22
#                               C16 , , -----
#                               +--| |-----| 2.2k |--+
#                               | ' ' nb51 '-----' |
#                               |                       |
#                               R17                   |
# *PZTFB* ----- | R93 ----- |
# >-----| 2.2k |-----| 22k |-----+
#         '-----' | '-----' |
#         |                       |
#         R32 nb52 R19             |
#         ----- | nb5_m|'. TLE2227 |
# >- - - | 2.2k |---| 6.8k |-----+-----+ -'. |
#         '-----' | '-----' | >-----+----->
# DAC offset | C9             +-----+ +,' nb5_o   *PZTHV*
#         --- |               | |.'
#         --- 10u |               | B_D21
#         |       |
#         ===     ===
r r17 1.5k nb2_o nb5_m # value in the schematic: 2.2k
r r93 22k  nb5_m nb5_o
c c16 370n nb5_m nb51 # value in the schematic: 200n
r r22 1.5k nb51 nb5_o # value in the schematic: 2.2k

```



```

r r19 6.8k nb5_m nb52 # DAC offset
c c9 10u nb52 gnd # "
op opb_d21 tle2227 gnd nb5_m nb5_o

# PZT HV amplifier
#
# differential receiver (5k), see picture above

r r162 10k nb5_o npa1_m
r r163 10k npa1_m npa1_o
r r164 10k gnd npa1_p
r r165 10k npa1_p gnd
op oppa_1 op27 npa1_p npa1_m npa1_o

# PZT pa85 stage
#
#           2.2n      R152
#           C5 , ,    -----
#           +---| |-----| 6.8k |--+
#           | ' ' npa21'-----' |
#           | R16 ----- |
#           +-----| 68k |-----+
#           | '-----' |
#           | | | | |
# R158      | npa2_m|'. PA85 | R 153
#>-----|-2.2k |-----+-----+ -'. | ----- npa22
# '-----' | >-----+---| 2.6k |-----+
#npa1_o      +-----+ +,' npa2_o '-----' |
#           | |.' | |
#           === PA_2 |
#
# +-----+-----+-----+-----+
# | ----- npa24 R e1 ----- npa25
# +---- | 33K |-----> >--+----- | 3k |--+
# | '-----' HV out | '-----' |
# .-. R 154 | | C e1 | | Piezo
# |1| | | |
# |M| R e2 --- ---
# | | --- 1n C e2 --- 3n
# '-) Monitor out | |
# +-----> | |
# .-. npa_mon === ===
# |1|
# |0|
# |k| R e3
# '-)
# |
# ===
#
r r158 2.2k npa1_o npa2_m
r r16 68k npa2_m npa2_o
c c5 2.2n npa2_m npa21
r r152 5.6k npa21 npa2_o
op oppa_2 pa85 gnd npa2_m npa2_o

```

```
r r153 2.6k npa2_o npa22
r r154 33k npa22 npa24

# extra filter box:
c ce1 1n npa24 gnd
r re1 3k npa24 npa25

# piezo and cable, etc.
c ce2 3n npa25 gnd

# monitor output pzt amp
r re2 1M npa22 npa_mon
r re3 10k npa_mon gnd
# stray capacitance
c ce3 1p npa22 npa_mon

uinput nain 1
uoutput nb5_o:db:deg

freq log 500 500k 400
```

Appendix H

LabView virtual instruments

This section shows screen-shots (Figures [H.1](#) to [H.3](#)) of the graphical user interface of the LabView virtual instruments used for controlling the frequency stabilisation system. The functional description of the virtual instrument ‘automation_stats’ is given below. The descriptions of the control programs for the mode cleaners and for the Power-Recycling cavity can be found in Section [2.8](#).

Each LabView program has a number of read and write channels. All LabView channels are archived by the data-acquisition system. A subset of these data channels that is of interest for the frequency control is listed in the following tables: Table [H.1](#) gives a list of read-signals used to monitor the status of the analogue filter, Table [H.2](#) lists the write-signals that can be used to change the behaviour of the control systems, and Table [H.3](#) lists a number of signals mostly used for debugging the system. Table [H.3](#) also lists signals used to switch on or off feedback signals.

H.1 Automation statistics

The virtual instrument ‘automation_stats’ is used to generate and display simple statistics with respect to the lock status of the various optical systems. This is useful as online information while working at the detector and also provides quick-look information on periods without human supervision.

Every 50 ms the program evaluates the status of the following optical systems:

- **Slave Laser:** No hardware indicator about the status of the slave-laser system is available. Instead, the slave-laser power is read. A simple variance of the power is generated by comparing the n -th to the $(n-1)$ -th data value. The variance is then low-pass filtered with a single pole at 0.1 Hz. From experience it is known that the variance of the free-running slave laser is at least two orders of magnitude larger than that of an injection-locked slave laser. Thus, a simple threshold can be used to determine the status of the slave laser.
- **MC1:** If the slave-laser status is ‘locked’, the MC1 visibility (light power reflected by the MC1) and the status bit of the MC1 servo are read as an indicator for the

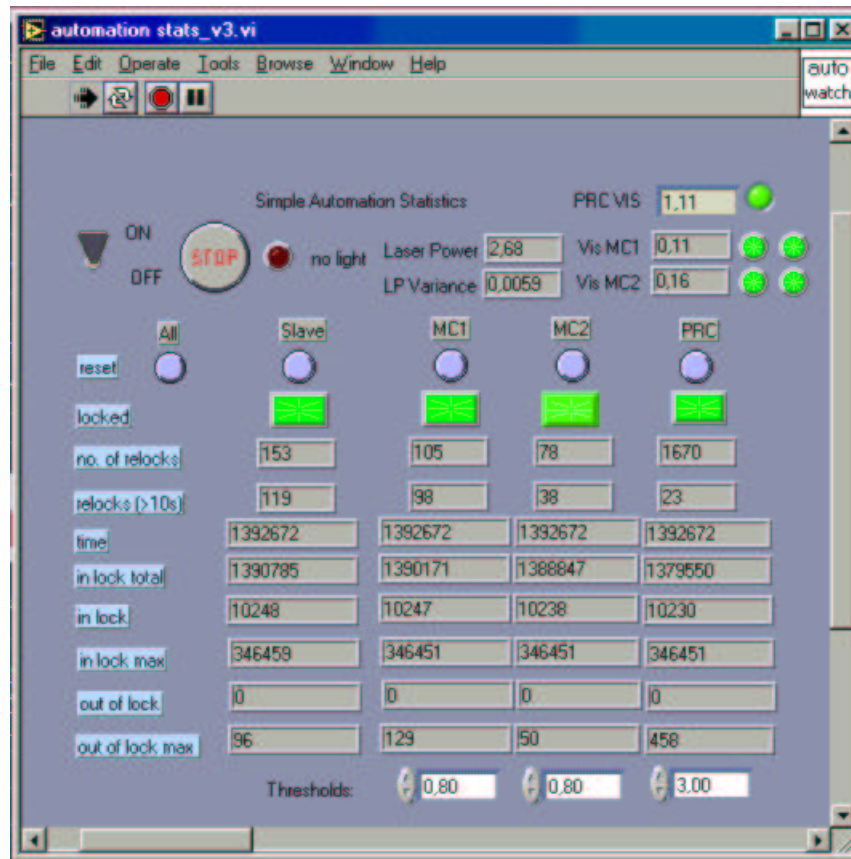


Figure H.1: Virtual instrument that records and displays some simple statistics about the lock status of the laser, the mode cleaners and the Power-Recycling cavity.

status of MC1. Two thresholds are used: light power too low means that there is no light on the photo diode. Light level high means that the light is fully reflected and the mode cleaner thus not locked. If the light level is in-between the two thresholds and the status bit from the MC1 servo is ON, the status for MC1 is set to locked.

- **MC2:** If the status for MC1 is set to locked, the visibility of MC2 is used to determine the lock status of MC2. The method is the same as for MC1.
- **PRC:** If the second mode cleaner is set to 'locked', the same method is used to determine the lock status of the Power-Recycling cavity.

The lower thresholds for the visibility signal are hidden, and the upper thresholds can be set via the user interface. The current status of the optical systems is indicated by a button that is changed from dark green (not locked) to bright green (locked). A number of counters are used to generate simple statistics from the lock status. All of these counters can be reset and show the following values with respect to the time of the last reset (or program start):

- **Number of locks:** A simple counter for the number of changes in the lock status from 'not locked' to 'locked'.
- **Number of locks longer than 10 seconds:** A simple counter for the number of times when the 'locked' status was on for at least 10 seconds. When the lock acquisition fails the system is usually 'in lock' for a short time so that this counter is not increased whereas the 'number of locks' counter is increased by one. The quality of the lock acquisition can be checked by the ratio of these two counters.
- **Total time in lock:** The total number of seconds for which the status was 'locked'. Together with the total number of seconds this can be used to compute a simple duty cycle in percent.
- **Duration of current lock:** Shows the duration of the current lock (or 0 if the status is 'not locked').
- **Duration of longest lock:** The maximum duration of a lock.
- **Duration of current 'out-of-lock' stretch:** Shows the duration of the current 'not locked' status (or 0 if the status is 'locked').
- **Duration of longest 'out-of-lock' event:** The maximum duration of an 'out-of-lock' status.

H.2 Mode-cleaner control



Figure H.2: Virtual instrument for supervising the control electronics for MC1 and MC2. The top left graph shows the visibility and error signals for both mode cleaners; the right graph shows the feedback signals. The center area contains various controls and indicators with respect to automatic operation. In particular, the green buttons (labeled ‘MC1’ and ‘MC2’) are used to switch the respective control loops to automatic operation. The lower part contains controls and indicators connected to the analogue loop filters: MC1 loop to the left and MC2 loop to the right.

H.3 Power-Recycling cavity control

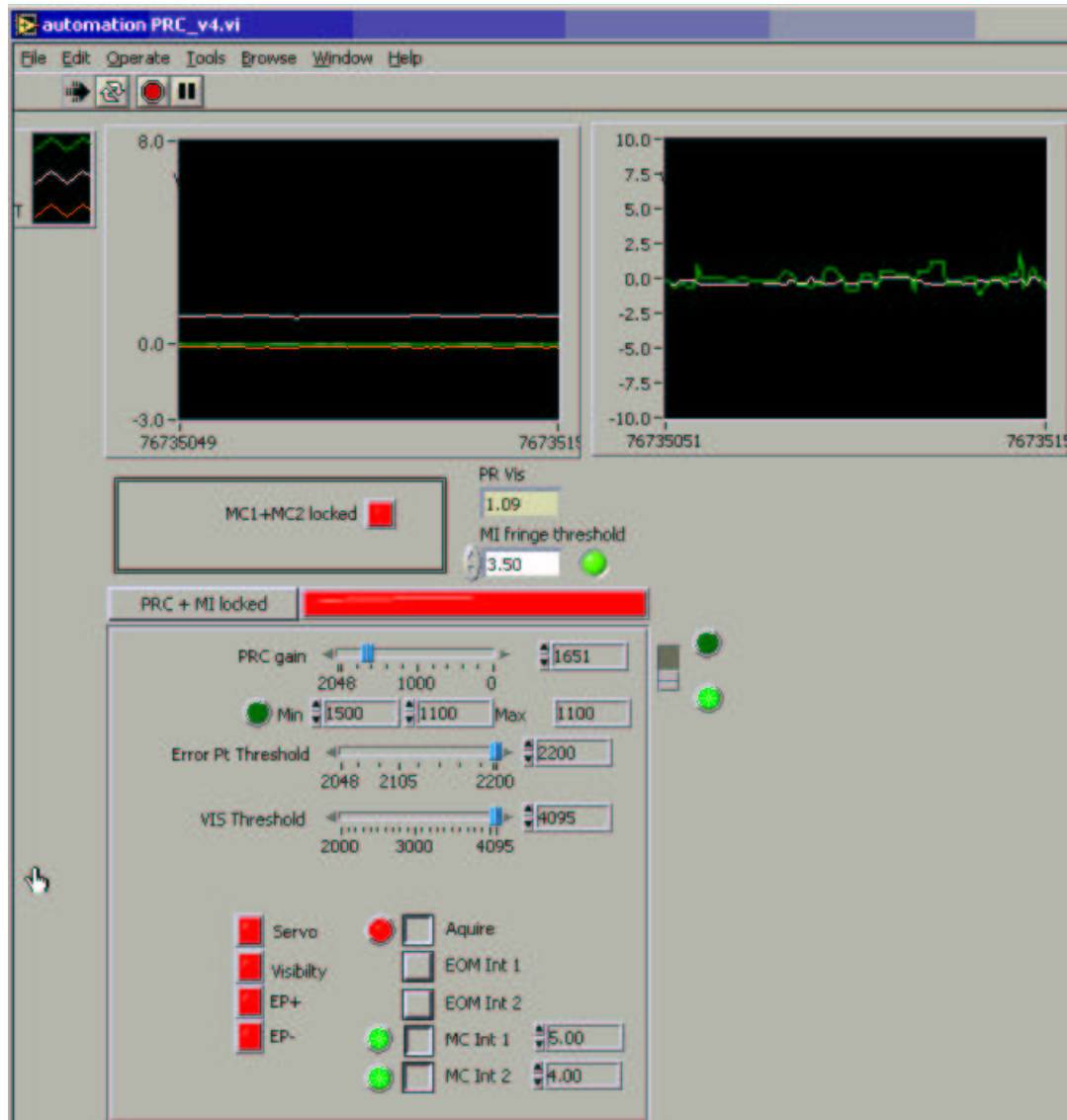


Figure H.3: Virtual instrument that controls the Power-Recycling cavity electronics. The top left graph shows the visibility and error signal (and the feedback of the master-laser PZT); the right graph shows the feedback signals. The lower part contains controls and indicators connected to the analogue loop filters. In addition, some intermediate controls for the automatic operation are present that will probably be removed in the future, see Section 2.8.3.

Name	Type	Description	Descriptor
Servo	bit	whether the servo is switched on	SMCSA:MC1:SERVO SMCSA:MC2:SERVO SLPRC:PRC:ON
Vis	float	visibility: the light power reflected from the cavity (not normalised)	SMCSA:MC1:VIS SMCSA:MC2:VIS SLPRC:PRC:VIS
DVis	bit	whether the visibility is above a set threshold	SMCSA:MC1:DVIS SMCSA:MC2:DVIS SLPRC:PRC:DVIS
Error point	float	the error point signal of the control loop	SMCSA:MC1:EP SMCSA:MC2:EP SLPRC:PRC:EP
Ep +	bit	Error point+: whether the error point signal is larger than the set threshold	SMCSA:MC1:EPPLUS SMCSA:MC2:EPPLUS SLPRC:PRC:EPPLUS
Ep -	bit	Error point-: whether the error point signal is smaller than minus the set threshold	SMCSA:MC1:EPMINUS SMCSA:MC2:EPMINUS SLPRC:PRC:EPMINUS

Table H.1: Selection of LabView signals read from the electronics. These signals are used to monitor the control loop. The status bit for the visibility (DVis) and the servo are used for the algorithm that decides whether the loop should be opened or closed.

Name	Type	Description	Descriptor
Acq	bit	switch for closing the control loop	SLMSCA:MC1:ACQ SLMSCA:MC2:ACQ SLPRC:PRC:ACQ
Gain	float	overall gain of the control loop	SLMSCA:LMC1:GAIN SLMSCA:MC2MC1:GAIN SLPRC:PRC:G_CTRL
Int	bit	switch for extra integrator	SLMSCA:MC1:INT1 SLMSCB:TEMP:INT1 SLMSCB:TEMP:INT2 SLMSCA:BYPASS:INT1 SLMSCA:BYPASS:INT2 SLPRC:MC:INT1 SLPRC:MC:INT2 SLPRC:EOM:INT1 SLPRC:EOM:INT2
Vis Threshold	float	threshold for the comparator that generated Dvis	SLMSCA:MC1:VISTH SLMSCA:MC2:VISTH SLPRC:PRC:VISTH
Ep Threshold	float	threshold for the comparator that generated Ep+ and Ep-	SLMSCA:MC1:EPTH SLMSCA:MC2:EPTH SLPRC:PRC:EPTH

Table H.2: Selection of LabView signals that are used in the virtual instrument to supervise the analogue control system.

Name	Type	Description	Descriptor
PZT	bit	feedback to master laser PZT	SLMSCB:MC1:PZTI
MC1 EOM	bit	feedback to master laser EOM	SLMSCB:MC1:EOM
MC1 Temp	bit	feedback to master laser temperature	SLMSCB:MC1:TEMP
Bypass	bit	bypass, feedback from MC2 into MC1 error point	SLMSCA:BYPASS:ON
MC2 mirror	bit	feedback from the PRC loop to MMC2b	SLPRC:PRC:MC-ON
PRC EOM	bit	feedback to PRC EOM	SLPRC:PRC:EOM-ON

Table H.3: Selection of LabView signals that are used enable or disable feedback signals.

Bibliography

- [Barthel] A. Barthel: ‘Abstimmbares Signal-Recycling mit externer Modulation’, Diploma Thesis, University of Hannover, 1997. [85](#)
- [Barr] B.W. Barr, G. Cagnoli et al.: ‘Silica research in Glasgow’, *Class. Quantum Grav.* **19** (2002), 1655–1662. [32](#)
- [Bayer-Helms] F. Bayer-Helms: ‘Coupling coefficients of an incident wave and the modes of a spherical optical resonator in the case of mismatching’, *Appl. Opt.* **23** (1983) 1369–1380. [182](#)
- [Brozek] S. Brozek: ‘Frequenzstabilisierung eines Nd:YAG-Hochleistungs-Laser-Systems für den Gravitationswellendetektor GEO 600’, Ph.D. Thesis, University of Hannover, 1999. [38](#), [52](#), [54](#)
- [Buonanno01] A. Buonanno, Y. Chen: ‘Quantum noise in second generation, signal recycled laser-interferometer gravitational-wave detectors’, *Phys. Rev. D* **64** (2001). [84](#)
- [Buonanno02] A. Buonanno, Y. Chen: ‘Signal recycled laser-interferometer gravitational-wave detectors as optical springs’, *Phys. Rev. D* **65** (2002). [84](#)
- [Cagnoli] G. Cagnoli, personal communication. [33](#), [39](#), [110](#)
- [Caves] C.M. Caves: ‘Quantum-mechanical radiation-pressure fluctuations in an interferometer’, *Phys. Rev. Lett.* **45** (1980) 75–79. [82](#)
- [Casey] M.M. Casey, H. Ward and D.I. Robertson: ‘Computer monitoring and control of the GEO 600 gravitational wave detector’, *Rev. Sci. Instrum.* **71** (2000) 3910. [72](#)
- [Centrovision] Data sheet for the Centrovision QD50-3T, 2002. [189](#)
- [Clubley] D.A. Clubley, G.P. Newton, K.D. Skeldon, J. Hough: ‘Calibration of the Glasgow 10 m prototype laser interferometric gravitational wave detector using photon pressure’, *Phys. Lett. A* **283** (2001) 85–88.
- [Drever83] R.W.P. Drever, J.L. Hall, F.V. Kowalski, J. Hough, G.M. Ford, A.J. Munley, H. Ward: ‘Laser Phase and Frequency Stabilization Using an Optical Resonator’, *Appl. Phys.* **B 31** (1983) 97–105. [xviii](#), [8](#), [41](#)

- [Drever] R.W.P. Drever et al.: in *Quantum Optics, Experimental Gravitation, and Measurement Theory*, eds. P. Meystre and M.O. Scully (Plenum Press, New York, 1983) 503–514. [25](#)
- [FINESSE] A. Freise: ‘FINESSE: Frequency domain interferometer simulation software’, internal note, 2002 (the program is currently available at <http://www.rzg.mpg.de/~adf>). [157](#)
- [Freise98] A. Freise: ‘Ein neues Konzept für Signal Recycling’, Diploma Thesis, University of Hannover (1998). [85](#)
- [Freise] A. Freise: ‘Simulating the frequency response of the dual-recycled 30 m prototype in Garching’, internal note, 1998. [99](#)
- [Freise00] A. Freise, G. Heinzl, K.A. Strain, J. Mizuno, K.D. Skeldon, H. Lück, B. Willke, W. Winkler, R. Schilling, A. Rüdiger, and K. Danzmann: ‘Demonstration of detuned dual recycling at the Garching 30 m laser interferometer’, *Phys. Lett. A* **277** (2000) 135–142. [26](#), [95](#)
- [Freise02] A. Freise, M.M. Casey, S. Gossler, H. Grote, G. Heinzl, H. Lück, D.I. Robertson, K.A. Strain, H. Ward, B. Willke, J. Hough, K. Danzmann: ‘Performance of a 1200 m long suspended Fabry-Perot cavity’, *Class. Quantum Grav.* **19** (2002), 1389–1397. [62](#)
- [GEO] K. Danzmann et al.: in *First Edoardo Amaldi Conference on Gravitational Wave Experiments*, Frascati 1994, (World Scientific, Singapore, 1995) 100–111. [1](#)
- [Gossler] S. Gossler, M.M. Casey, A. Freise, H. Grote, H. Lück, P. McNamara, M.V. Plissi, D.I. Robertson, N.A. Robertson, K. Skeldon, K.A. Strain, C.I. Torrie, H. Ward, B. Willke, J. Hough, K. Danzmann: ‘The modecleaner system and suspension aspects of GEO 600’, *Class. Quantum Grav.* **19** (2002), 1835–1842. [23](#)
- [Grote] H. Grote, personal communication. [105](#)
- [Grote02] H. Grote, G. Heinzl, A. Freise, S. Gossler, B. Willke, H. Lück, H. Ward, M.M. Casey, K.A. Strain, D.I. Robertson, J. Hough, K. Danzmann: ‘The automatic alignment system of GEO 600’, *Class. Quantum Grav.* **19** (2002), 1849–1855. [17](#), [45](#), [65](#), [77](#)
- [Gwo] D.H. Gwo: ‘Hydroxide-catalyzed ultra-precision bonding for optical materials in cryogenic applications’, *Proceedings of SPIE—The International Society for Optical Engineering* **3435** (1998) 136. [32](#)
- [Harms] J. Harms: ‘Quantum noise in the laser-interferometric gravitational-wave detector GEO 600’, Diploma Thesis, University of Hannover, 2002. [83](#), [84](#)
- [Heinzl96] G. Heinzl, J. Mizuno, R. Schilling, W. Winkler, A. Rüdiger, K. Danzmann: ‘An experimental demonstration of resonant sideband extraction for laser-interferometric gravitational wave detectors’, *Phys. Lett. A* **217** (1996) 305–314. [79](#)

-
- [Heinzel98] G. Heinzel, K.A. Strain, J. Mizuno, K.D. Skeldon, B. Willke, W. Winkler, R. Schilling, A. Rüdiger, and K. Danzmann: ‘Experimental Demonstration of a Suspended Dual Recycling Interferometer for Gravitational Wave Detection’, *Phys. Rev. Lett.* **81** (1998) 5493–5496. [24](#), [66](#), [85](#), [95](#)
- [Heinzel99] G. Heinzel: ‘Advanced optical techniques for laser-interferometric gravitational-wave detectors’, Ph.D. Thesis, University of Hannover, 1999. [26](#), [31](#), [43](#), [44](#), [76](#), [84](#), [85](#), [87](#), [95](#), [160](#), [162](#), [217](#)
- [Heinzel02] G. Heinzel, A. Freise, H. Grote, K. Strain, K. Danzmann: ‘Dual recycling for GEO 600’, *Class. Quantum Grav.* **19** (2002), 1547–1553. [95](#)
- [Hulse] R.A. Hulse, J.H. Taylor: ‘Discovery of a pulsar in a binary system’, *Astroph. Jour. (Letters)* **195** (L59) (1975) 51–53. [1](#)
- [Jennrich] O. Jennrich: ‘Das Quantenlimit in der Interferometrie’, Ph.D. Thesis, University of Hannover, 1998. [43](#)
- [Kane85] T.J. Kane and R.L. Byer: ‘Monolithic, unidirectional single-mode Nd:YAG ring laser’, *Opt. Lett.* **10**, (1985), 65–67. [7](#)
- [Klövekorn] P. Klövekorn: ‘Mounting unit report’, internal note, 2000. [17](#)
- [Kimble] H.J. Kimble, Y. Levin, A.B. Matsko, K.S. Thorne, S.P. Vyatchanin: ‘Conversion of conventional gravitational-wave interferometers into QND interferometers by modifying their input and/or output optics’, *Phys. Rev.* **D 65** (2002). [84](#)
- [Lawrence] M.J. Lawrence, B. Willke, M.E. Husman, E.K. Gustafson, R.L. Byer: ‘Dynamic response of a Fabry-Perot interferometer’, *J. Opt. Soc. Am. B* **16** (1999) 523–532. [63](#)
- [LIGO] A. Abramovici et al.: *Science* **256** (1992) 325–333. [1](#)
- [LISO] G. Heinzel: ‘LISO: Linear Simulation and optimisation of analog circuits’, see Appendix C of [Heinzel99]. [157](#), [190](#)
- [Maaß] D. Maaß: ‘Signal-Recycling with Schnupp modulation’, Diploma Thesis, University of Hannover, 1995. [85](#)
- [Man] C.N. Man, A. Brillet: ‘Injection locking of argon-ion lasers’, *Opt. Lett.* **9** (1984) 333–334. [6](#)
- [Mason] J.E. Mason: ‘Signal Extraction and Optical Design for an Advanced Gravitational Wave Interferometer’, Ph.D. Thesis, California Institute of Technology, 2001. [79](#)
- [Meers88] B.J. Meers: ‘Recycling in laser-interferometric gravitational-wave detectors’, *Phys. Rev.* **D 38** (1988) 2317–2326. [24](#), [85](#)
- [Meers89] B.J. Meers: ‘The frequency response of interferometric gravitational wave detectors’, *Phys. Lett.* **A 142** (1989) 465–470.

- [Meers91] B.J. Meers, K.A. Strain: ‘Modulation, signal and quantum noise in interferometers’, *Phys. Rev. A* **44** (1991) 4693–4703.
- [Meers91b] B.J. Meers, K.A. Strain: ‘Wave-front distortion in laser-interferometric gravitational-wave detectors’, *Phys. Rev. D* **43** (1991) 3117–3130.
- [Mizuno93] J. Mizuno, K. Strain, P.G. Nelson, J.M. Chen, R. Schilling, A. Rüdiger, W. Winkler, K. Danzmann: ‘Resonant sideband extraction: A new configuration for interferometric gravitational wave detectors’, *Phys. Lett. A* **175** (1993) 273–276. [79](#)
- [Mizuno95] J. Mizuno: ‘Comparison of optical configurations for laser–interferometric gravitational wave detectors’, Ph.D. Thesis, University of Hannover, 1995. [2](#), [25](#), [79](#), [117](#), [121](#), [171](#)
- [Mueller] G. Mueller: ‘The cross-coupled interferometer for gravitational wave detection’, *Class. Quantum Grav.* **19** (2002), 1997–2004. [79](#)
- [Nagano01] S. Nagano: ‘12 W Injection-locked laser performance’, internal note, 2001. [8](#), [10](#)
- [Nagano02] S. Nagano: ‘Design of mode-matching telescope for mode cleaner 1’, internal note, 2002. [20](#)
- [New Focus] Manual for the New Focus electro-optic phase modulator, model series 400x, 2001. [190](#)
- [OPTOCAD] R. Schilling: ‘OPTOCAD, A Fortran 95 module for tracing Gaussian beams through an optical set-up, Version 0.74’, internal note, 2002. [125](#)
- [Rüdiger] A. Rüdiger: ‘Phasenbeziehungen an einem symmetrischen Strahlteiler’, internal note, 1978. [160](#)
- [Rüdiger02] A. Rüdiger: ‘Shot Noise in Interferometers used for gravitational wave measurements’, unpublished. [83](#)
- [Rüdiger81] A. Rüdiger, R. Schilling, L. Schnupp, W. Winkler, H. Billing, K. Maischberger: ‘A mode selector to suppress fluctuations in laser beam geometry’, *Optica Acta* **28** (1981) 641–658. [12](#)
- [Schilling02] R. Schilling: ‘FFT simulation of the GEO 600 dual-recycled Michelson interferometer’, internal note, 2002. [34](#)
- [Schilling] R. Schilling, personal communication. [84](#)
- [Schnier97] D. Schnier, J. Mizuno, G. Heinzl, H. Lück, A. Rüdiger, R. Schilling, M. Schrempel, W. Winkler, K. Danzmann: ‘Power Recycling in the Garching 30 m prototype interferometer for gravitational–wave detection’, *Phys. Lett. A* **225** (1997) 210–216. [25](#)
- [Schnupp] L. Schnupp: talk at the *European Collaboration Meeting on Interferometric Detection of Gravitational Waves* (Sorrento, 1988). [37](#), [66](#), [92](#)

-
- [Seifert] F. Seifert: ‘Entwicklung einer quantenrauschbegrenzten Leistungsstabilisierung für ein Präzisionslasersystem’, Diploma Thesis, University of Hannover (2002). 10
- [Siegman] A.E. Siegman: ‘Lasers’, University Science Books, Mill Valley, 1986. 9, 146, 148, 157, 178
- [Shaddock] D. A. Shaddock: ‘Advanced Interferometry for Gravitational Wave Detection’, Ph.D. Thesis, Australian National University, 2000. 79
- [Skeldon] K.D. Skeldon, D.I. Robertson, M.M. Casey, K.A. Strain, H. Ward: ‘Longitudinal locking of GEO 600 Mode cleaner MC1’, internal note, 1999. 191
- [STAIC] Software Tools for Advanced Interferometer Configurations, <http://www.phys.ufl.edu/LIGO/LIGO/STAIC.html>. 157
- [Strain] K.A. Strain, personal communication. 91
- [Strain91] K.A. Strain, B.J. Meers: ‘Experimental Demonstration of Dual Recycling for Interferometric Gravitational-Wave Detectors’, Phys. Rev. Lett. **66** (1991) 1391–1394. 24, 85
- [TAMA] K. Tsubono et al., *ibid.*, 112–114. 1, 9
- [Taylor] J.H. Taylor, J.M. Weisberg: ‘A new test of general relativity: Gravitational radiation and the binary pulsar PSR 1913 + 16’, Astrophys. J. **253** 908–920. 1
- [VIRGO] C. Bradaschia et al.: Nuclear Instruments and Methods in Physics Research A **289** (1990) 518–525. 1
- [Willems] P. Willems, V. Sannibale, J. Weel, V. Mitrofanov: ‘Investigations of the dynamics and mechanical dissipation of a fused silica suspension’, Phys. Lett. **A 297** (2002) 37–48. 32
- [Willke00] B. Willke, S. Brozek, V. Quetschke, S. Gossler, K. Danzmann: ‘Frequency stabilisation of a monolithic Nd:YAG ring laser by controlling the power of the laser-diode pump source’, Opt. Lett. **25** 14 (2000) 1019–1021. 57
- [Willke01] B. Willke et al.: ‘The GEO 600 gravitational wave detector’, Class. Quantum Grav. **19** (2002), 1377–1387. 2
- [Winkler] W. Winkler, personal communication. 32
- [Winkler91] W. Winkler, K. Danzmann, A. Rüdiger, R. Schilling: ‘Heating by optical absorption and the performance of interferometric gravitational-wave detectors’, Phys. Rev. A **44** (1991) 7022–7036. 86
- [Winkler02] W. Winkler: ‘Fluctuating light pressure in recycled interferometers’, internal note, 2002. 112

Acknowledgements

I feel very fortunate to have been able to participate in the GEO 600 project. Such a project provides many interesting challenges, and the people in the Glasgow group, in Garching and in Hannover have constantly been showing a tremendous creativity in experimental physics. This work would not have been possible without the great work of all these people.

First of all, I would like to thank Karsten Danzmann for giving me the opportunity to take part in the search for gravitational waves. I greatly appreciate the generous personal support, the freedom and the creative input he offers. The productivity-hierarchy ratio in his group has always been extremely high.

My first experiences as a graduate and PhD student were strongly influenced by Stefan Traeger, Oliver Jenrich and Mathias Schrepel. Mathias taught me more in a few weeks than I usually learn in a year. Stefan and Oliver provided (whether they know it or not) much fun and orientation. I am also grateful for many interesting discussions with Guido Müller, who was always good for a lot of fun at numerous LSC meetings.

Since I have started to do science, Gerhard Heinzl has been a reliable source of invaluable help and support. In fact, his direct and indirect contributions to GEO 600 in general and to my work in particular are too numerous to list here. The rare combination of friendliness, productivity and great ability make him a very special person and scientist. This puts him in the same league as the Garching group of Albrecht Rüdiger, Roland Schilling and Walter Winkler. Even though I have had only a few opportunities to work with them yet, I have greatly profited from getting just a glance at the accuracy and pleasure they exhibit in their work. I would like to thank especially Roland for putting up with my general ignorance in numerous phone calls.

The work in Ruthe would not have been so much fun without the various members of the 'Ruthe team', for example, Walter Grass who can provide anything from coffee and fruits to remote manual locking of the mode cleaners or Harald Lück and Stefan Gossler with their amazing craftsmanship. Many colleagues from the Glasgow group have been helping with the installation work in Ruthe. I always enjoyed working with Paul McNamara, Geppo Cagnoli, David Robertson, Mike Plissi, Martin Hewitson and all the others. Kenneth Strain especially deserves a word of thanks for his never ceasing effort to keep all details and all the complexities in mind, providing a reliable reference to all of us.

By taking on unpleasant jobs and responsibilities, Benno Willke has been able to provide structure to many chaotic processes. I have continuously exploited his reliability in many ways, and the periods of his presence and absence have correlated to periods of fast and slow progress in the construction work of GEO 600. I am grateful for his taking care and would like to apologise for all the troubles I dumped on him.

During the past years I experienced a lot of great team work with Hartmut Grote. This work greatly benefited from his skills, especially with respect to electronics. I will def-

initely miss his constructive good-will, his readiness to discuss and tackle any kind of problem and, of course, our conference trips.

I would also like to thank Uta Weiland for providing prompt and efficient help whenever I needed it and for her effort to actually *do* things, Volker Quetschke for sharing with me the dullness of computer administration, Karsten, Kirsten, Klaus, Michaela, Michèle, Peter, Rolf and many others for being nice and friendly even though I (sometimes) was not, and ‘little Volker’ for the occasional game of chess.

I also thank Stefan Gossler, Hartmut Grote, Michaela Malec, Uta Weiland, Walter Winkler and especially Gerhard Heinzl, Albrecht Rüdiger, Roland Schilling, Benno Willke and my wife Katharina for proof-reading (parts of) this thesis.

Curriculum vitae

Andreas Freise
Steinmetzstraße 16
30163 Hannover

Born on May 24, 1971 in Hildesheim, Germany
Marital status: married, two children

- | | |
|---------------------|--|
| 10. 2000 – to date | Scientific Assistant, University of Hannover, Institut für Atom- und Molekülphysik (SFB 407) |
| 07. 1998 – to date | Doctoral Studies in Physics, University of Hannover |
| 07. 1998 – 09. 2000 | Scientific Assistant, Max-Planck-Institut für Quantenoptik (Garching) |
| 05. 1998 | Physik-Diplom, University of Hannover |
| 10. 1991 – 05. 1998 | Diploma Studies in Physics, University of Hannover |
| 10. 1995 | First Class Bachelor of Science with Honours, Napier University |
| 10. 1994 – 10. 1995 | Applied Physics with Microcomputing, Napier University (Edinburgh) |
| 07. 1990 – 06. 1991 | Compulsory Military Service, Instandsetzungskompanie 10 |
| 07. 1990 | Abitur, Gymnasium Himmelsthür |
| 08. 1983 – 07. 1990 | Gymnasium Himmelsthür |
| 08. 1981 – 07. 1983 | Orientierungsstufe Nordstemmen |
| 08. 1977 – 07. 1981 | Grundschule Nordstemmen |

Publications

- 1996 A. Freise, E. Spencer, I. Marshall, J. Higinbotham: ‘A comparison of frequency and time domain fitting of ^1H MRS metabolic data’, *Bull. Magn. Reson.* **17** 1–4, 302
- 1997 I. Marshall, J. Higinbotham, S. Bruce, A. Freise: ‘Use of Voigt lineshape for quantification of in vivo H-1 spectra’, *Magnetic Resonance in Medicine* **37**(5) 651 – 657
- 1998 A. Freise: ‘Ein neues Konzept für Signal Recycling’, Diploma Thesis, University of Hannover
- 1998 H. Lück and the GEO 600 team: ‘The vacuum system of GEO 600’ in: E. Coccia, G. Veneziano, G. Pizzella (eds.) *Gravitational Waves*. Singapore, 356–359
- 2000 A. Freise, G. Heinzl, K.A. Strain, J. Mizuno, K.D. Skeldon, H. Lück, B. Willke, W. Winkler, R. Schilling, A. Rüdiger, and K. Danzmann: ‘Demonstration of detuned dual recycling at the Garching 30 m laser interferometer’, *Phys. Lett. A* **277**, 135–142
- 2000 A. Rüdiger for the GEO 600 team: ‘Detecting gravitational waves from quasi-continuous sources: the German-British project GEO 600’ in: M. Kramer, N. Wex, R. Wieblinski (eds.) *Pulsar Astronomy - 2000 and Beyond*, APS Conf. Ser. 202, 733–734
- 2000 B. Willke and the GEO 600 team: ‘The GEO 600 gravitational wave detector’ in: S. Kawamura, N. Mio (eds.) *Gravitational Wave Detection II*. University Academy Press, Tokyo, 25–34
- 2000 H. Lück and the GEO 600 team: ‘The status of GEO 600’ in: S. Meshkov (ed.) *Gravitational waves AIP*, Melville; AIP Conf. Proc. 523, 119–127
- 2002 A. Freise, M.M. Casey, S. Gossler, H. Grote, G. Heinzl, H. Lück, D.I. Robertson, K.A. Strain, H. Ward, B. Willke, J. Hough K. Danzmann: ‘Performance of a 1200 m long suspended Fabry-Perot cavity’, *Class. Quantum Grav.* **19**, 1389–1397
- 2002 B. Willke et al.: ‘The GEO 600 gravitational wave detector’, *Class. Quantum Grav.* **19**, 1377–1387
- 2002 H. Grote, G. Heinzl, A. Freise, S. Gossler, B. Willke, H. Lück, H. Ward, M.M. Casey, K.A. Strain, D.I. Robertson, J. Hough, K. Danzmann: ‘The automatic alignment system of GEO 600’, *Class. Quantum Grav.* **19**, 1849–1855
- 2002 G. Heinzl, A. Freise, H. Grote, K. Strain, K. Danzmann: ‘Dual recycling for GEO 600’, *Class. Quantum Grav.* **19**, 1547–1553

- 2002 K. Kötter, C. Aulbert, S. Babak, R. Balasubramanian, S. Berukoff, S. Bose, D. Churches, C.N. Colacino, C. Cutler, K. Danzmann, R. Davies, R. Dupuis, A. Freise, H. Grote, G. Heinzl, M. Hewitson, J. Hough, H. Lück, M. Malec, S.D. Mohanty, S. Mukherjee, S. Nagano, M.A. Papa, D. Robertson, B.S. Sathyaprakash, B.F. Schutz, A.M. Sintes, K.A. Strain, I.J. Taylor, A. Vecchio, H. Ward, U. Weiland, B. Willke, G. Woan: ‘Data acquisition and detector characterization of GEO 600’, *Class. Quantum Grav.* **19**, 1399–1407
- 2002 S. Gossler, M.M. Casey, A. Freise, H. Grote, H. Lück, P. McNamara, M. V. Plissi, D.I. Robertson, N. A. Robertson, K. Skeldon, K.A. Strain, C. I. Torrie, H. Ward, B. Willke, J. Hough, K. Danzmann: ‘The modecleaner system and suspension aspects of GEO 600’, *Class. Quantum Grav.* **19**, 1835–1842